



HAL
open science

FeCr composites : from metal/metal to metal/polymer via micro/nano metallic foam, exploitation of liquid metal dealloying process

Morgane Mokhtari

► **To cite this version:**

Morgane Mokhtari. FeCr composites : from metal/metal to metal/polymer via micro/nano metallic foam, exploitation of liquid metal dealloying process. Materials. Université de Lyon; Tōhoku Daigaku (Sendai, Japon), 2018. English. NNT : 2018LYSEI088 . tel-02094192

HAL Id: tel-02094192

<https://theses.hal.science/tel-02094192>

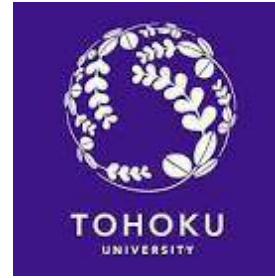
Submitted on 9 Apr 2019

HAL is a multi-disciplinary open access archive for the deposit and dissemination of scientific research documents, whether they are published or not. The documents may come from teaching and research institutions in France or abroad, or from public or private research centers.

L'archive ouverte pluridisciplinaire **HAL**, est destinée au dépôt et à la diffusion de documents scientifiques de niveau recherche, publiés ou non, émanant des établissements d'enseignement et de recherche français ou étrangers, des laboratoires publics ou privés.



INSA



N° d'ordre NNT : 2018LYSEI088

THESE de DOCTORAT DE L'UNIVERSITE DE LYON

opérée au sein de

INSA de Lyon

En cotutelle internationale avec

TOHOKU University

Ecole Doctorale N° EDA 034

Matériaux de Lyon

Spécialité / discipline de doctorat : matériaux

Soutenue publiquement le 15/11/2018, par :

Morgane Mokhtari

FeCr composites: from metal/metal to metal/polymer via micro/nano metallic foam, exploitation of liquid metal dealloying process

Devant le jury composé de :

Erica LILLEODDEN	Professeure	Helmholtz-Zentrum	Rapporteuse
Yannick CHAMPION	DR CNRS	Grenoble INP	Rapporteur
Alain HAZOTTE	Professeur	Université de Lorraine	Examinateur
Jean-Luc DUVAIL	Professeur	Université de Nantes	Examinateur
Jannick DUCHET-RUMEAU	Professeure	INSA de Lyon	Directrice de thèse
Eric MAIRE	DR CNR	INSA de Lyon	Directeur de thèse
Christophe LE BOURLOT	MCF	INSA de Lyon	Directeur de thèse
Hidemi KATO	Professeur	Tohoku University	Directeur de thèse
Takeshi WADA	Prof associé	Tohoku University	Directeur de thèse

Département FEDORA – INSA Lyon - Ecoles Doctorales – Quinquennal 2016-2020

SIGLE	ECOLE DOCTORALE	NOM ET COORDONNEES DU RESPONSABLE
CHIMIE	CHIMIE DE LYON http://www.edchimie-lyon.fr Sec : Renée EL MELHEM Bat Blaise Pascal 3 ^e etage secretariat@edchimie-lyon.fr Insa : R. GOURDON	M. Stéphane DANIELE Institut de Recherches sur la Catalyse et l'Environnement de Lyon IRCELYON-UMR 5256 Équipe CDFA 2 avenue Albert Einstein 69626 Villeurbanne cedex directeur@edchimie-lyon.fr
E.E.A.	ELECTRONIQUE, ELECTROTECHNIQUE, AUTOMATIQUE http://edeea.ec-lyon.fr Sec : M.C. HAVGOUDOUKIAN Ecole-Doctorale.eea@ec-lyon.fr	M. Gérard SCORLETTI Ecole Centrale de Lyon 36 avenue Guy de Collongue 69134 ECULLY Tél : 04.72.18 60.97 Fax : 04 78 43 37 17 Gerard.scorletti@ec-lyon.fr
E2M2	EVOLUTION, ECOSYSTEME, MICROBIOLOGIE, MODELISATION http://e2m2.universite-lyon.fr Sec : Sylvie ROBERJOT Bât Atrium - UCB Lyon 1 04.72.44.83.62 Insa : H. CHARLES secretariat.e2m2@univ-lyon1.fr	M. Fabrice CORDEY CNRS UMR 5276 Lab. de géologie de Lyon Université Claude Bernard Lyon 1 Bât Géode 2 rue Raphaël Dubois 69622 VILLEURBANNE Cédex Tél : 06.07.53.89.13 cordey@univ-lyon1.fr
EDISS	INTERDISCIPLINAIRE SCIENCES-SANTE http://www.ediss-lyon.fr Sec : Sylvie ROBERJOT Bât Atrium - UCB Lyon 1 04.72.44.83.62 Insa : M. LAGARDE secretariat.ediss@univ-lyon1.fr	Mme Emmanuelle CANET-SOULAS INSERM U1060, CarMeN lab, Univ. Lyon 1 Bâtiment IMBL 11 avenue Jean Capelle INSA de Lyon 696621 Villeurbanne Tél : 04.72.68.49.09 Fax :04 72 68 49 16 Emmanuelle.canet@univ-lyon1.fr
INFOMATHS	INFORMATIQUE ET MATHÉMATIQUES http://infomaths.univ-lyon1.fr Sec : Renée EL MELHEM Bat Blaise Pascal, 3 ^e étage Tél : 04.72. 43. 80. 46 Fax : 04.72.43.16.87 infomaths@univ-lyon1.fr	M. Luca ZAMBONI Bâtiment Braconnier 43 Boulevard du 11 novembre 1918 69622 VILLEURBANNE Cedex Tél :04 26 23 45 52 zamboni@maths.univ-lyon1.fr
Matériaux	MATERIAUX DE LYON http://ed34.universite-lyon.fr Sec : Marion COMBE Tél:04-72-43-71-70 –Fax : 87.12 Bat. Direction ed.materiaux@insa-lyon.fr	M. Jean-Yves BUFFIERE INSA de Lyon MATEIS Bâtiment Saint Exupéry 7 avenue Jean Capelle 69621 VILLEURBANNE Cedex Tél : 04.72.43 71.70 Fax 04 72 43 85 28 Ed.materiaux@insa-lyon.fr
MEGA	MECANIQUE,ENERGETIQUE,GENIE CIVIL,ACOUSTIQUE http://mega.universite-lyon.fr Sec : Marion COMBE Tél:04-72-43-71-70 –Fax : 87.12 Bat. Direction mega@insa-lyon.fr	M. Philippe BOISSE INSA de Lyon Laboratoire LAMCOS Bâtiment Jacquard 25 bis avenue Jean Capelle 69621 VILLEURBANNE Cedex Tél : 04.72 .43.71.70 Fax : 04 72 43 72 37 Philippe.boisse@insa-lyon.fr
ScSo	ScSo* http://recherche.univ-lyon2.fr/scso/ Sec : Viviane POLSINELLI Brigitte DUBOIS Insa : J.Y. TOUSSAINT Tél : 04 78 69 72 76 viviane.polsinelli@univ-lyon2.fr	M. Christian MONTES Université Lyon 2 86 rue Pasteur 69365 LYON Cedex 07 Christian.montes@univ-lyon2.fr

*ScSo : Histoire, Géographie, Aménagement, Urbanisme, Archéologie, Science politique, Sociologie, Anthropologie

Acknowledgements

First, I would like to thank Eric, Jannick and Kato-sensei for accepting me as student. I also want to thank Christophe and Wada-sensei for their good advices. Eric, Christophe, Jannick, Kato-sensei, Wada-sensei, thank you very much for your supervision and your support ! I also would like to thank Jérôme Chevalier and Etienne Fleury for welcoming me to their laboratories.

Then I would like to thank Yoshimi-sensei and Saida-sensei for reviewing my work on the Japanese side. I would like to thank Erica Lilleodden and Yannick Champion for reviewing and Alain Hazotte and Jean-Luc Duvail for being my examiners. Thank you all for spending time reading my work and listening to me and for all your feedbacks.

About funding, I thank ED34 for giving me a "contrat doctoral", Région Rhone-Alpes with the Explora sup program (CMIRA 138249) and European Union with Erasmus+ program which funded my stays in Japan, ESRF (Grenoble, France) and SLS, PSI (Villigen, Switzerland).

A lot of people contribute to this work due to their administrative support : Ito-san for being like a mum, Frida for spending time on mission order, Naoto Wada-sensei and Gael Sebald for their advices, Elyt max for the storage of my belongings and Jean-Yves Cavallé for making French and Japanese administration agree on my case.

For my experiments I would like to thank Jérôme, Sylvain, Nicolas, Xavier, Sophie, Joël, Gabriel, François, Oriane, Julie, Justine, Sebastien, Kader, Florian, Bérangère, Benjamin and others MATEIS members, Joo-sensei, Wei-sensei, Saito-san, Takamura-san, Park-san, Datekyu-san and others KINKEN members, Ly, Marion, Nour, Lucile, Sylvain, Baptiste, Jocelyn David, and others IMP members... and of course Eugénie for her help with all mechanical properties data she has collected. For synchrotron experiments I warmly thank Wolfgang, Anne and staff from ID11 (ESRF) and Tomcat (SLS) beamlines. I would like also to thank all people who should be on the previous lists and were forgotten. At the beginning of each chapter the people who helped to the chapter achievement will be cited.

I would like to thank Oriane, Gabriel, Thibaut and Alexandre for the warm atmosphere of our office, Oriane, Gwen, Justine, Théo and Sib for the funny meetings for preparing Christmas party and team building, Pierre-Antoine for having fun and having very useful scientific discussion about dealloying, all members of METAL and Kato-ken for sharing a lot of tea/lunch break and having fun together during parties. I will miss you all !

Finally I want to thank my family and friends for their love, their happiness and taking care of me during all these years.

Abstract

Nanoporous metals have attracted considerable attention for their excellent functional properties. The first developed technique used to prepare such nanoporous noble metals is dealloying in aqueous solution. Porous structures with less noble metals such as *Ti* or *Fe* are highly desired for various applications including energy-harvesting devices. The less noble metals, unstable in aqueous solution, are oxidized immediately when they contact water at a given potential so aqueous dealloying is only possible for noble metals. To overcome this limitation, a new dealloying method using a metallic melt instead of aqueous solution was developed. Liquid metal dealloying is a selective dissolution phenomenon of a mono-phase alloy solid precursor: one component (referred to as soluble component) being soluble in the metallic melt while the other (referred to as targeted component) is not. When the solid precursor contacts the metallic melt, only atoms of the soluble component dissolve into the melt inducing a spontaneously organized bi-continuous structure (targeted+sacrificial phases), at a microstructure level. This sacrificial phase can finally be removed by chemical etching to obtain the final nanoporous materials. Because this is a water-free process, it has enabled the preparation of nanoporous structures in less noble metals such as *Ti*, *Si*, *Fe*, *Nb*, *Co* and *Cr*.

The objectives of this study are the fabrication and the characterization of the microstructure and mechanical properties of 3 different types of materials by dealloying process : (i) metal/metal composites (FeCr-Mg), (ii) porous metal (FeCr) (iii) metal/polymer composites (FeCr-epoxy resin). The last objective is the evaluation of the possibilities to apply liquid metal dealloying in an industrial context.

The microstructure study was based on 3D observation by X-ray tomography and 2D analysis with electron microscopy (SEM, SEM-EDX, SEM-EBSD). To have a better understanding of the dealloying, the process was followed in situ by X-ray tomography and X-ray diffraction. Finally the mechanical properties were evaluated by nanoindentation and compression.

Résumé

Introduction

De nos jours, pour réduire les coûts et préserver les ressources naturelles, il est nécessaire de produire des matériaux toujours plus efficaces. Pour cette raison les matériaux architecturés sont de bons candidats. Parmi les matériaux architecturés on peut retenir les matériaux poreux qui peuvent être utilisés comme matériaux de structure s'ils préservent leurs propriétés mécaniques. Introduire des porosités traversantes ou en surface permet d'augmenter la surface active sans augmenter le volume, ce qui est utile pour des nombreuses applications notamment en électrochimie.

Depuis le début des années 2000, l'intérêt et le nombre de publications concernant les métaux nanoporeux s'est accentué considérablement (environ 40% d'augmentation par an [WIT 12]). A l'origine les métaux nanoporeux sont produits par désalliage en solution aqueuse [FOR 79] mais de nouvelles techniques telles que le désalliage dans un bain de métal liquide (technique adaptée aux métaux communs)[WAD 11b] ou encore le désalliage en phase vapeur (pour réduire la production de déchets chimiques)[SUN 16] sont en voie de développement. Le désalliage en solution aqueuse est la technique la plus souvent utilisée pour obtenir ces matériaux. Les métaux nobles comme l'or ont pu être préparés via cette méthode à partir d'alliages binaires. Les métaux moins nobles sont instables en solution aqueuse et s'oxydent immédiatement au contact de l'eau ce qui rend ce procédé inapplicable. Or les métaux de structure tels que le fer - qui allient bonnes propriétés mécaniques et coût limité - seraient utiles à l'état micro ou nanoporeux pour diverses applications.

Pour surmonter cette limitation, une méthode de désalliage dans un bain de métal liquide a été récemment développée au Japon. Le désalliage dans un bain de métal liquide permet une dissolution sélective d'une espèce chimique (l'élément soluble) à partir d'un alliage d'origine (le précurseur) composé de l'élément soluble et d'un élément cible (qui deviendra poreux) non soluble dans le bain de métal liquide. Quand le précurseur est plongé dans le bain de métal liquide, l'élément soluble va se dissoudre au contact du bain tandis que l'élément cible va se réorganiser spontanément afin de former une structure poreuse. Quand l'échantillon est retiré du bain, il est sous la forme d'une structure bicontinue composée de deux phases : l'une étant la structure poreuse composée de l'élément cible et l'autre est une phase dans laquelle est présente l'élément du bain avec l'élément en solution solide. Cette phase sacrificielle peut être dissoute par une attaque chimique afin d'obtenir le métal nano/micro poreux. Cette technique a déjà permis la préparation de nanométaux

purs moins nobles dont le Fe [WAD 13], Ti [WAD 11b], Ta [MCC 16c], des alliages microporeux (FeCr) [WAD 13] et de non-métaux nanoporeux (Si [WAD 14], C [YU 16]). Le choix des éléments du précurseur se fait par l'enthalpie de mélange [WAD 11b, TAK 05].

Objectifs

Cette étude est basée sur un des fondements de la science des matériaux : le tryptique procédé- microstructure-propriétés. Les objectifs principaux de cette thèse sont l'élaboration et la caractérisation microstructurale et mécanique de 3 différents types de matériaux par désalliage dans un bain de métal liquide : i) des composites métal-métal (FeCr-Mg), ii) des métaux poreux (FeCr) et iii) des composites métal-polymère (FeCr-matrice époxy). Le dernier objectif est l'évaluation du potentiel d'application de cette technique de désalliage à une problématique industrielle.

Cette étude est divisée en 9 chapitres.

Chapitre 1 : Etude bibliographique

L'étude bibliographique présentée dans ce chapitre est centrée sur le désalliage. Le chapitre est divisé en 4 parties. La première concerne les généralités sur les matériaux poreux notamment sur leur propriétés mécaniques. La seconde partie répond aux questions suivantes concernant le principe de désalliage : quels sont les mécanismes de désalliage ? Quelles sont les cinétiques de désalliage et de grossissements des ligaments ? Quels sont les matériaux employés ? Quelles sont les étapes de l'élaboration ? Comment la microstructure et la morphologie peuvent-elles être contrôlées ? Quelles sont les propriétés mécaniques obtenues ? Quelles sont les méthodes d'analyse employées ?

Ces études majoritairement basées sur le désalliage en solution aqueuse à partir d'alliages Au-Ag ont permis de mettre en évidence la présence de ligaments monocristallins [PET 09] dont la taille influence les propriétés mécaniques [HOD 07]. Une loi d'échelle a été proposée pour la prédiction de la limite d'élasticité [HOD 07] mais aucune loi n'est encore fiable pour prédire le module de Young. Des expériences *in/ex situ* ont déjà été menées sur l'or ce qui a permis d'améliorer la compréhension du désalliage [CHE 12a, CHE 13c, CHE 13d, PET 09, MAH 18, CHE 17]. Cependant, du fait d'importantes difficultés expérimentales, il n'existe pas de précédent d'expériences *in situ* de désalliage dans un bain de métal liquide (qui fera l'objet du chapitre 3).

Dans une troisième partie, les précédentes expériences d'élaboration de matériaux composites à partir de matériaux désalliés sont explicitées [MCC 16d, MCC 16b]. Les composites métaux/métaux ont été obtenus après désalliage et avant l'attaque chimique de la phase sacrificielle. Faciles à manipuler, ils ont souvent été utilisés pour étudier les cinétiques de désalliage/grossissement [WAD 16b, MCC 16c]. Les composites métaux/polymères ont été obtenus après infiltration de la mousse métallique par des polymères. Il a été démontré que l'infiltration permet d'améliorer les propriétés mécaniques des mousses tout en ayant un impact limité sur leur masse [WAN 13, WAN 15a, OKU 17,

OKU 18a]. Pour ces raisons des composites métal/métal et métal/polymères ont également été étudiés (voir chapitre 4, 6 et 7).

Enfin les études précédentes concernant le précurseur employé dans cette étude (Fe-(Cr)-Ni) ont été détaillées. Les cinétiques du désalliage et du grossissement ont été en partie étudiées et il a été prouvé que la température et le temps de désalliage sont des facteurs clés pour contrôler l'élaboration [SAI 16, TSU 14, WAD 13, ZHA 17]. Cependant l'influence de la composition du précurseur (présence ou non du Cr, ratio Fe/Ni) n'a pas été étudiée. Comme les précédentes études concernent les premières étapes du désalliage, la morphologie (chapitre 53) et la microstructure (chapitre 6) de structures "mûres" ont été étudiées ici. Leurs propriétés mécaniques ont été étudiées dans le chapitre 7.

Chapitre 2 : Acquisition et traitement d'images

Dans ce chapitre, les stratégies employées pour caractériser la microstructure, l'infiltration par les polymères et les propriétés mécaniques sont développées. La morphologie des composites, la microstructure des grains et la composition des échantillons ont été principalement analysées en 2D par microscopie électronique (MEB, MEB-EDX, MEB-EBSD) et par diffraction des rayons X (DRX). Des analyses 3D ont été principalement employées pour la caractérisation de la morphologie des mousses avec des reconstructions réalisées par tomographie aux rayons X. Les propriétés mécaniques ont été mesurées par nanoindentation et compression. La morphologie, la microstructure et les propriétés mécaniques ont été analysées à différentes échelles (du submicronique jusqu'à l'échelle du mm/cm). Les évolutions de la morphologie et de la structure cristallographique ont été étudiées pour différents temps via des analyses post-mortem et des analyses *in situ* (environ toutes les 2s pour la DRX et environ toutes les minutes pour la tomographie aux rayons X).

La combinaison d'instruments variés a permis une caractérisation multi-échelle et temporelle.

Chapitre 3 : Observation *in situ* du désalliage dans un bain de métal liquide par tomographie aux rayons X et diffraction des rayons X

Dans ce chapitre l'élaboration a été suivie *in situ* par tomographie aux rayons X et diffraction des rayons X.

Pour suivre le désalliage qui s'effectue à haute température et sous atmosphère contrôlée, un montage expérimental a dû être mis au point. La solution retenue a été d'encapsuler sous vide un morceau de précurseur taillé en pointe avec des copeaux de Mg dans un capillaire en quartz. Le chauffage laser présent sur la ligne [FIF 12] a été utilisé pour le suivi en tomographie et un chauffage par induction dans le cas de la diffraction. Toutes les expériences ont été réalisées à partir du précurseur $(\text{Fe}_{80}\text{Cr}_{20})_{30}\text{Ni}_{70}$.

Grâce au suivi par tomographie aux rayons X, l'observation du front de désalliage a été possible (cf. Fig. 1) et la cinétique du désalliage a été mesurée. Les résultats obtenus ont

été comparés aux simulations. Il a été démontré que la forme du précurseur et la quantité de Mg influe sur la cinétique. En effet, quand le Mg est saturé en Ni la progression du front de désalliage est stoppée.

Le désalliage observé par la DRX correspond à une transformation $CFC \rightarrow CC$. Une légère diminution du paramètre de maille au prémisses du grossissement due à la dissolution du Ni résiduel dans les ligaments est observée. Pendant le refroidissement, la phase de Mg et les ligaments de FeCr interagissent, créant des contraintes résiduelles thermiques dues aux différents coefficients de dilatation thermique.

Durant l'attaque chimique, la taille des ligaments de FeCr et de Mg/air ainsi que la progression du front de la gravure ont été imagées par tomographie aux rayons X. Les ligaments de FeCr ne sont pas attaqués par la solution d'acide nitrique. Une expansion globale de la mousse est néanmoins observée ce qui peut être comparé au délaminage observé dans le Chapitre 4. Cette expansion est plus élevée là où l'échantillon présente des défauts morphologiques.

Ce chapitre a montré la faisabilité du suivi *in situ* de l'élaboration par désalliage dans un bain de métal liquide. Cependant ces expériences ont été réalisées avec un contrôle limité de la température et de la quantité de Mg autour du précurseur ce qui rend la comparaison entre les échantillons difficiles. Pour que cette étude quantitative soit possible le montage expérimental doit être amélioré.

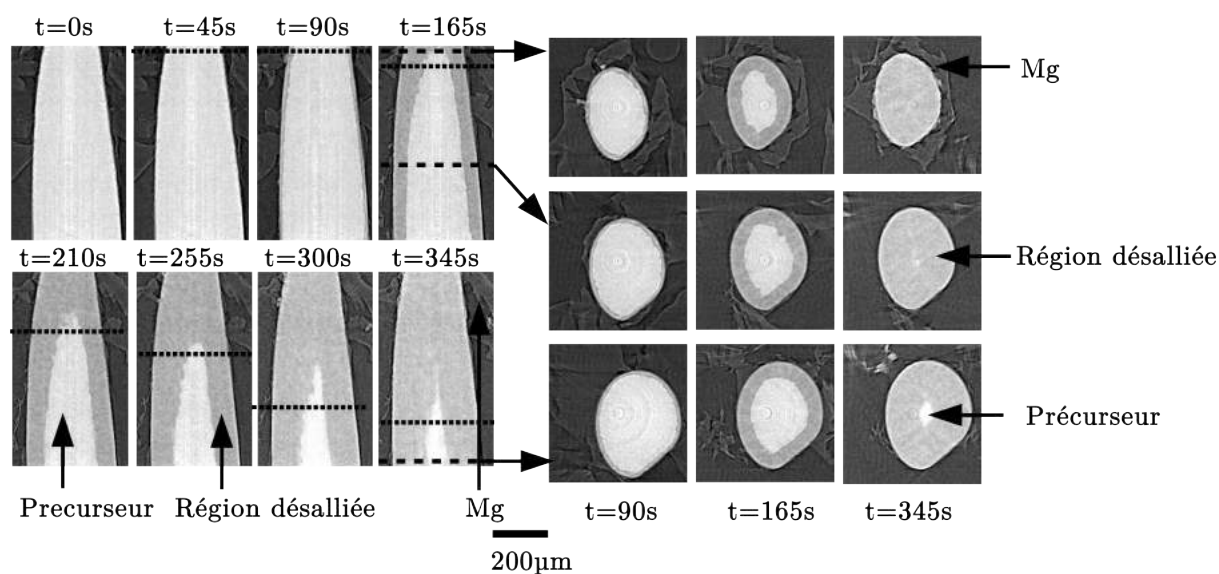


Figure 1: 2D images extraites des reconstructions 3D montrant l'évolution du front de désalliage.

Chapitre 4 et 5 : Elaboration et caractérisation des matériaux

Le chapitre 4 présente les différentes étapes nécessaires à l'élaboration des différents matériaux produits pour cette étude (cf. Fig. 2) et le chapitre 5 présente la caractérisation par tomographie aux rayons X de la morphologie des matériaux poreux.

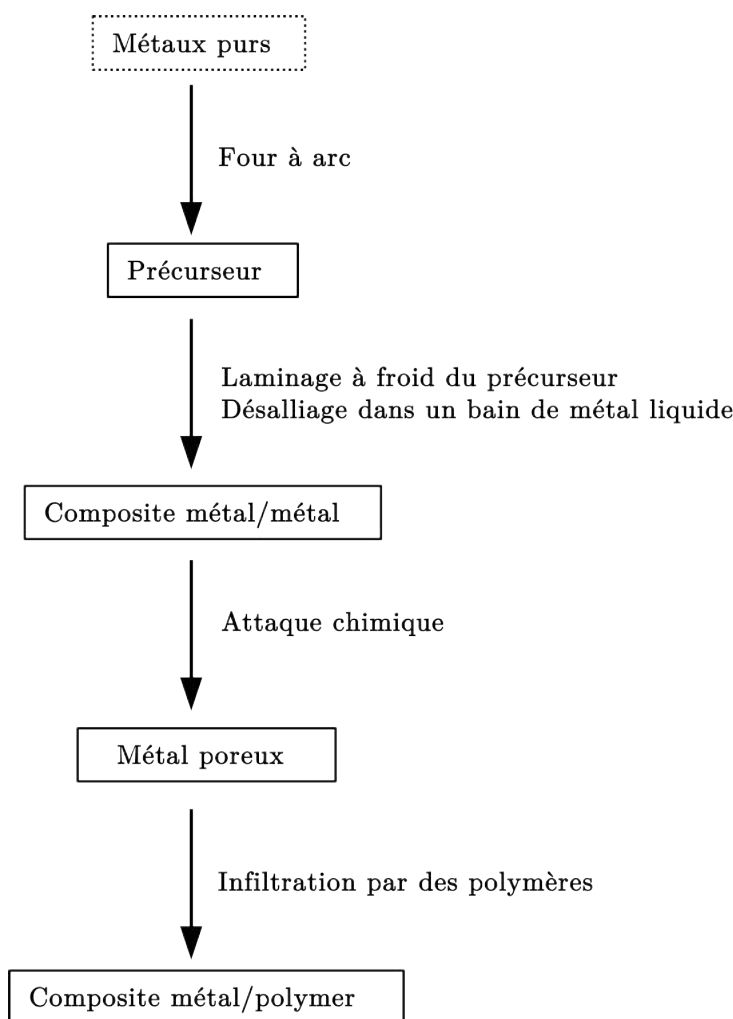


Figure 2: Les différentes étapes de l'élaboration.

Tout d'abord un précurseur (FeCr-Ni) a été élaboré par four à arc. Après immersion du précurseur pendant 1h à 820 °C dans un bain de Mg liquide un composite métal-métal (FeCr-Mg) a été obtenu. La porosité varie entre 30 et 70% environ. Les ligaments obtenus ont une taille moyenne d'environ 5 μm indépendante de la composition d'origine. En contrepartie la taille des pores varie entre 3 et 8 μm . La phase de Mg a été dissoute par attaque chimique pour obtenir un métal poreux (FeCr). Après infiltration de résines polymères (réseau époxy-amines) des composites métal/polymère ont été obtenus.

Pour cette étude 3 types de précurseurs ont été élaborés afin de modifier la porosité ($(\text{Fe}_{80}\text{Cr}_{20})_{30}\text{Ni}_{70}$, $(\text{Fe}_{80}\text{Cr}_{20})_{50}\text{Ni}_{50}$ and $(\text{Fe}_{80}\text{Cr}_{20})_{70}\text{Ni}_{30}$. Pour faire varier le comporte-

ment mécanique du composite métal/polymère, le pré-polymère époxy (DGEBA) a été polymérisé avec deux durcisseurs amines différentes : la Jeffamine D2000 pour produire un polymère caoutchoutique ou l'IsoPhorone Diamine (IPD) pour produire un polymère vitreux.

Les paramètres influençant la morphologie ont été étudiés :

- La porosité (la fraction d'air) est liée à la composition du précurseur (la porosité est quasiment égale au pourcentage de Ni dans le précurseur).
- La taille des ligaments et des pores augmente avec le temps et la température de désalliage.
- La taille des pores est contrôlée par la composition du précurseur et est du même ordre de grandeur que les ligaments [TSU 13, MIK 07, MCC 16c, GES 15, QIA 07, ERL 11]
- La surface spécifique (S) peut être évaluée à partir de la formule $S = \frac{3,7}{\rho d}$ avec ρ la densité et d la taille de ligament [DET 11].
- La tortuosité et la connectivité sont proches de 1 et indépendantes de la densité. La connectivité prouve la présence d'une structure bicontinue. La faible valeur de tortuosité promet de bonnes propriétés de transport [THO 09].

L'influence de l'attaque chimique a un impact modéré sur la morphologie de la mousse. Cependant pour les faibles densités un délaminage causé par l'étape de laminage à froid est observé. Mais dans l'ensemble, la morphologie de la phase de FeCr est préservée tout au long du processus. Il est donc maintenant possible de choisir la morphologie de la mousse en adaptant la composition du précurseur et les paramètres de désalliage. L'infiltration complète des pores de 0.8 μm à 8 μm a pu être menée à bien pour les 2 systèmes.

Chapitre 6 : Étude de l'évolution de la microstructure durant le désalliage

Dans ce chapitre l'effet du désalliage sur la microstructure a été étudié par MEB-EBSD avec des cartographies sur le précurseur et après désalliage.

Dans un premier temps, pour limiter le nombre de paramètres, il a été décidé de travailler sur un précurseur Fe₃₀Ni₇₀ pourvu de large grains. Comme dans l'étude précédente [SAI 16], les grains cubiques faces centrés (CFC) du précurseur ont été transformés en plusieurs grains cubiques centrés (CC) après désalliage et les ligaments sont monocristallins. Les effets du temps et de la température de désalliage sur la taille des grains désalliés ont été étudiés. Comme pour les transformations austénite-ferrite, la taille des grains désalliée est proportionnelle au temps et à la température de désalliage.

Puis l'influence du ratio Fe/Ni sur la microstructure a été mise en évidence :

- Cas d'un précurseur avec un faible ratio FeCr/Ni (cf. Fig. 3(haut)). Après désalliage les grains sont formés de quelques ligaments. Ceci s'explique par la réaction de désalliage qui progresse rapidement ce qui promeut la diffusion et la formation de ligaments CFC. Les ligaments subissent ensuite une transformation displacive CFC \rightarrow CC. En conséquence la nucléation de nouveaux grain est facilitée [SAI 16].

- Cas d'un précurseur avec un ratio élevé FeCr/Ni (cf. Fig. 3(bas)). Après désalliage des grains colonnaires avec une compétition d'orientation sont observés. Le front de désalliage progresse lentement et les atomes de Fe et Cr sont nombreux ce qui facilite une transformation diffusive et la croissance cristalline [POR 09, KUR 98].

Bien que la quantité de Ni ait une faible influence sur la morphologie (taille des ligaments indépendantes de la composition, faibles tortuosités...), elle contrôle les cinétiques de désalliage et la microstructure. L'ajout de Cr en quantité limitée permet la passivation des ligaments pendant l'attaque chimique mais influence peu la microstructure et la morphologie obtenue.

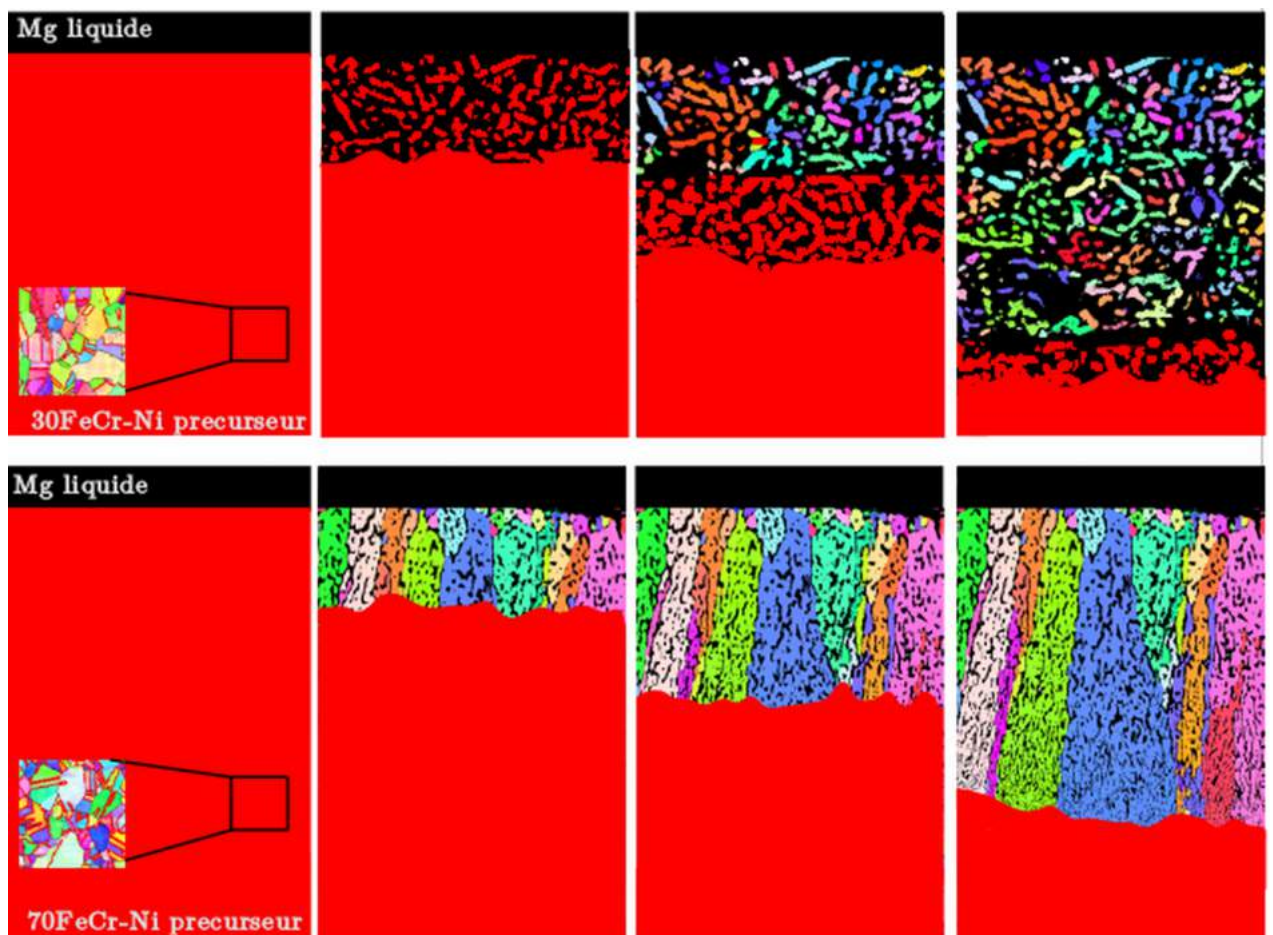


Figure 3: Les différents mécanismes de la formation des grains désalliés. Cas d'une transformation displacive pour les précurseurs à faible teneur en FeCr (haut). Cas d'une transformation diffusive pour les précurseurs avec une quantité élevée de FeCr (bas).

Chapitre 7 : Etude des propriétés mécaniques

Dans ce chapitre les propriétés mécaniques des composites FeCr-Mg et FeCr-polymère et des échantillons de FeCr poreux avec 2 tailles différentes de ligaments (5 et 1.5 μm) ont été évaluées par nanoindentation et compression.

Les modules de Young sont proportionnels au ratio FeCr/seconde phase et donc indépendants de la taille des ligaments (cf. Fig. 4). Les modules des composites sont inclus dans les limites proposées par le modèle de HASHIN et SHTRIKMAN [HAS 63] qui considère une distribution isotropique de fibres dans une matrice. A contrario les valeurs de module obtenus pour les mousses sont plus faibles que celles des différents modèles proposés dans la littérature. Cependant l'hypothèse selon laquelle les ligaments seraient uniquement soumis à de la flexion est vérifiée [GIB 97].

Par ailleurs, la dureté - et plus généralement le comportement plastique - est impactée non seulement par le ratio FeCr/seconde phase et le type de la seconde phase mais aussi par la taille des ligaments. Les ligaments les plus fins arborent de meilleures limites d'élasticité. Dans le chapitre 1, il a été mentionné que l'infiltration de micro/nanoporeux métallique par des polymères permet une amélioration des propriétés mécaniques. Ce résultat a été confirmé pour l'infiltration du réseau DGEBA-IPD (polymère vitreux) mais le polymère caoutchoutique n'a pas eu l'effet escompté : les propriétés mécaniques ont seulement été maintenues.

Le comportement des matériaux élaborés à partir du précurseur $(\text{Fe}_{80}\text{Cr}_{20})_{70}\text{Ni}_{30}$ présente des propriétés mécaniques correspondantes à celles des métaux. C'est intéressant dans le cas des échantillons poreux qui permettent la circulation d'un fluide à travers les pores tout en maintenant des propriétés mécaniques suffisantes (module de Young de 30 GPa, limite d'élasticité à 150 GPa). En revanche les propriétés mécaniques des composites FeCr-polymère et FeCr poreux élaborés à partir des deux autres précurseurs sont comparables à celles des autres matériaux poreux et composites élaborés par désalliage [OKU 18a, OKU 18b, WIT 12, MAM 16]: un faible module pour une grande limite d'élasticité ce qui est particulièrement intéressant pour des applications biomédicales.

Ces propriétés mécaniques peuvent être facilement contrôlées en faisant varier la densité, les tailles de ligaments et de grains et le type de la seconde phase (air ou polymère).

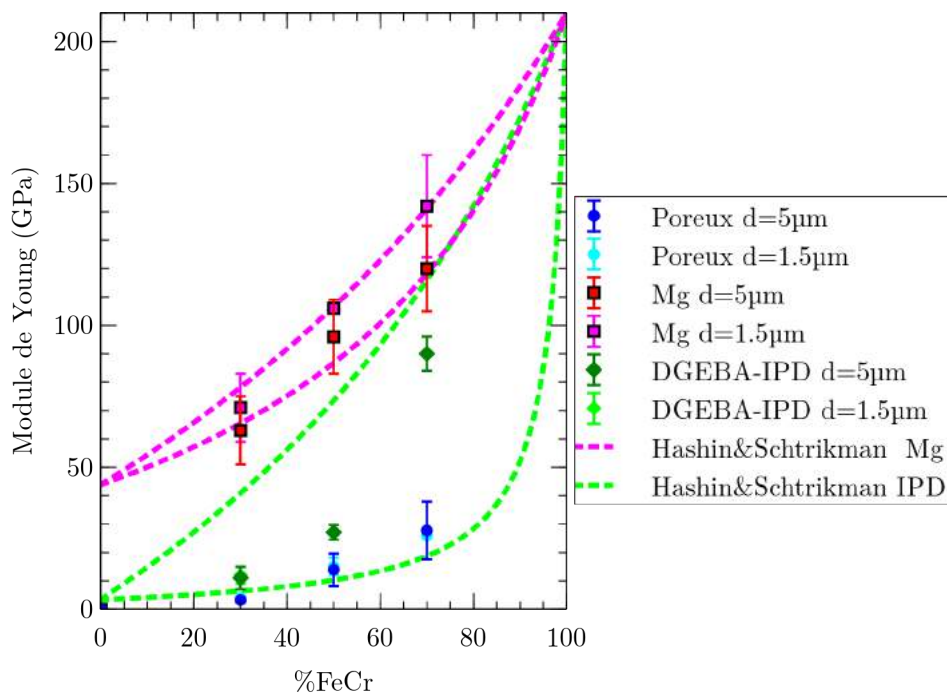


Figure 4: Evolution du module de Young avec le %FeCr pour différents composites. Les lignes pointillées correspondent aux limites calculées avec le modèle de HASHIN et SHTRIKMAN [HAS 63].

Chapitre 8 : Application du désalliage à un alliage commercial

Pour pouvoir industrialiser le procédé de désalliage il est important d'avoir un précurseur facile à obtenir et peu coûteux ce qui n'est pas le cas des précurseurs élaborés au four à arc à partir de métaux purs.

Une idée pour remplacer ces précurseurs coûteux serait d'utiliser des alliages commerciaux. Deux freins sont mis en avant : (i) pour que le désalliage s'effectue dans toute l'épaisseur du précurseur la quantité d'élément sacrificiel doit être supérieure à 20% dans le cas d'un précurseur CFC [ART 09], (ii) les alliages commerciaux comportent de nombreux éléments d'alliage qui, même présents en faible quantité, peuvent drastiquement changer les cinétiques du désalliage.

Dans ce chapitre, le cas de 3 alliages commerciaux ont été étudiés.

Le premier l'acier 310S comporte environ 18% de Ni et peu d'éléments d'alliage. Il a été montré que la quantité de Ni est insuffisante pour que le désalliage soit complet. L'épaisseur maximum de désalliage (environ 120 µm) est atteinte en moins de 10 min pour différentes températures. Il est donc possible de fonctionnaliser facilement la surface par un procédé peu sensible au temps et à la température et de choisir la taille des ligaments en adaptant la température.

Le deuxième alliage étudié est un superalliage de Ni l'Incoloy 800, choisi pour sa composition proche du précurseur maison $(\text{Fe}_{80}\text{Cr}_{20})_{70}\text{Ni}_{30}$. Après désalliage un acier ferritique poreux avec des ligaments d'environ $3\ \mu\text{m}$ a été obtenu, ce qui montre que l'ajout de quelques pour-cents de Si permet de diminuer la taille des ligaments, ce qui est bénéfique.

Le troisième cas étudié est celui de l'Incoloy 825, un autre superalliage de Ni. Il présente une quantité plus importante de Ni que le précédent et davantage d'éléments d'addition (Ti, Si, Mo, Cu..). Il a été désallié à 3 températures différentes menant à 3 microstructures différentes (cf. Fig. 5). La microstructure désalliée dépend de la microstructure du précurseur. Pour un précurseur présentant des inclusions, les inclusions et la matrice seront désalliés séparément, aboutissant à des variations de taille de ligaments sur la surface. A haute température [KAT 16], après formation des ligaments, un deuxième front de désalliage a été observé, aboutissant à une structure "hiérarchique" riche en Mo avec une distribution de pores bi-modale.

Le grossissement est contrôlé par la diffusion en surface qui varie avec la température de désalliage. On montre ici que l'ajout d'une petite quantité de Mo ou de Si joue le rôle d'inhibiteur du grossissement

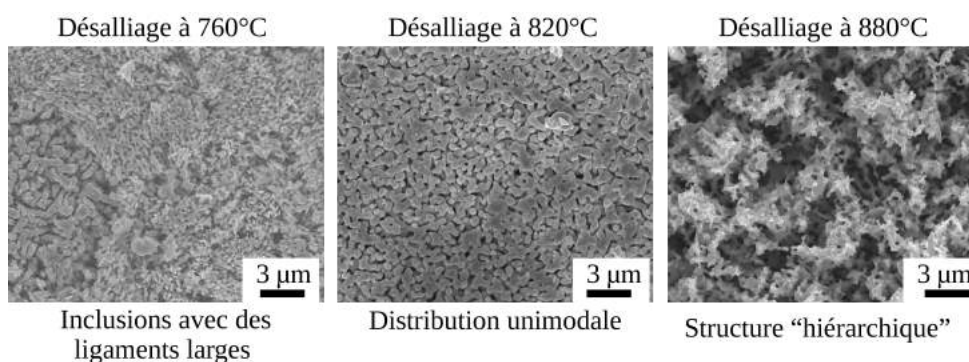


Figure 5: Les différentes microstructures obtenues après désalliage de l'Incoloy 825 à différentes températures.

Chapitre 9 : Conclusion générale

3 types de composites (métal/métal, métal poreux et métal/polymère) ont été élaborés par désalliage dans un bain de métal liquide à partir de précurseurs de différentes compositions.

Relations élaboration-microstructure

Tout d'abord les relations entre l'élaboration et la microstructure ont été étudiées. Les paramètres clés contrôlant le procédé ont été analysés.

La composition du précurseur est un paramètre prépondérant. La quantité d'élément sacrificiel va permettre ou empêcher le désalliage total et contrôler la cinétique de désalliage qui elle-même va influencer sur le mécanisme de formation des grains désalliés.

La composition du précurseur va elle aussi influencer le grossissement, certains éléments d'alliages mineurs vont jouer le rôle d'inhibiteur. La composition locale va également influencer sur la taille des ligaments locaux, permettant ainsi la création de morphologies complexes. La température et le temps de désalliage sont également des paramètres importants : plus la température est élevée ou le temps long plus le grossissement sera rapide. La vitesse de désalliage peut être proportionnelle ou inversement proportionnelle à la température de désalliage selon la composition du précurseur.

Les effets de l'attaque chimique et de l'infiltration sur la morphologie ont eux aussi été étudiés. La morphologie de la mousse n'est presque pas impactée par l'attaque chimique. Cependant, pour les échantillons de faible densité, un délaminage est observé ce qui rend la manipulation de ces échantillons difficiles. Ce phénomène peut être contrecarré par l'infiltration de polymère permettant le maintien de la mousse par la prévention du délaminage. L'infiltration ne présente presque aucune porosité résiduelle et la température de transition vitreuse n'est pas impactée par la présence de la mousse.

Relations microstructure-propriétés mécaniques

Les propriétés mécaniques ont été mesurées par nanoindentation et compression. Plus la quantité de FeCr est élevée meilleures sont les propriétés mécaniques. De même les propriétés mécaniques des composites métal/métal sont supérieures à celles des composites métal/polymère eux-mêmes supérieures à celles des échantillons poreux.

Le choix du polymère se révèle déterminant pour les propriétés mécaniques. Dans le pire des cas, les propriétés de la mousse sont préservées alors qu'avec un choix judicieux, les propriétés peuvent être améliorées.

Le choix de la seconde phase du composite et le ratio entre les phases permettent d'ajuster les propriétés mécaniques. Les mousses et les composites métal/polymères préparées à partir de précurseurs avec un ratio faible en FeCr présentent des propriétés mécaniques cohérentes avec les autres matériaux obtenus par désalliage.

Les propriétés mécaniques peuvent être améliorées en sélectionnant un meilleur polymère et en modifiant la taille des grains et des ligaments, le tout menant à une nouvelle classe de matériaux de basse rigidité mais de grande limite d'élasticité, hautement exploitable pour des applications biomédicales.

Application du désalliage à un contexte industriel

Pour appliquer le désalliage à un contexte industriel les alliages commerciaux sont de bons candidats. Selon la proportion en élément sacrificiel une fonctionnalisation de la surface ou une mousse sera créée. Les éléments d'alliage mineurs peuvent jouer le rôle d'inhibiteur du grossissement ce qui permet d'améliorer la surface spécifique.

Perspectives

Relations élaboration-microstructure

L'influence des paramètres sur le procédé a été étudiée, cependant les relations entre la microstructure avant-après désalliage n'est pas parfaitement clarifiée. La prédiction de la taille et de l'orientation des grains désalliés doivent être améliorées.

Relations microstructure-propriétés mécaniques

Concernant les propriétés mécaniques les mesures expérimentales doivent se poursuivre notamment pour clarifier l'impact de la taille des ligaments sur le comportement plastique, le comportement en tension etc. Il est possible d'envisager des tests *in situ* pour observer le comportement individuel des ligaments. Les propriétés magnétiques, thermiques, électriques, la résistance à la corrosion etc. n'ont pas été étudiées ici. Mais les mousses présentent généralement des propriétés de transports intéressantes et les aciers des propriétés magnétiques ce qui laisse espérer d'autres domaines d'applications possibles pour ces matériaux.

Application du désalliage à un contexte industriel

Les premiers résultats de désalliage d'alliage commerciaux sont très prometteurs. Ce travail pourrait être étendu à d'autres alliages. L'influence des éléments d'alliage sur les cinétiques de désalliage et la morphologie finale doit être étudiée plus en détails. Un autre frein à l'industrialisation du procédé est le remplacement du Mg - imposant de travailler sous atmosphère inerte - par un bain stable dans l'air.

Contents

Liste des ecoles doctorales	i
Acknowledgements	iii
Contents	xix
Introduction	xxv
1 Literature Review	1
1.1 Porous metals	2
1.2 Dealloying	4
1.2.1 Dealloying mechanisms	4
1.2.1.1 Dealloying principle	4
1.2.1.2 Dealloying kinetics	7
1.2.1.3 Coarsening	8
1.2.2 Elaboration	8
1.2.2.1 Precursor elaboration	9
1.2.2.2 Dealloying in aqueous solution	9
1.2.2.3 Liquid metal dealloying	10
1.2.2.4 Vacuum dealloying	12
1.2.3 Microstructure characterization	12
1.2.3.1 Foam morphology	12
1.2.3.2 Grain microstructure	14
1.2.4 Mechanical properties characterization	14
1.2.4.1 Correction of ASHBY and GIBSON law	15
1.2.4.2 Nanoindentation tests	15
1.2.4.3 Compression tests	16
1.2.5 <i>In/ex situ</i> dealloying experiments	17
1.2.5.1 Dealloying followed by X-ray imaging	17
1.2.5.2 Dealloying followed by X-ray diffraction	18
1.2.5.3 Dealloying followed by 2D imaging	19
1.2.5.4 Dealloying followed by electrochemical measurement	19
1.2.6 Composites produced from dealloying	19
1.2.6.1 Metal-metal composites	20
1.2.6.2 Metal-polymer composite	21

1.3	Dealloying from <i>Fe-(Cr)-Ni</i> precursors	22
1.3.1	Dealloying kinetics	22
1.3.2	Foam morphology	22
1.3.3	Grain microstructure	23
1.4	Conclusion	24
2	Images acquisition and processing	25
2.1	3D imaging : X-ray tomography	26
2.1.1	Principle	26
2.1.1.1	Set-up	26
2.1.1.2	Absorption contrast tomography	27
2.1.1.3	Phase contrast tomography	27
2.1.2	Volume processing	28
2.1.2.1	Definition	28
2.1.2.2	Image presentation and treatment	28
2.1.2.3	Binarisation	30
2.1.3	Quantitative analysis	31
2.1.3.1	Phase fraction	31
2.1.3.2	Connectivity	32
2.1.3.3	Geometrical tortuosity	32
2.1.3.4	Specific surface	33
2.2	2D imaging : SEM	34
2.2.1	SEM techniques	34
2.2.1.1	Surface imaging	34
2.2.1.2	Composition analysis	34
2.2.1.3	Grain microstructure analysis	35
2.2.2	Sample preparation	36
2.2.2.1	Porous samples	36
2.2.2.2	Composites samples	36
2.3	Conclusion	37
3	<i>In situ</i> observation of the liquid metal dealloying process by X-ray to-	39
	tomography and X-ray diffraction	
3.1	<i>In situ</i> observation of liquid metal dealloying by X-ray tomography	40
3.1.1	Experimental process	40
3.1.2	Case 1	41
3.1.3	Case 2	42
3.1.4	Simulation	45
3.1.4.1	Presentation of the diffusion model	45
3.1.4.2	Effect of precursor shape	47
3.1.4.3	Effect of <i>Mg</i> amount	48
3.2	<i>In situ</i> dealloying followed by X-ray diffraction	51
3.2.1	X-ray diffraction (XRD)	51
3.2.2	Experimental process	51
3.2.3	Results	52

3.3	<i>In situ</i> chemical etching followed by X-ray tomography	55
3.3.1	Experimental process	55
3.3.2	Results	56
3.4	Conclusion	58
4	Materials elaboration and characterization	59
4.1	<i>Fe-(Cr)-Ni /Mg</i> system	60
4.1.1	Mixing enthalpy	60
4.1.2	Phase diagrams	61
4.2	Precursors	63
4.2.1	Elaboration	63
4.2.2	Characterization	63
4.3	Metal/metal composites by liquid metal dealloying	65
4.3.1	Elaboration	65
4.3.2	Characterization	65
4.3.2.1	Validation of dealloying process	65
4.3.2.2	2D microstructure characterization	67
4.3.2.3	Sample homogeneity characterization	67
4.4	Porous metal	68
4.4.1	Elaboration	68
4.4.2	Chemical etching effect on foam microstructure	68
4.5	Metal/polymer composites	71
4.5.1	Epoxy-amine networks	71
4.5.2	Methods	71
4.5.2.1	ThermoGravimetric Analysis (TGA)	71
4.5.2.2	Differential Scanning Calorimetry (DSC)	73
4.5.3	Elaboration	73
4.5.4	Characterization	74
4.5.4.1	Polymer infiltration	75
4.5.4.2	Polymerization	76
4.5.4.3	Infiltration effect on foam microstructure	77
4.6	Conclusion	78
5	Study of porous samples morphologies by X-ray tomography	79
5.1	Qualitative analysis	80
5.2	Quantitative analysis	80
5.2.1	Volume fraction	80
5.2.2	Phase thickness	81
5.2.3	Specific surface	83
5.2.4	Connectivity	85
5.2.5	Geometrical tortuosity	86
5.3	Conclusion	87
6	Grain microstructure evolution during dealloying	89
6.1	Dealloying from $Fe_{30}Ni_{70}$ precursor	90

6.1.1	Effect of precursor preparation on precursor grain microstructure . . .	90
6.1.1.1	Cast alloy	90
6.1.1.2	Unidirectional melting and annealing	91
6.1.2	Effect of dealloying parameters on grain microstructure	92
6.2	Dealloying from $(FeCr)_xNi_{1-x}$ with $x = 30, 50$ and 70 precursors	94
6.2.1	From cold-rolled precursor samples	94
6.2.2	From recrystallized precursor samples	96
6.2.3	Partial dealloying	97
6.2.3.1	Different diffusion process	97
6.2.3.2	Microstructure analysis	98
6.2.4	Phase transformation during dealloying : model	100
6.3	Effect of Cr addition on grain microstructure	101
6.4	Conclusion	102
7	Mechanical properties of FeCr based composites	103
7.1	Nanoindentation	104
7.1.1	Nanoindentation parameters	104
7.1.2	Young's modulus	105
7.1.3	Hardness	107
7.1.4	Focus on porous FeCr	107
7.1.4.1	Comparison with existing models	107
7.1.4.2	Experimental data fitting	109
7.2	Compression	110
7.2.1	Methods	110
7.2.2	Comparison of the composites	110
7.2.3	Effect of $FeCr$ phase fraction	111
7.2.3.1	FeCr-Mg composite	111
7.2.3.2	Porous FeCr	111
7.2.4	FeCr-polymer composites	113
7.2.5	Densification	113
7.3	Comparison with others materials produced by dealloying	113
7.4	Conclusion	115
8	Application of liquid metal dealloying to commercial alloys	117
8.1	Commercial precursor	118
8.1.1	Research pressure	118
8.1.2	Parting limit pressure	118
8.1.3	Industrial pressure	118
8.1.4	Precursor's choice	119
8.2	Case of S310 stainless steel	120
8.2.1	Dealloying result	120
8.2.2	Dealloying kinetics	121
8.2.3	Coarsening behaviour	123
8.3	Case of Incoloy 800 nickel superalloy	124
8.4	Case of Incoloy 825 nickel superalloy	127

8.4.1	Dealloying Results	127
8.4.1.1	Phase analysis	127
8.4.1.2	Dealloying at 660 and 710 °C	127
8.4.1.3	Dealloying at 760 °C	128
8.4.1.4	Dealloying at 820 °C	129
8.4.1.5	Dealloying at 880 °C	130
8.4.1.6	Foam morphology	132
8.4.2	Dealloying kinetics	133
8.5	Conclusion	134
9	Conclusion and Perspectives	135
	References	139

Introduction

Nowadays to reduce costs and preserve raw materials, more and more efficient materials are expected. For these reasons, recently architected materials have become increasingly attractive. For example, porous materials are lighter than bulk materials and can be used as structural materials as long as they keep good mechanical properties. Making a porous material is also a solution to keep the volume constant while drastically increasing the surface. A high surface is necessary for many applications like catalyst or thermal exchanger...

Recently the interest for open-cell nanoporous metal foams increased. Originally produced by dealloying in aqueous solution, new techniques like dealloying in metallic melt, for common metals, or by vacuum dealloying (to reduce chemical wastes) were developed. Dealloying is a very simple process to get macroscopic-sized metals with micro/nano pores. Dealloying consists in the corrosion of the less noble element (known as soluble element) of an alloy (known as precursor). The remaining element (known as targeted element) of the alloy will self-organize into a 3D bicontinuous structure network of interconnected nanoscale ligaments. The most well known example is the nanoporous gold produced from *Au-Ag* precursor alloy.

Nanoporous metals made by dealloying present a plastic behaviour at nanoscale while they present a rather brittle fracture behaviour at macro-scale, especially during tensile test. In the last years, in order to improve the mechanical properties and to increase the possible applications from this porous metal, some composite materials have also been investigated: metal-metal composites and metal-polymer composites.

One of the basic in material science is the Elaboration/Process-Microstructure-Properties relationship triangle. The present work will also be based on this triangle in the case of porous $Fe_{80}Cr_{20}$ chosen for its abundance, low cost and good mechanicals properties. For this study, investigated properties will be mechanical properties as shown in Fig. 6.

The objectives of this study are:

1. To elaborate 3 different types of materials by dealloying process :
 - (a) metal/metal composites (FeCr-Mg);
 - (b) porous metal (FeCr);
 - (c) metal/polymer composites (FeCr-epoxy resin);
2. To understand how the microstructure (density, ligament size, pore size, grain sizes...) can be controlled.
3. To measure the resulting mechanical properties.
4. To evaluate the possible applications of dealloying in an industrial context.

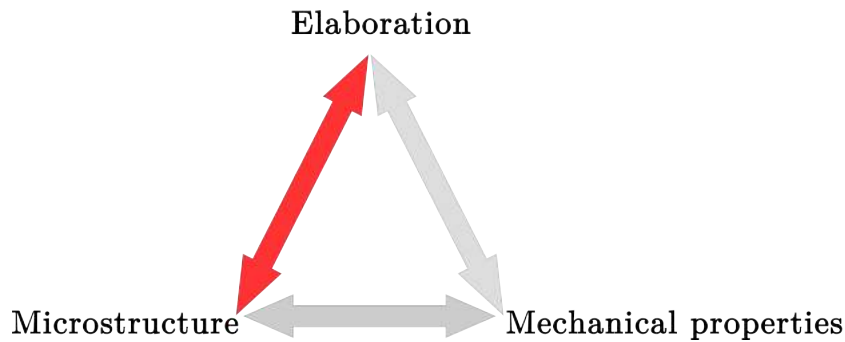


Figure 6: Elaboration-Microstructure-Mechanical properties relationship triangle.

This manuscript will be divided into 9 chapters.

- **Chapter 1** will present a literature review. After a quick focus on porous metals, the literature about dealloying will be investigated: principle, elaboration, characteristics of these materials. Then the background on *in/ex situ* experiments made on these materials will be investigated. The composite materials made from dealloyed materials will be described.
- **Chapter 2** will present the image processing. In order to characterize the microstructure, common tools of materials science used to characterize the microstructure will be exploited and described in this chapter. First, the microstructural characterization tools will be developed: foam morphology with 2D/ 3D imaging methods and grain microstructure characterization tools will be described. Then a focus on image processing and methods for image quantitative analysis will be done.

- **Chapter 3** will present an analysis of the process by *in situ* elaboration. Dealloying and etching front have been both studied *in situ* under synchrotron radiations. First dealloying will be followed by X-ray tomography, then by X-ray diffraction. To explain the effect of some experimental parameters on dealloying kinetics, some simulations will be presented. Then the chemical etching will be imaged by X-ray tomography.
- **Chapter 4** will answer to the first objective of this study by presenting the different steps to obtain metal/polymer samples. First, precursor samples will be melted by arc-melting. Then metal/metal composites will be produced by liquid metal dealloying. To get porous samples, one phase of the metal/metal composites will be chemically etched. Finally after pores infiltration of the porous sample by epoxy resin, metal/polymer samples will be obtained. For each step, the effect of the step on the resulting morphology and composition will be studied.
- **Chapter 5** will study by X-ray tomography the morphology of the obtained foams. Qualitative and quantitative analysis with density, characteristics lengths and topologically parameters analysis will be presented.
- **Chapter 6** will present the grain microstructure evolution during dealloying. The effect of the process on precursor grain microstructure will be studied. Then the effect of dealloying parameters (time and temperature) and precursor (composition and microstructure) on dealloyed grain microstructure will be investigated. To complete this study the microstructure and the composition of partially dealloyed samples will be analysed.
- **Chapter 7** will answer to the third objective of this study by investigating the mechanical behaviour of the 3 types of composites previously elaborated. Young's moduli and yield stresses will be investigated by nanoindentation. The comparison of the different mechanical behaviours will be done by compressive tests.
- **Chapter 8** will evaluate the possible applications of dealloying in an industrial context. The strategy employs in this work is the use of commercial precursors. Three cases will be studied : dealloying from a stainless steel precursor and dealloying from two different nickel superalloy precursors. The effect of dealloying parameters and minor alloying elements on resulting microstructure will be investigated.
- The last chapter, **Chapter 9** will present the general conclusions and the perspectives of this work.

Chapter 1

Literature Review

In this chapter, a literature review focused on dealloying, will be presented. This chapter is divided into four parts. In the first part a general overview on porous metals will be presented, like elaboration, characteristics and general mechanical behaviour. Then literature about dealloying will be investigated: principle, elaboration, characteristics of these materials will be outlined, followed by a background on *in/ex situ* experiments made on these materials. The composites made from dealloyed materials will be described. The last part will focus on recent studies on dealloying from *Fe-(Cr)-Ni* precursors.

Contents

1.1	Porous metals	2
1.2	Dealloying	4
1.2.1	Dealloying mechanisms	4
1.2.2	Elaboration	8
1.2.3	Microstructure characterization	12
1.2.4	Mechanical properties characterization	14
1.2.5	<i>In/ex situ</i> dealloying experiments	17
1.2.6	Composites produced from dealloying	19
1.3	Dealloying from <i>Fe-(Cr)-Ni</i> precursors	22
1.3.1	Dealloying kinetics	22
1.3.2	Foam morphology	22
1.3.3	Grain microstructure	23
1.4	Conclusion	24

1.1 Porous metals

Porous materials are good candidates in order to reduce matters amounts and costs. They can be used for materials lightening or to increase the specific surface.

The elaboration of porous metals may imply several different techniques. Some of them are similar to those used for porous polymers or porous ceramics processing. These methods may be ranked in different categories which sometimes require a lot of steps [BAN 01]:

1. from liquid metal (ex.: casting);
2. from solid metal (ex.: metallic powder in additive manufacturing);
3. from metal vapour (ex.: vapour deposition);
4. from metal ion solution (ex.: electrochemical deposition);

The method used as part of this study may be classified as a method from solid metal.

To describe the microstructure of a porous metal, different parameters should be considered [KRI 03]:

- microstructure, by observation of grains and phases including solid phase; it will be called grain microstructure in this study (cf. Chapter 2).
- geometric structure, by observation of the structure: arrangement of walls and pores as cell type (open or closed), connectivity, density, phase thickness etc. It will be called composite/foam morphology in this study (cf. Chapter 2).

Multiscale microstructure observation To observe the morphology of the porous metal, one method is to use standard 2D microscopy like optical and electronic microscopy [MAI 12]. Because of the low depth of field of optical microscopy, the observed sections must be polished, a difficult task for porous materials. On the opposite, Scanning Electron Microscopy (SEM) observations enable the measurement of the size of walls and pores [TAP 10] and the observation of fracture surface and SEM-EBSD (Electron Back Scattered Diffraction, please refer to Chapter 2) enables the observation of grain microstructure [GOU 04].

In order to obtain a global representation of porous metals and to be able to see the connectivity, the 3D study of these materials is also very important. These methods can be divided in two kinds of characterization methods: destructive or non-destructive [MAI 12]. Only non-destructive techniques will be involved as part of this work, as presented in Chapter 2.

Mechanical properties The mechanical behaviour of all cellular materials is largely described by GIBSON and ASHBY [GIB 97]. GIBSON and ASHBY laws consider low density porous materials with an elementary cell which must be representative of materials skeleton. Materials of this study are open-cell materials so this case will be the only one described. Equations 1.1 and 1.2 link the Young's modulus/yield stress (E_p/σ_p) of porous materials with materials relative density (ρ_r) and the Young's modulus/yield stress (E/σ) of its bulk constituent:

$$E_p = C\rho_r^n E \quad (1.1)$$

$$\sigma_p = C\rho_r^n \sigma \quad (1.2)$$

C and n are constant parameters, depending on the morphology of the porous sample. Suggested values for open-cell foam are $C = 1$ and $n = 2$ for the modulus and $C = 1/3$ and $n = 1.5$ for the yield stress if a bending dominated behaviour is considered.

Fig. 1.1 illustrates the compression stress-strain curve for a foam with a bending-dominated behaviour. The curve can be divided in 3 parts [ASH 06]:

1. below the yield stress the curve is similar to other compression curves: the foam presents a linear elasticity.
2. on the second part the stress is constant even if the strain increases: it corresponds to the "plateau stress" because the pores collapse.
3. then the pore size decreases, the ligaments impinge and the stress starts to drastically increase corresponding to the densification part.

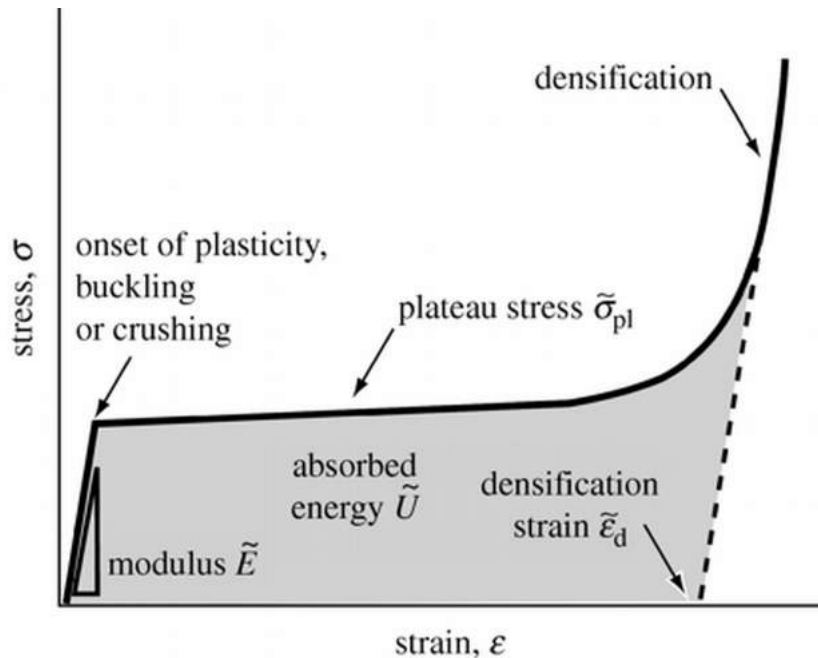


Figure 1.1: Typical stress-strain compression curve for foam showing an elastic part, a plateau stress and densification [ASH 06].

1.2 Dealloying

The first use of dealloying was reported on 15th century artifacts. Native South Americans were practising a form of dealloying. They immersed copper-gold or silver-gold based alloy into salty water that induced a surface dealloying. To get the color of pure gold at the surface, they were burning the materials after dealloying [LEC 71].

Dealloying is a very simple process to obtain nanoporous metals with cm-scale size. Dealloying consists in the corrosion of the less noble element (known as soluble element) of an alloy. The remaining element (known as targeted element) of the alloy will self-organize in a 3D bicontinuous structure network of interconnected nanoscale ligaments. The first experimental works were reported in the 60's [PIC 63], but A. J. Forty (in the 70's) is regarded as the inventor of dealloying. At the time, this technique was called “depletion gilding” rather than dealloying [FOR 79].

The interest in nanotechnologies recently increased, making dealloying a promising technique to get nanoporous materials with high potential for various applications [WIT 12]. An exemple of nanoporous gold is shown in Fig. 1.2.

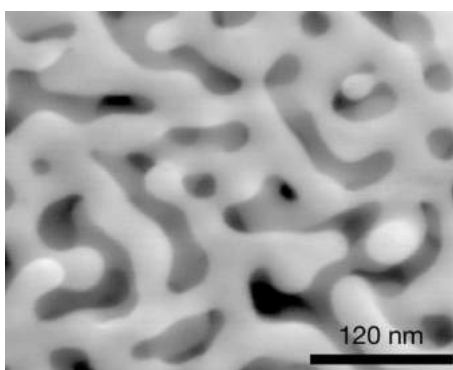


Figure 1.2: SEM image of *Au* dealloyed from $Au_{26}Ag_{74}$ precursor [ERL 01].

1.2.1 Dealloying mechanisms

1.2.1.1 Dealloying principle

The pores formation during dealloying is regulated by two main phenomena: the dissolution of the soluble element and the surface diffusion of the targeted element to form ligaments and to enable dealloying reaction to progress deeper in the sample. The main developed ideas are displayed in Fig. 1.3. Dealloying and coarsening behaviour were studied experimentally and analytically from the structural, thermodynamic and kinetic points of view [ERL 01, ERL 03, ERL 04, ERL 09, ERL 11, ERL 12, KOL 11]. However a lot of question as for example the influence of each parameters on the final foam morphology and grain microstructure are remaining.

In aqueous solution Dealloying in aqueous solution is sometimes controlled by the electrochemical potential at the metal/electrolyte interface. Below the critical potential the surface remains smooth, uncorroded and targeted element-rich. Above the critical potential, dealloying occurs. The critical potential depends on many factors but the precursor alloy composition is a key one [PIC 67, PIC 83]. Below a critical soluble element amount, there is no critical potential. Kinetic Monte Carlo simulation give the minimum amount of *Ag* as 55% for an *Au-Ag* precursor [ART 09]: it is defined as the parting limit. On the dealloying front some interface instabilities appear because of the competition between roughening phenomenon and smoothing phenomenon. These interface instabilities lead to the ligaments formation. To reduce the surface area ligaments are coarsening. Coarsening proceed by pinch-off and Rayleigh instabilities which can lead to large voids inside the ligaments. To control and slow down coarsening, a third element like *Pt* can be introduced into the precursor which will segregate at the reaction interface because of its lower mobility [ERL 11, KOL 11, WIT 12, MCC 16a].

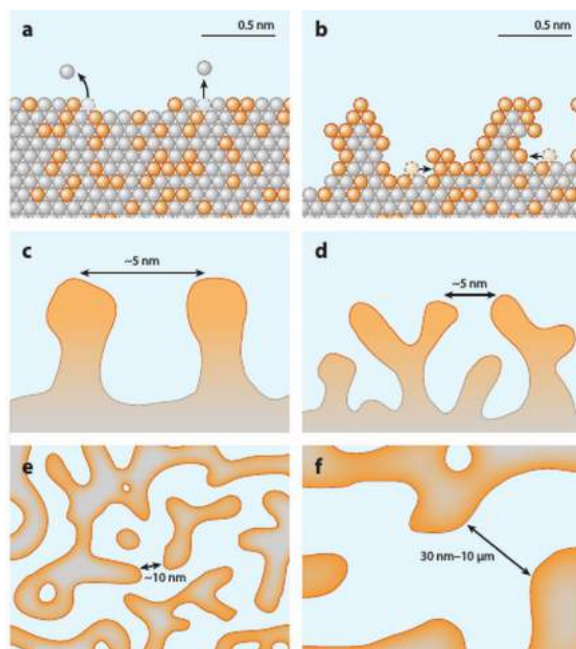


Figure 1.3: Working model for porosity evolution in dealloying in the *Ag-Au* alloy system (*Ag*, gray; *Au*, orange). (a) The rate-limiting step is the formation of terrace vacancies, which then grow into lateral vacancy clusters. (b) As dissolution proceeds layer by layer, surface diffusion passivates low-coordination sites with *Au*, leading to surface roughening. (c,d) As dealloying continues, there is insufficient *Au* to fully passivate the increasing surface area, leading to undercutting and bifurcation of ligaments. (e) The result of this process is a bicontinuous porous structure in which ligaments have *Au*-rich surfaces and *Ag*-rich interiors. (f) As coarsening increases the length scale of the initial structure, residual *Ag* atoms are exposed and dissolved, leaving a final structure with far reduced *Ag* content [MCC 16a].

Liquid metal dealloying Let's now focus on the liquid metal dealloying principle. This method was developed in the 2010's to overcome the limitation of dealloying in aqueous solution. First the production of α and β *Ti* [WAD 11b, WAD 11a] then *FeCr* [WAD 13], *Nb* [KIM 14], *Si* [WAD 14].... In this case, the aqueous solution is replaced by liquid metal. Liquid metal dealloying also presents a kinetic competition between dissolution and interface diffusion. First it will present an interfacial spinodal decomposition with the formation of rich targeted element domain at nanoscale for the early dealloying (cf Fig. 1.4 (left top)). Then, this rich targeted element droplet will become disconnected aligned filament while dealloying front reaction progress (cf Fig. 1.4 (left bottom)). And finally the progression of this reaction, they will become interconnected ligaments (cf Fig. 1.4 (right)). Some similarities with eutectic solidification can be found [GES 15, MCC 18a, WAD 16b].

One of the main differences between chemical and liquid metal dealloying is the temperature. For liquid metal dealloying, a high temperature is necessary to melt bath element and to thermally activate the liquid metal dealloying reaction. This high temperature implies higher dealloying front velocity because the soluble element diffusivity in the molten bath increases with the temperature. That makes liquid metal dealloying sometimes limited by the diffusion of the dissolving component in the molten metal while in chemical dealloying, dealloying rate is controlled by detachment kinetics of the soluble component (interface limited) [GES 15, MCC 18a].

The presence or absence of a bicontinuous structure is determined by precursor composition. Below the parting limit, a partial dealloying will occur whereas beyond this limit the sample will be fully dealloyed and present a bicontinuous structure. A high limit also exists for the sacrificial element: if its concentration is too high, continuity will be lost for the targetted element, leaving small porous particles of the targetted element in the molten bath [GES 15, WAD 16a, MCC 16c].

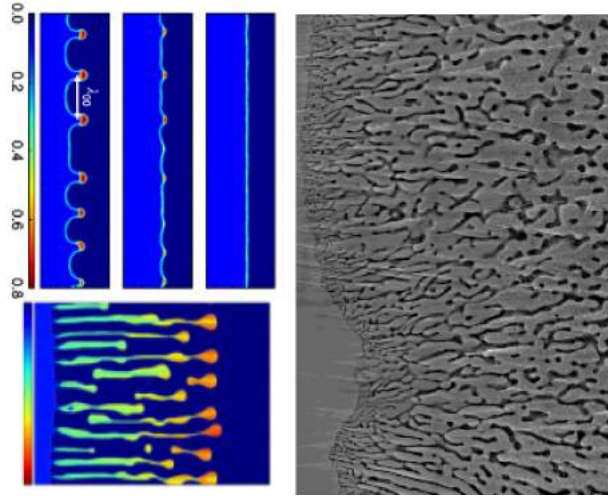


Figure 1.4: Interfacial spinusoidal decomposition : 2D phase-field simulation showing the formation of A-rich compositional domains and the resulting corrugation of the solid-liquid interface (left top) [GES 15], diffusion-coupled growth : 2D phase-field simulation showing lamellar structure growth (left bottom) [GES 15], SEM micrograph of partial dealloying showing disconnected aligned filaments transforming into connected ligaments (right).

1.2.1.2 Dealloying kinetics

In the case of a planar interface, the dealloying front reaction is also planar. The dealloying depth is defined by the dealloyed layer thickness. To calculate the dealloying depth (x) depending on the time (t), the expression presented in equation 1.3 is often used [WAD 16b, TSU 13, MIK 07, MCC 16c, GES 15], introducing the constant n .

$$x = (kt)^n \quad (1.3)$$

where k can be expressed depending on a constant (k_0), the activation energy (E), the gas constant (R) and the temperature T in equation 1.4

$$k = k_0 \exp\left(\frac{-E}{RT}\right) \quad (1.4)$$

In equation 1.3, $n = 0.5$ corresponds to layer growth controlled by diffusion, $n = 1.0$ corresponds to an interface reaction. Therefore if $n = 1$ dealloying is limited by extraction of soluble component atoms from precursors sample while when $n = 0.5$ the dealloying is limited by soluble component atoms diffusion in the melt bath. For liquid metal dealloying, an n coefficient close to 0.5 is experimentally and numerically measured, which means that dealloying is controlled by diffusion of soluble element [WAD 16b, TSU 13, MCC 16c, KIM 16, GES 15].

1.2.1.3 Coarsening

Dealloyed materials are known to continuously increase their ligament diameter during dealloying. It was previously shown that for both chemical and liquid metal dealloying coarsening behaviour are regulated by one dominant mass transport mechanism, following Herring's grain growth in polycrystalline solid analysis. The ligaments size (d) depending on coarsening time (t) and initial ligament size (d_0) can be calculated with equation 1.5 where n' is a constant (coarsening component), k' the pre-exponential factor and D' the surface diffusivity [TSU 13, HER 50, MCC 18b].

$$d^{n'} - d_0^{n'} = k'D't \quad (1.5)$$

D' can be expressed depending on a constant (D'_0), the activation energy (E'), the gas constant (R) and the temperature (T) in equation 1.6 .

$$D' = D'_0 \exp\left(\frac{-E'}{RT}\right) \quad (1.6)$$

In equation 1.6, $n' = 4$ suggests that coarsening happens because of relaxation of the roughened surface by surface diffusion while $n' = 3$ suggests a reaction led by volume diffusion [HER 50, DON 93]. Both dealloying in aqueous solution and in metallic melt bath result in n' coefficient around 4 [TSU 13, MCC 16c, QIA 07, LUO 13, HU 16]. For liquid metal dealloying, n' have sometimes been found between 3 and 4 which could suggest that diffusion inside the solid or inside the metallic bath also occurs.

1.2.2 Elaboration

There are currently three main techniques to obtain nanoporous metal by dealloying. Many noble porous metals are prepared by dealloying in aqueous solutions including *Au*, *Ag*, *Pt*, *Pd*, *Ni* and *Cu* from respectively *Au-Ag* [FOR 79], *Au-Cu* [MOR 11], *Au-Ni* [ROU 07], *Ag-Al* [LU 07], *Pt-Cu* [PUG 03], *Pd-Co* [HAK 09a], *Ni-Cu* [HAK 09b] and *Cu-Mn* [MIN 94] precursors.

However it is difficult to get common metal by dealloying in aqueous solution because they usually oxidizes in water, that's why common metal/alloys and elements like *Ti*/*Ti*-based alloy, *Fe*/*Fe*-based alloy, *Cr*, *Nb*, *Si*, *C* and *Ta* are usually elaborated by liquid metal dealloying from respectively *Ti-Cu* [WAD 11b], *Fe-Ni* [WAD 13], *Cr-Ni* [WAD 13], *Nb-Ni* [KIM 14], *Si-Mg* [WAD 14], *C-Mn* [YU 16], *Ta-Ti* [MCC 16c] precursors.

The third method appeared recently: the vacuum dealloying with the preparation of porous *Co*, *Cu* and stainless steel from respectively *Co-Zn* [LU 18], *Cu-Zn* [SUN 16] and high-manganese 316L stainless steel-*Mn* [REN 17] precursors.

Even if many porous materials can be produced by dealloying, nanoporous gold prepared from *Au-Ag* precursor has been the primary subjects so there are the most documents in the literature. Therefore the result of this study will be often compared with nanoporous gold.

1.2.2.1 Precursor elaboration

The precursor preparation determines the shape, the composition, the grain microstructure...of dealloyed samples. To control precursor homogeneity, precursor grain size and grain energy, the elaboration strategy was investigated. Most of precursor alloys are crystallines and are prepared by arc-melting or induction melting. The post-process after arc-melting/induction melting differs from one team to another. The most common is homogenization treatment [HAK 07, JIN 09] which can be followed by cold-rolling [HAK 09b]. Except homogenization, post-treatment may imply tilt-casting [KIM 16, MCC 16c], cold-rolling [WAD 13]...

Amorphous sample of noble alloys (gold or silver based alloy) or common metal alloys (Ti based alloy) are prepared by melt spinning after arc-melting of pure elements [SCA 12, WAN 14, BAR 16b]. Thin metallic glass films prepared by magnetron sputtering are also used as precursor for dealloying process [WAN 14].

Bulk precursors can also be single crystals produced by Czochralski method [REN 06]. The utilization of powder for preparing precursor by SPS [KON 15] or by mixing by ball milling, compacted by dry pressing facility and then melt by arc melting [CHE 16], were also reported. Some precursors are directly processed into their final shape as nanowire [LIU 12], nanoparticles [CHE 13e], powder [WAD 14, YU 16] and thin film [SEK 08].

1.2.2.2 Dealloying in aqueous solution

Dealloying in aqueous solution is the most common technique to obtain nanoporous noble metals. This technique is mainly used for noble metal however some experiments on common metal were also performed on $Fe-Mn$ precursor. The resulting nanoporous Fe was partially oxidized as expected from the low standard potential of Fe [HAK 11]. Aqueous solutions of nitric acid (HNO_3) with various concentrations are commonly used [WAN 15d] but it was also reported for examples the utilization of HF [WAN 15c], HCl [WAN 15b], H_2SO_4 [LUO 13], H_3PO_4 [CHE 12b], HBF_4 [ZHA 13], $NaOH$ aqueous alkali [LIU 12], $NaCl$ saline solution [ZHA 10], $HClO_4$ [YE 16], $(NH_4)_2SO_4$ [QIU 14] and $AgNO_3$ [SNY 08].

Two different types of dealloying in aqueous solutions have been used :

1. Dealloying by free corrosion:

It is the simplest and the oldest method to get nanoporous metals. The precursor is simply immersed in an electrolyte and a selective dissolution occurs [WIT 12]. Dealloying by free corrosion is difficult to control and leads to cracks formation especially on thin films [SUN 08, LU 07]. Fig. 1.5 displays thin nanoporous gold film with through-thickness cracks owing to high film stress during dealloying.

2. Dealloying by using electrochemical cell:

To facilitate the dissolution of the soluble element, a current may be applied to the system thanks to a convectional three-electrode electrochemical cell. A potentiostat regulates the electrical potential which leads to the control of the dissolution and diffusion rate of the alloy compounds [WIT 12]. During dealloying, the alloy serves as

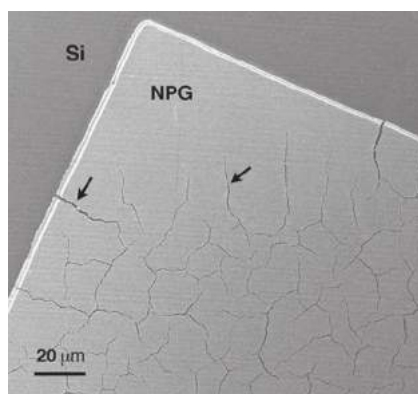


Figure 1.5: Nanoporous gold prepared from $Au_{30}Ag_{70}$, with through-thickness cracks owing to high film stress during dealloying [WIT 12].

the anode of the electrochemical cell, and a positive potential is applied to induce the selective dissolution. To induce this reaction, the critical potential must be found. The potentiostatic dealloying is held around the critical potential. After a long dealloying time, it leads to a crack free nanoporous metal. When a higher potential is selected, the soluble element residue is decreasing and the process is faster but some cracks may appear and a surface oxide monolayer is forming [WIT 12].

The galvanostatic dealloying prevents the direct control of soluble element dissolution rate by controlling the area current with the control of the anodic current. This method is useful for fabrication of crack-free thin uniform nanoporous metal films constrained by a substrate [WIT 12]. However, on bulk materials, large shrinkages (up to 30% of the volume) were noticed [PAR 06]. Cracks and shrinkage can be prevented by increasing residual soluble element amount.

1.2.2.3 Liquid metal dealloying

Even if the metal alloy corrosion in molten baths and salt was firstly reported in 1959 [HAR 59, MCC 16a], the liquid metal dealloying was developed in the 2010's. Liquid metal dealloying is the generalization of aqueous dealloying to all liquids. Common metals are unstable in aqueous solution, which make dealloying in these kind of solutions impossible. Liquid metal dealloying method is a selective dissolution phenomenon of a solid alloy precursor: one component (known as soluble component) is soluble in the metallic melt while the other (known as targeted component) is not. When the solid precursor is immersed in the metallic melt, only atoms of the soluble component dissolve into the melt, inducing a spontaneously organized bicontinuous microstructure formed by the targeted and a sacrificial phases (the atoms of the sacrificial phase in solution in the melt phase). After cooling down to room temperature, this sacrificial phase can be removed by selective chemical etching to obtain the final nanoporous materials with the targeted composition. Nanoporous *Ti* resulting of dealloying from *Ti-Cu* precursor in *Mg* melt can be found in Fig. 1.6. The elements selection strategy to design the dealloying reaction is based on the interaction (enthalpy of mixing) between atoms: targeted and soluble elements should

be able to be mixed together and soluble and bath elements should also be able to be mixed together while targeted element and bath element should not be able to be mixed [WAD 11b]. Mixing enthalpy values can be observed in [TAK 05]. This process is also possible with a solid metal bath instead of a liquid metal bath [WAD 16b].

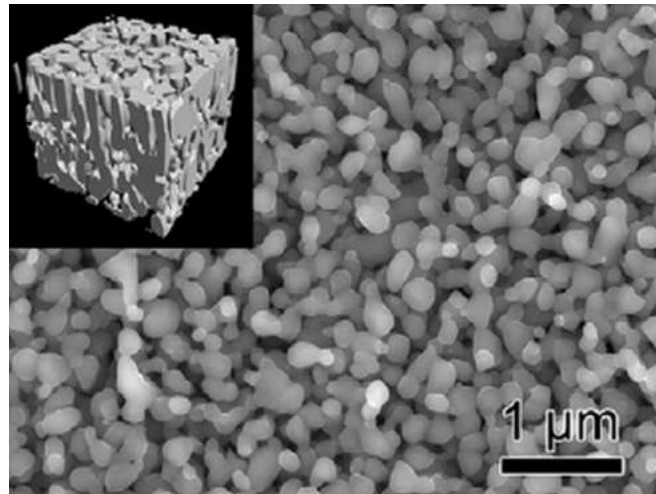


Figure 1.6: Nanoporous Ti prepared by liquid metal dealloying from $Ti_{30}Cu_{70}$ precursor [WAD 11b].

1.2.2.4 Vacuum dealloying

This recent technique enables to get nanoporous metals without using any chemical agent. The precursor sample is introduced in a under vacuum furnace then heated. If the saturation vapour pressure of precursor constituents are different, one element can be vaporized while the other will re-organize and form a nanoporous structure [LU 18, SUN 16, REN 17].

In conclusion, there is no standardized preparation neither for precursor nor for dealloying that make difficult the comparison between different samples.

1.2.3 Microstructure characterization

1.2.3.1 Foam morphology

This part focuses on foam morphology: ligaments and pores size. The most important fact to remember is maybe that the pores and ligaments size increases with dealloying time and temperature. The ligament size is linked with the specific surface which is a preponderant factor for electrochemistry applications. Therefore the smallest morphology is often desired.

Aqueous dealloying For aqueous dealloying by free corrosion, typical ligaments lower size is around 30 nm [ERL 09, YE 14]. When using an applied voltage it is possible to decrease characteristics lengths until reaching about 2 nm [SNY 10, SNY 08, PAR 06]. On the contrary after a long time or a high temperature coarsening, pores can reach up to 100 nm, ligaments up to 200 nm [CHE 16, LI 16] and even few micrometers with heating treatment [CHE 12a, KER 10]. Pores and ligaments size are controlled by electrolyte (type and acid concentration), electric potential, temperature and precursor compositions. Obtaining small pores requires a low temperature or a very high potential. Foam morphology was also studied [ZIE 16, DET 11, MAN 17].

The amount of residual sacrificial element increases when the pore decreases. In case of *Au-Ag* precursor the residual amount of *Ag* can vary from 0 to 25%. Small pores ligaments are highly desired while small pores implies the presence of residual *Ag* which can be critical for mechanical properties [SNY 08, QIA 07, KRE 17].

The influence of time and acid concentration on ligaments and pores size is shown in Fig. 1.7. Low acid concentration and long dealloying time implies a large coarsening.

Liquid metal dealloying Concerning liquid metal dealloying, ligaments lower reported size is 45 nm [WAD 16a, WAD 11a, YU 16] and about some micrometers for the highest reported ligaments size [WAD 13, MCC 16c], with a few hundred nanometers as standard values [KIM 14, WAD 14].

Pores sizes were also investigated by simulation, predicting pores size from several nanometers to several micrometers [GES 15], which is consistent with experimental values [YU 16, WAD 13, CHE 13b]. The evolution of pores size with dealloying depth was also investigated by simulation [GES 15].

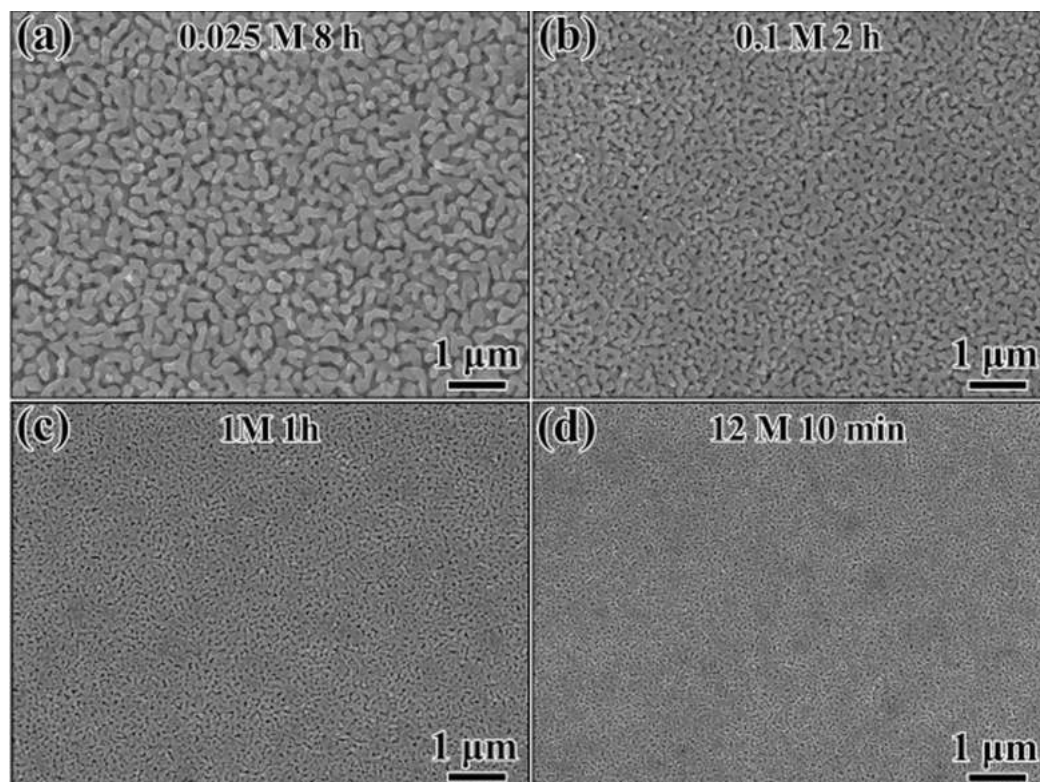


Figure 1.7: Surface morphologies of the resulting nanoporous *Ag* dealloyed from $Ag_{45}Mg_{35}Ca_{20}$ precursor at room temperature in (a) 0.025 mol L^{-1} *HCl* solution for 8 h, (b) 0.1 mol L^{-1} *HCl* solution for 2 h, (c) 1 mol L^{-1} *HCl* solution for 1 h and (d) 12 mol L^{-1} *HCl* solution for 10 min [LI 16].

The variation of ligaments/pores size is smaller in the case of liquid metal dealloying because of the limited temperature range where the metal bath is on liquid form.

Relationship between melting temperature and ligament size The evolution of the ratio of dealloying temperature/targeted element melting point with the ligament size was investigated. A linear relation was found between both parameters and this relation could be applied on both liquid metal and aqueous dealloying. Therefore, taking a high melting element as targeted element can be a solution to obtain a small morphology [MCC 18a, CHE 13a].

1.2.3.2 Grain microstructure

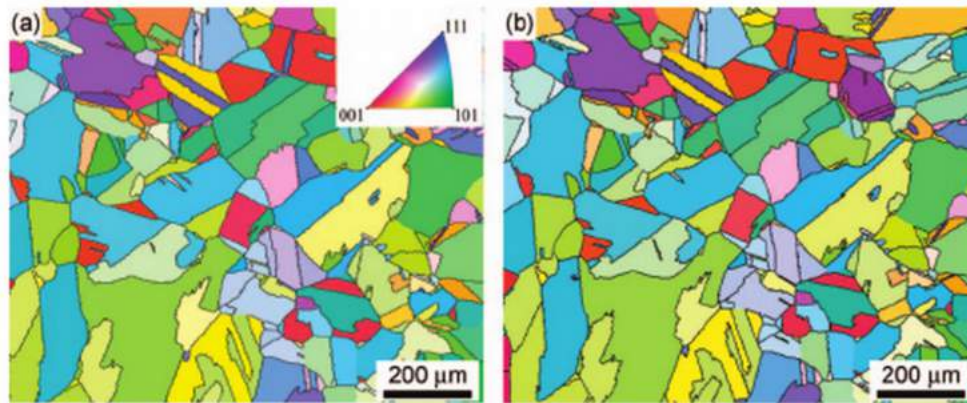


Figure 1.8: SEM-EBSD inverse pole figure maps showing the grain structure and orientation of nanoporous gold produced from $Au_{30}Ag_{70}$ (a) before and (b) after dealloying [PET 09].

The microstructure of precursor depends on the fabrication conditions. Precursors prepared by arc melting and heating treatment have grains from few tens to several hundreds of micrometers [JIN 09, MCC 16c, PET 09, GWA 16]. The smallest grain size precursor could be obtained by ball-milled method (around 200 nm) [GWA 16]. It was shown that the microstructure is preserved through dealloying process [MCC 16c, PET 09]. The SEM-EBSD map of Fig. 1.8 shows a nanoporous gold grain microstructure almost not affected by dealloying process. Each ligament is a single crystal and one crystal includes many ligaments.

In conclusion, it is very easy to control the grain microstructure when there is no phase transformation between precursor and metallic foam. Therefore it is very important to control the precursor microstructure thus the process.

1.2.4 Mechanical properties characterization

Mechanical properties of nanoporous metals have been already investigated. Porous materials show an asymmetrical behaviour between tensile and compression test. Because dealloyed samples are low density materials, when densification happens in compression test, they show a ductile behaviour and a high strain rate before breaking [ASH 06] [WIT 12].

At the nanoscale, dealloyed samples show plasticity while at the macro-scale the fracture behaviour is rather brittle, especially in tensile test. For nanoporous gold dealloyed from $Au-Ag$ precursor the fracture behaviour depends on residual Ag amount. For low residual Ag amount the fracture is smooth and intergranular while for high residual amount the fracture follows grain boundaries [HOD 09]. Experiments and simulations show a high dislocation activities that makes difficult the acquisition of a coherent and macroscopic plasticity [JIN 09, BRI 14, FAR 13].

1.2.4.1 Correction of Ashby and Gibson law

General mechanics of porous materials is described by GIBSON and ASHBY [GIB 97] in part 1.1, with macroscopic behaviour taken into account. However the nanoscale effect of the structure on the macroscopic material like [WEI 09]:

1. the action of capillary forces
2. the plastic behaviour of the ligaments, which is different from the bulk material
3. the ligament size

are not taken into account in such a simple analytical approach.

Many reports show an increasing yield stress and sometimes also Young's modulus with decreasing ligaments size. To take ligaments size effect into account, a Hall-Petch relationship for the yield stress calculation was introduced in equation 1.7 with A and m constants and σ_0 the lattice resistance to slip [HOD 07]

$$\sigma_p = \sigma_0 + Ad^{-m} \quad (1.7)$$

σ_0 can be neglected [DOU 09]. Combining equation 1.7 and equation 1.2, the yield stress is described in equation 1.8

$$\sigma_p = C\rho_r^n Ad^{-m} \quad (1.8)$$

In part 1.2.3.2, the microstructure reveals single crystal ligament, therefore a Hall-Petch exponent $m = 0.5$ is expected [MCC 16a]. However experimental data for nanoporous gold gives m about 0.6 [WEI 09, JIN 09]. From equation 1.8 it is expected to have a higher yield stress when ligament size decreases.

Reported Young's modulus values for nanoporous gold vary from several hundred MPa to several tens GPa [MAM 16] and yield stress values vary from several MPa to several hundred MPa depending on materials, density and ligaments size [MCC 16a] [MAM 16].

A link between nanoporous metals/composites ligament connectivity and material's strength and stiffness was unveiled [LIU 16]. The connectivity can explain the fact that the measured properties are lower than the expected ones. Reducing ligament's bending could lead to better mechanical properties [WAN 15a, GRI 17, BAR 16a].

In the existing literature, the mechanical behaviour of nanoporous metal has been investigated by different experimental tests, like nanoindentation [BAR 17, HOD 07, LEE 07, VOL 06], compression [BIE 05, MAM 16], traction [BRI 14, SUN 15] but also simulation [MAN 17, SUN 13].

1.2.4.2 Nanoindentation tests

The yield stress can be estimated from the hardness obtained from nanoindentation stress-strain curves. For bulk samples and porous samples with relative densities > 0.3 , the yield stress is the hardness divided by 3. For porous samples with relative densities < 0.3 , the yield stress is considered equal to the hardness [BIE 05, HOD 07, JIN 09]. The relation between hardness and yield stress for low density nanoporous materials leads to only

plastic deformation and an almost null plastic Poisson's ratio [BIE 05]. However these results are controversial [WEI 09].

1.2.4.3 Compression tests

Compression tests can be divided into two categories : tests on macroscopic samples and tests on microscopic samples. On microscopic samples *in situ* compression with a flat indent of micropillar nanoporous samples can be cited. It was shown that the micropillar diameter does not affect the yield stress contrary to ligament size [VOL 06] [GIA 11].

Compression tests are also performed on macroscopic samples. Stress-strain curves show a typical porous material behaviour. The ligament size has also an influence on mechanical properties as shown in Fig. 1.9.

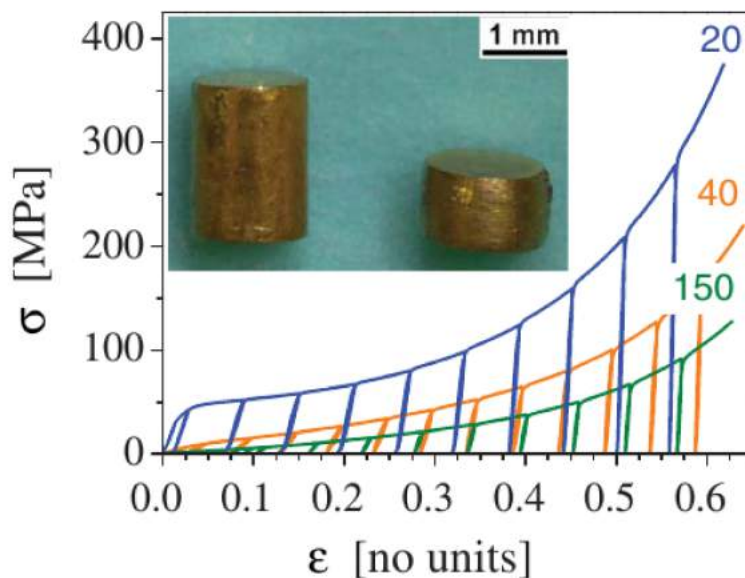


Figure 1.9: Compression stress-strain curves for nanoporous gold at a strain rate of $10^{-4}/s$ [MAM 16].

In conclusion, ligaments size highly influence the mechanical behaviour. A scaling law to predict yield stress was established, however there is not scaling law to predict Young's modulus.

1.2.5 *In/ex situ* dealloying experiments

Some *in/ex situ* mechanical tests are reported in the literature. For example SEM *in situ* compression tests were performed on nanoporous gold micropillar to measure directly the strain [GIA 11, VOL 06, WAN 17]. *Ex situ* SEM-EBSD was also performed during compression test, which showed an homogeneous plastic deformation due to a coherent crystal lattice [JIN 09]. However, the rest of this section will be focused on *in/ex situ* dealloying experiments.

1.2.5.1 Dealloying followed by X-ray imaging

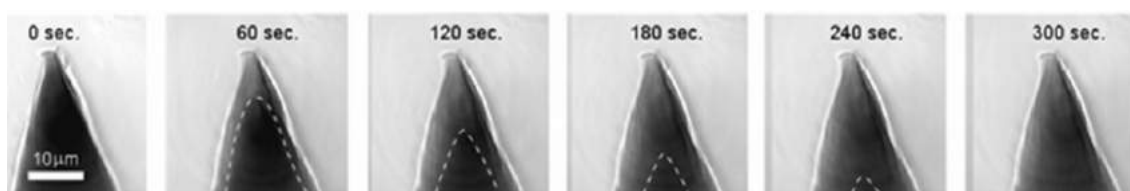


Figure 1.10: Evolution of dealloying front followed by X-ray transmission images. Dashed lines represent the approximate position of the dealloying front [CHE 13c].

X-ray tomography experiments on nanoporous gold was firstly performed in 2010 by [CHE 10], quickly followed by *in/ex situ* experiments [CHE 12a, CHE 13c, CHE 13d]. The first experiment provided 3D images of the coarsened structure. Results show an anisotropic morphology and the microstructure have a typical topology of bicontinuous structures produced by phase separation [CHE 10]. The coarsening of nanoporous gold was then *ex situ* analysed at various temperatures. An increased temperature results in a faster sintering of the structure. The specific area decreases as coarsening increases but it was not possible to determine if bulk or surface diffusion controls the coarsening (i.e. $n' = 3$ or 4 in equation 1.5). The anisotropy also increases with the coarsening time [CHE 12a]. The *in situ* imaging of the dealloying front illustrated by Fig. 1.10 was also succeeded. A constant propagation rate of the dealloying front was measured (however higher at the tip than at side of the sample) which give an interface controlled process by the *Ag* dissolution or *Au* surface diffusion [CHE 13c]. On the latest study transmission X-ray microscope was used. The effect of precursor element ratio and acid concentration were analysed on the dealloying front rate and on the crack formation mechanism [CHE 13d].

1.2.5.2 Dealloying followed by X-ray diffraction

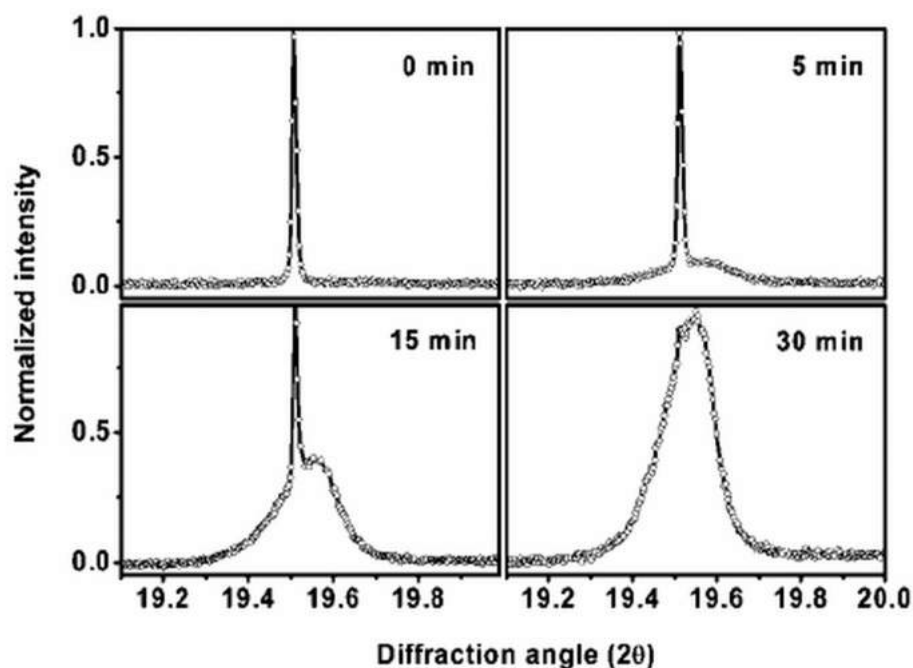


Figure 1.11: Evolution of (311) diffraction peak during dealloying. The maximum intensity is normalized to 1 [PET 09].

The initial step of dealloying was studied by *in situ* X-ray diffraction of $Cu_3Au(111)$ precursor and a complementary experiment by *ex situ* AFM. These studies reveal that in the early stage of dealloying, below the critical potential, a gold passivation layer was formed and prevent dealloying. Depending on potential the layer was either gold-rich and thin or composed of pure and relaxed gold island. At higher potential *Au* ligaments nucleate and grow below the passivation film [REN 06, REN 08].

In situ diffraction experiment coupled with SEM-EBSD was also completed to follow the evolution of grain orientation during gold dealloying. The (311) diffraction peak as function of dealloying time is displayed in Fig. 1.11. The grain orientation was roughly not affected by dealloying (cf. Fig. 1.8). A small resulting stress was however measured [PET 09].

A more recent study followed the gold crystal lattice strain during dealloying. The results show the compression of the lattice along the axis of cylindrically shaped ligaments and the expansion in radial direction. A surface curvature after dealloying enables to obtain a strain relaxation of the surface layer [MAH 18].

Moreover the stress along the {111} plane during dealloying of *Au-Ag* nano-crystal was *in situ* followed by Bragg coherent X-ray diffractive imaging. Due to volume shrinkage during dealloying, compressive strain was measured in the dealloyed region implying tensile stress into the crystal. At the surface, strain could be relaxed by atomic rearrangement while the crystal atomic rearrangement was constrained at deeper regions, therefore a

higher strain was observed. The strain evolution was also measured at grain boundaries where high local tensile and compressive strains were observed [CHE 17].

1.2.5.3 Dealloying followed by 2D imaging

Dealloying was also followed by 2D imaging. At nanoscale, AFM and STM was used. By STM the initial surface dissolution was followed with a precursor below the parting limit. STM provides an atomistic view, however the chemical sensibility is weak [OPP 91] [CHE 93]. At microscale, dealloying front can be followed by SEM [ZHA 15].

1.2.5.4 Dealloying followed by electrochemical measurement

Dealloying in aqueous solution is often followed by electrochemical measurement. It is possible to cite among others the study of dealloyed film by hard X-ray photoelectron spectroscopy [RAJ 13], dealloying of fuel cell catalyst electrode layer by *in situ* voltametry [SRI 09] the amount of dissolution element by *in situ* electrochemical noise [ZHA 16], influence of potential and time on dealloying process by *in situ* Raman spectra [CHE 09, RAJ 13]... The aim of these experiments is not only to understand the dealloying mechanisms but also to control the potential, thus control the dealloying reaction. These measurements may be coupled with volume measurements with a dilatometer [PAR 06, JIN 09, CHA 05].

In conclusion, *in/ex situ* dealloying experiment are possible and is a powerful method to have a better understanding of dealloying process. One can note however that because of obvious experimental difficulties, liquid metal dealloying has not been studied *in situ* so far using these techniques.

1.2.6 Composites produced from dealloying

Some nanoporous gold based composites were reported in the literature. The initial development of this kind of materials was for electrochemical applications. The first report concern the synthesis of gold precursor wire into an anodic aluminium oxide by electrodeposition: the wire precursor was dealloyed to form nanoporous gold wire anodic aluminium oxide composites flow-through type catalytic reactions [LIU 08]. Electrochemical supercapacitors hybrid structures made of nanoporous gold and nanocrystalline MnO_2 were developed to enhance conductivity [LAN 11]. To increase the magnitude of actuator of metallic muscle, a nanocoating of polyaniline doped with sulphuric acid was grown onto the ligaments of nanoporous gold [DET 13]. Nanoporous metals were also simply impregnating the pores of nanoporous gold with aqueous electrolyte to produce piezoelectric gold [STE 16, WIL 18]. However, this part will focus on metal/metal composite and metal/polymer composite by polymer infiltration.

1.2.6.1 Metal-metal composites

It is easy to get a metal/metal composite from liquid metal dealloying. Just after dealloying and before the etching step is indeed a metal/metal composite. In some cases, to study dealloying mechanism (depth, ligament size...), measures were done on metal/metal composite [WAD 16b, MCC 16c] and not at the porous state. However only Ta-Cu metal/metal composite from dealloying *Ta-Ti* precursor in *Cu* melt, some measurements were performed directly on metal/metal composites. The mechanical properties of this composite were investigated by compression and nanoindentation tests. Stress-strain curves (cf. Fig. 1.12) show a ligament size effect. The yield stress increases when ligaments size decreases. It was shown that the yield stress follows a Hall-Petch model with $m = 0.5$ for ligaments size until $3\ \mu\text{m}$. For larger ligaments a single arm source dislocation model was applied [MCC 16d]. An heterogeneity was also reported in the mechanical properties, depending on the local composition under indent [MCC 16b].

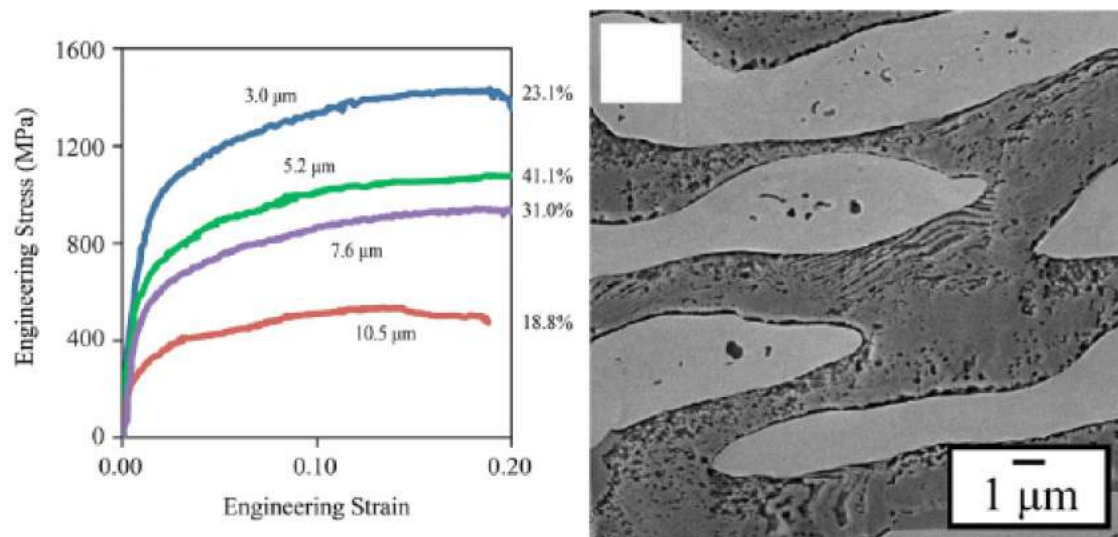


Figure 1.12: Compression stress-strain curves for *TaCu* composite (left) and SEM micrograph of a deformed *TaCu* composite near to failure, showing delamination between the *Ta* and *Cu* phases [MCC 16d].

Because they can be polished and are easier to manipulate, metal/metal composites can be a good way to study the foam morphology and/or the dealloying kinetics. Their yield stress for ligaments until $3\ \mu\text{m}$ varies with ligament size with a Hall-Petch relationship.

1.2.6.2 Metal-polymer composite

To obtain nanowire a well-known method is to infiltrate it into a porous membrane [DUB 99, DUV 02, LON 11, DUC 98]. This method inspires the second way to get a composite from dealloyed sample. The pores of nanoporous gold was under vacuum infiltrated by epoxy and polyurethane resin to improve mechanical properties, especially ductility [WAN 13, WAN 15a]. The mechanical properties of those composites were also simulated by finite element analysis [GRI 17, BAR 16a].

These composites are stronger and harder than each individual phase in both tension and compression. The tensile ductility is improved compared to nanoporous gold. The ligament scaled links with their mechanical properties are also present as shown in Fig. 1.13.

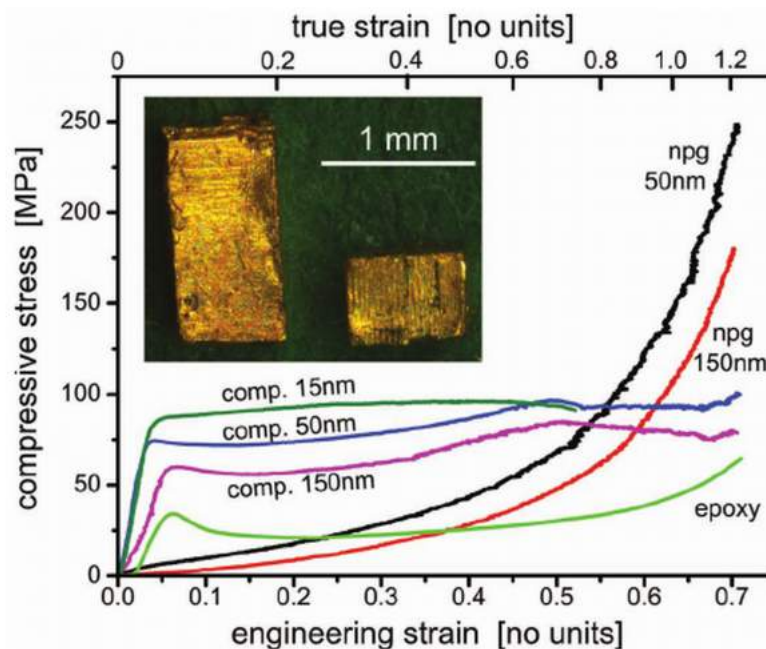


Figure 1.13: Compression stress-strain curves for nanoporous gold, polymer and nanoporous gold/polymer composites at a strain rate of $10^{-4}/s$ [WAN 13].

Infiltration of porous samples prepared by liquid metal dealloying has also been achieved by infiltrating epoxy resin into pores of *Ti* alloys foams [OKU 17, OKU 18a]. The mechanical behaviour was studied by compression tests. These tests showed that polymer brings ductility and that the composite is stronger than each individual phase. Moreover these composites match the elastic behaviour of human bones [OKU 17, OKU 18a].

To improve mechanical properties of porous metals with a limited impact on the weight, the fabrication of metal/polymer composites can be a good solution.

1.3 Dealloying from *Fe-(Cr)-Ni* precursors

Stainless steels micro/nano porous foams would be very interesting technological materials therefore they will be mostly studied in this thesis. Several works were already performed involving *Fe-(Cr)-Ni* precursors dealloyed in a *Mg* bath.

1.3.1 Dealloying kinetics

Dealloying kinetics were studied for dealloying from $(Fe_{80}Cr_{20})_{50}Ni_{50}$ precursor into a solid *Mg* bath. Dealloying kinetic follows, as expected, equation 1.3 with $n = 0.5$, therefore a diffusion controlled kinetics is involved. For a given time, dealloying depth becomes larger with the raise of the temperature [WAD 16b].

Kinetics were also studied for dealloying from $Fe_{50}Ni_{50}$, $(Fe_{80}Cr_{20})_{50}Ni_{50}$ and $(Fe_{80}Cr_{20})_{30}Ni_{70}$ precursor into a liquid *Mg* bath at different temperature and for different precursor preparation (single crystal and multi-crystalline samples). Different behaviours were observed depending on temperature and composition. For $Fe_{50}Ni_{50}$ at low temperature ($T < 750\text{ }^{\circ}\text{C}$) and for $(Fe_{80}Cr_{20})_{30}Ni_{70}$, a diffusion controlled kinetic is present ($n = 0.5$ in equation 1.3) while for $Fe_{50}Ni_{50}$ at high temperature dealloying and for $(Fe_{80}Cr_{20})_{50}Ni_{50}$ dealloying is limited by interface reaction ($n = 1$). Let's mention another interesting fact: for a given time, dealloying depth decreases with the raise of the temperature. Activation energies were also determined (cf. equation 1.3) [SAI 16, TSU 14]. Precursor preparation has a limited influence on dealloying kinetics.

Dealloying from SUS316L commercial stainless steel precursor with 12 at% *Ni* was investigated. Because the soluble element is below the parting limit, only precursor surface (50 μm layer) was dealloyed [KAT 16].

1.3.2 Foam morphology

Ligaments coarsening behaviour during dealloying from $Fe_{30}Ni_{70}$ precursor into a *Mg* melt bath was studied [WAD 13]. From equation 1.5, a coarsening component respectively $n' = 3.44$ and an activation energy respectively $E' = 120\text{ kJ/mol}$ were measured (cf. equation 1.5) [WAD 13].

Foam microstructure and composition analyses of dealloyed samples from $(Fe_{80}Cr_{20})_{30}Ni_{70}$, $(Fe_{80}Cr_{20})_{50}Ni_{50}$ and $(Fe_{80}Cr_{20})_{70}Ni_{30}$ precursors at 700 $^{\circ}\text{C}$ and 800 $^{\circ}\text{C}$ for 1, 5 and 10 min were done. These show that porosity and pores size decrease while the dealloying time increases due to shrinkage. Interfacial shape distribution shows mainly saddle shape for samples dealloyed from $(Fe_{80}Cr_{20})_{50}Ni_{50}$ and $(Fe_{80}Cr_{20})_{70}Ni_{30}$ precursors while cylindrical shapes with concave ends are also noticed for samples dealloyed from $(Fe_{80}Cr_{20})_{30}Ni_{70}$ precursors. While increasing porosity, the structure evolves from a channel-like to a bi-continuous structure. Interfacial shape distribution is almost stable with dealloying time that corresponds to the observation during coarsening of a roughly self-similar structure. Considering the composition residual *Ni* inside ligaments which decreases while dealloying time increases, it can be concluded that the dealloying is a continuous process during coarsening [ZHA 17].

From a FeCrNiMn precursor sample, it was possible to obtain a bimodal pore distribution by a 2 steps process. The first step is the first dealloying in Mg to form porous FeCrMn with large ligaments. Then the second step is a second dealloying in Bi to dealloy Mn from large ligaments to create the smallest structure of this hierarchical structure [WAD 18].

1.3.3 Grain microstructure

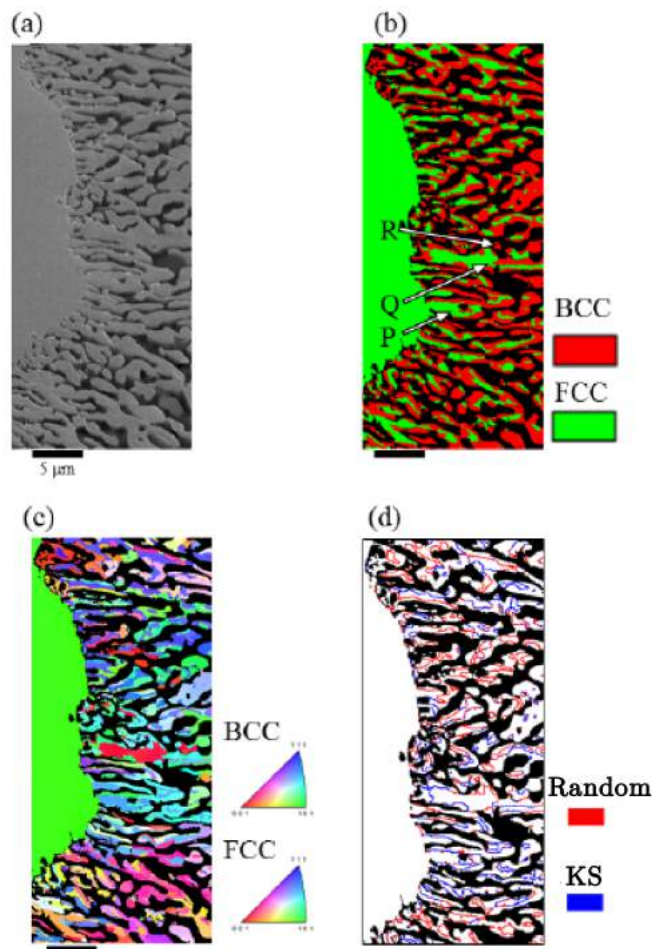


Figure 1.14: SEM-EBSD grain microstructure analysis during dealloying (a) SEM micrography with on left part precursor sample and on right part dealloyed part with ligaments (b) Phase map of (a). The composition was analysed on P, Q and R point (c) IPF of (a), (d) FCC/BCC phase separation of (b) : red line corresponds to random FCC/BCC phase boundaries while blue line corresponds to phase boundaries presenting Kurdjumov-Sachs (KS) relationship [SAI 16].

Grain microstructure during dealloying was studied from a $Fe_{50}Ni_{50}$ single crystal. Fig. 1.14 presents the main result of this study with SEM-EBSD analysis of partial dealloying. Fig. 1.14(a) shows a SEM micrograph of partially dealloyed sample : left part corresponds

to the precursor and right part to dealloyed part. Fig. 1.14(c) presents the Inverse Pole Figure (IPF) map confirming a single crystal while dealloyed part is multi-crystalline. Fig. 1.14(b) presents phase map. Precursor sample is FCC and ligaments far from dealloying front are BCC (cf. phase diagrams in Chapter 4). Ligaments near dealloying front are a mixture of FCC and BCC phase. Points Q and R are FCC because they present a high Ni percentage (respectively 25 and 48 at%) while P is BCC and present almost no residual Ni . This result confirms that dealloying continues during coarsening, after ligaments formation [ZHA 17]. Some phase boundaries presented in Fig. 1.14(d) are random phase separations while others are linked by Kurdjumov-Sachs (KS) relationship [SAI 16].

Kurdjumov-Sachs (KS) relationship corresponds to the most common model linking FCC grain orientation with BCC grain orientation after FCC-BCC phase transformation. From 1 FCC grain orientation, 24 different orientations are possible for the BCC grains [MUR 98]. Another relationship common model linking FCC grain orientation with BCC grain orientation after FCC-BCC phase transformation is Nishiyama-Wassermann (NW) relationship [HEL 11].

1.4 Conclusion

In this chapter, literature was reviewed. Materials, process, microstructure and mechanical characterizations for dealloyed materials were listed. General theories about dealloying principle, kinetics, coarsening and mechanical behaviour were explained. Recent developments with *in situ* experiments and composite from dealloyed materials were analysed. Then, a focus on dealloying from $Fe-(Cr)-Ni$ precursors was done. On these materials, the dealloying and coarsening behaviour were already investigated. However, the influence of the precursor composition on dealloying kinetics and coarsening behaviour have not been clarified yet. Grain microstructure and foam morphology were investigated during the early stages of dealloying, therefore a coarsened structure will be studied here. Mechanical properties of dealloyed materials from $Fe-(Cr)-Ni$ precursors were not measured. Dealloyed based composite samples show interesting mechanical properties therefore from $Fe-(Cr)-Ni$ precursors, composites materials will be produced in this study.

In conclusion, some studies have been carried out on this topic however there is a lot of questions remaining. This work will both try to answer some of them and to open new perspectives.

Chapter 2

Images acquisition and processing

The purpose of this work is to analyse the relation between elaboration, microstructure and mechanical properties. Common tools of materials science used to characterize the microstructure will be exploited and described in this chapter. First, the 3D tools with a focus volume processing will be described. Then 2D tools and sample preparation will be mentioned.

Contents

2.1	3D imaging : X-ray tomography	26
2.1.1	Principle	26
2.1.2	Volume processing	28
2.1.3	Quantitative analysis	31
2.2	2D imaging : SEM	34
2.2.1	SEM techniques	34
2.2.2	Sample preparation	36
2.3	Conclusion	37

As explained in Chapter 1, in case of architectural materials, the word microstructure can have several meanings. Grain microstructure (size, orientation, crystallographic phases etc.) and composite/foam morphology (shape, phase ratio, phase thickness etc.) will be distinguished. For both kinds of microstructure, imaging will be a preponderant tool in two dimensions and in three dimensions. To complete this characterization X-ray Diffraction (XRD) will be also involved.

To manage an accurate analysis of foam morphology, at least 5 ligaments and 5 pores should be analysed in each directions and an elementary representative volume (ERV) will be taken into account with a cube of size of at least $70\ \mu\text{m}$ side.

2.1 3D imaging : X-ray tomography

2.1.1 Principle

2.1.1.1 Set-up

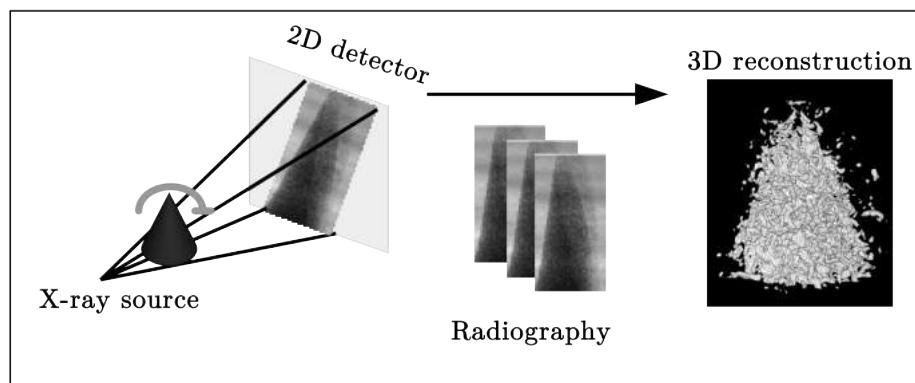


Figure 2.1: Principle of X-ray tomography : X-ray tomographic device is composed of a X-ray source, a rotation platform and a detector. To complete a software provides the 3D reconstruction.

X-ray tomography is a non-destructive technique to obtain a three dimensional image of the sample. Fig. 2.1 presents the principle of a X-ray tomographic device which is composed of a X-ray source, a rotation platform and a detector. In case of synchrotron radiation, X-ray beams are parallel while in laboratory X-ray beams are conical. The sample is fixed on a rotating platform. For each rotation angle a X-ray radiography is acquired. From this stack of 2D images a 3D reconstruction of the sample is provided by a software. A X-ray tomography acquisition will be referred as a scan in this study.

In laboratory set-up configuration, to have a very high resolution, samples should be close to the X-ray beam therefore a very thin sample is necessary to obtain a very high resolution. Moreover for absorbent materials, the thinner the sample, the higher the possible resolution is. Because samples are rotating, they should have cylindrical shapes

to have the same thickness in all directions. Samples were polished into tip shapes until reaching at the bottom of the tip, a diameter of 300-400 μm .

Different devices are used depending on where the experiment is performed. Experimental parameters are given in Table 2.1. Two different types of experiments have been performed:

- *In situ* : direct observation of the process while the process is in progress.
- *Post mortem*: the sample is prepared before and scanned after the process is completed.

	VtomeX	EasyTom Nano	Tomcat beamline
Company	GE Phoenix	RX solution	SLS, PSI
Country	Germany	France	Swiss
Beam shape	conical	conical	parallel
Energy (keV)	100	100	25
Projection number	1200	1200	1001
Acquisition time (s)	0.333	10	0.02
Voxel size (μm)	around 6	around 0.3	0.16/0.32
Scan duration	around 7 min	around 3 h	around 10 min / around 45 s

Table 2.1: Tomography acquisition parameters. When two values are present the first one corresponds to *post mortem*, the second one corresponds to *in situ* experiment.

The utilization of different devices will enable the samples analysis at different scales (global shape or foam morphology) and at different time (*post mortem* or directly during the process with very short scan (less than 1 min)).

2.1.1.2 Absorption contrast tomography

This technique is based on the absorption of the X-rays by the sample. The X-ray are absorbed depending on the composition and density of each area of the sample. The absorption coefficient μ depends on the atomic number of element and incident beam energy follows the Beer-Lambert law [THI 13]. The reconstruction will be a volume with the intensity of each voxel proportional to the local materials density. To have a good contrast between each area of the sample, each one should be composed of elements with large different atomic number. The most absorbent phase will be the whitest phase after reconstruction. The different absorption coefficient will permit a contrast between *FeCr* and *Mg* or between *FeCrNi* and *FeCrMg*. However *Fe*, *Cr*, and *Ni* are highly absorbing elements while *Mg* and air are not, therefore the contrast between air and *Mg* is very weak when both are present.

2.1.1.3 Phase contrast tomography

Absorption contrast tomography is not usable to distinguish two areas with same or close elements. In this case, phase contrast tomography should be used. When a spacial coherent

beam crosses a volume with different electron density, a change of phase can be observed : it is called phase contrast tomography [STO 08]. For this type of tomography the distance between the sample and the detector is important. On Tomcat beamline, an optimized reconstruction algorithm called “Paganin” reconstruction was used. [PAG 02].

2.1.2 Volume processing

2.1.2.1 Definition

From X-ray tomography or SEM, grey level images were obtained. A scan is a 3D matrix of numbers, each number defines the grey level of the voxel (3D pixel) A volume is presented as a stack of 2D images. One of these images is called a slice. Image/volume analysis is performed with Fiji software [SCH 12].

2.1.2.2 Image presentation and treatment

To have an optimized contrast, some image parameters could be adjusted. Fig. 2.2 shows the same image with different parameters: (a) corresponds to the original image and (b) after a brightness and contrast adjustment. The contrast between one of the phase and air is low, so a logarithmic scale can be used in order to improve this contrast (Fig. 2.2(c)) or some optimized false colour can be assigned for each phase (Fig. 2.2(d)).

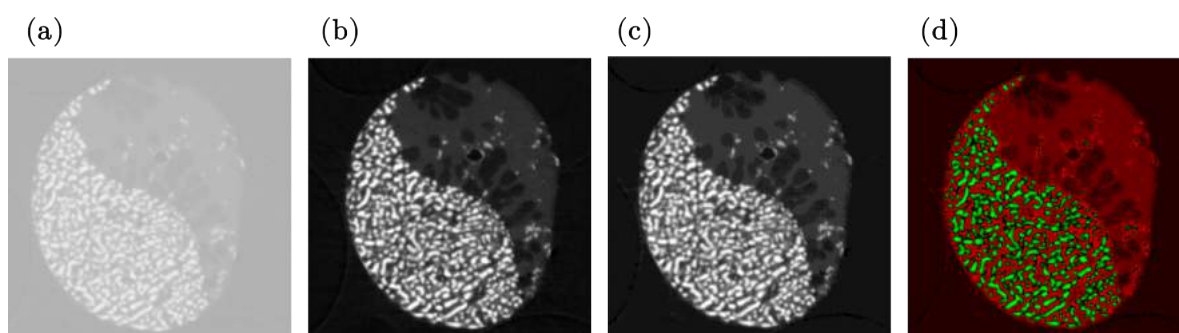


Figure 2.2: (a) original caption (b) brightness and contrast adjustment (c) logarithmic scale (d) false color.

Volume can present some noise or artefact which will be a problem for quantitative analysis. The removal of this noise is done with filters. Fig. 2.3(1)(a) presents some noise: phases are not composed of only one grey level. During the phases separation, some isolated voxels will be present in the opposite phase, emphasized by a black circle in Fig. 2.3(1)(b). After applying a bilateral filter (Fig. 2.3(1)(c)) the isolated voxels are not visible any more.

Commonly observed artefacts with highly absorbing elements or with a laboratory tomography is beam hardening. In that case, the sample edge is very bright compared to the center of the sample as shown in Fig. 2.3(2)(a). The grey scale level of each phase differs between the edge and the center. During the phase separation the same grey levels

can either correspond to $FeCr$ phase in the center or Mg phase at the edge emphasized by a black circle in Fig. 2.3(2)(b). After applying a FFT bandpass filter (Fig. 2.3(2)(c)) the grey scale levels are homogenized on the whole sample.

Another common artefact is ring artefact. When the detector presents some dead voxels, several rings appear on the volume as shown in Fig. 2.3(3)(a). During the phase separation, a circle appears on the second phase as shown in Fig. 2.3(3)(b). After applying median filter (Fig. 2.3(3)(c)), the rings artefact is removed.

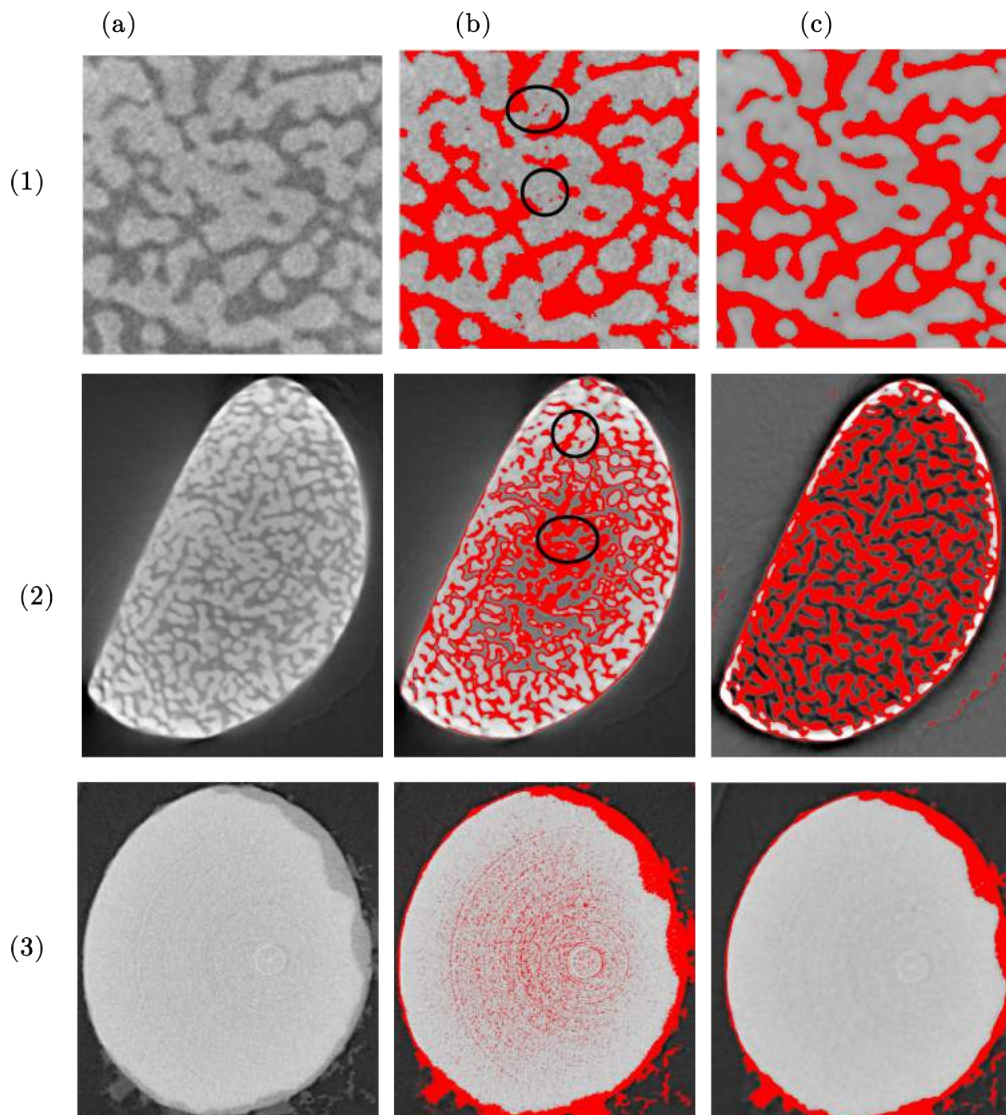


Figure 2.3: Filter effect (1) Bilateral filter (2) FFT Bandpass filter (3) Median filter (a) original imaged (b) problem manifestation (c) filter effect.

2.1.2.3 Binarisation

The first prerequisite for sample characteristics extraction is the capability to separate each phase. For this separation it is necessary to define the grey level boundary values corresponding to each phase. This step is called *threshold*: one phase will appear white and the second one black (binary volume). After image treatment a good contrast between the two phases remains (Fig. 2.4(a)). On the intensity histogram presented in Fig. 2.4, two peaks appear corresponding respectively to each phase. The boundaries between each phase are simply labelled by the dashed red line. In this case only 2 peaks are present so 8 bits images provide enough informations (and the size of the file is divided by 2). Each pixel/voxel is therefore defined by a number between 0 (black) and 255 (white). After threshold Fig. 2.4(b) is obtained. To check if the process is consistent Fig. 2.4(c) is created by superposition of image (a) and the outline of image (b): the outline of (b) corresponds to the phase separation of (a). Most of the physical characteristics are measured from binary volumes: phase fraction, phase thickness, intercept connectivity, tortuosity, specific surface etc.

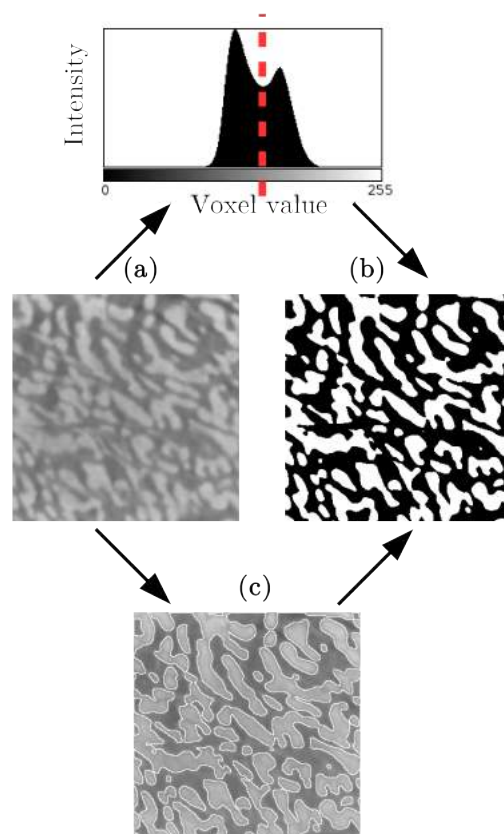


Figure 2.4: Threshold process (a) optimized gray level values after image treatment, (b) image (a) after threshold, (c) superposition of (a) and the outline of (b). Top : Intensity distribution of (a). The dashed red line corresponds to the value used for the threshold.

2.1.3 Quantitative analysis

2.1.3.1 Phase fraction

Phase fraction is easily determined by enumeration of white voxels and division of this result by the total volume. Phase fraction is equivalent to volume ratio. For a foam it is equivalent to foam density.

Phase thickness

1. “Local thickness” function

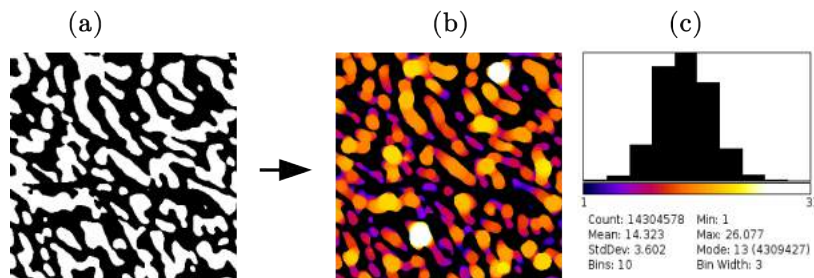


Figure 2.5: Effect of local thickness (a) one slice (b) the same slice after local thickness (c) phase thickness size distribution and statistics.

Phase thickness can be measured with the “local thickness” function of Fiji software. The local thickness is a local measurement: corresponding to the diameter of the largest sphere that fits inside the object, including this point [HIL 96] [SAI 94]. Fig. 2.5 shows the result given by the “local thickness” function on one sample. In order to compare the distribution without the influence of phase fraction, all phase thickness size distribution are normalized. However it is not possible to detect the presence of anisotropy in the samples with “local thickness” function.

2. Intercept plugin

A linear intercept method is used to measure anisotropy [HOR 49]. Linear intercept method consists in counting the number of occurrence of one phase and the length of each occurrence along a line. This procedure is repeated for each line in each direction. Fig. 2.6 explains with a 2D example how intercept is calculated for the white phase. In this case intercepts size distributions are not similar in both x and y directions, which means that the sample is not perfectly isotropic. A home made intercept plugin working in 3D was implemented in Fiji.

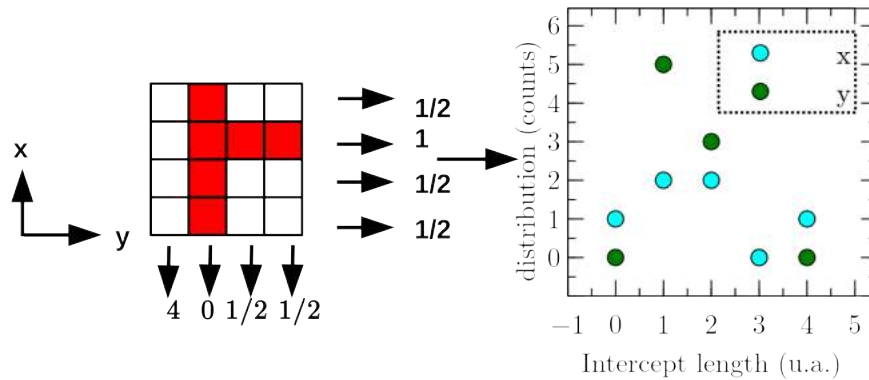


Figure 2.6: Example of 2D intercepts measurement and results for the white phase.

2.1.3.2 Connectivity

The connectivity is the ratio of the largest connected area divided by the total volume of this phase. The “Find Connected Region” function of Fiji software is used to measure the largest connected area [LON]. Diagonal connexion between voxels is not allowed and the non connected volume at the surface of the sample is not taken into account.

The connectivity value is a good way to measure if the structure is perfectly connected or not. Euler characteristic and genus are also often used for this purpose [MIC 03, MAN 16, CHE 10, LIL 18]. Genus (G) is defined by equation 2.1 and corresponds to the number of tori in a connected sum decomposition of the surface; intuitively, the number of "handles" [MIC 03, MAN 16, CHE 10, LIL 18]. Therefore a torus has a genus of 1 and "8" a genus of 2. Euler number was measured with Morpholibj plugin [LEG 16].

$$G = 1 - \frac{EulerNumber}{2} \quad (2.1)$$

$$(2.2)$$

2.1.3.3 Geometrical tortuosity

The geometrical tortuosity is defined by the ratio of the length of the curve (blue line) to the distance between the ends of the curve (black line) as shown in Fig. 2.7(a). The geometrical tortuosity is calculated by a home made plugin implemented in Fiji [MAI 12]. Because volume are not continuous but divided in voxels, the distance is calculated from one voxel center to an other voxel center of a neighbour voxel. Three criteria could define two voxels as neighbours: to have a common face considers 6 neighbours in 3D (geometrical tortuosity 6), to have a common edge considers 12 neighbours in 3D (geometrical tortuosity 12), or to have a common face or edge or corner considers 26 neighbours in 3D (geometrical tortuosity 26).

Fig. 2.7(b) explains with a 2D example the difference between geometrical tortuosity 6 (4 neighbours in 2D) and 26 (8 neighbours in 2D) to go from A to B. In this case the value for geometrical tortuosity 8 (red arrow) is 1 while for geometrical tortuosity 4 (green arrow) the value is $\sqrt{2}$. The geometrical tortuosity is also depending on the calculation way. To prevent under and overestimations, both geometrical tortuosity 6 and geometrical tortuosity 26 are calculated and the displayed results is the mean value of these results.

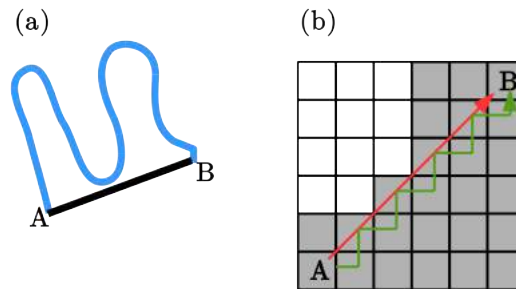


Figure 2.7: (a) Geometrical tortuosity definition (b) Example of 2D distance measurement of grey phase. Green and red arrows correspond to the given way between A and B respectively for tortuosity 4 (6 in 3D) and 8 (26 in 3D).

2.1.3.4 Specific surface

The specific surface is the solid/pore surface for one kg or for one m^3 . The real surface of the foam is calculated after volume binarisation with a home made Fiji software plugin using a marching cube algorithm [MAI 12].

2.2 2D imaging : SEM

2.2.1 SEM techniques

2.2.1.1 Surface imaging

The scanning electron microscope (SEM) is a powerful instrument to observe the topography of the surface. Images with a resolution below micrometer scale with an important depth of field can be obtained [RUS 13]. The large depth of field enables the observation of porous/non flat surface samples. SEM could be coupled with other instruments.

SEM observation requires conductive surface to avoid charging (electrons which are accumulated at the sample surface). Because polymers of this study are non conductive, observations were done in partial vacuum mode.

Quantitative analysis as described in 2.1.3 can also be performed on SEM image.

The spatial resolution is better than X-ray tomography, so this technique is useful to characterize porous sample with small ligaments/pores when X-ray tomography could not be used. In this study SEM is also involved to observe metal/metal composites, porous metal and metal/polymer composites morphology and indents shape after nanoindentation.

2.2.1.2 Composition analysis

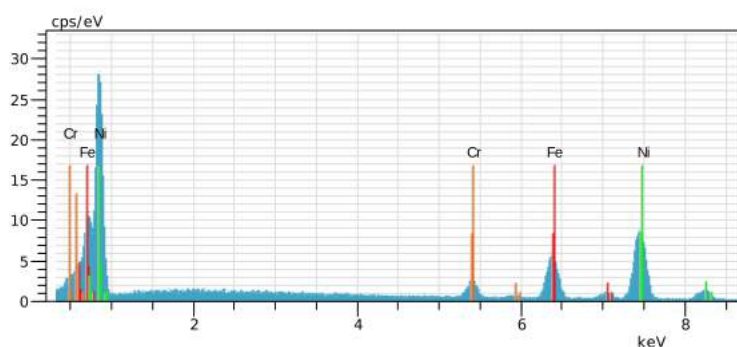


Figure 2.8: Exemple of EDX spectrum obtained on 30FeCr-Ni sample.

To characterize the composition of a sample Energy Dispersive Spectroscopy (EDS) or Energy Dispersive X-ray Spectroscopy (EDX) was primarily used in this study. The EDX enables to know the chemical nature of elements and their proportion. The SEM-EDX combined method enables to focus the analysis on a small part of the sample to know the local composition or the different elementary compositions of different phases. This technique is based on the measurement of photons energy. An electron beam strikes a material which emits X photons. The energetic analysis enables to characterize the elements contained in the material. An example of EDX spectrum is given in Fig. 2.8.

One of the most important parameters is the energy of incident electron beam fixed by the acceleration voltage. This energy should be higher than the transition energy of the targeted element [RUS 13].

For the purpose of this study SEM-EDX will be mainly used to check the composition after arc-melting and dealloying process by a Hitachi S-4800 microscope equipped with an EDAX Genesis XM2 (Tokyo, Japan).

One of the limitations of SEM-EDX is the detection of very light elements like carbon, oxygen etc... which are the main components of polymers. To detect polymer presence and enhance the contrast between metallic foam, air and polymer, the backscattered mode is used.

2.2.1.3 Grain microstructure analysis

Several methods have been used to measure the grain orientation of a crystal. Since the beginning of 1990s, the Electron Back Scattered Diffraction/Pattern method (EBSD) or (EBSP) has been developed. This system is included in some SEM. Fig. 2.9 shows the principal elements of this method : a localized electron beam (15 to 30 keV) furnished by SEM, a fluorescent screen on which backscattered electrons form a Kikuchi diagram, and a low level light camera which captures picture of diagrams in real-time. The sample is tilted of 70° to have a maximum emission of back scattered electrons. After penetration in the sample, the incident electrons are diffused in a large angle. Some of them are in Bragg condition with the different atomic planes. The diffracted electrons by atomic plane form 2 diffraction cones. The intersection of these cones with the screen gives two pairs of Kikuchi lines on the screen. Because of the large aperture angle of the cones, the lines appear almost as straight lines and form a band limit [BAU 10].

Indexation of Kikuchi diagram is especially difficult. First, diffraction must happen (the gauge volume need to be a perfect crystal, not a grain boundary for example), and a perfect surface is necessary. Phase proportion, grain size and grain orientation will be extracted from the EBSD map taken before and after dealloying.

All EBSD analyses were performed with JEOL 7100F SEM (JEOL, Japan) with OIM acquisition and analysis softwares with 20 keV energy, 70° tilted sample and a working distance of $WD= 25$ mm.

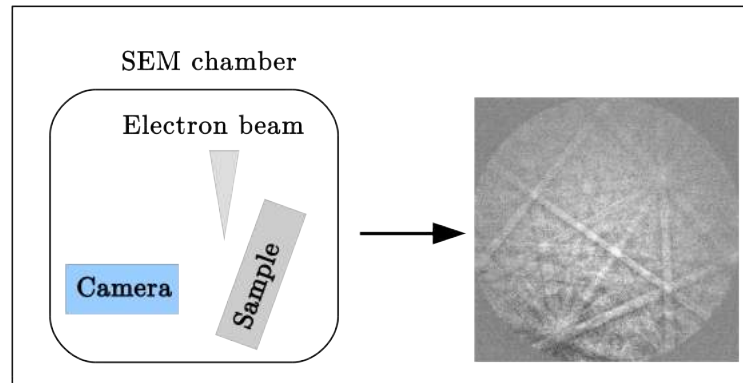


Figure 2.9: Principle of EBSD: after penetration in the tilted sample, the incident electrons are diffused in a large angle. Some of them are in Bragg condition with the different atomic planes. The diffracted electrons by atomic plane form 2 diffraction cones. The intersection of these cones with the screen gives two pairs of Kikuchi lines on the screen. The indexation is provided by the software.

2.2.2 Sample preparation

2.2.2.1 Porous samples

SEM observation and composition analysis on porous sample were done directly after etching without further surface treatment.

2.2.2.2 Composites samples

The SEM-EBSD observation is made with samples tilted of 70° which does not allow the observation of porous samples. SEM-EBSD requires a perfectly planar surface therefore the SEM-EBSD in this study must be performed on perfectly polished metal/metal composites. However, *Mg* has poor mechanical properties compared to *FeCr* and is very reactive to water which makes hand polishing difficult and not suitable for SEM-EBSD measurement.

Observations of the metal/metal composites were done with samples polished by an *Ar* ion beam polisher (EM-3500 Hitachi, Japan) and, concerning the metal/polymer composite, an Ilion II (Gatan, USA) ion polisher was used. For both cases the cross-section of the materials was polished from the surface. The polished area in yellow presents similar shape and size as shown in Fig. 2.10

To observe metal/metal and metal/composite surface, ion beam polishers have been used. The observation area after polishing is around 200-400 μm depth from the surface and around 1 mm length. Ion polishing limits the observation area and can create some waves on the surface thus can create noise on SEM/SEM-EBSD images.

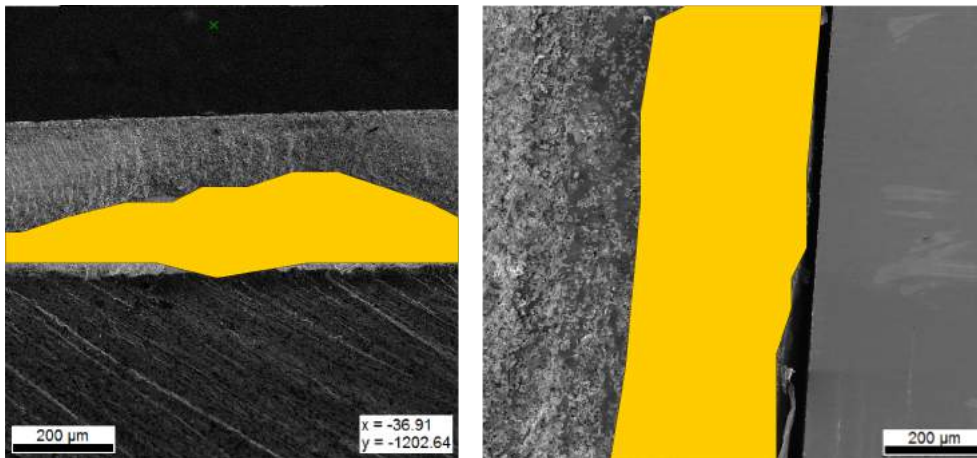


Figure 2.10: Sample polished with Ar ion beam polisher (70°, left), with Ilion II (right) Yellow area corresponds to polished area.

2.3 Conclusion

In this chapter the strategy for characterizing the microstructure and the morphology was developed.

Different tools as X-ray tomography and Scanning Electron Microscope (SEM-EDX/SEM-EBSD) enables the characterization of the composition, the morphology and the microstructure.

The morphology and the microstructure will be analysed at different scales (from sub- μm to mm/cm scale). The evolution of morphology analysis will be done at different times with *in situ* (less than 1 min for X-ray tomography) and *post-mortem* measurements. The morphology will be characterized in 2D and 3D.

The combination of various tools will enable a multiscale characterization.

Chapter 3

In situ observation of the liquid metal dealloying process by X-ray tomography and X-ray diffraction

The effects of liquid metal dealloying and chemical etching on foam morphology and grain microstructure will be respectively studied in Chapters 4, 5 and 6 by *post mortem* experiments. To understand that really happened during the process *in situ* experiments are needed. However the dealloying and etching processes have never been directly observed yet. To solve it, a challenging experiment will be presented in this chapter.

Dealloying and etching front have been both studied *in situ* under synchrotron radiations. First the result of the observation of dealloying by X-ray tomography, then by X-ray diffraction will be introduced. To understand the effect of some experimental parameters on dealloying kinetics, some simulations will be presented. Then the results of the observation of chemical etching by X-ray tomography will be mentioned. In this part all reported experiments have been carried out using $(Fe_{80}Cr_{20})_{30}Ni_{70}$ precursors.

Contents

3.1	<i>In situ</i> observation of liquid metal dealloying by X-ray tomography	40
3.1.1	Experimental process	40
3.1.2	Case 1	41
3.1.3	Case 2	42
3.1.4	Simulation	45
3.2	<i>In situ</i> dealloying followed by X-ray diffraction	51
3.2.1	X-ray diffraction (XRD)	51
3.2.2	Experimental process	51
3.2.3	Results	52
3.3	<i>In situ</i> chemical etching followed by X-ray tomography	55
3.3.1	Experimental process	55
3.3.2	Results	56
3.4	Conclusion	58

I would like to thank those who contributed to this chapter:

- Anne Bonnin (TOMCAT beamline, SLS) and Wolfgang Ludwig (ID11 beamline, ESRF): without their help these experiments would be impossible.
- Julie Devillard (MATEIS) and François Cadiou (MATEIS) helped during synchrotron experiments.
- Jérôme Adrien (MATEIS) helped a lot before and during synchrotron experiments.
- Pierre-Antoine Geslin (MATEIS and Tohoku University) provided useful discussions about diffusion models and wrote scripts used in the simulation part.

3.1 *In situ* observation of liquid metal dealloying by X-ray tomography

In this section two different experimental behaviours (case 1 and 2) will be analysed then some simulations will be performed to explain the difference between both cases.

3.1.1 Experimental process

This experiment was performed on the TOMCAT beamline (SLS, PSI, Switzerland) with an energy of 25 keV and continuous acquisition of respectively 45 s (dealloying) and 130 s (chemical etching) scans. The full volumes were reconstructed with a voxel lateral isotropic size of $0.32 \mu\text{m}$ and 20 ms acquisition of 501 projections and energy of 25 keV. More details about X-ray tomography experimental parameters can be found in Chapter 2.

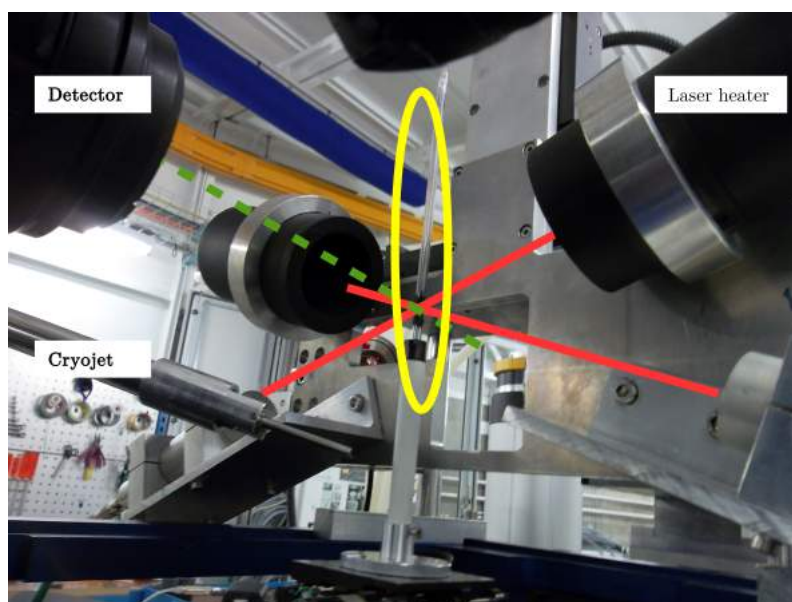


Figure 3.1: Picture of the experimental set-up. Red lines correspond to laser heater, green line to X-ray beam and yellow circle to the reactor.

The *in situ* dealloying experiments required a dedicated reactor to handle the liquid magnesium at more than 650 °C and allowing us a 360° field of view for tomography. It was achieved by under-vacuuming the encapsulated precursor and magnesium (introduced in the form of flakes) in a 2.5 mm inside diameter quartz tube as shown in Fig 3.1. The cold-rolled precursor plates were cut into 1x1x10 mm parallelepipeds of which one end was polished until getting a 300 μm diameter tip shape. These tips were fixed with high temperature resistance glue on top of 2 mm diameter steel sticks inside a 1 mm diameter drilled hole. X-ray transparent black painting was applied on the outside of the tubes and a laser heater provided on the TOMCAT line was used for the thermal cycles [FIF 12].

3.1.2 Case 1

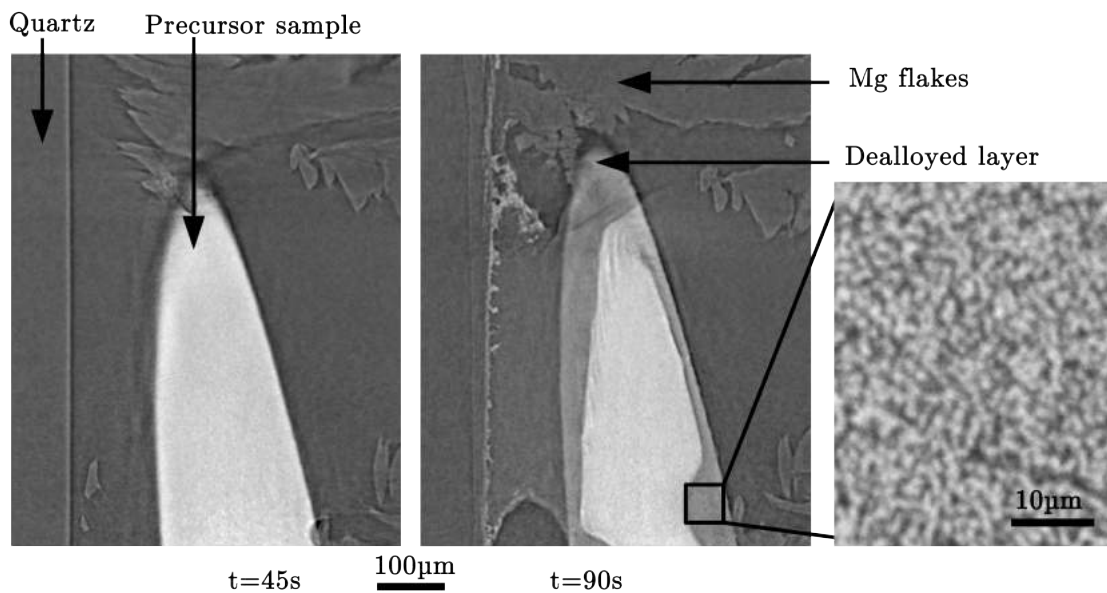


Figure 3.2: 2D view extracted from 3D reconstruction of the evolution of dealloying front during dealloying step.

Fig. 3.2 shows 2D views extracted from 3D reconstruction. The gray intensity is inversely proportional to the density of the material; therefore air/vacuum and magnesium are dark-gray while the precursor's tip is pale-gray. The dealloyed part of the tip, a bi-phased microstructure rich in magnesium, is lighter than the precursor phase and appears on the volume as darker. The dealloyed front is then clearly visible. In the background, *Mg* flakes are visible around the tip. Due to their shape and arrangement, there is a lot of space between the flakes, and it can be seen that there is not so much magnesium around the tip and in contact direct with the precursor.

The evolution with time of the dealloying front is observed. At the beginning ($t = 45$ s) only light phase corresponding to precursor phase is present: the reactor is heated with

the laser system, but the sample does not reached immediately the targeted temperature to start the dealloying process. An incubation time is necessary to heat the whole system and assure contact between *Mg* and precursor surface. At $t = 90$ s, both precursor and dealloyed phases are clearly visible. The dealloyed phase is larger near the *Mg* flakes where an irregular dealloying front is observed. On the right part of Fig. 3.2, a picture of the dealloyed region is presented at higher magnification, clearly showing the expected bicontinuous structure. Even if the system is heated more than $t = 90$ s the progression of the dealloying front is not observed any more, probably due to surrounded *Mg* flaxes which are probably saturated in *Ni* that stops dealloying.

3.1.3 Case 2

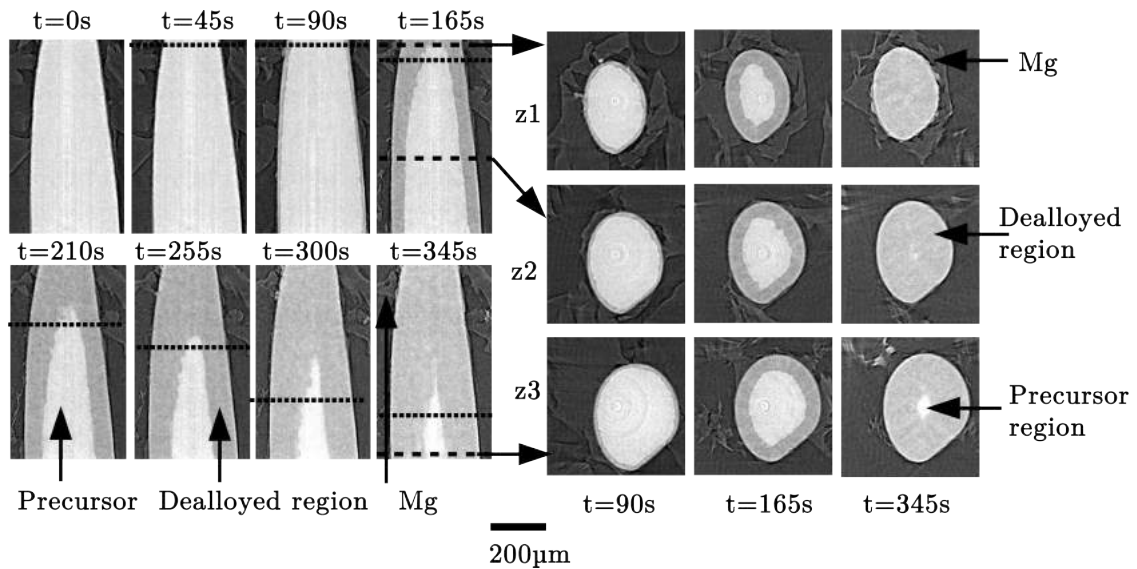


Figure 3.3: 2D view extracted from 3D reconstruction of the evolution of dealloying front during dealloying step. z_1 , z_2 and z_3 correspond to different samples height.

This case corresponds to a standard dealloying experiment. Fig. 3.3 shows 2D views extracted from 3D reconstruction. As explained in previous part, the dealloyed front is clearly visible on this figure. The amount of *Mg* near the tip is higher than in previous part.

The evolution with time of the dealloying front is observed. At the beginning ($t = 0$ s and $t = 45$ s), the dealloying is not observed because of the incubation time as explained in previous part. From $t = 90$ s to $t = 345$ s, both precursor and dealloyed phases are present. At $t = 390$ s all visible part of the sample has been dealloyed.

For this sample, the dealloying process needed around 5 min to be completed.

Fig. 3.4 shows the 3D morphology evolution of precursor phase during dealloying. A first important observation is that the shape of the precursor sample stays almost constant during the dealloying process, only the microstructure is changed.

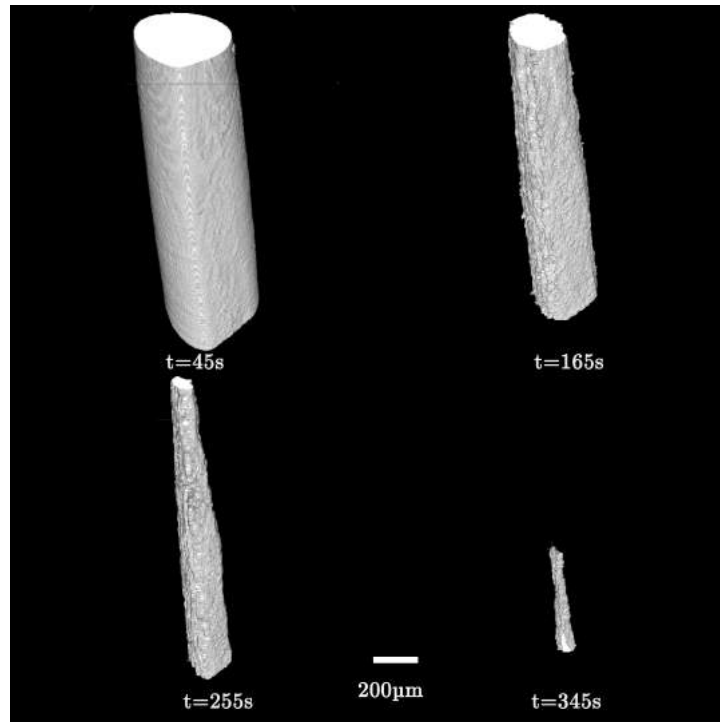


Figure 3.4: 3D precursor morphology evolution during dealloying

Ligaments In the dealloyed area, *FeCr* ligaments can not be individually seen because of their size. From results performed on *Fe-Ni* samples, ligaments size can be expected around $0.8\ \mu\text{m}$ [WAD 13]. The spatial resolution is often taken at two voxels size [MAI 14], leading in this case to a value of $0.64\ \mu\text{m}$, the order of magnitude of the expected ligament size.

Dealloying front At a given time the dealloying thickness along the tip appears rather constant, suggesting that in spite of the heterogeneity of the *Mg* flakes distribution around the tip, the dealloying process occurs everywhere. It is also suggested that the dealloying rate during the process is homogeneous.

The irregularities on dealloying front, as observed in Fig. 3.3 ($t = 165\ \text{s} / z1$) for example, do not seem to be connected to the *Mg* flakes distribution but are similar to observations of grain boundary positions as achieved by [MCC 16c]. That would suggest a first step of recrystallization of the precursor microstructure before the beginning of the dealloying, from highly deformed cold-rolled microstructure to recrystallized large grains microstructure, as it will be explained in Chapter 6.

Dealloying kinetics For every reconstructed volume, dealloyed and precursor phases were segmented and phase thickness were measured using Fiji software “local thickness” function (cf. Chapter 2). As the tips are manually prepared, cross-sections are not perfect

circles and tips thickness is not constant along the length: the tip is thinner on the top. To quantify dealloying evolution, only the body part of the tips is used, far from the top, as illustrated in Fig. 3.3. During the process, the top can be fully dealloyed while the dealloying front can still be seen on the bottom. To simplify, only fully dealloyed part shown below dashed line in Fig. 3.3(a) was used for the analysis.

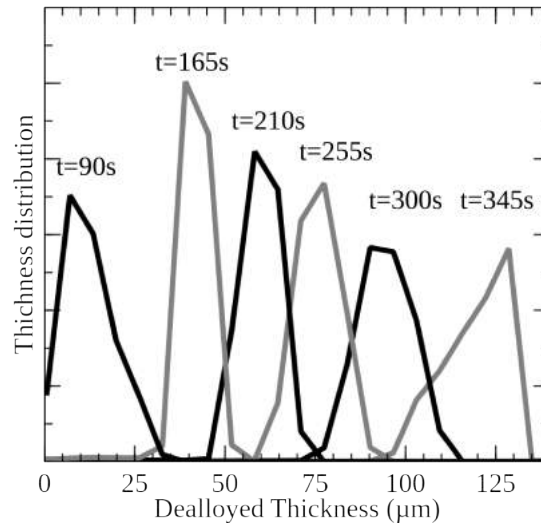


Figure 3.5: Evolution of dealloying thickness distribution with time.

The evolution of dealloyed phase thickness size distribution is displayed in Fig. 3.5. Dealloying layer thickness increases with time as expected; the step $t = 390$ s is not shown because it is already fully dealloyed.

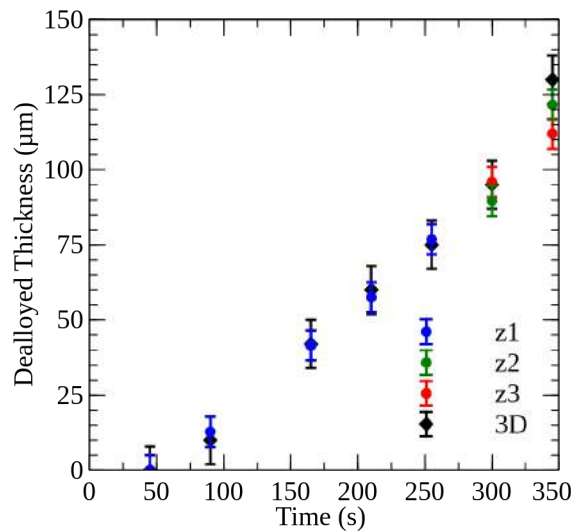


Figure 3.6: Evolution of dealloying thickness with time for 2D and 3D measurements.

From Fig. 3.5, the 3D average dealloyed phase thickness can be extracted and plotted in Fig. 3.6. From Fig. 3.3 the 2D dealloying rate for different height (z_1, z_2, z_3) is manually measured by taking the average of around ten measurements and is also plotted in Fig. 3.6. All data are very close showing the validity of the previous hypothesis: dealloying rate is independent of the height and constant in the three dimensions.

From Fig. 3.6 calculated dealloying rate is $0.42 \pm 0.03 \mu\text{m s}^{-1}$ and incubation time of $61 \pm 3 \text{ s}$.

The observation of the evolution of dealloying front of *Au-Ag* precursor by free corrosion shows also that the dealloying rate is constant in the 3D direction. However it is around 17 times lower, probably due to a very low temperature compared to this experiment [CHE 13c]. These results confirms similarities in mechanisms between liquid metal dealloying with “standard” dealloying by free corrosion.

The dealloying kinetics observed here seems to be not proportional of \sqrt{t} as previously measured by *post mortem* experiments [TSU 13, WAD 16b, MCC 16c]. But compared to all these experiments two majors differences can be considered: the precursor shape (a tip, not a plate) and the limited amount of *Mg* near the precursor tip.

3.1.4 Simulation

In the first part two different experimental behaviours were described and the most important difference was the amount of *Mg* around the precursor sample. To better understand the effect of precursor shape and the *Mg* bath size on dealloying kinetics, some simple simulations based on an 1D diffusion model have been performed.

3.1.4.1 Presentation of the diffusion model

In this model, the dissolution of an element into a molten bath will be considered. The concentration designed by c of the soluble element (*Ni*) in the metallic bath (*Mg*) is assumed to follow the FICK diffusion equation [FIC 55, MCC 16c]:

$$\frac{\partial c}{\partial t} = D\Delta c \quad (3.1)$$

where D corresponds to the diffusion coefficient of the soluble element in the liquid bath. Previous studies suggested that the role of convection is small in the dealloyed region due to the presence of ligaments blocking convection currents [GES 15, MCC 16c].

The interface velocity (v) is controlled by the amount *Ni* going from precursor to *Mg* bath at the solid (c_{sol})/liquid (c_{liq}) interface (int). Assuming that :

- the diffusion only takes place in the liquid (because of the low temperature diffusion in the solid phase can be neglected);
- there is soluble elements conservation at the interface (all *Ni* from precursor is dissolved into the *Mg* bath);
- the concentration in *Ni* at the dealloying reaction interface is fixed by the phase equilibrium;
- a finite size bath, the *Ni* flux at the border is null;

- the influence of ligaments on the *Ni* diffusion in *Mg* bath is not considered;

then the following relation can be obtained [MCC 16c]

$$v = \frac{D}{c_{sol} - c_{liq}} \left. \frac{\partial c(r, t)}{\partial r} \right|_{int} \quad (3.2)$$

with r the position of the dealloying reaction interface

From *post mortem* experiments it was shown that dealloyed thickness is constant on the sample. Dealloyed reaction front is perpendicular to dealloying reaction interface: in case of rectangle geometry (if precursor has a sheet shape), dealloying front will be planar (planar model) while in case of cylindrical geometry (if precursor has a tip shape) dealloying front will be a circle (cylindrical model) [CHE 13c, MCC 16c, TSU 13, WAD 16b]. The precursor (sheet or cylinder) is large/long enough to neglect border effects and consider a 1D model.

Planar shape In the case of planar model (Cartesian coordinate), equation 3.1 will depend on the dealloying depth (x) and become:

$$\frac{\partial c(x, t)}{\partial t} = D \cdot \frac{\partial^2 c(x, t)}{\partial x^2} \quad (3.3)$$

The resolution of this equation can be done analytically [BIR 06, BOK 05, MEH 07], giving a parabolic solution for the dealloying depth as a function of time and a constant k (depending on boundary conditions and diffusion coefficient):

$$x = (kt)^{0.5} \quad (3.4)$$

Cylindrical shape In the case of cylindrical model (cylindrical coordinate), equation 3.1 will depend on the dealloying thickness (r) and the cylinder radius (R) and become:

$$\frac{\partial c((R - r), t)}{\partial t} = D \frac{1}{R - r} \frac{\partial}{\partial (R - r)} \left((R - r) \frac{\partial c((R - r), t)}{\partial (R - r)} \right) \quad (3.5)$$

Because the diffusion equations are different depending on coordinate (precursor shape), different dealloying kinetics can be expected. An analytical solution could be obtained in case of Cartesian coordinate (cf. equation 3.4) but it is not the case for cylindrical coordinate.

Numerical integration Equations 3.2, 3.3 and 3.5 are integrated numerically after discretization on a grid. The numerical integration of the model's equation gives access to the composition profiles of *Ni* in the dealloyed region and the evolution of dealloyed depth with time.

Following parameters will be used :

- $R_{init} = 160 \mu\text{m}$ corresponds to the radius of precursors tips measured on X-ray tomography images;

- $c_{liq} = 18$ at% corresponds to the maximum Ni solubility in Mg bath measured by SEM-EDX after partial dealloying at low temperature and also corresponds to solubility of Ni in Mg from phase diagram at 665° (for more details please refer to Chapter 4 and Chapter 6);
- $c_{sol} = 70$ at% corresponds to the amount of Ni in the precursor;
- $c_{init} = 0$ at% corresponds to the initial concentration of Ni inside Mg bath. There is no Ni inside Mg bath before starting dealloying;
- $D = 10^{-9} \text{m s}^{-2}$ corresponds to the diffusion coefficient of Ni inside liquid Mg , because experimental coefficient is not known [NIM], this value was chosen but should be considered as an order of magnitude only for diffusion in liquid metals;

The influence of bath size will be studied, this value will be specified for each result.

3.1.4.2 Effect of precursor shape

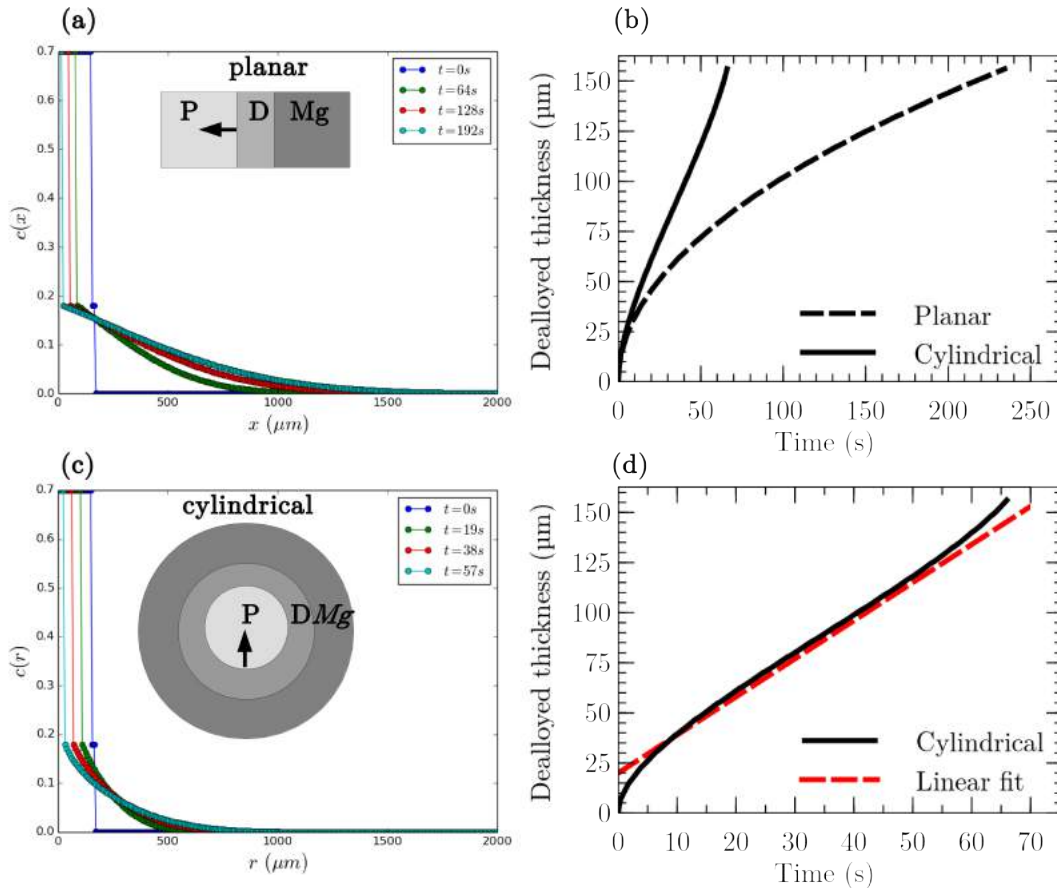


Figure 3.7: Evolution of Ni concentration in Mg bath and dealloyed front position in case of a planar interface (respectively a and b), cylindrical interface (respectively c and d). P corresponds to precursor and D to dealloyed region, Mg to the Mg bath and the arrow to dealloying reaction direction.

First the effect of the precursor shape on dealloying kinetics was investigated. To mimic the situation of an infinite bath, a large bath (10 times larger than precursor thickness) was considered in the simulation. Fig. 3.7 displays the evolution of concentration profiles for both the planar (a) and cylindrical (c) interfaces. Fig. 3.7(b) compares the evolution of dealloyed depths for planar and cylindrical interfaces and (d) compares the dealloying kinetics of cylindrical interface with a linear kinetic. The fit was done for the whole data.

Concentration profile It is noticeable that the geometry has a significant influence on the evolution of the concentration profiles and dealloying kinetics. In contrast with the planar case, the length of the dealloying front reaction in cylindrical geometry gets smaller along dealloying process while dealloying front reaction length in planar geometry is constant. Therefore the dealloying kinetics are different for samples with different shapes.

Evolution of dealloyed thickness The evolution of dealloying front with time shows that dealloying is faster in case of cylindrical shape (around 65 s *vs* 250 s for planar interface)(cf. Fig. 3.7(c)). In case of planar interface, the dealloying depth evolves with the square-root of time (cf. equation 3.4) whereas it is notably different for the cylindrical geometry. At the beginning of dealloying when dealloyed thickness is very small compared to precursor thickness, both geometries show a similar behaviour (until around 20 μm). Then for the case of cylindrical interface (Fig. 3.7(d)) the curve becomes almost linear (until 120 μm). Finally when the precursor thickness is very small dealloying rate accelerates.

Interface shape has a significant influence on dealloying kinetics : curve shape and necessary time to dealloyed the sample are different.

3.1.4.3 Effect of Mg amount

This work focuses now on investigating the influence of the size of the liquid Mg bath on dealloying kinetics for cylindrical shape precursors. Fig. 3.8 presents the evolution of Ni composition in Mg bath in case of a $R_{bath} = 80 \mu\text{m}$ (a) corresponding to the estimated bath size measured on X-ray tomography reconstruction of case 1, $R_{bath} = 240 \mu\text{m}$ (b) corresponding to the estimate bath size measured on X-ray tomography reconstruction of case 2. Fig. 3.8 shows the evolution of dealloying depth with time for different bath size.

Case 1 In case 1, Ni concentration evolution can be seen in Fig. 3.8 (a). The maximum amount in Ni allowed into the bath is reached during dealloying because concentration curves become flats ($t=13$ s). When bath saturation occurs, dealloying is stopped, visible on (c) by the plateau of the red curve (from around $t=12$ s). Indeed until $t = 5$ s, the evolutions of dealloying front are similar for all cases, however when bath is very rich in Ni dealloying kinetics decreases to 0 and dealloying stops: dealloying thickness stays constant. It corresponds to what is experimentally observed when the dealloying depth does not increase even if the reactor is continuously heated.

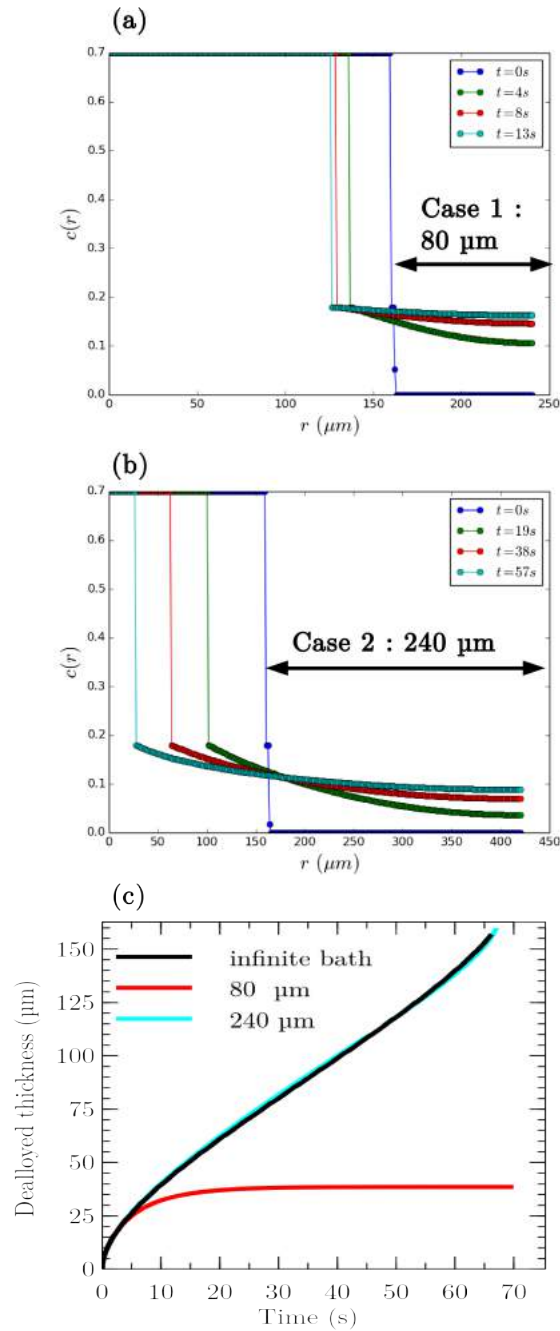


Figure 3.8: Evolution of Ni concentration in Mg bath in case of a $R_{bath} = 80 \mu m$ corresponding to experimental bath size of case 1 (a), $R_{bath} = 240 \mu m$ corresponding to experimental bath size of case 2 (b), evolution of dealloyed front position with time for bath size (c) for cylindrical shape precursor.

Case 2 In case 2, Ni concentration evolution can be seen in Fig. 3.8 (c). The bath gradually gets richer and richer in Ni , however saturation is not reached. Bath size has here a minor influence on dealloying kinetics: additional few seconds are necessary to dealloy the whole sample compared to infinite bath. In case 2, the amount of Mg seems to be enough to have a negligible impact on the dealloying kinetics.

Experimentally, the evolution of the dealloying depth with time of case 2 (cf. Fig. 3.9 dots) is comparable to its simulation (line). The bath thickness was measured on the X-ray tomography reconstruction. To match results the diffusion coefficient value was adjusted ($D = 0.2 \times 10^{-9} \text{m s}^{-2}$). This low value can be explained by the presence of ligaments inside the bath which modify the kinetics and were not taken into account in the model.

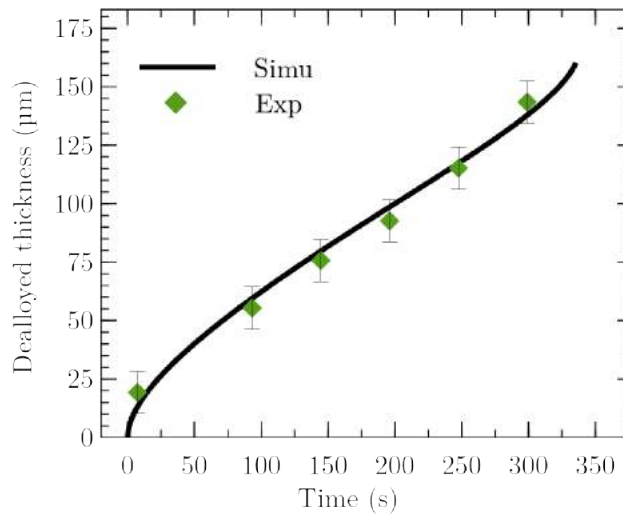


Figure 3.9: Evolution of experimental (dots) and simulated (line) dealloying thickness with time.

Both interface shape and amount of Mg has an influence on dealloying kinetics. It was possible to explain the different experimental behaviours with a diffusion model to simulate dealloying process. The consistence between experimental and simulated values proves that the process is controlled by the diffusion of Ni in the bath.

3.2 *In situ* dealloying followed by X-ray diffraction

3.2.1 X-ray diffraction (XRD)

XRD is a powerful experimental technique to measure crystallinity, crystallographic phase in presence, residual strain etc... When a monochromatic X-ray wave impacts a sample surface, one part of the incident amplitude will be reflected by each atomic plane of the sample. The X-ray wavelength is similar to the inter-atomic plan distance, the waves interference will be alternatively constructive and destructive. Therefore the quantity of photons X will differ depending on the diffraction phenomenon.

To observe atoms' diffraction, atoms should follow the Bragg's condition [PAR 83]. Bragg's condition is defined by the Bragg law:

$$\lambda = 2d \sin \theta \quad (3.6)$$

with λ the X-ray wavelength, d the distance between two atomic planes and θ the incidence angle of the X-ray beam on the sample.

3.2.2 Experimental process

XRD measurements in synchrotron were performed on ID11 (ESRF, France) with an energy of 35.1 keV and acquisition time of 214ms with 1 s break. 2D ring patterns were recorded in transmission geometry. Rings integration were done using an azimuthal integration ("caking") with PyFai program [KIE 13a] [KIE 13b] to get the evolution of intensity with 2θ as shown in Fig. 3.10.

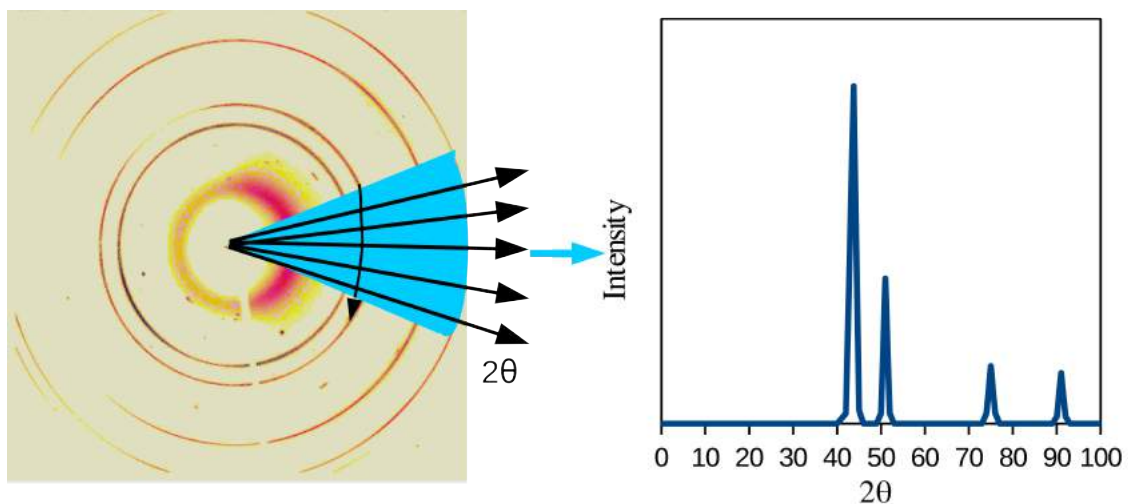


Figure 3.10: Principle of rings integration from a 2D diffraction pattern.

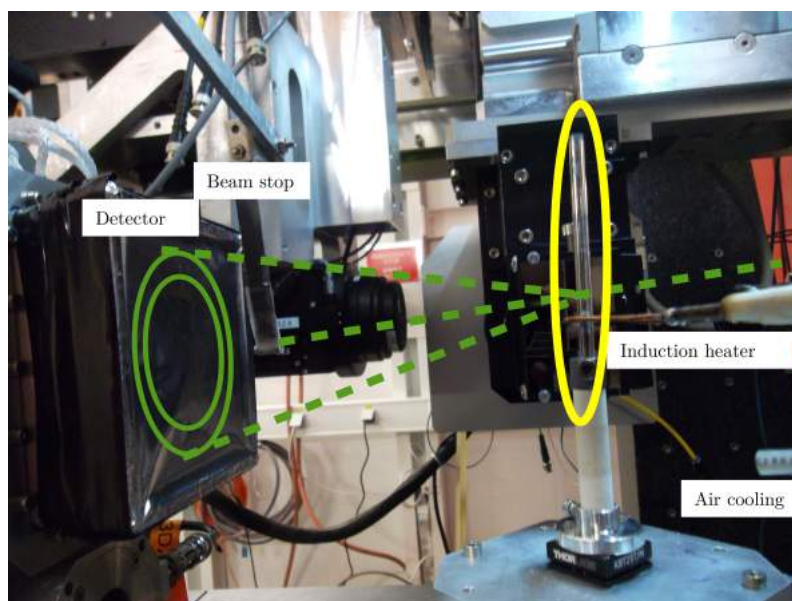


Figure 3.11: Picture of the experimental set-up. Green lines correspond to X-ray beam and yellow circle to the reactor.

The *in situ* dealloying experiments required a dedicated reactor described in part 3.1.1 to handle the liquid magnesium at high temperature.

An induction heater was used for the thermal cycles. The induction loop was placed around the steel sticks. Temperature was transmitted from the steel stick to the whole reactor. Such a set-up does not allow a fine control of the temperature, a rough calibration was done with a non sealed quartz with the precursor tip inside. The thermocouple was set in contact with precursor tip.

3.2.3 Results

The dealloying corresponds to a FCC-BCC phase transformation in this part. With the X-ray diffraction, the evolution of strain during dealloying process can be calculated. Fig. 3.12 shows in dashed line the evolution of intensity and in plain line the evolution of the strain. To calculate the strain, the original peaks position of FCC phase before heating and the peaks position after cooling down for BCC phase are taken as reference. Each color corresponds to one different diffraction peak. Blue and orange colors correspond to FCC peaks and red and green to BCC ones.

Heating At the initial step only FCC peaks are present because precursor are only FCC phase (XRD pattern and phase diagram will be shown in Chapter 4). The intensity of precursors peak is the highest. When the heating starts the relative strain increases because of thermal dilatation.

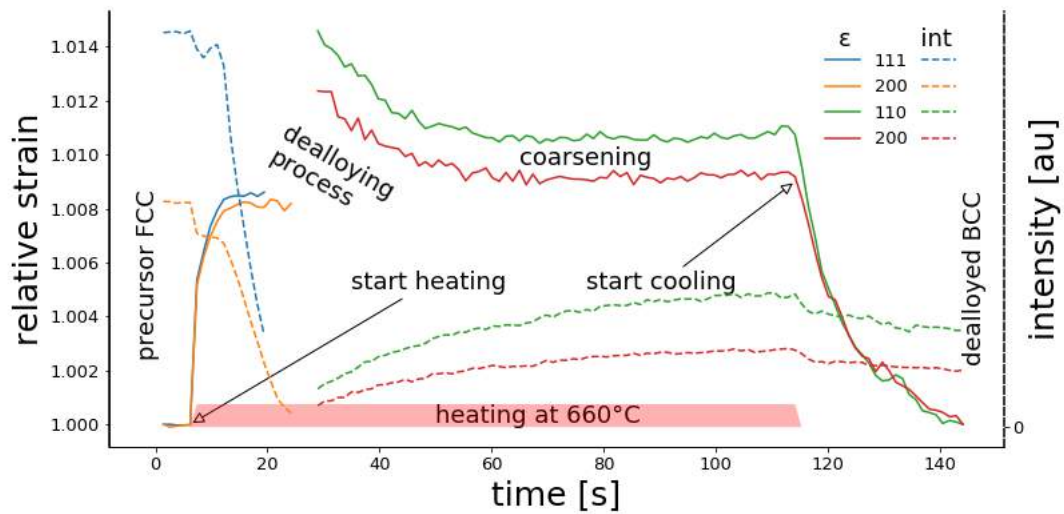


Figure 3.12: Evolution of relative strain and intensity of 4 different diffraction peaks during dealloying.

Dealloying The intensity is also decreasing. This can be explained by the fact that the amount of FCC/precursor phase is decreasing during dealloying. As simultaneous FCC/precursor peaks intensity decreases while BCC/dealloyed sample peaks intensity increases corresponding to dealloying process is expected. However intensities were here too low to be measured and the early stage of dealloying could not be captured.

Coarsening At the first steps after dealloying, relative strain continues to decrease until stabilizing for ligaments coarsening (around 20-30 s) that could be explained by the dissolution of *Ni* remaining in the solid phase after ligaments formation. During ligament coarsening, intensity becomes higher and higher because of ligaments size (grain size) is increasing from few hundred nanometers to few micrometers.

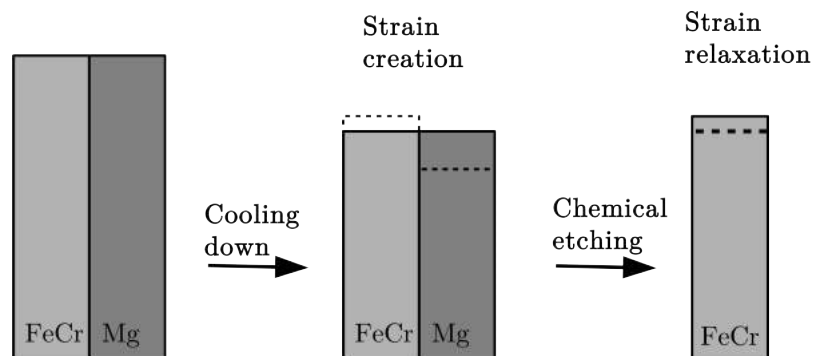


Figure 3.13: Schema of strain evolution during cooling and chemical etching.

Cooling Just after dealloying step, porous *FeCr* is infiltrated by Mg-rich melt. While the heater is stopped, *Mg* based phase will solidify and both phase will be cooled together during cooling step. The relative strain will decrease due to thermal shrinkage. *FeCr* phase has lower coefficient than *Mg* phase as written in Table 3.1. *Mg* based phase will suffer from shrinkage more than *FeCr* phase if both phases were independent and not interconnected as in the present study. Because both phase can not shrink as they would normally do, stress will be generated in both phases. The interaction of the 2 phases can be noticed around 120s, when relative strain curves become irregular instead of keeping the same slope due to thermal contraction along the cooling step.

Taking a simple model composed of 2 parallel bars one made *FeCr* and one made *Mg* (cf. Fig 3.13). Considering the difference of mechanical properties, the first materials which will plastify is *Mg* phase for at most 190 MPa stress [KAY]. Therefore the maximum residual elastic stress inside *FeCr* are evaluated to be 0.09%. The stress in the *Mg* phase after cooling was also noticed in finite element analysis measurement [SAI 16].

	<i>Fe₇₅Cr₂₅</i>	<i>Mg₉₅Ni₅</i>
α [10^{-6}K^{-1}]	11.7	29.7

Table 3.1: Linear thermal expansion coefficient α measured at 327 °C [TOU 75].

At the early stage of coarsening a lattice parameter diminution probably due to the dissolution of *Ni* which was remaining in the solid phase after ligaments formation was observed. During cooling the interaction of ligaments and *Mg* phase is noticeable. This interaction creates residual strains.

3.3 *In situ* chemical etching followed by X-ray tomography

3.3.1 Experimental process



Figure 3.14: Picture of the experimental set-up. Green line corresponds to X-ray beam. Yellow circle corresponds to the sample tip.

This experiment was performed on the tomcat beamline (SLS, PSI, Switzerland). The X-ray tomography experimental parameters can be found in Chapter 2. A scan was acquired every 1.5 min. FeCr-Mg composite was prepared in the same conditions as described and characterized in Chapter 4 and Chapter 5 from $(Fe_{80}Cr_{20})_{30}Ni_{70}$ precursor. The sample is cut into a rectangular rod with 0.5 – 1 mm sides and 1 cm in length and then polished into a tip shape. The tip is introduced in a polymer tube with low concentrated nitric acid (4% volume concentration), the dissolution of the solid-state solution of *Mg* is followed during 75 minutes. The experimental set-up is shown in Fig. 3.14.

Mg bath after solidification will be referred to as *Mg* phase in this part.

3.3.2 Results

FeCr characteristic sizes Fig. 3.15(a) presents a 2D view extracted from 3D reconstruction for $t = 1048\text{s}$ and the red highlight corresponds to a defect. Both phases are present: *FeCr* ligaments and *Mg* phase. As mentioned in previous studies, the propagation of the dissolution front is perpendicular to reaction interface. Fig. 3.15 (b) shows the evolution of *FeCr* ligaments and *Mg/air* phase thickness during etching step measured on an around $100\ \mu\text{m}^3$ in the center of the tip. Both systems present a unimodal distribution which is similar to previous studies and similar to the ones of Chapter 5 [LIU 12, JIN 17]. The average *FeCr* ligaments size was estimated to be $4.5 \pm 1.5\ \mu\text{m}$.

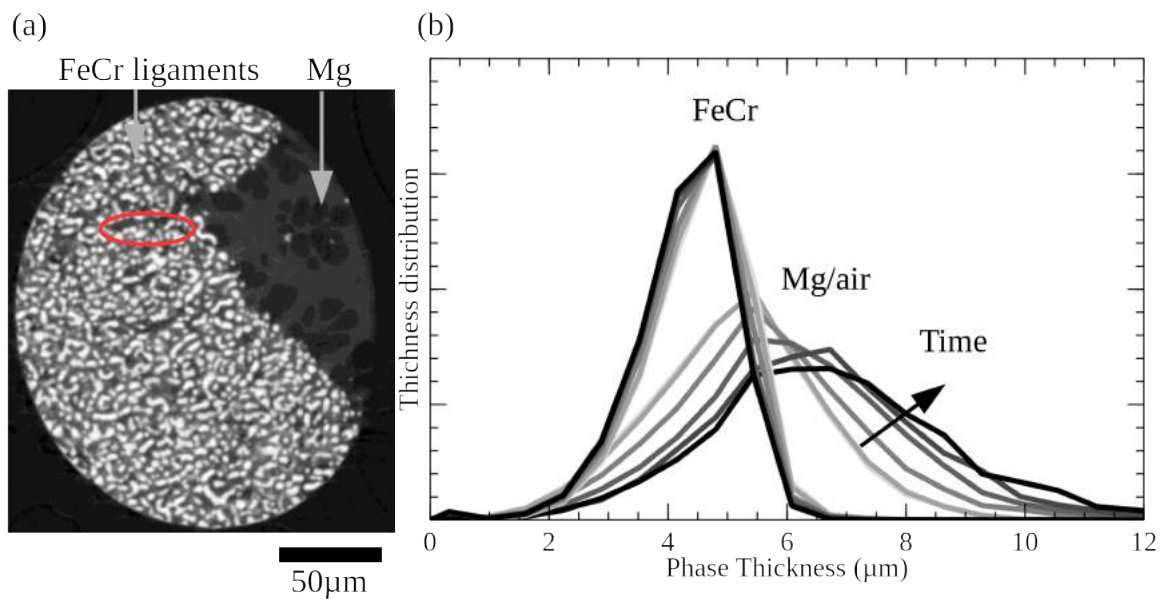


Figure 3.15: (a) 2D view extracted from 3D reconstruction for $t=1048\text{s}$. Red circle highlights a defect (b) Evolution of *FeCr*, *Mg/air* phases thickness during sacrificial phase etching step.

Mg/pores characteristic sizes During the etching step, contrary to the *FeCr* phase thickness which was slightly shifted to smaller size, the average thickness of *Mg/air* phase was increasing from $5.5\ \mu\text{m}$ to more than $6.7\ \mu\text{m}$. This shift of *Mg/air* average thickness means that the space between ligaments becomes larger when etching step occurs. This expansion was locally more important where the sample presents defects.

At the end of the etching step, a global expansion of the foam is therefore observed. As mentioned in previous part, after the cooling process *FeCr* phase is under compression (cf. previous section with dealloying followed by XRD). The suggested lattice strain estimated in the previous section is very small so can not be visible with this X-ray tomography experiment. This global expansion (except peeling) is not observed for bulk sample therefore it is suggested that mechanical stresses was accumulated during preparation for X-ray tomography measurement. The stress releases observed here is the relaxation of mechanical stresses and peeling formation.

Comparison with literature Previous study on dealloyed *TiCrZr-Mg* to give porous *TiCrZr* after *Mg* etching also showed that *TiCrZr* ligaments size were almost not affected by etching step (slightly increasing) [CHE 13b]. However they calculated smaller pore characteristic length than *Mg* one. The difference between this two results can be explained by different measuring techniques : in this study pore size was measured while on [CHE 13b] pores size was calculated.

Etching kinetic From Fig. 3.15(a) and all reconstructions, the evolution of the etching front can be manually measured by taking the average of around five measurements of *Mg* phase thickness. The measured etched thickness is plotted in Fig. 3.16. The etching rate is constant during etching step. The evolution of the etching front appears as linear with time: the etching rate can be fitted at 20 nm s^{-1} which is quite low. This rate could be increased by increasing nitric acid concentration [WAD 11a].

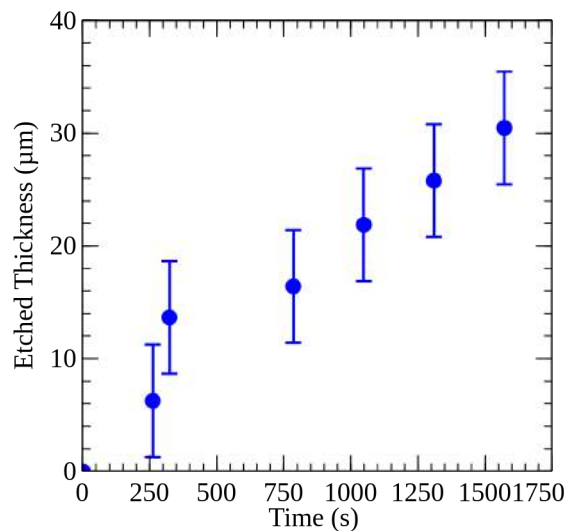


Figure 3.16: Evolution of etched front with time during *Mg* phase etching step.

The *in situ* observation of chemical etching step shows: *Cr* addition protects ligaments from chemical etching. A volumetric expansion of the foam due to stress relaxation. The evolution of the etching front appears linear with time.

3.4 Conclusion

In this chapter, the elaboration was *in situ* followed by X-ray tomography and X-ray diffraction measurements from $(Fe_{80}Cr_{20})_{30}Ni_{70}$ precursors. The *Ni* concentration in *Mg* bath influences dealloying kinetics. Dealloying front reaction progresses until bath saturation. Dealloying kinetics is linked with precursor shape. It was possible to simulate the evolution of dealloying front. The consistence between experimental and simulated values proves that the process is controlled by the diffusion of *Ni* in the bath.

XRD measurements show at the early stage of the coarsening a slight decrease of the lattice parameter of the BCC phase. This is probably due to the dissolution of the residual *Ni* which remains in the solid phase after ligaments formation. During cooling the interaction of ligaments and *Mg* phase is noticeable. This interaction will create residual thermal stresses due to the different thermal dilation coefficients.

FeCr ligaments are almost not attacked by nitric acid solution. But the etching step shows a noticeable volumetric expansion of the foam due to stress relaxation. This relaxation is higher where the sample presents some microstructure defects. Therefore it is important to preserve foams from defects.

This chapter showed the feasibility of *in situ* observations during dealloying and etching process with qualitative analysis. However these experiments were realized with a weak control of temperature and *Mg* amount around precursor tip that make impossible the evaluation of the influence of other parameters like precursor composition/preparation on dealloying kinetics. To evaluate the influence of these parameters the experimental set-up should be improved.

Chapter 4

Materials elaboration and characterization

This chapter will present the different steps required to obtain the different materials produced for this study. A summary of this process is presented in Fig. 4.1. First, a precursor sample will be prepared and melted by arc-melting. Then a metal/metal composite will be produced by liquid metal dealloying. To get a porous sample, one phase of the metal/metal composite will be chemically etched. Finally, after pores infiltration of the porous sample by epoxy resin, a metal/polymer sample will be obtained. For each step the resulting microstructure will be studied, mainly by X-ray tomography, SEM and SEM-EDX.

Contents

•	4.1	<i>Fe-(Cr)-Ni /Mg</i> system	60
	4.1.1	Mixing enthalpy	60
	4.1.2	Phase diagrams	61
	4.2	Precursors	63
	4.2.1	Elaboration	63
	4.2.2	Characterization	63
	4.3	Metal/metal composites by liquid metal dealloying	65
	4.3.1	Elaboration	65
	4.3.2	Characterization	65
	4.4	Porous metal	68
	4.4.1	Elaboration	68
	4.4.2	Chemical etching effect on foam microstructure	68
	4.5	Metal/polymer composites	71
	4.5.1	Epoxy-amine networks	71
	4.5.2	Methods	71
	4.5.3	Elaboration	73
	4.5.4	Characterization	74
	4.6	Conclusion	78

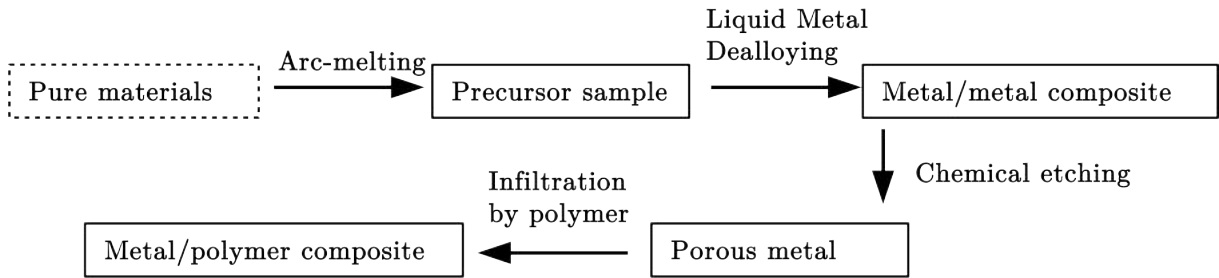


Figure 4.1: Process to obtain a metal/polymer composite from pure materials. This process is the one used along this study.

I would like to thank Jérôme Adrien (MATEIS) for his helped for performing X-ray tomography experiments.

In this work, to change porosity, 3 different precursors compositions will be involved: $(Fe_{80}Cr_{20})_{30}Ni_{70}$, $(Fe_{80}Cr_{20})_{50}Ni_{50}$ and $(Fe_{80}Cr_{20})_{70}Ni_{30}$. Precursors are presented in a $(Fe_yCr_{1-y})_xNi_{100-x}$ form. To simplify, they will be referred to as xFeCr-Ni. After dealloying these precursor samples, the bicontinuous sample will be referred to as xFeCr-Mg. After chemical etching of Mg based phase, sample will be referred to as xFeCr. To produce metal/polymer composite a pre-polymer epoxy (DGEBA) will be polymerized with an amine hardener Jeffamine D2000 to produce a rubbery polymer or IsoPhorone Diamine (IPD) to produce a glassy polymer. The metal/polymer composite will be referred to as xFeCr-D2000 or xFeCr-IPD depending on the hardener used for the polymerization.

4.1 *Fe-(Cr)-Ni / Mg* system

4.1.1 Mixing enthalpy

Fe, *Ni*, *Cr* present suitable mixing enthalpy (as presented in Table 4.1) to be mixed together as precursor samples then only *Ni* can be dealloyed in *Mg* melt to get *in fine* porous *FeCr*.

Fig. 4.2 and Fig. 4.3 presents *Fe*, *Cr*, *Ni* phase diagrams respectively at room and dealloying temperature (827 °C). Precursor samples are mostly FCC while dealloyed samples are BCC [MAR 39, HAY 90]. For further discussion about present phases, please refer to section 4.2.2. Phase diagram shows the miscibility of precursor components. Theoretical parting limit for FCC/BCC lattice is 20/25 at% Ni [ART 09, MCC 16c].

Mixing enthalpy (kJ/mol)	Fe	Cr	Ni	Mg
Fe	x	-1	-2	18
Cr	-1	x	-7	24
Ni	-2	-7	x	-4
Mg	18	24	-4	x

Table 4.1: Mixing enthalpy. Red color corresponds to mixing component in precursor samples, green color to component able to be mixed with element bath, blue color to components not able to be mixed with element bath [TAK 05].

4.1.2 Phase diagrams

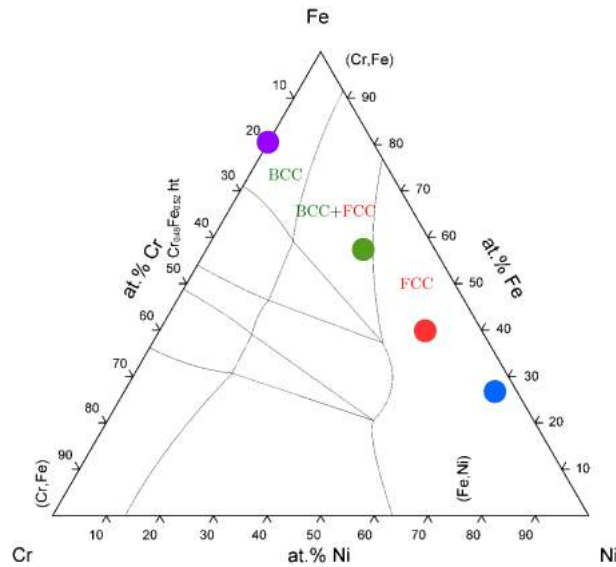


Figure 4.2: *Fe*, *Cr*, *Ni* phase diagram at room temperature, blue color correspond to 30FeCr-Ni, red to 50FeCr-Ni green to 70FeCr-Ni and violet to FeCr after dealloying [MAR 39].

The Ni-Mg phase diagram is displayed in Fig. 4.4. *Mg* melting point is 650 °C and boiling point 1090 °C. Dealloying temperature range is around 400 °C [GUI 09]. When dealloying starts, there is only pure *Mg*. Then during dealloying *Mg* will enrich in *Ni*. For low amount in *Ni*, the Mg-Ni phase diagram presents an eutectic.

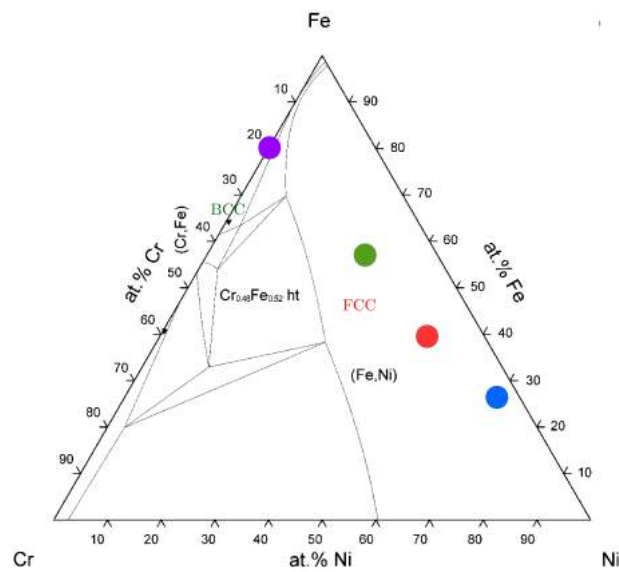


Figure 4.3: *Fe, Cr, Ni* phase diagram at dealloying temperature, blue color correspond to 30FeCr-Ni, red to 50FeCr-Ni green to 70FeCr-Ni and violet to FeCr after dealloying [HAY 90].

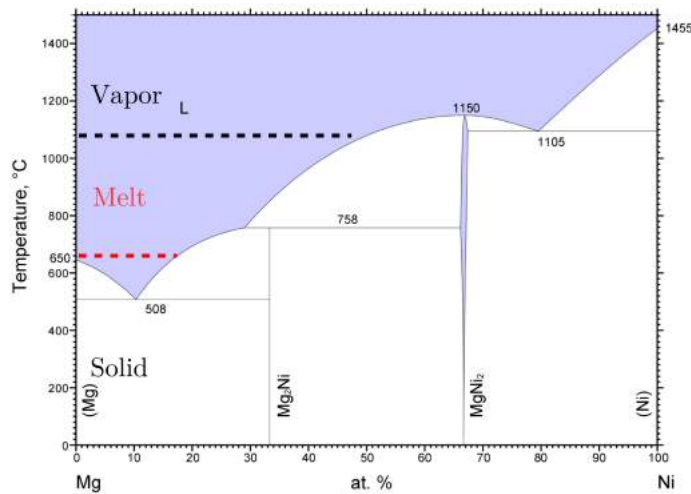


Figure 4.4: *Ni-Mg* phase diagram. Dashed red line correspond to *Mg* melting temperature and black dashed line to *Mg* vaporization temperature [MIE 08a].

4.2 Precursors

4.2.1 Elaboration

Precursor samples were elaborated by arc-melting furnace (ACM-0145, Diavac Limited, Japan). The principle of arc-melting furnace is described in [KRA 99]. Pure *Fe*, *Cr* and *Ni* (with a purity exceeding 99.99%) introduced in the right proportion were melt under a highly pure *Ar* atmosphere during 1 min with an intensity of 100 A then during 2 min at 200 A on each face. This last step was repeated 3 times.

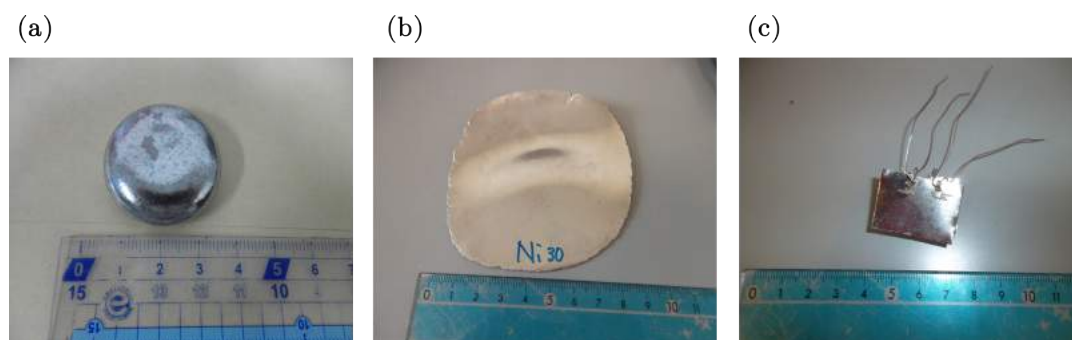


Figure 4.5: Precursor samples images (a) after arc-melting (b) after cold-rolling (c) before dealloying.

4.2.2 Characterization

Resulting precursor ingots had the shape of disks about 2.5 cm diameter and 1 cm height with a weight of about 30 g (cf. Fig. 4.5(a)). Table 4.2 shows the comparison between the expected composition and real composition measured by SEM-EDX. Both values are close, which means that there was not matter lost during arc-melting process. Fig. 4.6 shows SEM-EDX element maps and Fig. 4.7 shows the diffraction pattern of precursor samples. Only FCC phase was experimentally observed for all precursors. Because same phases are presented in all precursor, element maps and XRD pattern are shown only for one composition but are similar for other precursor composition. From phase diagrams, 30FeCr-Ni and 50FeCr-Ni should be FCC phase at room and dealloying temperature without allotropic transformation between both. However 70FeCr-Ni should be composed of both FCC (main) and BCC phases at room temperature [MAR 39, HAY 90]. At higher temperature (over 400 °C) 70FeCr-Ni is composed of only FCC phase [PUG 03]. Because of low inter-diffusion coefficient between *Fe* and *Ni*, it is probably more difficult to reach equilibrium at low temperature. This is a good explanation why BCC phase could not be experimentally observed [CAC 10].

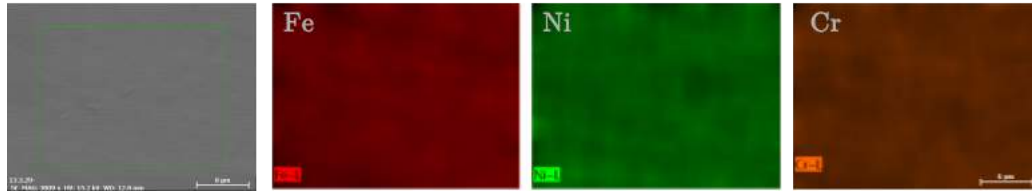


Figure 4.6: SEM micrograph and elemental mappings (SEM-EDX) for precursor sample. The composition is homogeneous on the surface.

	Fe	Cr	Ni
Expected amount (%at)	24	6	70
Real amount (%at ± 1)	24.4	5.6	70.0
Expected amount (%at)	40	10	50
Real amount (%at ± 1)	40.8	9.8	49.4
Expected amount (%at)	56	14	30
Real amount (%at ± 1)	56.1	14.0	29.9

Table 4.2: Precursor samples composition.

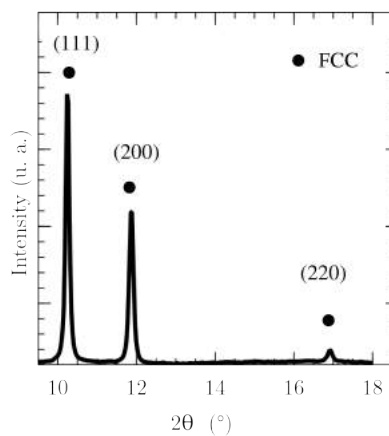


Figure 4.7: A typical XRD diffraction pattern of precursor samples. Precursor samples present a FCC lattice.

Resulting precursor samples from arc-melting were cold-rolled in two normal directions until reaching the thickness of 1 mm (cf. Fig. 4.5(b)). The precursor sheets were cut into rectangular shapes 30×20 mm. They are drilled on the top corners in order to be able to hang them during dealloying process (cf. Fig. 4.5(c)).

4.3 Metal/metal composites by liquid metal dealloying

4.3.1 Elaboration

Liquid metal dealloying was performed in a special furnace (VIC international, Japan) shown in Fig. 4.8. Dealloying furnace was working under a high purity *Ar* atmosphere. *Mg* was melt by an induction coil. A thermocouple was introduced in the crucible to check the temperature. Two samples were dealloyed simultaneously. The two samples were bound on the same branch and a *Fe* wire is weld at the bottom of the samples to keep a gap between them. Most of the samples were dealloyed for 1 h at 820 °C. In some cases, different dealloying times and temperatures are applied, which will be notified.

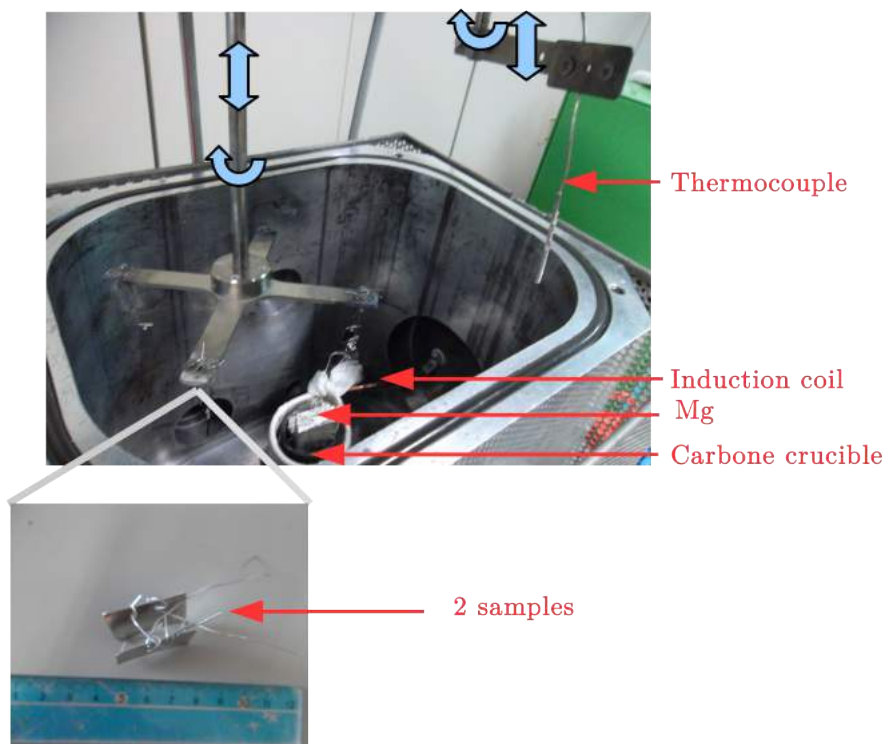


Figure 4.8: Picture of dealloying furnace before liquid metal dealloying experiment. The *Mg* is melt into a *C* crucible. An induction coil heats the system. A thermocouple measures the temperature.

4.3.2 Characterization

4.3.2.1 Validation of dealloying process

Fig. 4.9 presents SEM micrographs and elemental mappings (SEM-EDX) for dealloyed samples from (a) $(FeCr)_{30} Ni_{70}$ (b) $(FeCr)_{50} Ni_{50}$ (c) $(FeCr)_{70} Ni_{30}$ precursors. In all these cases, a bicontinuous structure composed of a *FeCr* phase and a *Mg* based phase is present. In the *Mg* based phase some intermetallics compounds of *Mg* and *Ni* are present

with an eutectic structure [MAS 90]. Table 4.3 shows the composition measured by SEM-EDX after dealloying. This result corresponds to an average of several measurements. The ligaments phase composition analysis shows that the residual amount of *Ni* is negligible and that the ratio *Fe/Cr* is preserved during dealloying. The *Mg* based phase presents a wide dispersion : area without intermetallic compounds are almost *Ni* free while areas with intermetallic compounds present about 12 % *Ni*. However values presented in Table 4.3 are averaged for both areas.

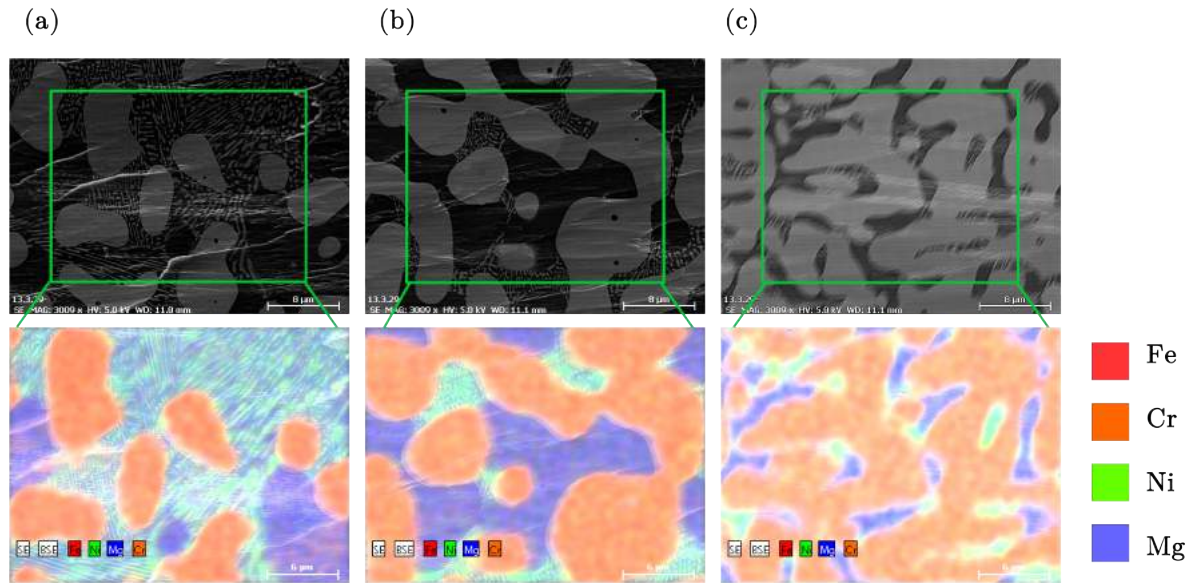


Figure 4.9: SEM micrograph and elemental mappings (SEM-EDX) for dealloyed samples from (a) $(FeCr)_{30} Ni_{70}$ (b) $(FeCr)_{50} Ni_{50}$ (c) $(FeCr)_{70} Ni_{30}$ precursors. A phase separation between FeCr and MgNi phases is observed.

atomic proportion (%at ± 1)		Fe	Cr	Ni	Mg
From $(FeCr)_{30} Ni_{70}$ precursor	global	27	6	4	63
	ligament phase	79	19	0.3	1.7
	Mg based phase	0.5	0.5	5	94
From $(FeCr)_{50} Ni_{50}$ precursor	global	34	10	2	54
	ligament phase	79	20	0.6	0.4
	Mg based phase	2.5	1	6.5	90
From $(FeCr)_{70} Ni_{30}$ precursor	global	48	17	2	33
	ligament phase	79	19	0.4	1.7
	Mg based phase	7	2	6	85

Table 4.3: Compositions of samples different phase after dealloying for 1 h at 820 °C.

4.3.2.2 2D microstructure characterization

Table 4.4 presents a quantitative analysis on 2D images of phase fraction, ligaments size and pores size. The results are very close to the 3D quantitative analysis (cf. Tables 4.5 and 5.2) of Chapter 5 . However the accuracy of these values is lower than the 3D values because only a couple of ligaments are considered in 2D and also the cross-section of 3D ligaments are not necessary done on the middle of ligaments and then ligaments thickness are likely to be underestimated [SAL 13]. Therefore, a 2D measurement can give a good estimation of density or ligaments thickness but a 3D measurement is preferable when it is possible.

	30FeCr-Mg	50FeCr-Mg	70FeCr-Mg
Average Ligaments thickness (μm) ($\pm 2 \mu\text{m}$)	5.2	5.2	4
Average Mg phase thickness (μm) ($\pm 2 \mu\text{m}$)	7	3.6	1.1
FeCr phase fraction (vol%) (± 5)	35	52	26

Table 4.4: Morphological characteristics lengths and phase fraction measured in 2D after dealloying from different precursor composition.

4.3.2.3 Sample homogeneity characterization

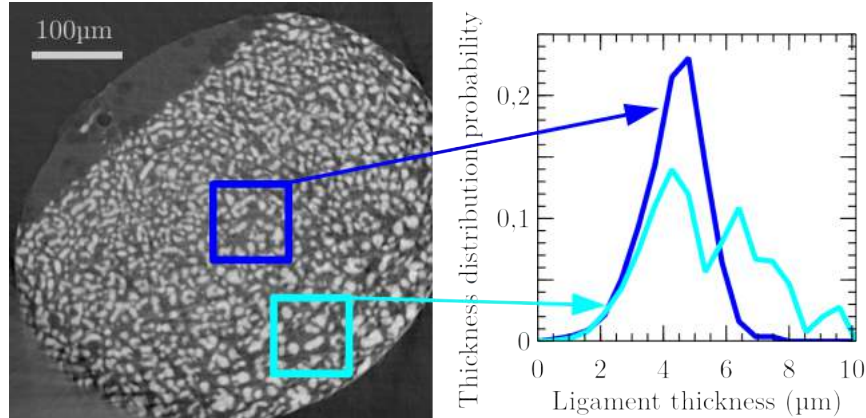


Figure 4.10: Slice extracted from 3D reconstruction of metal/metal composites (left) Ligaments thickness distribution in two areas (center and edge of the sample).

Fig. 4.10 shows a slice which is a section of a 3D reconstruction of metal/metal composites. The two ligament size distributions done on the 3D reconstruction include respectively the area shown on the slice. Ligaments inside an area near the center of the sample present homogeneous ligament size distribution while ligaments at the edge of the sample present inhomogeneous ligament size distribution with the presence of large ligaments. It corresponds to boundaries effect during coarsening [GES 15]. To avoid this boundary effect, all further analysis will be done on an ERV (cf. Chapter 2) volume at the center of the tip.

After liquid metal dealloying, a bicontinuous structure composed of one *Ni* free *FeCr* phase and one sacrificial phase were obtained. The sacrificial one shows an almost *Ni* free *Mg* area. Some intermetallics compounds of *Mg* and *Ni* are also present with a eutectic structure [MAS 90]. The total residual amount of *Ni* in the sample is less than 5 at%. The edge of the sample present inhomogeneous ligament size distribution with the presence of large ligaments while the center of the sample presents an homogeneous distribution. Further analysis will be done on volumes in the center of the sample.

4.4 Porous metal

4.4.1 Elaboration

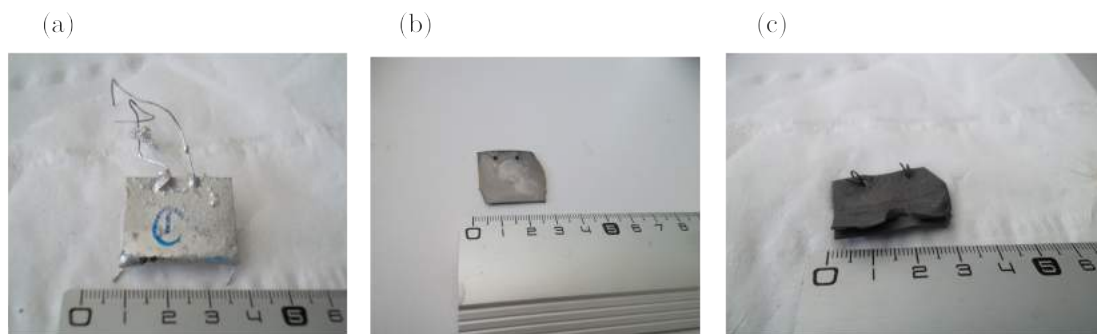


Figure 4.11: Dealloyed sample images (a) before chemical etching, (b) and (c) after chemical etching. Sample on (c) images presents some peeled sites.

In order to get a porous metal, the *Mg* based phase of the metal/metal composite was removed by selective etching using nitric acid aqueous solution (3 mol/L) during 2 h. Fig. 4.11 shows a sample after dealloying and before dissolution (a) and two samples after dissolution (b) and (c). The sample shown in Fig. 4.11 (b) seems to be unaffected by dissolution while sample on 4.11 (c) presents some peeled sites probably due to the cold-rolling step (Fig. 4.5 (b)).

4.4.2 Chemical etching effect on foam microstructure

Table 4.5 presents the *FeCr* volume ratio for *FeCrMg* composite and porous *FeCr*. Chemical etching had no effect on foam density. Because the same phases were present in all porous samples, XRD pattern is shown only for one composition in Fig. 4.12 but are similar for all the different precursors composition. The $Fe_{80}Cr_{20}$ phase is composed of a single BCC phase, in good agreement with the phase diagrams [MAR 39, MAS 90].

Dealloyed from	30FeCr-Ni	50FeCr-Ni	70FeCr-Ni
<i>FeCr</i> in <i>FeCrMg</i> (%vol \pm 3)	29	52	68
<i>FeCr</i> in porous <i>FeCr</i> (%vol \pm 3)	28	46	68

Table 4.5: *FeCr* volume ratio for *FeCrMg* composite and porous *FeCr* measured by “Fiji” software. *FeCr* volume ratio is not affected by chemical etching.

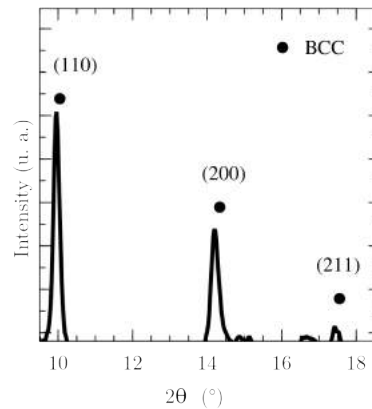


Figure 4.12: A typical XRD diffraction pattern of $(FeCr)_{30} Ni_{70}$ precursor dealloyed for 1 h at 820 °C and chemically etched.

Fig. 4.13 and Fig. 4.14 show a slice extracted from the 3D reconstruction of the same sample before and after dissolution and their respective phase thickness distributions. For both samples, ligaments thickness were not affected by dissolution, demonstrating the good impact of *Cr* to passivate. Fig. 4.13 presents some artefacts in the microstructure : some lines are present between ligaments which could correspond to precursor grain boundaries. After dissolution the size of these artefacts increases. A sample without defect is reported in Fig. 4.14 which has the same pores size as *Mg* phase (before etching). The influence of dissolution on foam microstructure is weak and can be neglected. More experiments and discussions on the effect of dissolution were detailed in Chapter 3.

After chemical etching, porous FeCr was obtained. The effect of chemical etching on foam morphology is negligible. The 3D morphology analysis of the different obtained foams is described in Chapter 5.

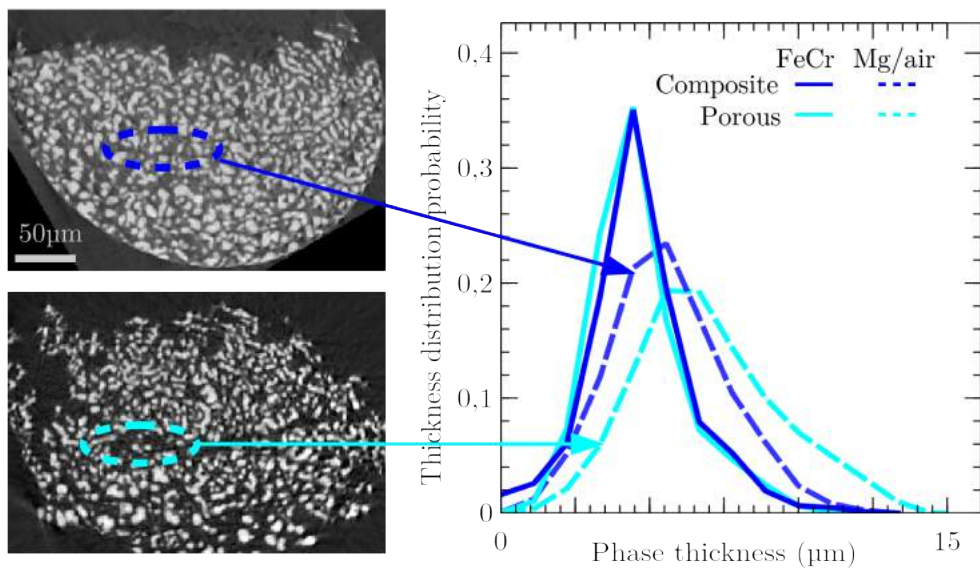


Figure 4.13: Slice extracted from 3D reconstruction of 30FeCr-Mg before (top) and after (bottom) chemical etching and respective phase thickness distribution.

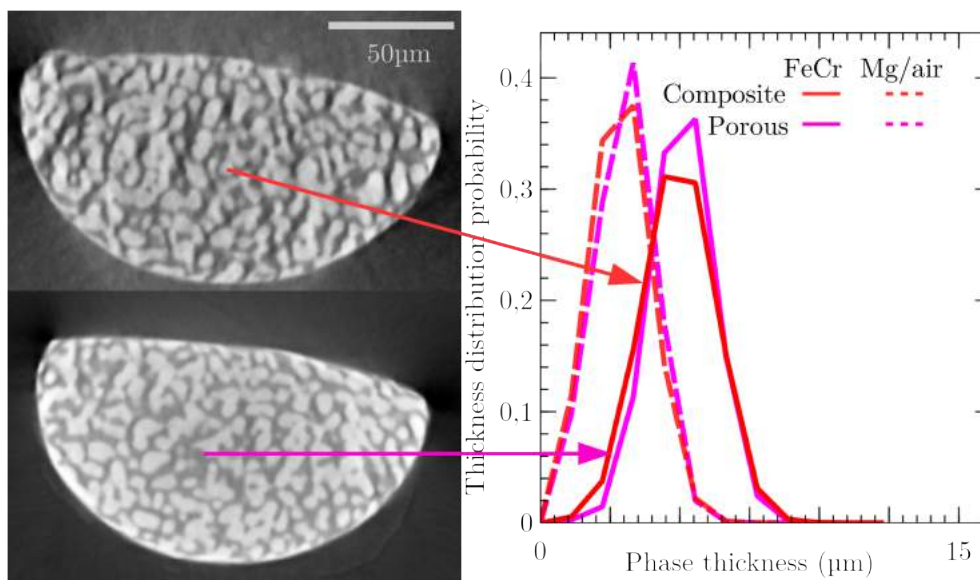


Figure 4.14: Slice extracted from 3D reconstruction of 50FeCr-Mg before (top) and after (bottom) chemical etching and respective phase thickness distribution.

4.5 Metal/polymer composites

4.5.1 Epoxy-amine networks

Epoxy networks are thermosetting polymers composed of an infusible and insoluble 3D network. Their good properties make them common polymers in various fields like painting, adhesive, electronic applications and also as polymer matrix for composite materials (for example structure lightening for aerospace applications) [REN 05]. They are synthesised from an epoxy pre-polymer (in this study : DiGlycidyl Ether of Bisphenol A (DGEBA)) and an hardener (in this study: amine) [PAS 02]. They are two main reactions and one side reaction implied in the formation of epoxy networks by a step-growth polymerisation. They are shown in Fig. 4.15. The first reaction corresponds to the hydrogen addition of primary amine on epoxy group to form secondary amine. This secondary amine can react with an other epoxy group to give tertiary amine shown on the second reaction. The side reaction is an esterification reaction between epoxy and hydroxyl groups and occurs at high temperature ($T > 120\text{ }^{\circ}\text{C}$) and for low amine concentration, therefore this reaction occurs usually at the polymerization end [RIC 86, PAS 10, DUŠ 77]. For the purpose of

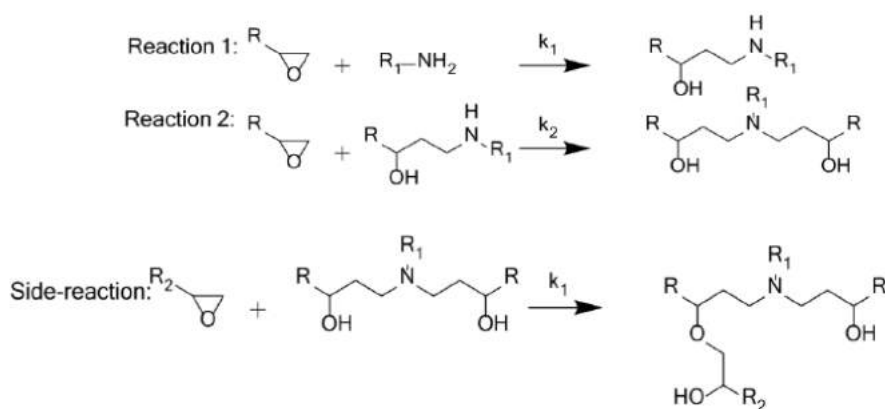


Figure 4.15: Polymerization reactions for epoxy-amine network processing [NGU 16].

this study, the involved epoxy pre-polymer will be Diglycidyl Ether of Bisphenol A (refer to as DGEBA). The chemical formula can be found in Fig. 4.16. Two different amines will be used as hardener IsoPhorone Diamine (refer to as IPD) with chemical Jeffamine D2000 (refer to as D2000). Their chemical formula are drawn in Fig. 4.16 (b) and (c) respectively. From porous xFeCr, after infiltration by D2000 or IPD the obtained composite will be respectively referred to as xFeCr-D2000 and xFeCr-IPD.

4.5.2 Methods

4.5.2.1 ThermoGravimetric Analysis (TGA)

The ThermoGravimetric Analysis (TGA) measures the variation of sample weight with temperature evolution under a controlled atmosphere [WIR 14]. Experiments are performed using a Q500 thermogravimeter analyzer (TA instruments) from $25\text{ }^{\circ}\text{C}$ to $700\text{ }^{\circ}\text{C}$

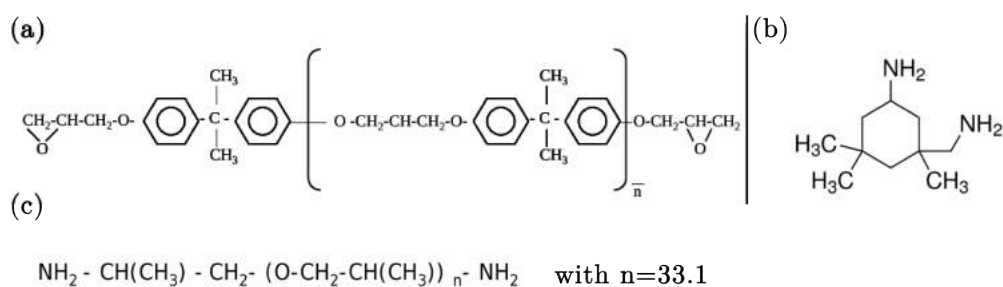


Figure 4.16: Chemical formula of (a) Diglycidyl Ether Bisphenol A (DGEBA), (b) IsoPhorone Diamine (IPD) and (c) Jeffamine D2000.

under a nitrogen atmosphere with a heating rate of $20\text{ }^\circ\text{C min}^{-1}$ on around 20 mg samples.

Fig. 4.17 presents one typical curve of TGA result analysed with TA software. The weight loss and the degradation temperature can be determined from these curves.

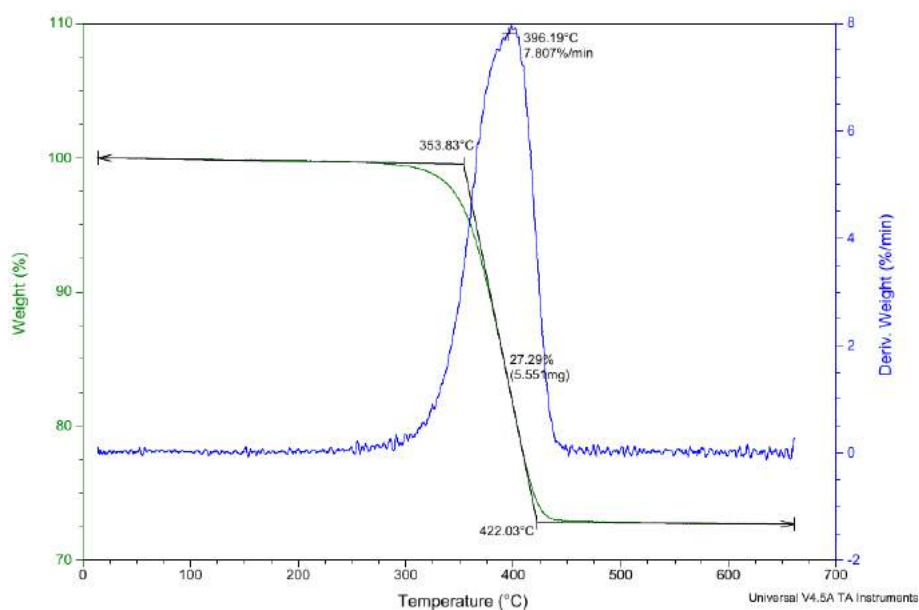


Figure 4.17: Snapshot of TGA analysis with TA software.

4.5.2.2 Differential Scanning Calorimetry (DSC)

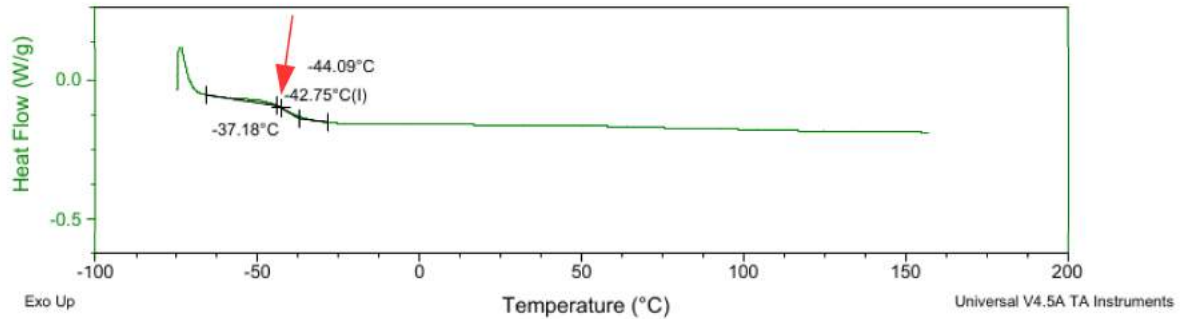


Figure 4.18: Snapshot of DSC analysis with TA software. The number followed by (I) corresponds to the glass transition temperature and the glass transition is highlighted by a red arrow.

The Differential Scanning Calorimetry (DSC) is based on the measurement of the difference of the necessary heat to warm up the sample and a reference. It is used into various applications like the measurement of allotropic transformation, crystallization temperature or even glass transition for polymers [GRE 10]. Measurements are operated on Q20 (TA instrument) under a nitrogen flow of 50 mL min^{-1} with 5 mg samples encapsulated in *Al* hermetic capsule and air as a reference sample. Each epoxy-amine network is heated from room temperature to 280 °C for DGEBA-IPD system or from -75 °C to 160 °C for DGEBA-D2000 system with a 10 K min^{-1} rate. The glass transition is determined on the second heating ramp to measure glass transition temperature after performing curing. Fig. 4.18 presents a typical curve of DSC result analysed with TA software. The glass transition temperature is measured automatically by tangent method.

4.5.3 Elaboration

After chemical etching, porous metals are obtained. Pores are infiltrated by polymer resin in order to get a metal/polymer composite. Porous samples were rinsed in ultra pure water, dried and heated at 120 °C during 10 min and then kept under vacuum before polymer infiltration. Fig. 4.19 shows the experimental procedure for polymer infiltrations. Porous samples were hung by a wire and immersed into a DGEBA-D2000 or DGEBA-IPD mixture with the reactive system introduced in stoichiometric proportions. The beaker were set in a vacuum bell during 20 min. Then the excess polymer mixture on the sample surface were removed and samples were set on a *Al* plate in a oven for curing. Curing cycles are detailed in Table 4.6.

	DGEBA/D2000	DGEBA/IPD
Weight ratio (g)	1:2.945	100:24.8
Curing cycle	4 h @ 80 °C and 3 h @ 125 °C	2 h @ 80 °C and 2 h @ 160 °C

Table 4.6: Stoichiometric ratio and polymerization cycle of DGEBA-D2000 and DGEBA-IPD [LEP 02, SBI 11].

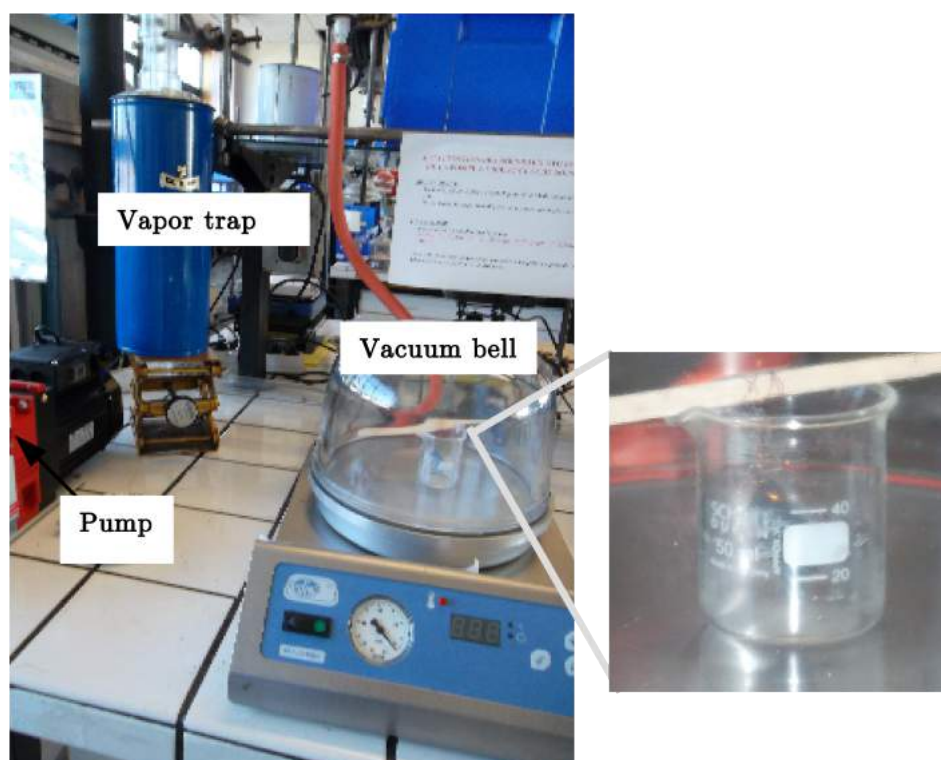


Figure 4.19: Picture of polymer infiltration experimental procedure.

4.5.4 Characterization

Fig. 4.20 shows at room temperature DGEBA-D2000 and DGEBA-IPD samples after polymerization. DGEBA-D2000 is rubbery while DGEBA-IPD looks glassy and brittle.

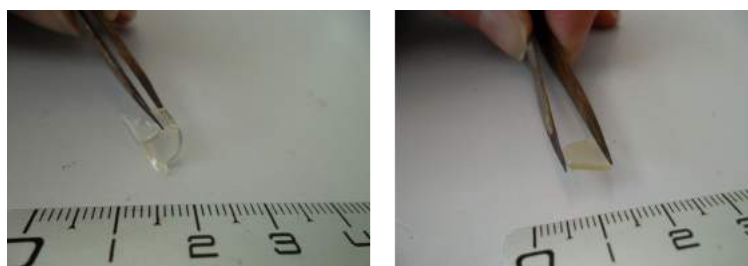


Figure 4.20: Picture of rubbery polymer DGEBA-D2000 (left) and glassy polymer DGEBA-IPD (right) after polymerization.

4.5.4.1 Polymer infiltration

TGA measurements were performed to measure the weight of the polymer inside the foam. TGA measurements were done for weight below 20 mg: it was not possible to perform measures on the whole sample. A tiny part of the sample was picked up for TGA. To check if infiltration was homogeneous, the reproducibility has been checked. From the materials density and materials weight, the volume of air can be calculated. Then the mass of polymer is calculated considering that whole air was replaced by polymer. This value is considered as the theoretical polymer mass. The filling ratio is the ratio of the calcined polymer mass divided by theoretical polymer mass. Measured filling ratio were $(98 \pm 5)\%$.

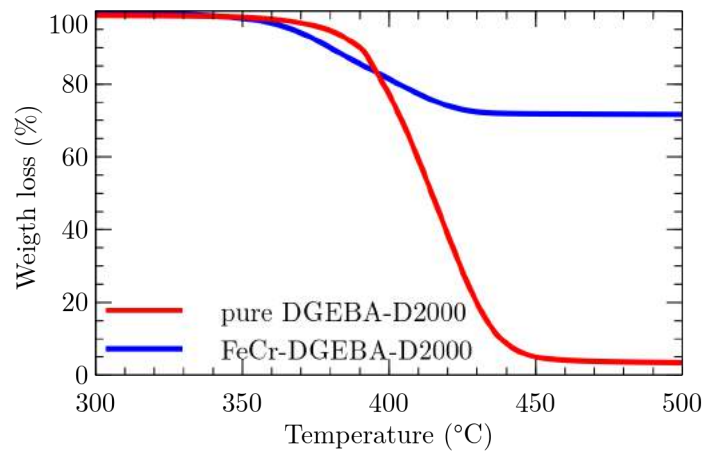


Figure 4.21: TGA curves of DGEBA-D2000 with (blue) and without (red) metallic foam.

The presence of the foam slightly modify the calcination behaviour of polymer resin. Fig. 4.21 shows TGA curves of DGEBA-D2000 with (blue) and without (red) metallic foam. With metallic foam the calcination started at lower temperature and ended at higher temperature. Table 4.7 gives the calcination temperatures measured as the top of the derivative weight curve as presented in Chapter 2. DGEBA-IPD system has a lower calcination temperature. Those temperatures are common for epoxy networks [PAS 10].

	with metallic foam	without metallic foam
DGEBA-D2000 ($^{\circ}\text{C} \pm 5$)	400	420
DGEBA-IPD ($^{\circ}\text{C} \pm 5$)	365	380

Table 4.7: Calcination temperature measured by TGA.

Fig. 4.22 presents one picture of two different samples after polymer infiltration. Left picture corresponds to 30FeCr infiltrated by DGEBA-D2000 with large pores (around 8 μm). Some pores are presents as shown in the red circle. The filling ratio is about 96% which is consistent with TGA measurement. Right image corresponds to 70FeCr infiltrated by DGEBA-IPD with small pores (around 670 nm). Infiltration is successful with two mechanically different epoxy networks for two different pore scales.

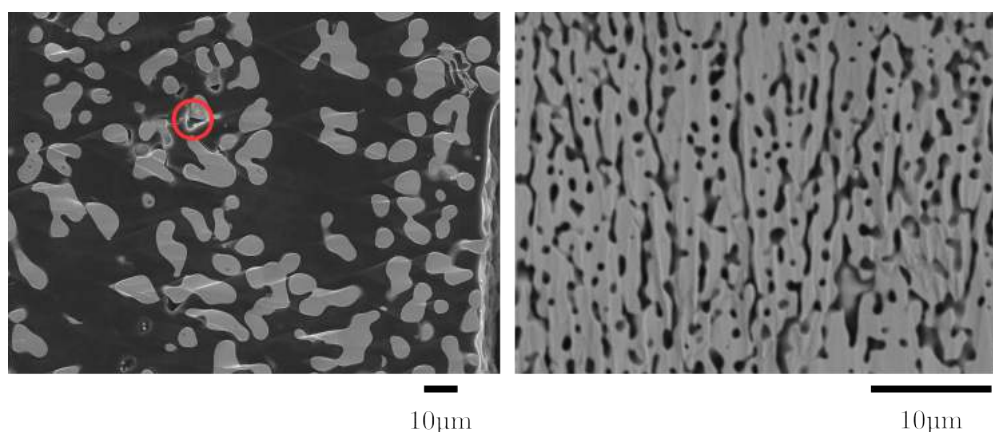


Figure 4.22: SEM picture of 30FeCr infiltrated by DGEBA-D2000 (left) and 70FeCr infiltrated by DGEBA-IPD (right). Some pores are present highlighted by a red circle.

4.5.4.2 Polymerization

Two methods were used to know if the polymer is well polymerized. A small piece of polymer with and without metallic foam was immersed in tetrahydrofuran during 10 min in an ultrasonic cleaning bath. Their weight were measured before and after immersion. DGEBA is soluble in tetrahydrofuran but DGEBA-IPD and DGEBA-D2000 are not. Therefore in case of pre-polymer DGEBA presence, a weight change is observed meaning that the polymerization was not completed. However in the case of both reactive systems no weight change was observed which suggests a full polymerization.

The glass transition temperatures (T_g) were measured from DSC curves to check the effect of metallic foam on polymerization (cf. Fig. 4.23). The results are presented in Table 4.8. DSC capsule allows only a 5 mg sample, therefore when the metallic foam was present the amount of polymer was low (around 1 mg). The glass transition was less visible on the DSC curve for metal/polymer composite also the errors on glass transition temperature is larger (cf. Fig. 4.23). Glass transition values were consistent with literature for these two systems [ERN 17, KNO 12]. Glass transition temperatures were not affected by the metallic foam presence which means that there is no interaction between foam ligaments and polymer network in contrary to some epoxy network reinforced with fibres or nanoparticules [SBI 10, PAS 10]. Polymerization inside metallic foam is successful and glass transition temperature is not affected by the metallic foam.

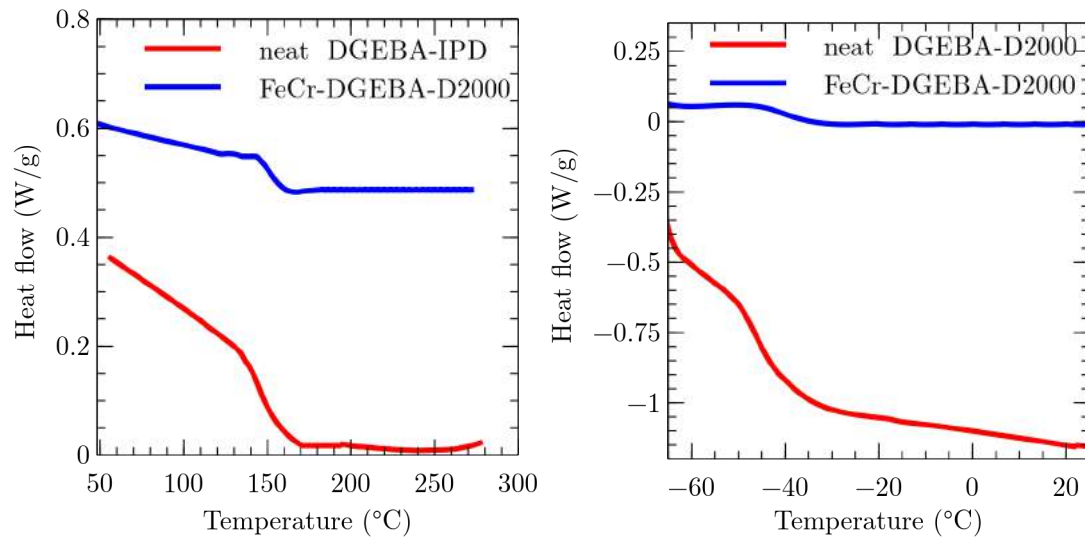


Figure 4.23: DSC thermogram of epoxy-amine network polymerized inside/outside metallic foam. T_g is not affected by the metallic foam.

	with metallic foam	without metallic foam
DGEBA-D2000 (°C)	-44 ± 3	-43 ± 1
DGEBA-IPD (°C)	141 ± 4	144 ± 2

Table 4.8: Glass transition temperature measured from DSC curves for neat polymers and metal/polymer composites.

4.5.4.3 Infiltration effect on foam microstructure

Fig. 4.24 presents one slice extracted from 3D reconstruction of 30FeCr before infiltration (top) and after infiltration by DGEBA-IPD system (bottom). The samples present some macroscopic layers which can produce some peeled sites as shown in Fig. 4.11. Between some layers, a large space is sometimes visible (as shown in the superimposed black ellipse). This space was previously a metal layer before the sample fractures prior to the tomography acquisition. After infiltration, the global size of sample presents no change and polymer brings some cohesion to the sample. Fig. 4.25 presents the phase thickness distribution for two different 30FeCr samples: one porous and the second one infiltrated by DGEBA-D2000. Ligaments thickness distribution is not affected by polymer infiltration but the large pores are retracted as a consequence of the polymer infiltration.

After polymer infiltration metal/polymer composites were obtained. Polymer infiltration had no impact on *FeCr* phase thickness but had a significant impact on foam microstructure by peeling prevention.

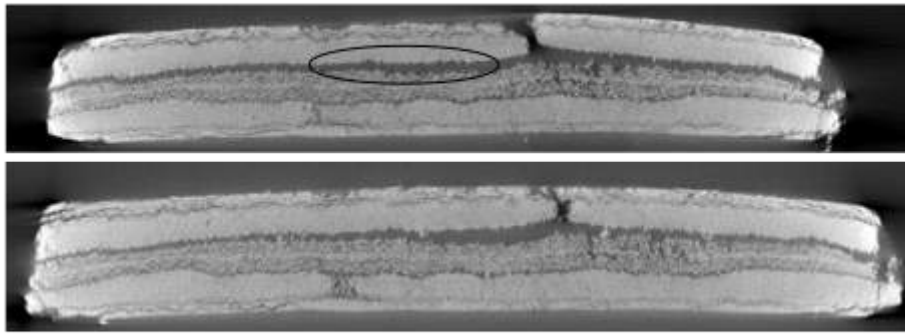


Figure 4.24: Slice extracted from 3D reconstruction of 30FeCr before infiltration (top) and after infiltration by DGEBA-IPD system (bottom).

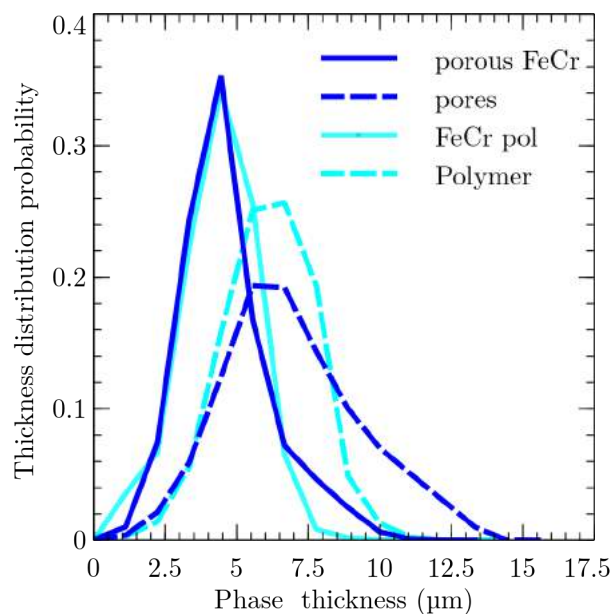


Figure 4.25: Phase thickness distribution before and after infiltration of porous 30FeCr by DGEBA-D2000. Large pores are retracted by the polymer infiltration.

4.6 Conclusion

This chapter describes the materials elaboration process: precursor elaboration, liquid metal dealloying, chemical etching and polymer infiltration. This has been done for three different precursor compositions: $(Fe_{80}Cr_{20})_{30}Ni_{70}$, $(Fe_{80}Cr_{20})_{50}Ni_{50}$, $(Fe_{80}Cr_{20})_{70}Ni_{30}$. The obtained ligaments are *Ni* free. The influence of etching step on foam morphology is very limited. The foam morphology is preserved during the process. The full polymer infiltration of pores from $0.8\ \mu\text{m}$ to $8\ \mu\text{m}$ was successful by two different epoxy-amine resins. Polymers properties was not affected by the metallic foam.

Chapter 5

Study of porous samples morphologies by X-ray tomography

After presenting the different steps required to obtain porous structure in Chapter 4, this chapter will be focused on the morphology of the porous structures. The long dealloying times of this study (1 h) enables to have a coarsened structure with no residual sacrificial element inside the ligaments. The influence of the parameters on these morphologies will be investigated by X-ray tomography. This chapter is divided into two parts : a qualitative and a quantitative analysis of the volumes.

Contents

5.1	Qualitative analysis	80
5.2	Quantitative analysis	80
5.2.1	Volume fraction	80
5.2.2	Phase thickness	81
5.2.3	Specific surface	83
5.2.4	Connectivity	85
5.2.5	Geometrical tortuosity	86
5.3	Conclusion	87

I would like to thank Jérôme Adrien (MATEIS) for his helped for performing X-ray tomography experiments.

One tip of 30FeCr, one of 50FeCr and one of 70FeCr were imaged. From these reconstructions, qualitative and quantitative analysis were done.

5.1 Qualitative analysis

Fig. 5.1 shows a reconstructed slice for each sample extracted from the X-ray tomography reconstruction of porous samples. Two phases are visible. The lighter phase corresponds to the *FeCr* phase and the darker phase to the air. The amount of white phase is qualitatively coherent with the samples expected composition.

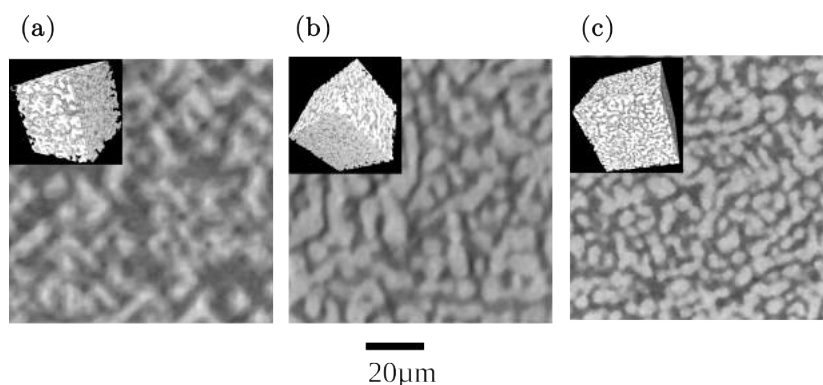


Figure 5.1: 2D images extracted from 3D volume of (a) 30FeCr (b) 50FeCr (c) 70FeCr. The inset corresponds to the 3D view of the porous structure.

5.2 Quantitative analysis

5.2.1 Volume fraction

The value of porous *FeCr* volume fraction presented in Table 5.1 is close to the one expected from the *FeCr/Ni* atomic fraction of the precursor. During the dealloying reaction, *Ni* atoms are removed from the *FeCr-Ni* lattice and the remaining *FeCr* atoms reconstruct a *FeCr* lattice. According to the reported lattice parameter of *FeCr-Ni* and *FeCr*, the volume of the unit cell, the number of atoms per cells, the theoretical *FeCr* volume fraction divided by precursor atomic fraction is 1.03. The experimental results are in good agreement with this predicted value [DYS 70, DOR 72, WAD 16a, MOH 17].

	30FeCr	50FeCr	70FeCr
Experimental relative density (%vol \pm 3)	28	46	68
Theoretical relative density	31	52	71

Table 5.1: Theoretical and experimental relative densities. Values are consistent with each others.

5.2.2 Phase thickness

Fig. 5.2 presents the phase thickness distribution of *FeCr* and *Air* phases for all samples. As already mentioned in literature for a similar process, phases display an unimodal and somewhat scattered thickness distribution [LIU 12, CHE 13b]. In Table 5.2, the average phase thickness of both phases is reported. Remarkably, *FeCr* phase thickness distributions are similar for all samples. This clearly shows that in this case, ligaments size are independent from precursor composition. Because *FeCr* phase thickness distributions are similar and materials densities are different, pore distributions must on the contrary be dependent on the composition of the precursor. This is clearly shown in Fig. 5.2(right). To calculate the theoretical pore size, it was considered that pore volume fraction is equal to pores size divided by characteristic length (pore + ligament size) and that structures are composed of a perfect succession of ligaments and pores. Theoretical formula is found in equation 5.1 with p , d and ρ_r respectively the pores size, the ligaments size and the foam density. Theoretical and experimental values are similar.

	30FeCr	50FeCr	70FeCr
Average Ligaments size (μm)	4.5 ± 1.3	5.0 ± 1.2	4.8 ± 1.6
Average Pores size (μm)	6.5 ± 2.2	4.1 ± 1.2	3.0 ± 0.6

Table 5.2: Average phase thickness of samples with different densities.

$$\frac{p}{d} = \frac{\rho_r}{1 - \rho_r} \quad (5.1)$$

From Fig. 5.2, the average ligament size was $4.8 \pm 0.3 \mu\text{m}$ for 1 h dealloying at 820°C . In [WAD 13], $Fe_{30}Ni_{70}$ precursors were dealloyed with similar conditions, therefore some of their results can be extrapolated. Fig. 3b in their paper shows the evolution of the ligament size (measured by SEM), for different dealloying times. By using the equation (3) of this paper with the time and temperature used in this study, the expected ligament size should be $5.08 \mu\text{m}$. This is very close to what have been measured in Table 5.2. Similar ligament sizes for different precursors compositions suggests similar activation energy. This bunch of results shows that the addition of *Cr* has a limited influence on the coarsening behaviour.

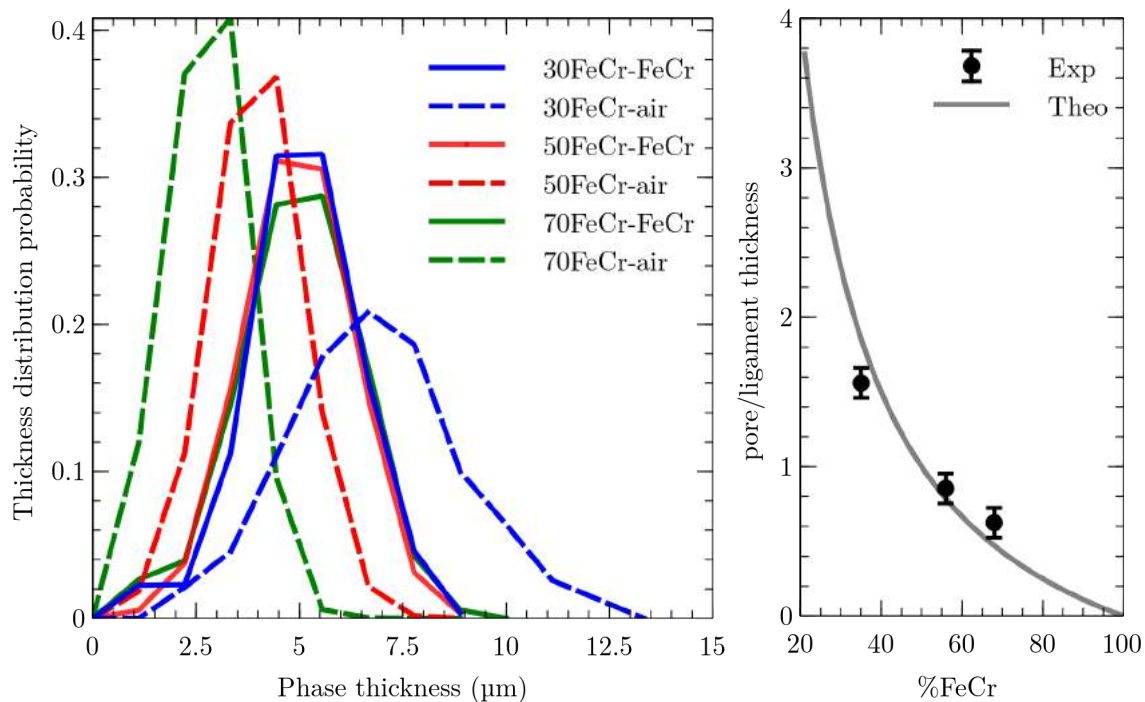


Figure 5.2: Evolution of ligaments and pores thickness of foam with different densities (left) Evolution of pore/ligament size with volume fraction (right).

Fig. 5.3 presents the cumulative intercept distribution for 30FeCr, 50FeCr and 70FeCr samples, and a comparison of cumulative intercept and “local thickness” function for phase thickness measurement. For the 3 samples and in both phases, the cumulative intercept distributions in every direction are very close to each other. Anisotropy is not measured even if samples were cold-rolled before dealloying, while in case of nanoporous gold the anisotropy increased with coarsening time [CHE 12a, MAN 16]. The last graph of this figure compares phase thickness measured with intercept and with “local thickness” function. The average ligament size is consistent with both methods. Both methods also show that pores are larger than ligaments. However the pore thickness is less homogeneous than ligament thickness, which is shown by a larger peak with “local thickness” function and by the presence of large intercept due to the low pores sphericity.

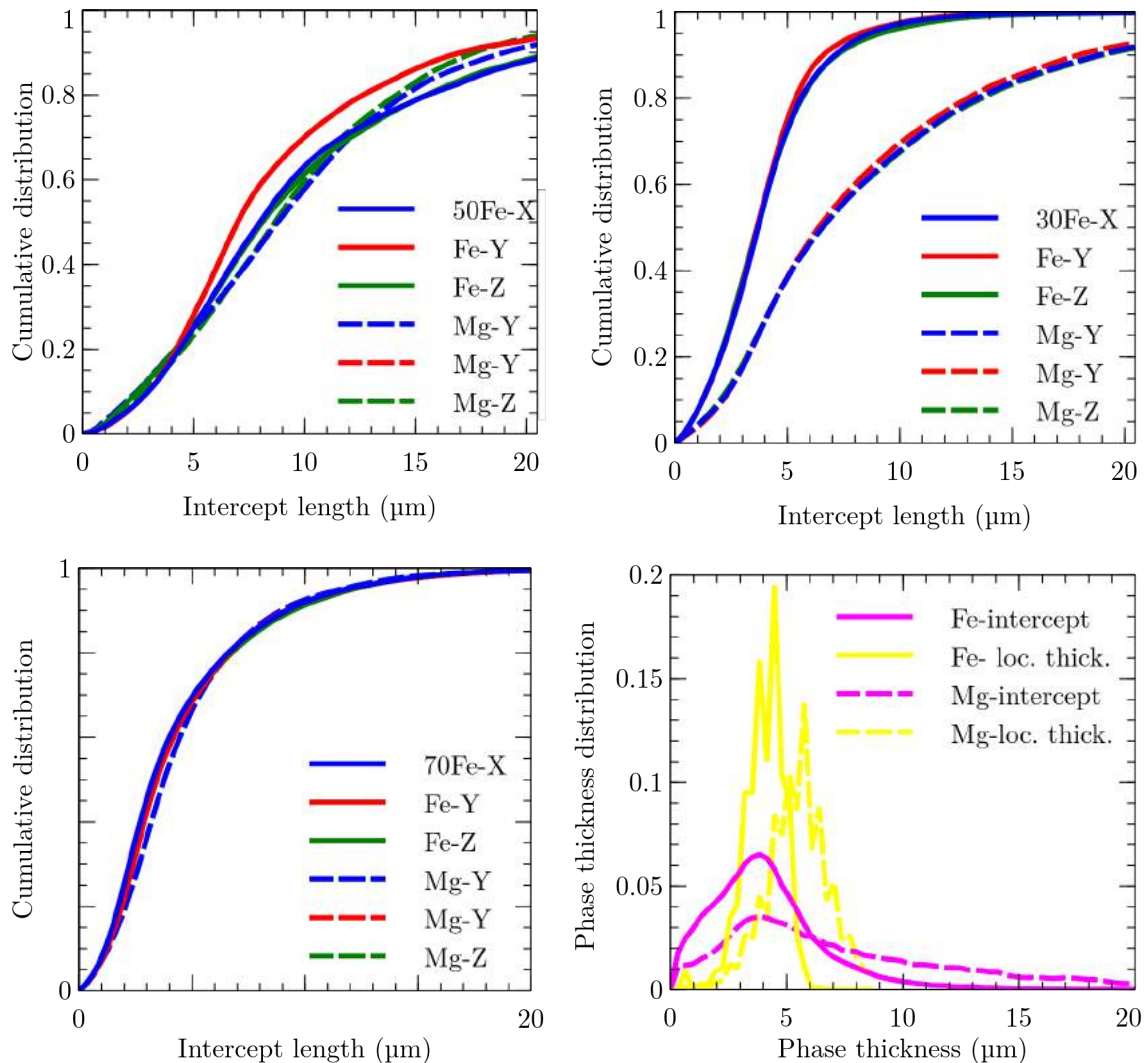


Figure 5.3: Cumulative intercept distribution for 30FeCr, 50FeCr and 70FeCr samples and comparison of intercept and “local thickness” for phase thickness measurement.

5.2.3 Specific surface

One of the main interests of porous materials is their large specific surface area. Specific surface area in (m^2/kg) and (m^2/m^3) are displayed in Table 5.3. For different compositions, specific surface is different while ligaments size is constant. This means that the specific surface area depends on sample density. These values of specific surface area are comparable to porous *NiCr* obtained by liquid metal dealloying with a long coarsening time, that is to say very low (at least 30 times lower) compared to nanoporous gold obtained by dealloying in aqueous solution [LAK 15]. In the present study, the samples were not specifically designed to obtain very small ligaments. However, if necessary, ligament size can be easily decreased for example by using solid metal dealloying reaction (reported

ligament size down to 200 nm in [WAD 16b]) or even liquid metal dealloying at lower temperature and shorter dealloying time (reported ligament size down to 650 nm in [WAD 13]) which can increase at least by 10 the specific surface.

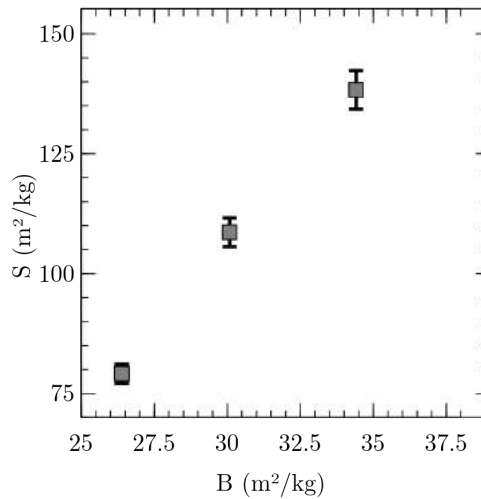
	30FeCr	50FeCr	70FeCr
Specific surface area (m^2/kg)	138 ± 4	109 ± 3	79 ± 2
Specific surface area (m^2/m^3)	$(3.0 \pm 0.2) * 10^5$	$(3.8 \pm 0.2) * 10^5$	$(4.1 \pm 0.2) * 10^5$

Table 5.3: Samples specific surface.

Detsi and al. linked the specific surface area (S) with the foam's characteristics: ligament size (d), bulk density (ρ) and a dimensionless constant C in equation 5.2 [DET 11].

$$S = \frac{C}{d * \rho} = C * B \quad (5.2)$$

Specific surface *vs* B is plotted in Fig. 5.4.

Figure 5.4: Specific surface area as a function of B . By linear fit $C = 3.7 \pm 0.4$ is measured.

The value of the C constant can be extracted graphically. $C = 3.7 \pm 0.4$ was measured. Values reported in the literature for nanoporous gold is $C = 3.7$, and $C = 3.4$ for the simulation of single gyroid nanostructure [DET 11, LAK 15]. This clearly shows that the structure of the materials can be treated as a single gyroid structure. Finding a similar C for nanoporous gold and the material exhibits another similarity with the structure of materials elaborated by different dealloying processes. Equation 5.2 is therefore validated for these materials and can thus be used to calculate the suitable ligament size for a given specific surface area and or to predict specific surface from ligaments size (therefore from dealloying parameters).

5.2.4 Connectivity

For various applications where the transport of electrical charges is a key property (such as capacitors), it is important to have a perfectly connected structure and a high specific surface area [ERL 09, SNY 10, LAN 11, CHE 09]. Measured connectivity of both phases for all samples is equal to 1 (Table 5.4). This value validates the fact that the materials exhibit a perfect bi-continuous structure.

	30FeCr	50FeCr	70FeCr
<i>FeCr</i> phase	1	1	1
Air phase	1	1	1

Table 5.4: Samples phase connectivity.

The connectivity value is a good way to measure if the structure is perfectly connected or not. To know the number of connection into the structure, it is necessary to measure Euler number or genus [MIC 03, MAN 16, CHE 10, LIL 18]. Genus and scaled genus values for these samples are displayed in Table 5.5. It was measured respectively around 500, 1300 and 3000 connections for 30FeCr, 50FeCr and 70FeCr. As expected, the number of connections increases with the amount of solid phase in the sample. However the genus of 70FeCr is 6 times higher than the one of 30FeCr whereas the ratio of the amount of solid phase is only 2.3. This means that 70FeCr is better connected than 30FeCr. Dividing the genus per unit volume with the cube of the specific area provides a dimensionless genus called scaled genus. The scaled genus of these materials are comparable with the one's found for nanoporous gold (from 0.0015 to 0.147) [MAN 16, CHE 10, LIL 18].

	30FeCr	50FeCr	70FeCr
Genus of FeCr phase (± 100)	$5 * 10^2$	$13 * 10^2$	$32 * 10^2$
Scaled Genus of FeCr phase (± 0.02)	0.02	0.03	0.06

Table 5.5: Samples genus and scaled genus measured on the FeCr phase.

5.2.5 Geometrical tortuosity

Transport properties, diffusivity and conductivity properties depend on the tortuosity. The geometrical tortuosity (τ) is a factor which only depends on the foam's geometry. Geometrical tortuosity of both phases can be found in Table 5.6. Geometrical tortuosity is defined by the ratio of the length of the curve to the euclidean distance between the ends of the curve. A geometrical tortuosity equal to one corresponds to pores parallel to the transport direction (like honey comb cells for example). A geometrical tortuosity included between 1 and 3 means that the transport properties are lower than the intrinsic transport properties of the conductive phase. It also means relatively good connectivity and low meandering of the pores [XUE 14]. A geometrical tortuosity equal to 3 corresponds to an isotropic spatial distribution of the pores [BEA 72]. In this case, bicontinuous structure does not enable to have isotropic pores/matters so this is consistent with a tortuosity below 3. All values are rather small, between 1 and 1.4. The low geometrical tortuosity of these materials suggests that the materials should exhibit good diffusion and transport properties. This geometrical tortuosity is comparable with microporous *TiCrZr* obtained by liquid metal dealloying [CHE 13b].

	30FeCr	50FeCr	70FeCr
<i>FeCr</i> phase (± 0.2)	1.2	1.1	1.2
Air phase (± 0.2)	1.3	1.4	1.2

Table 5.6: Samples phase tortuosity.

In 1935, the volume fraction of the studied phase (ρ) and the tortuosity were linked by Bruggeman [BRU 35] by the equation 5.3 where γ and a are constants depending on the morphology, porosity, material, and particle-size distribution in the material. Usually people take $\gamma = 1$ and adjust a , or take $a = 1.5$ and adjust γ [THO 09]. The simplest case corresponds to $\gamma = 1$ and $a = 1.5$ [THO 09, CHE 13b].

$$\tau = \gamma \cdot \rho^{1-a} \quad (5.3)$$

Fig. 5.5 corresponds to the plot of equation 5.3.

The values from the present study show a good agreement with Bruggeman law for foam with low density thus for high amount of air. However in case of 70FeCr, geometrical tortuosity differs from Bruggeman law: geometrical tortuosity of air phase should increase when air phase fraction decreases also 70FeCr should present the highest geometrical tortuosity. It could be explained by different grains formation mechanisms observed and discussed in Chapter 6.

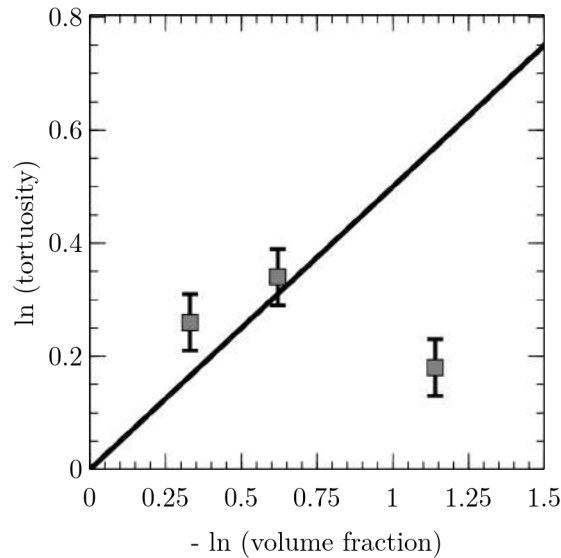


Figure 5.5: Evolution of geometrical tortuosity factor of air phase with volume fraction. The line corresponds to Bruggeman relation with $\gamma = 1$ and $a = 1.5$.

5.3 Conclusion

In this chapter, the morphology of the porous structures was investigated by X-ray tomography. It has been shown that foam morphological parameters can be precisely chosen:

- Porosity (air fraction) is directly linked to precursor composition.
- Ligaments size can be increased by increasing dealloying time and/or dealloying temperature.
- Pores size is controlled by precursor composition and have the same magnitude as ligaments size.
- Specific surface can be calculated knowing the ligaments size by equation 5.2.
- The tortuosity and connectivity are close to 1 and independent of the volume fraction.

This connectivity proves the presence of bicontinuous structures. The low tortuosity values lead to good transport properties.

In conclusion, it is quite easy to tailor the foam morphology.

Chapter 6

Grain microstructure evolution during dealloying

In this chapter, the grain microstructure will be investigated.

On the first part it was decided to work on $Fe_{30}Ni_{70}$ precursor to limit the parameters. The effect of the elaboration process on precursor grain microstructure will be studied then the effect of dealloying time and temperature on dealloyed grain microstructure will be investigated.

In the second part the investigation will be enlarged on the main materials of this study ($(FeCr)_xNi_{1-x}$ with $x = 30, 50$ and 70 precursors). The microstructure before and after dealloying will be investigated. To complete this study the microstructure and the composition of partial dealloyed samples will be analysed.

Contents

6.1 Dealloying from $Fe_{30}Ni_{70}$ precursor	90
6.1.1 Effect of precursor preparation on precursor grain microstructure	90
6.1.2 Effect of dealloying parameters on grain microstructure	92
6.2 Dealloying from $(FeCr)_xNi_{1-x}$ with $x = 30, 50$ and 70 precursors	94
6.2.1 From cold-rolled precursor samples	94
6.2.2 From recrystallized precursor samples	96
6.2.3 Partial dealloying	97
6.2.4 Phase transformation during dealloying : model	100
6.3 Effect of Cr addition on grain microstructure	101
6.4 Conclusion	102

I would like to thank Sophie Cazottes (MATEIS) and Pierre-Antoine Geslin (MATEIS/Tohoku University) for the useful discussion about SEM-EBSD results.

Fig. 6.2 shows an example of inverse pole figure extracted from an SEM-EBSD map of $Fe_{30}Ni_{70}$ precursor sample. This figure allows us to give some general definitions useful for this chapter.

In this chapter, all Inverse Pole Figure (IPF) will be drawn compared to the normal direction (ND) and will have the same color keys as presented in Fig. 6.1. SEM-EBSD confirms XRD analysis: all precursor samples present FCC phase and all FeCr phase of dealloyed samples present BCC phase.

Even if on some figures, the microstructure is shown before and after dealloying samples are never the same for SEM-EBSD maps before and after.

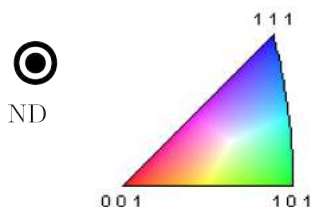


Figure 6.1: Inverse Pole Figure (IPF) color keys used for all maps in this chapter.

In this chapter, the RD array will always correspond to the cold-rolling direction and DD array to the dealloying reaction direction.

6.1 Dealloying from $Fe_{30}Ni_{70}$ precursor

In this section, to understand the effect of dealloying time and temperature on dealloyed grain microstructure, a precursor with large and homogenized grain is necessary. To get the suitable precursor several steps have been necessary.

6.1.1 Effect of precursor preparation on precursor grain microstructure

6.1.1.1 Cast alloy

The grain microstructure was firstly analysed just after arc-melting (cf. Fig. 4.5). A typical casting microstructure is observed with a skin grain area (some hundred micrometers thickness), a columnar grain area and then equiaxed grain area as shown in Fig. 6.2 [BEE 01, OHN 76].

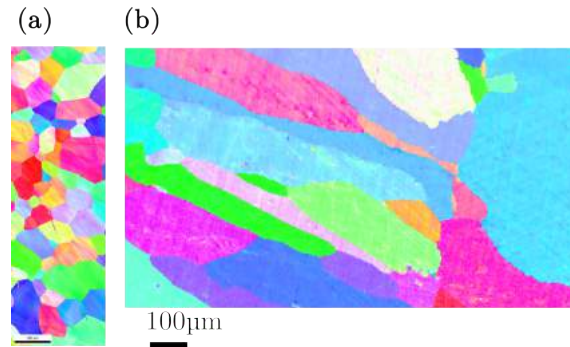


Figure 6.2: IPF map of a $Fe_{30}Ni_{70}$ precursor as cast alloy (a) skin area (b) columnar and equiaxed areas.

6.1.1.2 Unidirectional melting and annealing

A post-treatment was investigated from resulting cast alloy after arc-melting. A cast alloy ingot (cf. Fig. 6.3 (a)) was cut into slices and the slices were aligned in a mold (cf. Fig. 6.3 (b)). The mold was inserted in arc-melting furnace and samples were directionally melt then reversed and remelt until getting an ingot. This resulting ingot was cut into 2 pieces (cf. 6.3 (c) dashed line). The left part was annealed 72 h at 1000 °C. The red and blue lines correspond to the positions where the cross-section were analysed by SEM-EBSD (cf. 6.4).

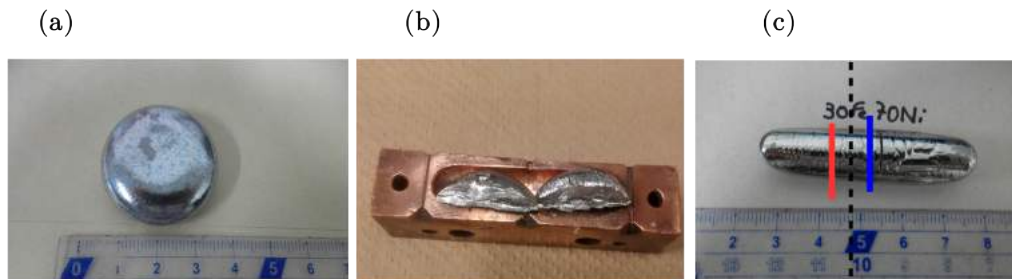


Figure 6.3: Precursor samples images (a) after arc-melting (b) prepared for unidirectional melting (c) after unidirectional melting left part was annealed. Red and blue lines correspond to the positions where the cross-section were analysed by SEM-EBSD.

Fig. 6.4 presents the grain microstructure after unidirectional melting and after annealing. MD corresponds to the unidirectional melting direction. After unidirectional melting, grains are large (1 mm) and presents a texture due to the temperature gradient. After annealing, a slight grain growth is observed (grain diameter around 1.2 mm) and texture is preserved.

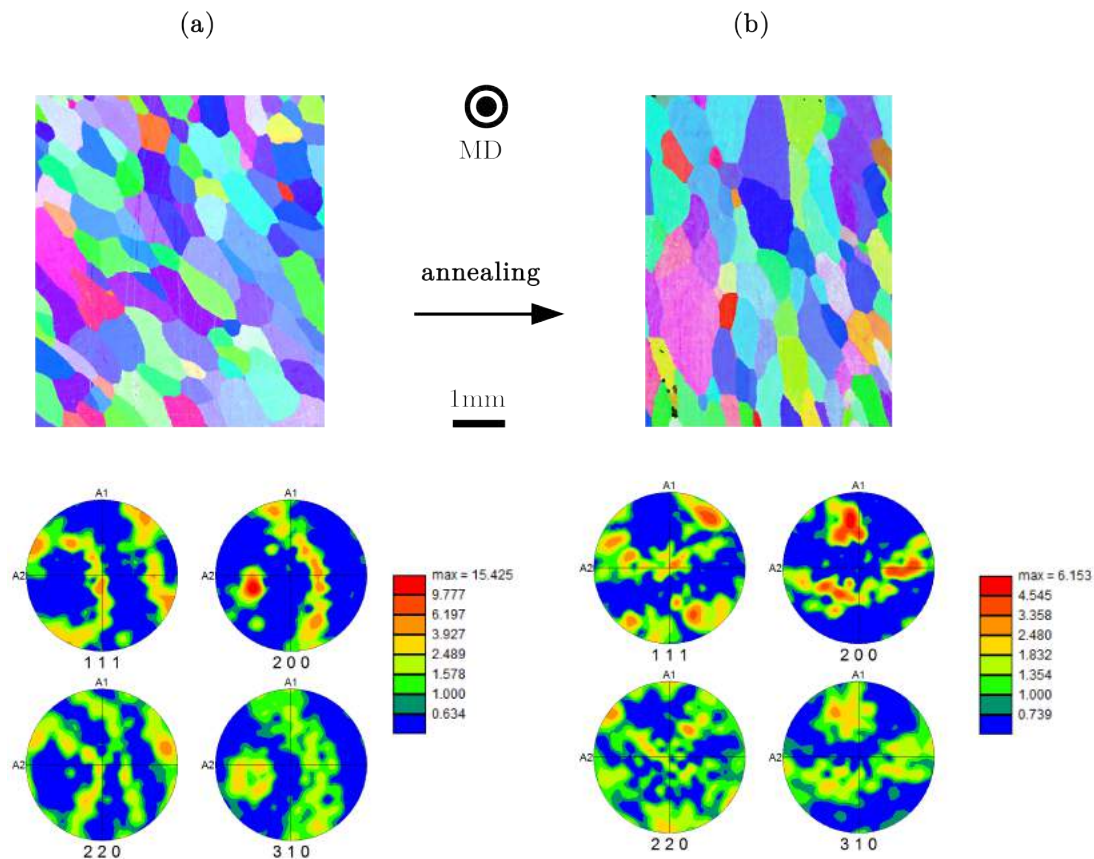


Figure 6.4: IPF and PF maps of precursor sample after unidirectional melting treatment (a) and after annealing (b). MD correspond to the unidirectional melting direction.

- The cast alloy presents standard casting ingot microstructure.
- After unidirectional melting and annealing treatment very large grains are obtained. It is a suitable microstructure to study the effect of dealloying parameters on the final microstructure.

6.1.2 Effect of dealloying parameters on grain microstructure

After dealloying, the black area in SEM-EBSD maps corresponds to Mg phase and coloured areas to $FeCr$ ligaments. Dealloyed grains are smaller than precursors grains. This result is different compared to previous studies where no microstructure changes were observed between precursor and dealloyed samples [MCC 16c, PET 09, GWA 16]. In these cases however, dealloying occurs at high temperature and phase transformation occurs between precursor and dealloyed samples.

Fig. 6.5 presents the grain microstructure after 3 different dealloying conditions: 1 h at 750 °C gives grain diameter about 50 μm , 1 h at 820 °C gives grain diameter about 100 μm and 10 min at 820 °C gives grain diameter about 70 μm . After dealloying each ligament is a single crystal as expected [PET 09], however resulting grains are much smaller than precursor grains and their size depends on dealloying time and temperature.

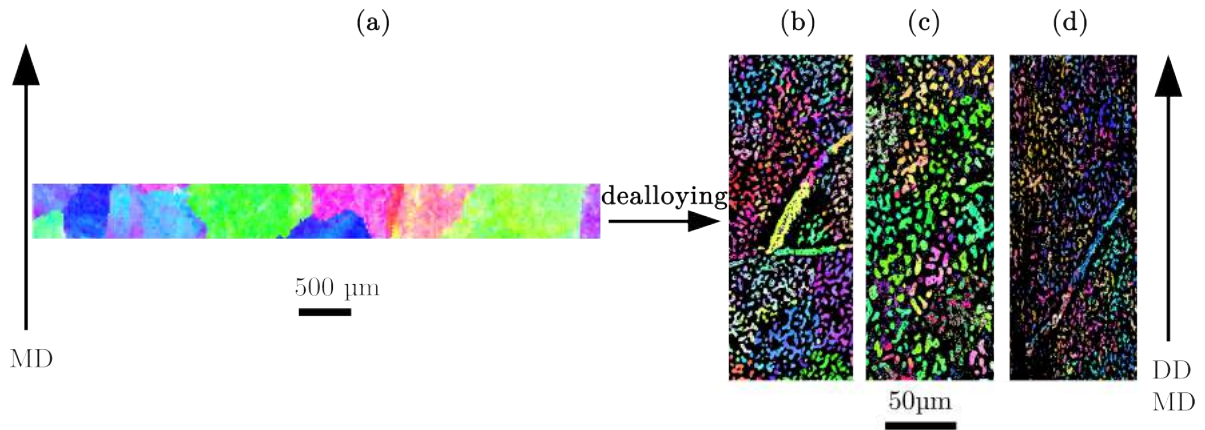


Figure 6.5: IPF maps of precursor sample (a), after 1 h at 750 °C dealloying (b), after 1 h at 820 °C dealloying (c), after 10 min at 820 °C dealloying (d). MD corresponds to the unidirectional melting direction.

The change in the microstructure between precursor and dealloyed sample is due to the phase transformation from FCC to BCC. When a phase transformation from austenite to ferrite occurs, resulting grains are smaller than austenite's ones due to a nucleation/growth mechanism [LIU 06, MUR 98]. The effect of time and temperature on grain size is consistent with grain growth theories from [ROL 04].

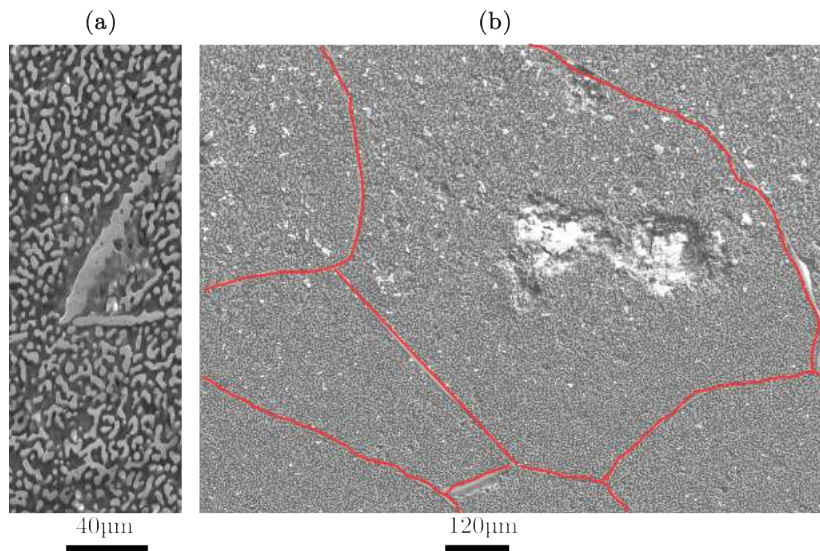


Figure 6.6: (a) SEM micrograph of Fig. 6.5 (b) lower magnification of (a, red lines corresponding to large ligaments).

In Fig. 6.5(b), some large ligaments are observed and can also be shown in Fig. 6.6(a). These large ligaments should be precursor grain boundaries [MCC 16c, MCC 16d]. While observing this samples with lower magnification (cf. 6.6(b)), the large ligaments drawn in red presents similar shapes and sizes compared to precursor grains (cf. 6.5(a)). In Fig. 6.7, a micrograph of a partially dealloyed sample is presented. The dealloying front is irregular. While observing at higher magnification (right), it appears that the irregularities come from precursor grain boundaries because grain boundaries and grains are dealloyed with different kinetics [MCC 16c].

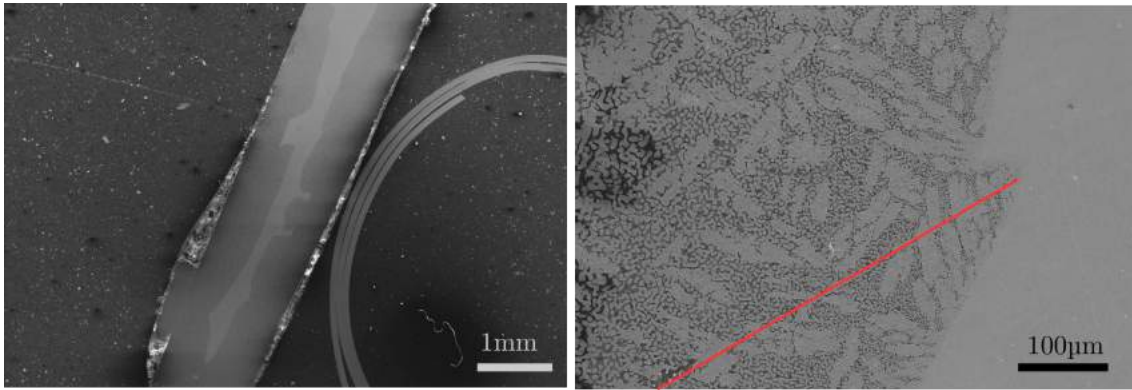


Figure 6.7: SEM micrograph of a partially dealloyed sample at 2 different magnifications. The red line corresponds to a large ligament corresponding to precursor grain boundaries.

When precursor sample presents large grains, the precursor grain boundaries are preserved as large ligaments. Each precursor grain is transformed into smaller grains during dealloying. Grain size increases with dealloying time and temperature.

6.2 Dealloying from $(FeCr)_xNi_{1-x}$ with $x = 30, 50$ and 70 precursors

6.2.1 From cold-rolled precursor samples

$(FeCr)_x - Ni_{(1-x)}$ precursors were prepared as described in Chapter 4. In this part the SEM-EBSD maps on precursor samples were acquired directly after cold-rolling without recrystallization. Fig. 6.8 presents the grain microstructure before and after dealloying with Index Quality (IQ) + Inverse Pole Figure (IPF) maps. Before dealloying the microstructure is highly affected by cold-rolling: grains are elongated along the cold-rolling direction and the degree of indexation is low: most of the maps are black i.e. non-indexed. The influence of the composition of precursor samples on SEM-EBSD map is not evident. After dealloying 30FeCr and 50FeCr present small randomly oriented grains composed of a small number of ligaments while 70FeCr presents large grains, each grain including many ligaments of similar orientation.

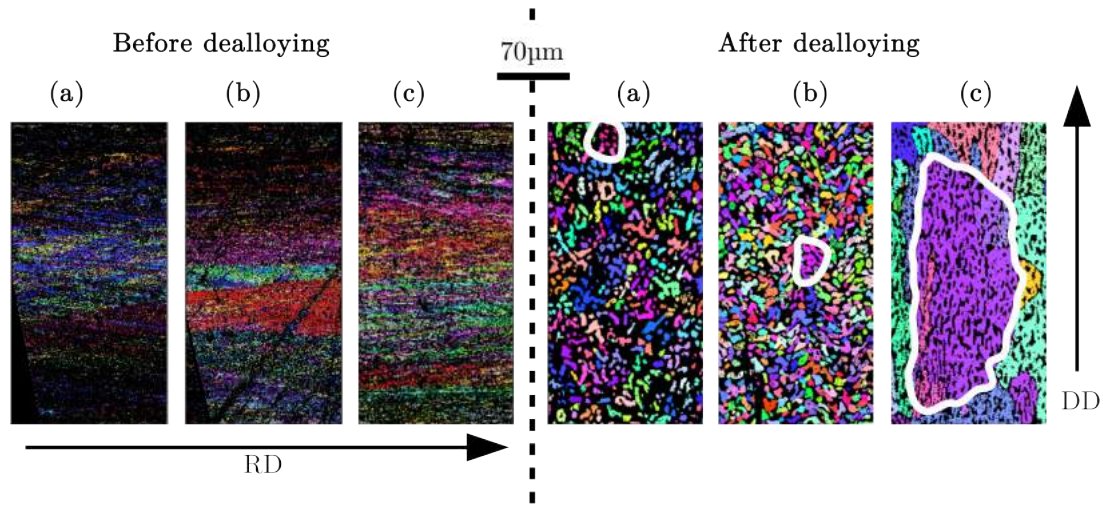


Figure 6.8: IQ+IPF EBSD map before and after dealloying from precursor after cold-rolling without recrystallization from (a) 30FeCr-Ni (b) 50FeCr-Ni (c) 70FeCr-Ni samples. Arrows correspond to cold-rolling direction (RD) and dealloying reaction direction (DD). White circle corresponds to one grain.

Table 6.1 presents the average grain size measured by two methods (i) given by OIM analysis software (ii) calculated from the average value of six manual measurements on the SEM-EBSD map. After dealloying one grain for each map is circled in white in Fig. 6.8 to highlight what is considered as a grain in this manual measurement. When the amount of solid increases in the foam, the difference between the two methods decreases. In fact, for 30FeCr, the measurement given by the software corresponds to ligaments size and not grain size because of the 2D analysis and the not obvious connection between ligaments, while for 70FeCr even in 2D the connection between ligaments is present: OIM analysis software could capture the full porous grain.

Grain size μm	software	manual
30FeCr	6.4 ± 0.6	37 ± 17
50FeCr	8.0 ± 3.0	28 ± 5
70FeCr	105 ± 5	125 ± 8

Table 6.1: Comparison between grain size given by the software and manual measurement on the map. For 30 and 50FeCr samples, the software actually measures the ligament size.

Before dealloying, grains are highly affected by cold-rolling. Because dealloying is performed at high temperature, recrystallization of the precursor sample prior or during dealloying can be expected [CHB 14, BAR 15].

The difference between 30/50FeCr-Ni and 70FeCr-Ni could be explained by different recrystallization rates or/and dealloying rates and/or FCC-BCC transformation type. The first hypothesis checked in this study is: 70FeCr-Ni have enough time to fully recrystallize

before dealloying to perform the dealloying on large grain while for the two other ones (30/50FeCr-Ni), recrystallisation is slower and dealloying is performed on small grains. To check this hypothesis a recrystallization step after cold-rolling step and before dealloying step is performed.

6.2.2 From recrystallized precursor samples

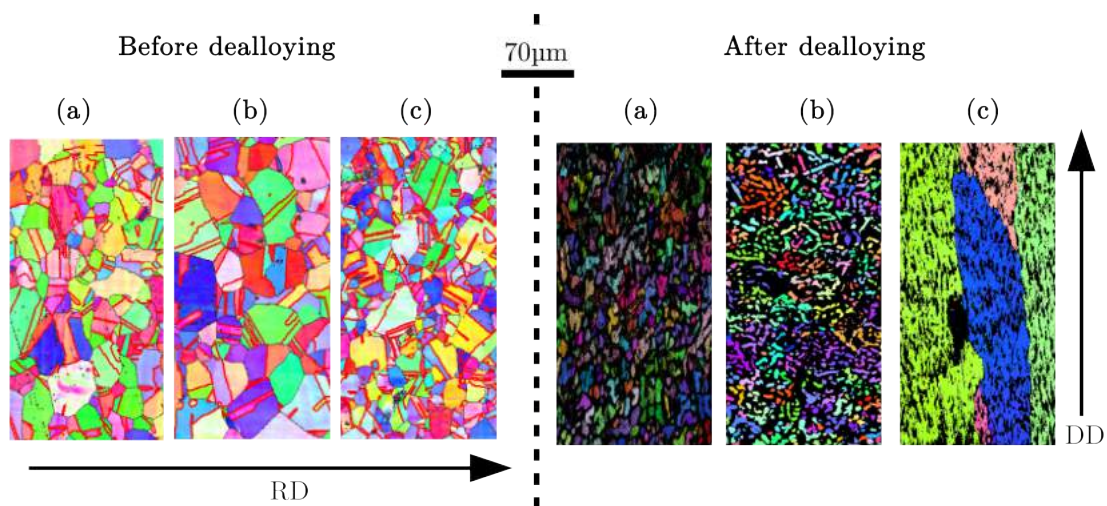


Figure 6.9: IQ+IPF EBSD map before and after dealloying from precursor after cold-rolling with recrystallization from (a) 30FeCr-Ni (b) 50FeCr-Ni (c) 70FeCr-Ni samples. Arrows correspond to cold-rolling direction (RD) and dealloying reaction direction (DD). Red lines on precursors maps correspond to Σ 3 twin boundaries.

In this part, cold-rolled precursor samples were subsequently recrystallized for 5 h at 820 °C under highly vacuumed atmosphere, then air quenched. Fig. 6.9 presents the grain microstructure before and after dealloying with Index Quality (IQ) + Inverse Pole Figure (IPF) maps. After recrystallization, grains exhibit a rather polygonal shape with an average diameter of about 25 μm and a lot of Σ 3 twin boundaries are present. It is the typical microstructure of austenetic steel/nickel alloy [SHI 15, QIN 16, ABE 17].

Before dealloying the effect of the composition on the microstructure is weak. 30FeCr and 50FeCr presents small grains composed of a couple of ligaments which look randomly oriented while 70FeCr presents large grains including many ligaments.

The precursor microstructure presented by large ligaments after dealloying is not noticed either on Fig. 6.9 nor on larger observed area on SEM (not shown here).

While comparing Fig. 6.8 and Fig. 6.9 after dealloying, no significant difference is observed. This means that the different behaviour between 30/50FeCr and 70FeCr could not be explained by the absence of recrystallization treatment after cold-rolling step.

6.2.3 Partial dealloying

To have a better understanding of the process precursor samples were dealloyed for 3 min at 820°C or 665°C to observe dealloying front reaction.

6.2.3.1 Different diffusion process

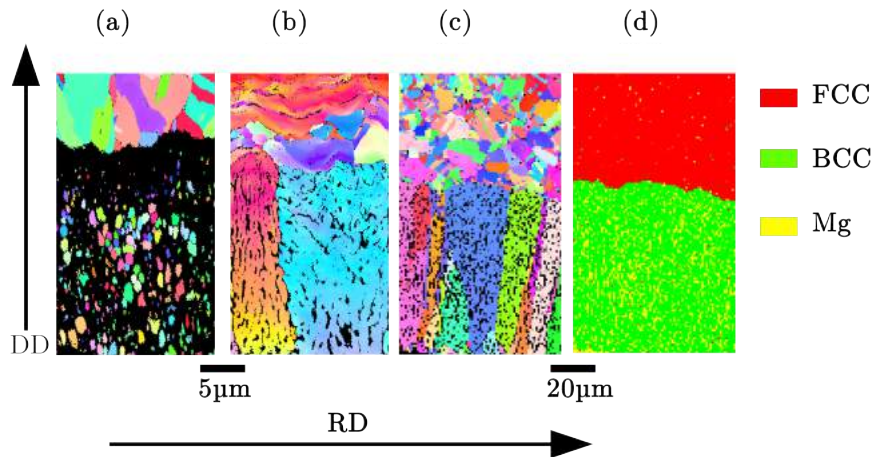


Figure 6.10: IQ+IPF EBSD map after dealloying 3 min from precursor after cold-rolling from (a) 30FeCr-Ni at 665°C (b) 70FeCr-Ni at 665°C (c) 70FeCr-Ni at 820°C samples. (d) phase maps of (c). Arrows correspond to cold-rolling direction (RD) and dealloying reaction direction (DD).

From Fig. 6.10 (a) and (b), it is possible to see that in only 3 min, precursor samples already recrystallized. Grains shape and grains size are very similar to previous ones from Fig. 6.9. However Fig. 6.10 (b) presents the recrystallization front: the precursor near dealloying interface is recrystallized while far from the interface it presents cold-rolled grains. Recrystallisation rate differs depending on temperature and precursor composition.

From the early beginning of dealloying different behaviour depending on precursor composition (nucleation/growth) is observed: very small grains with low $FeCr$ content ((a)) and long grains for precursor with high content of $FeCr$ ((b) and (c)).

In Fig. 6.10 (c) on the dealloyed part, grain growth competition is observed: for some orientations, grains become larger [DUN 49, CHE 08]. In Fig. 6.10 (d) the phase map of (c) is presented. Precursor sample presents only FCC phase, dealloyed part only BCC phase and between ligaments, Mg grains are detected.

Results of dealloying at 665°C for 50FeCr-Ni precursor and at 820°C for 30FeCr-Ni and 50FeCr-Ni precursors are not detailed here but have a fully recrystallized precursor and very small dealloyed grains as presented in Fig. 6.10 (a).

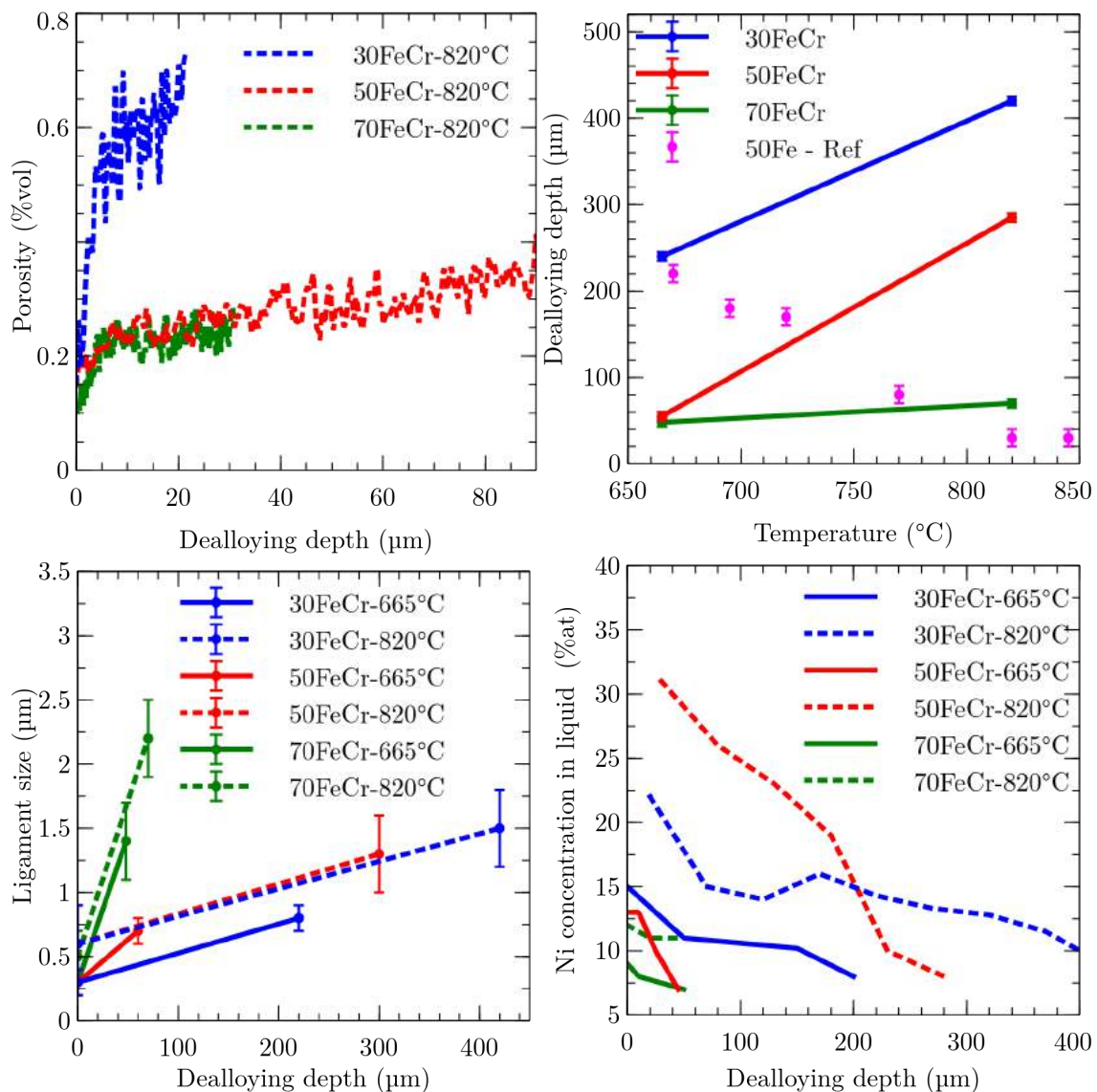


Figure 6.11: Evolution of porosity with dealloying depth (top left), Evolution of dealloying depth with temperature (top right), Evolution of ligament size with dealloying depth (bottom left), Evolution of Ni at% in liquid phase with dealloying depth. A dealloying depth equal to 0 corresponds to the dealloying front reaction.

6.2.3.2 Microstructure analysis

A partial dealloying can also give some informations about the evolution of the structure and about dealloying and coarsening kinetics.

Porosity Fig. 6.11 (top left) presents the evolution of porosity with dealloying depth. Porosity increases with dealloying depth until stabilizing. Those stabilized values are very close to the expected ones (cf. Chapter 5) and consistent with previous studies [ZHA 17].

Dealloying depth Fig. 6.11 (top right) presents the evolution of dealloying depth with temperature. The data for the 50Fe-Ni precursor curve (50Fe-Ref) can be found in [SAI 16]. When Cr is present, dealloying depth increases with temperature while when Cr is not present the opposite behaviour is observed: dealloying depth decreases while increasing temperature.

From equation 1.3 (cf. Chapter 1) it is suggested that dealloying depth should increase with temperature for a constant activation energy. The result for 50Fe-Ni precursor suggests that the activation energy depends on temperature [SAI 16].

While decreasing the amount of Ni , the dealloying rate also decreases as already mentioned in [TSU 14].

While adding Cr the local equilibrium between precursor, ligaments and liquid composition changes and enables the modification of dealloying kinetics.

Ligaments size Fig. 6.11 (bottom left) presents the evolution of ligaments size with dealloying depth.

30FeCr and 50FeCr present a similar behaviour while 70FeCr ligaments presents a higher coarsening rate. This result is different compared to the one in Chapter 5 where the same ligaments size was obtained after the same dealloying time. Dealloying kinetic of 70FeCr-Ni precursor is really slow compared to 50FeCr-Ni and 30FeCr-Ni. Therefore 70FeCr coarsening time is smaller than 30FeCr and 50FeCr for the same dealloying time which implies a different coarsening behaviour.

Coarsening rate is higher at high temperature which is consistent with equation 1.5 (cf. Chapter 1). Near dealloying interface ligaments created at higher temperature are larger than the ones formed at lower temperature, which is consistent with coarsening law.

Ni concentration in liquid Fig. 6.11 (bottom right) presents the evolution of Ni at% in liquid phase with dealloying depth. From the dealloying reaction interface to Mg bath, the Ni concentration decreases. This result was also observed with different materials in [MCC 16c].

The Ni concentration in the case of 30FeCr and 50FeCr are close to each others and the Ni in Mg maximum solubility from phase diagram is reached near the dealloying interface for both temperature [MIE 08b]. 70FeCr presents experimentally smaller solubility than others samples. The experimental result is probably underestimated because the Mg phase was not easy to detect. Therefore one can imagine that the real solubility of Ni in Mg is not dependant on precursor phase ratio.

Dealloying depth depends on precursor composition:

- the dealloying kinetics is proportional to the amount of Ni .
- dealloying depth increases with dealloying temperature for samples including Cr while for samples without Cr , the opposite behaviour is observed.

6.2.4 Phase transformation during dealloying : model

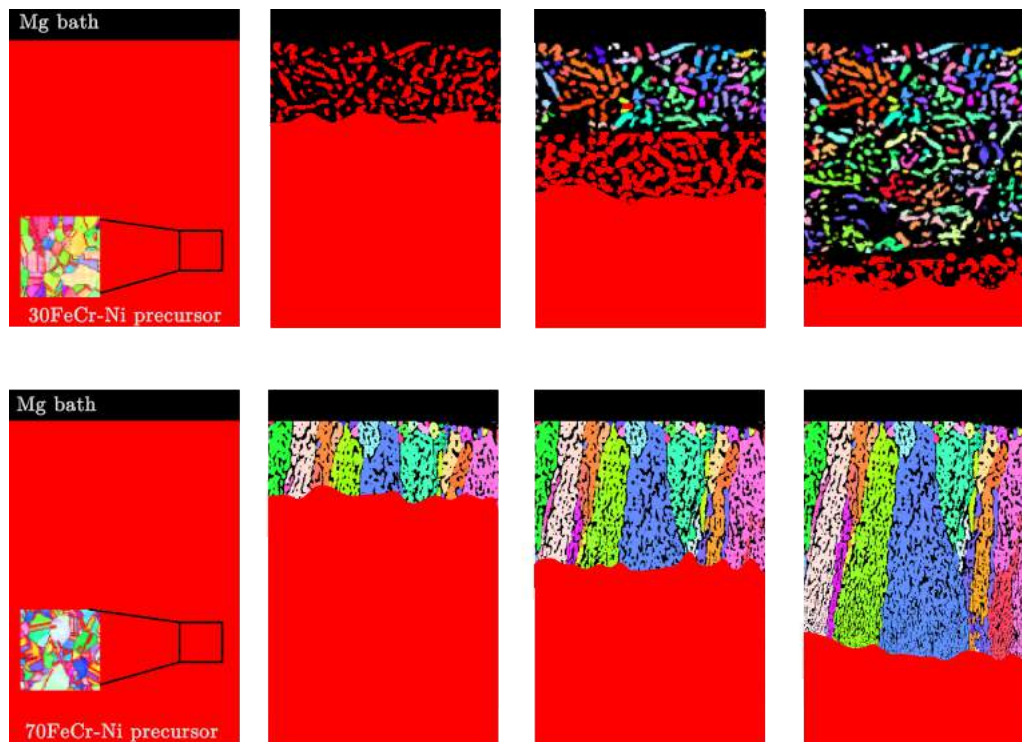


Figure 6.12: Grain formation during dealloying: for low amount of $FeCr$, the high kinetics of dealloying promotes a morphological transformation with the formation of FCC ligaments followed by a displacive transformation (top), for a high amount of $FeCr$, the slow kinetics of dealloying promotes a diffusive transformation with the direct formation of BCC ligaments (bottom).

Fig. 6.12 schematically presents the grain formation mechanism during dealloying depending on the precursor $FeCr/Ni$ fraction.

If one considers the same interface precursor/dealloyed sample:

- when the amount of $FeCr$ is low (cf. Fig. 6.12), the dealloying front reaction moves fast which promotes diffusion and then the formation of FCC ligaments followed by a displacive transformation. As a consequence, the nucleation of new grains is easier.
- when the amount of $FeCr$ is high (cf. Fig. 6.12), the dealloying front reaction moves slowly. Fe and Cr are closer to each other so it is easier to have a diffusive phase transformation with grain growth rather than nucleation of new grains [POR 09, KUR 98].

6.3 Effect of Cr addition on grain microstructure

To observe the influence of Cr addition on grain microstructure, $Fe_{30}Ni_{70}$ precursor was prepared in similar conditions than $FeCrNi$ precursor : precursor was cold-rolled after casting. Then, this cold-rolled precursor was dealloyed for 1 h at $820^{\circ}C$ and result is shown in Fig. 6.13(b). After dealloying the sample presents small randomly oriented grains composed of a small number of ligaments.

While comparing Fig. 6.13(a) and Fig. 6.13(b) where only the Cr amount differs, the effect of Cr addition on dealloyed microstructure seems to be weak compared to dealloying parameters (cf. Fig. 6.5) and precursor microstructure (comparing Fig. 6.13(b) and Fig. 6.5(c)).

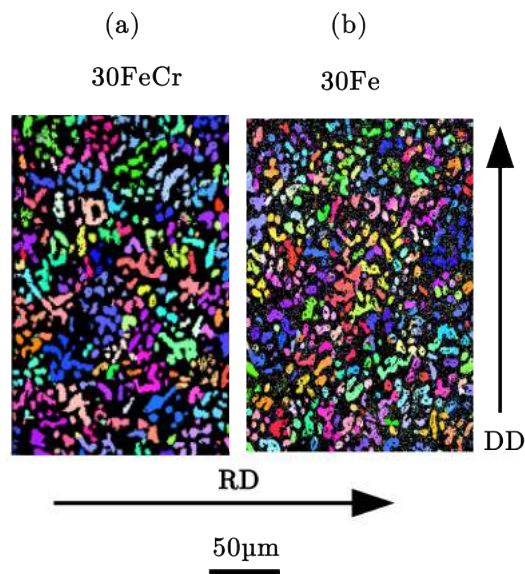


Figure 6.13: IPF maps after 1 h at $820^{\circ}C$ dealloying from 30FeCr-Ni precursor (a) and 30Fe-Ni precursor (b).

6.4 Conclusion

In this chapter the grain microstructure was investigated.

Different FCC/BCC phase transformation mechanisms during dealloying were noticed:

- low $FeCr$ precursor: a FCC/BCC displacive transformation is observed. This transformation shows similarities with austenite/ferrite phase transformation.
- high $FeCr$ precursor: a FCC/BCC diffusive transformation is observed. Dealloyed grains are columnar grains with grain orientation competition.

To find the composition where the transformation mechanism changes, the use of precursor with a Ni composition gradient could be a solution.

Even if precursor Ni ratio has a high influence during dealloying (kinetics and grain formation), the precursor composition has a low influence on foam morphology (same ligaments size, same tortuosity and connectivity...)(cf. Chapter 5). The Cr addition has a limited influence on grain microstructure and foam morphology (cf. Chapter 5) however it highly affects dealloying kinetics.

The effect of dealloying time and temperature on grain microstructure from $Fe_{30}Ni_{70}$ precursor with large and homogenized grains was studied: each FCC precursor grain was transformed into several BCC dealloyed grains. The FCC grain boundaries become large ligaments during dealloying. As austenite-ferrite phase transformation, the dealloyed grain size are proportional to dealloying time and temperature.

Chapter 7

Mechanical properties of FeCr based composites

After the materials elaboration, the morphology and microstructure characterization in Chapters 4, 5 and 6, in this chapter the mechanical properties of FeCr-Mg, porous FeCr and FeCr-polymer composites with different phase fractions will be investigated by nanoindentation and compression. The effect of the composition and morphology with ligament size on Young's modulus and hardness will be studied. The mechanical resistance will be measured by compression tests.

Contents

7.1	Nanoindentation	104
7.1.1	Nanoindentation parameters	104
7.1.2	Young's modulus	105
7.1.3	Hardness	107
7.1.4	Focus on porous FeCr	107
7.2	Compression	110
7.2.1	Methods	110
7.2.2	Comparison of the composites	110
7.2.3	Effect of <i>FeCr</i> phase fraction	111
7.2.4	FeCr-polymer composites	113
7.2.5	Densification	113
7.3	Comparison with others materials produced by dealloying	113
7.4	Conclusion	115

I would like to thank those who contributed to this chapter:

- Sylvain Dancette (MATEIS) for his help on nanoindentation experiments.
- Eugénie Godet (M2) and Gabriel L'Hôte (MATEIS) for their participation in nanoindentation and compression experiments

7.1 Nanoindentation

In this part, 2 series of composites and porous samples with different volume fractions (30/50/70FeCr-Ni) presented in Chapter 4 will be analysed. These samples were prepared by dealloying for 1 h at 820 °C and 6 min at 700 °C respectively. Resulting ligament size was estimated at around 5 μm and at around 1.5 μm respectively and will be referred to as large ligaments samples and small ligaments samples respectively. To measure the mechanical properties of polymers, some neat polymers were polymerized.

7.1.1 Nanoindentation parameters

Nanoindentation technique consists in the indentation of a material with a high stiffness tip. The indented depth (from few nanometers to few micrometers) and load (with an accuracy of 1 N) are recorded during the operation. A load/unload cycle is necessary to obtain the load-indentation curve. From the unload part, it is possible to know the indented surface and then to determine the hardness and the Young's modulus by a model developed by Oliver and Pharr. More details can be found in [SNE 65, OLI 92, MAC 07]. Nanoindentation tests were performed using a Nanoindenter Agilent G200 device (Agilent Technologies, USA). On each sample at least one batch of 9 indents were performed with a continuous stiffness measurement mode (CSM) using a Berkovich diamond tip for a maximum depth of 5 μm on composite samples and with a steel 70 μm diameter flat punch indent for a maximum depth of 10 μm on porous samples. The results are analysed with the Nanosuite software and the Berkovitch tip was calibrated by indentation on a fused silica sample.

Even if in nanoindentation, the interaction area should be considered as 10 times the indentation depth [WES 24], to have a better accuracy it was chosen to include several ligaments under indents. To check if indentation depth is enough to include several ligaments, SEM observations were performed after nanoindentation experiments. Some pictures are shown in Fig. 7.1. Even for large ligaments with the lowest concentration of *FeCr* phase (30FeCr-Mg with large ligaments) the indent position, shown by red dashed lines, includes more than one ligaments. The measured behaviour is here global as it was expected.

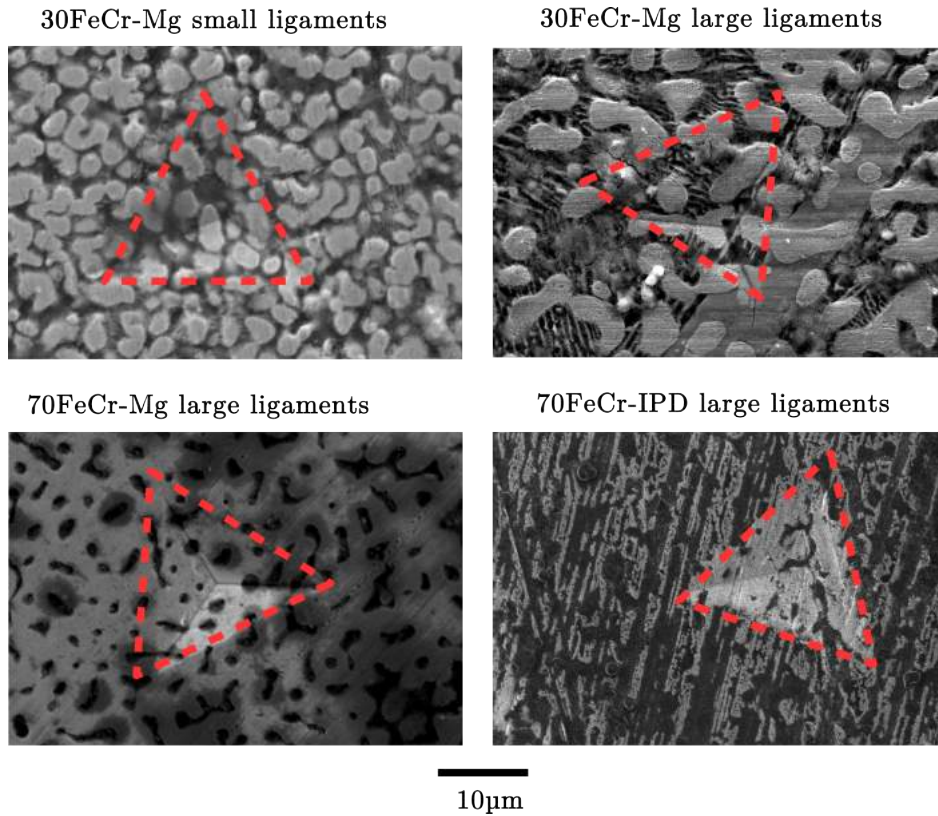


Figure 7.1: Different samples surface imaged by SEM after nanoindentation. Red dash lines highlight the indent position.

7.1.2 Young's modulus

Composite materials theoretical Young's moduli are bounded by VOIGT and REUSS mixing law. VOIGT law corresponds to the upper case considering homogeneous strain in the volume, corresponding to the moduli arithmetic average (fibres aligned with load) while REUSS law corresponds to the lowest case considering homogeneous stress in the volume, corresponding to the moduli harmonic average (fibres perpendicular to the load) [BOR 01]. As shown in Chapter 5, ligaments present an isotropic distribution. Therefore it is expected to get experimental values between VOIGT and REUSS values. Young's modulus boundary values in case of isotropic composites materials were defined by HASHIN and SHTRIKMAN [HAS 63].

Table 7.1 presents bulk materials Young's modulus from literature for metals [KAY] or measured in this study by nanoindentation on pure polymer DGEBA-IPD. Measured value for polymer is consistent with values from tensile tests [SBI 11].

	FeCr [KAY]	Mg [KAY]	DGEBA-IPD (nanoindentation)
Young's Modulus (GPa)	210	44	3.7

Table 7.1: Young's modulus of different elements.

Fig. 7.2(left) displays the evolution of Young's modulus as a function of $FeCr$ phase fraction for FeCr-Mg composites, porous FeCr and FeCr-IPD composites.

Some measurements were also performed on FeCr-D2000 composites. However this epoxy network is very ductile with a rubbery behaviour at room temperature and similar to elastomer. Therefore indentations were not successful.

All measured Young's moduli are included in boundaries curves expressed by VOIGT and REUSS laws and as expected modulus increases when the $FeCr$ phase fraction increases. Because ligaments present an isotropic distribution, it is consistent to have experimental results between the maximum and minimum values given by the mixture law established for isotropic materials by HASHIN and SHTRIKMAN. Moreover as expected the stiffness is higher for metal/metal composite than metal/polymer even if metal/polymer is stiffer than porous samples. The effect of ligament size on Young's modulus is negligible if the errors bars are considered.

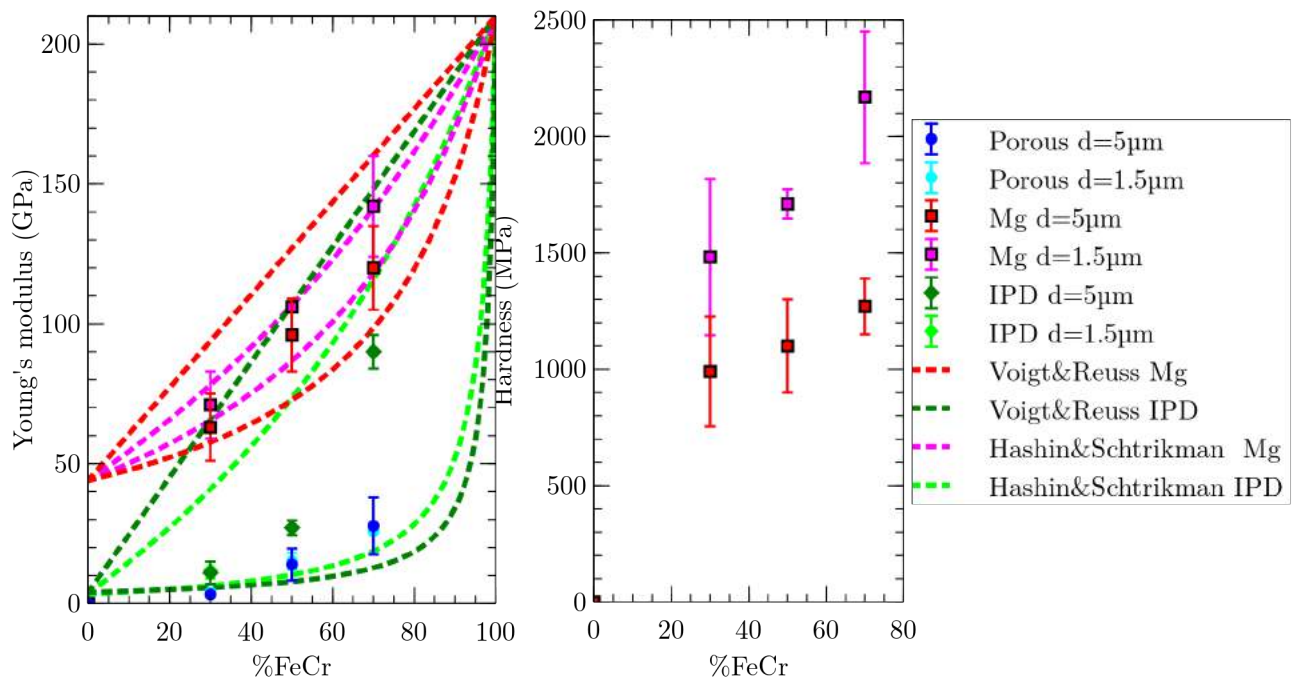


Figure 7.2: (left) Evolution of Young's modulus with FeCr fraction of FeCr-Mg, porous FeCr and FeCr-IPD composites. The red/pink and greenw dashed lines correspond to mixing laws for FeCr-Mg and FeCr-IPD composites respectively (right) Evolution of Young's modulus with FeCr fraction of FeCr-Mg for 2 different ligaments size.

7.1.3 Hardness

Nanoindentation allowed to assess sample's hardness. The evolution of FeCr-Mg composites hardness with *FeCr* phase fraction is displayed in Fig. 7.2(right). The hardness increases when the amount of *FeCr* increases which is consistent with a higher hardness of *FeCr* compared to *Mg* [KAY]. Large ligaments present lower hardness than small ligaments which is consistent with literature [WIT 12, MCC 16d].

FeCr-Mg values present a large standard deviation which can be partially explained by the effect of surface preparation. Nanoindentation is very sensitive to the surface preparation [LAU] and composites are very difficult to polish. Moreover the local composition, especially Ni-rich area in *Mg* phase, can affect the nanoindentation results [MCC 16b].

7.1.4 Focus on porous FeCr

As explained in Chapter 1, the theoretical Young's modulus and yield stress established by GIBSON and ASHBY are not valid for dealloyed materials. A scaling law to calculate theoretical yield stress was established. However there is actually no reference model to predict the Young's modulus of nanoporous materials produced by dealloying.

7.1.4.1 Comparison with existing models

In this part, the experimental values will be compared with existing models. Fig. 7.3 displays the evolution of Young's modulus with density. In addition of the experimental data some models are plotted. Because it is difficult to get these experimental parameters, other models based on real connectivity measured *in situ* during mechanical test or models considering cells morphology will not be discussed here [LIU 16, MAN 16, PIA 13, LIL 18, HU 16]. As explained in Chapter 1, E_p corresponds to the Young's modulus of porous materials and (ρ_r) to the relative density.

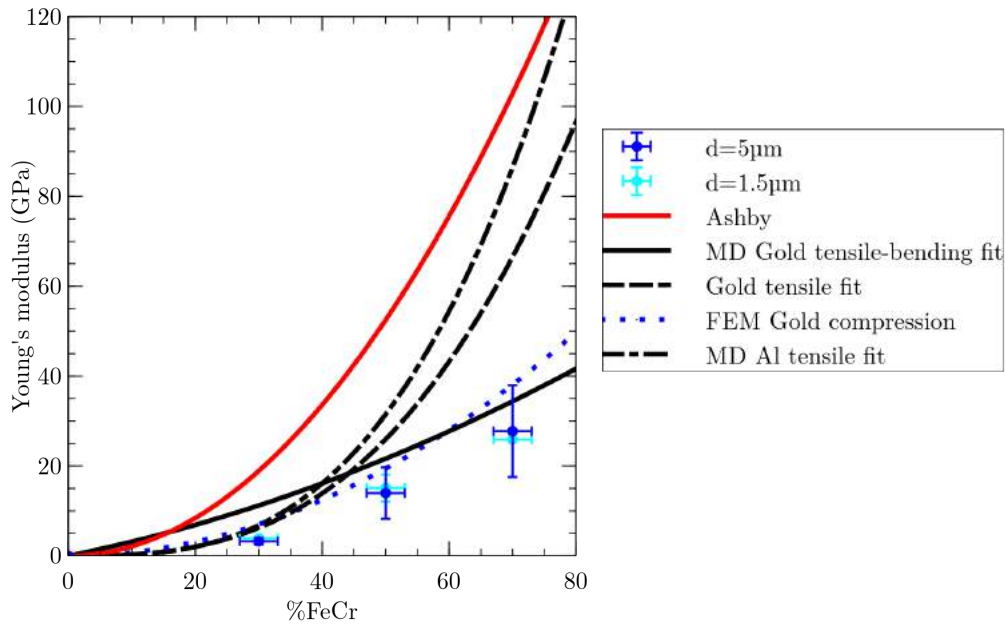


Figure 7.3: Comparison of porous FeCr Young's moduli obtained by nanoindentation (dots) with different theoretical models (lines).

Ashby corresponds to the GIBSON and ASHBY presented in Chapter 1 ($E_p = EC\rho_r^n$) with $C = 1$ and $n = 2$ [GIB 97]. This law is valid until 30% porosity.

MD Gold tensile-bending fit corresponds to $E_p = EC_1(\rho_r^2 + C_2\rho_r)$ with C_1 and C_2 corresponding respectively to the bending behaviour of ligaments and the tensile deformations of ligaments and evaluated at respectively 0.14 and 0.97 for nanoporous gold [SUN 13].

Gold tensile fit corresponds to a fit of experimental values on tensile test on nanoporous Gold by GIBSON and ASHBY law: $E_p = 0.86E\rho_r^{2.8}$ [BAD 17].

FEM Gold compression corresponds to a scaling law depending on the extension of nodal connections between the ligaments. The solid fraction can be described depending on the cell geometry and the scaling law can be written as: $E_p = 0.37E\rho_r^2$ [HUB 14].

MD Al tensile fit corresponds to molecular dynamic simulation of nanoporous aluminium mechanical behaviour leading to this scaling law $E_p = 1.2E\rho_r^3$ [NIC 16].

GIBSON and ASHBY law is not valid even for low density. Scaling laws established for nanoporous metals are closer to the experimental values than Gibson and Ashby law but no one fits perfectly well the presented values. It is not surprising because most of these predictions were established with tensile test and with lower density nanoporous gold.

7.1.4.2 Experimental data fitting

Because the experimental data were not perfectly fitted with existing model, in this part, the experimental data were fitted with different parameters based from ASHBY and GIBSON models. The results are shown in Fig. 7.4.

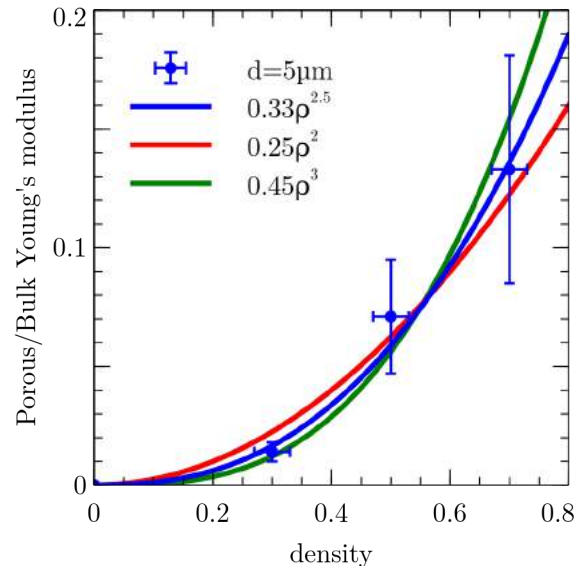


Figure 7.4: Fit with different parameters of experimental evolution of Young's modulus with foam density.

- The first fit (blue) corresponds to the fit of the general GIBSON and ASHBY model ($E_p = E(C\rho_r^n + C'\rho_r)$) with respectively $C.\rho_r^n$ the bending contribution and $C'.\rho_r$ the compression contribution. Fitting parameters are $C = 0.33$, $n = 2.5$ and $C' = 0.001$. The compression contribution can be neglected and only the bending behaviour can be considered here then the fitting equation becomes $E_p = 0.33E\rho_r^{2.5}$.
- The second fit (red) corresponds to the fit of [FEM Gold compression model] $E_p = EC\rho_r^2$. Fitting parameter is $C = 0.25$, it is lower than the one of [FEM Gold compression] which means that the ratio between ligaments diameter and distance between 2 nodes are different therefore the morphologies are different.
- The last fit (green) corresponds to the fit of $E_p = EC\rho_r^3$. Fitting parameter is $C = 0.45$, it is lower than the one of [MD Al tensile fit]. [MD Al tensile fit] was realized for densities similar to the ones of this study (from 36 to 84%). For high densities, an exponential factor higher than 2 seems necessary to fit the data.

- Young's moduli are not dependent of ligaments size whereas hardness is.
- Composites Young's moduli are included in boundaries curves expressed by HASHIN and SHTRIKMAN laws.
- Porous Young's moduli are very low compared to the ones predicted by GIBSON and ASHBY model even for low density foam (6 times lower for 30FeCr). The experimental values was fitted with $E_p = 0.33E\rho_r^{2.5}$.

7.2 Compression

In this section all samples presents around 5 μm ligaments size.

7.2.1 Methods

In order to gain a better understanding of the mechanical behaviour, compression tests are performed on tensile/compressive machine (Instron 5967, High Wycombe,UK), with a load sensor of 30 kN on sample with 9 mm surface and 1 mm height at a deformation rate of 3.10^{-4} s^{-1} . The deformation measurement is done with a digital video extensor system. At least two curves for each sample have been recorded. In case of porous samples, a load-unload cycle was performed after every 100 μm displacements. Tests were stopped far from failure after a displacement of 0.7 mm.

7.2.2 Comparison of the composites

The compression test curves can be found in Fig. 7.5 where the engineering stress *versus* the true strain is plotted. Each graph corresponds to each composition 30FeCr, 50FeCr and 70FeCr based samples. The scale is different for each graph to be optimized. The comparison between different compositions will be done in the next section. Colour code is kept along all this section.

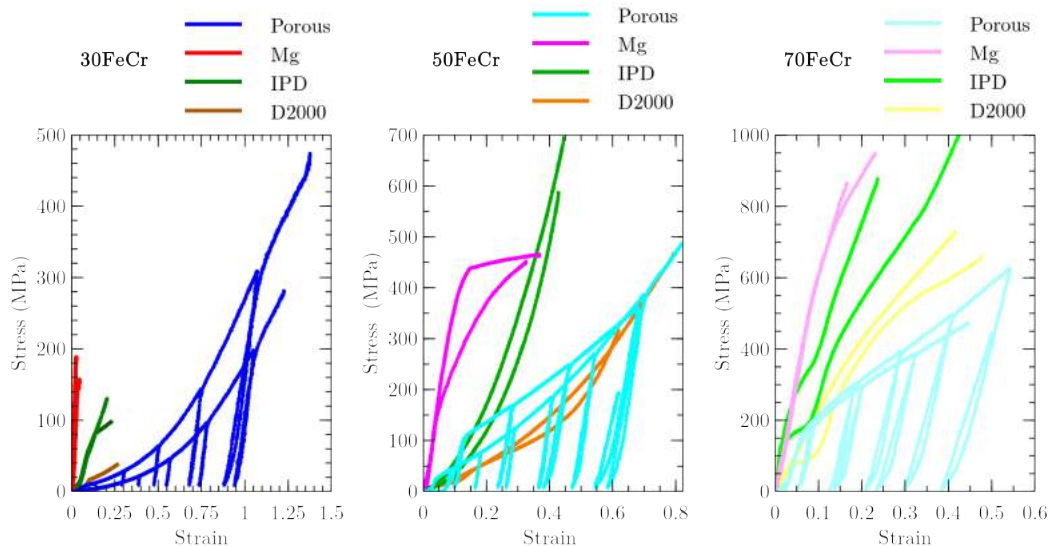


Figure 7.5: Evolution of compression engineering stress-true strain curves of FeCr-Mg, FeCr-air, FeCr-D2000 and FeCr-IPD composites with a FeCr phase fraction of 30% (left), 50% (middle) and 70% (right). All composites presents 5 μm thick FeCr ligaments.

First a quite good reproducibility can be noticed, the yield stress is measured at the knee between the elastic and plastic part and results are written in Table 7.2. The evolution of mechanical resistance is the same as Young's modulus. FeCr-Mg composites are the uppermost curves as expected. Also as expected FeCr-IPD composites curves are above the porous one. The reinforcement of porous samples produced by infiltration by polymer resin was already noticed in the literature for gold and Ti-based alloys [WAN 13, WAN 15a, OKU 18a].

However this result is not obvious for D2000 based epoxy resin composites. For 30FeCr and 50FeCr, the polymer addition effect is negligible whereas 70FeCr-D2000 shows an improvement compared to porous 70FeCr.

Yield stress (MPa)	30FeCr-X	50FeCr-X	70FeCr-X
X=Mg	190 ± 10	380 ± 30	600 ± 30
X=air	?	70 ± 30	150 ± 20
X=IPD	75 ± 20	?	180 ± 20

Table 7.2: Yield stress measured on compression curves. When it was not possible to extract the yield stress from the curves the symbol “?” is written.

7.2.3 Effect of *FeCr* phase fraction

The compression curves are presented depending on *FeCr* phase fraction in Fig. 7.5, however it is also important to compare the influence of the *FeCr* phase fraction for the same second phase that is presented in Fig. 7.6. In this figure, each graph corresponds to the same second phase: *Mg*, air or polymer (respectively (a) (b) (c)) with different *FeCr* phase fraction.

7.2.3.1 FeCr-Mg composite

Fig. 7.6(a) shows that the mechanical resistance is proportional to the *FeCr* phase fraction. The behaviour of the metal/metal composite shows a fair amount of ductility in compression.

7.2.3.2 Porous FeCr

Fig. 7.6(b) shows the case of porous samples. In case of 50FeCr and 70FeCr the elastic deformation before the yield strength being very substantial, the plastic deformation is visible while for 30FeCr, only a plastic deformation is visible. Such a low yield strength was observed for nanoporous gold with large ligaments and similar density [WAN 13, WAN 15a, MAM 16].

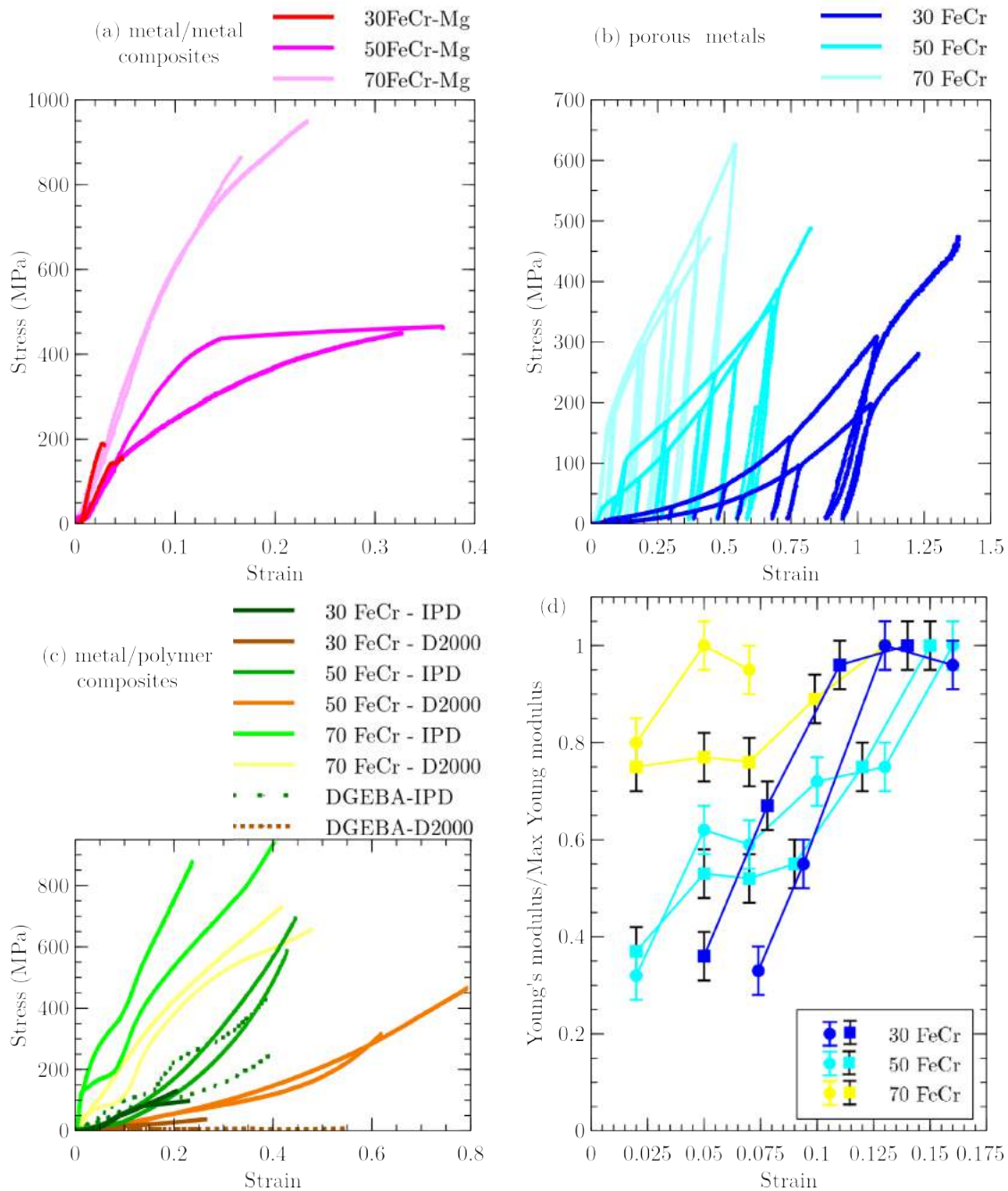


Figure 7.6: Evolution of compression engineering stress-true strain curves with the fraction of *FeCr* phase of (a) FeCr-Mg composites (b) Porous FeCr (c) FeCr-polymer composites and neat polymers. (d) graph presents the evolution of the secant Young's modulus measured on load-unload cycle from graph (b). 30FeCr and 50FeCr presents higher increase than 70FeCr.

7.2.4 FeCr-polymer composites

Fig. 7.6(c) shows the case of FeCr-polymer composites. For comparison, the experiments were also done on neat polymers. The curve corresponding to the neat Epoxy-D2000 network is close to the x axis. As expected, the metal/polymer composites present a better mechanical behaviour than neat polymers in bulk [WAN 13, WAN 15a, OKU 17, OKU 18b]. Even if Young's moduli are similar for both polymers [SBI 11, LEP 02], mechanical behaviour are different. Neat D2000 epoxy network presents a large plastic deformation and a lower resistance than neat IPD epoxy network. For all composite materials, the mechanical resistance is proportional to the FeCr phase fraction.

7.2.5 Densification

For each load curve of Fig. 7.6(b) the Young's modulus was extracted and divided by the maximum Young's modulus measured on the same sample during the same experiment. Fig. 7.6(d) shows the evolution of a normalized Young modulus with the stress. In case of 70FeCr a small densification occurs leading to an increase of the modulus while for 30 and 50FeCr a large densification occurs. The densification was also observed with other nanoporous metals made by dealloying [MAM 16, OKU 18a].

Mechanical resistance and yield stress are proportional to the *FeCr* phase fraction. Glassy epoxy network can be used to reinforce metal matrix while rubbery epoxy network can not. Densification is observed for 30FeCr and 50FeCr while almost not in 70FeCr. Therefore from compression curves, the mechanical behaviour of 70FeCr based composite materials can be rather as bulk materials considered than a porous ones.

7.3 Comparison with others materials produced by dealloying

To compare the materials of this study with other materials and more specifically materials made by dealloying, mechanical results will be presented on ASHBY maps. Young's modulus *vs* density, ASHBY maps is displayed in Fig. 7.7 (a). All FeCr-Mg and all 70FeCr composites are included in the metal area. 30FeCr and 30FeCr-IPD are included in the polymer areas. However 50FeCr and 50FeCr-IPD with other dealloyed based materials are in an empty area between metal, porous ceramic and polymers. Porous TiZr shows properties very close to 30/50FeCr and 30/50FeCr-polymer.

Young's modulus *vs* yield stress, ASHBY map is displayed in Fig. 7.7 (b). Yield stress is very sensitive to ligaments size (cf. Chapter 1), therefore only materials with the same range of ligaments are displayed here (nanoporous gold is not). As the previous graph, all FeCr-Mg and 70FeCr-IPD composites are included in the metal areas. Others dealloyed materials presents mechanical properties in the mineralized tissue area. Moreover some of them presents mechanical properties close to bones.

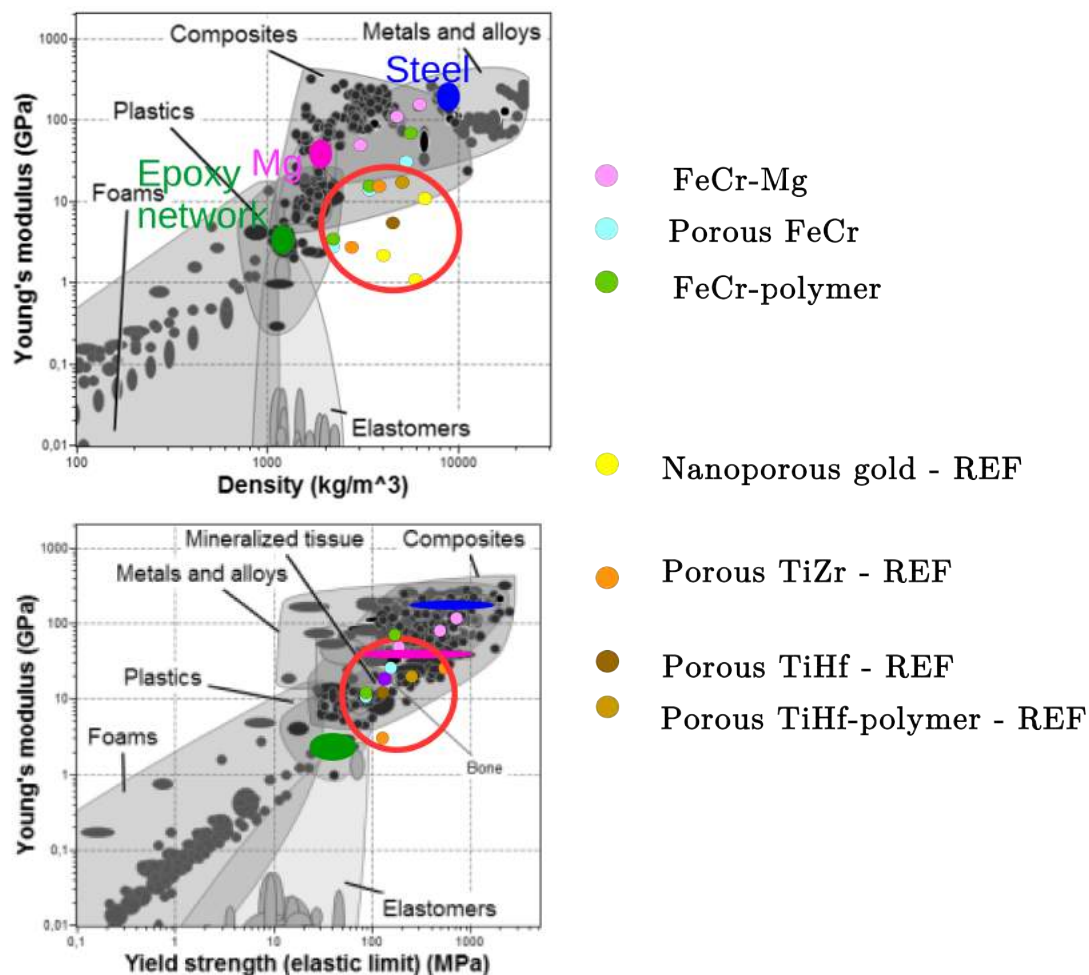


Figure 7.7: Comparison of different materials using Ashby maps (top) Young's modulus *versus* density (bottom) Young's modulus *versus* Yield stress. Small dots corresponds to experimental results on dealloyed based materials from this study or literature studies. Large dots corresponds to area on Ashby maps for respectively steel, *Mg* and epoxy network for dark blue, dark pink and green. References datas provided from [WIT 12, MAM 16] for *Au*, [OKU 18a] for TiHf based materials and [OKU 18b] for TiZr.

Metal/metal composites and composites with a high *FeCr* phase fraction, mechanical properties are in the metal area. However for 30/50FeCr, 30/50FeCr-IPD and porous 70FeCr, they show as others dealloyed materials very interesting mechanical properties and they occupy an new area between metal, polymer and ceramic in ASHBY maps that is useful for many applications as biomaterials. If the ligament size is optimized, the yield strength can be increased leading to a new class of materials with low Young's modulus and high yield strength.

7.4 Conclusion

In this chapter the mechanical properties of different composites were investigated by nanoindentation and compression.

The Young modulus of foam samples of this study is only proportional to their density (ratio *FeCr*/air) and therefore independent on the ligament sizes. On the contrary hardness and more generally plastic properties are highly impacted by foam density, morphology and ligaments sizes.

Measured porous Young's moduli are lower compared to the ones predicted by different models. However the hypothesis of a pure bending behaviour is checked. Experimental data were fitted with $E_p = 0.33E\rho_r^{2.5}$ corresponding to $C = 0.33$ and $n = 2.5$ of GIBSON and ASHBY model.

The polymer's choice is important for the mechanical properties. An hard polymer will improve the mechanical properties while a soft polymer keeps it.

The mechanical behaviour of porous metal and metal/polymer composite with high *FeCr* phase fraction are included in the metal area on Ashby maps and Young's modulus can reach the value of 30 GPa for a density of 70%. This is very interesting for industrial applications because inside the pores, a fluid circulation is possible for metal mechanical properties.

The mechanical behaviour of low density *FeCr* is consistent with others dealloyed based materials. The mechanical properties can be easily designed by optimizing density, ligaments and grains sizes, leading to a new class of materials with low Young's modulus and high yield stress.

Chapter 8

Application of liquid metal dealloying to commercial alloys

After studying the effect of the dealloying and etching step (Chapters 3, 4 and 6) and the effect of precursor composition and dealloying parameters (Chapter 5 and 6) on dealloying kinetics and resulting samples microstructure, an application of liquid metal dealloying to commercial alloy will be investigated.

This chapter will be divided into 4 parts. First the advantages and drawbacks of using commercial alloy as precursor will be explained. Then 3 cases will be studied: dealloying from a stainless steel precursor and dealloying from 2 nickel superalloy precursors.

Contents

8.1	Commercial precursor	118
8.1.1	Research pressure	118
8.1.2	Parting limit pressure	118
8.1.3	Industrial pressure	118
8.1.4	Precursor's choice	119
8.2	Case of S310 stainless steel	120
8.2.1	Dealloying result	120
8.2.2	Dealloying kinetics	121
8.2.3	Coarsening behaviour	123
8.3	Case of Incoloy 800 nickel superalloy	124
8.4	Case of Incoloy 825 nickel superalloy	127
8.4.1	Dealloying Results	127
8.4.2	Dealloying kinetics	133
8.5	Conclusion	134

XRD measurements of this chapter was performed on Rigaku Ultima IV (Tokyo, Japan) with a $Cu K\alpha$ radiation.

8.1 Commercial precursor

8.1.1 Research pressure

Commercial alloys has various compositions and shapes, are very easy to get and low cost compared to commercial pure metals. However dealloying studies from commercial alloys are very rare. Why ? The main reasons for using bi-elements/tri-elements precursors prepared by arc-melting or induction melting from pure elements (cf. Chapter 1) is the possibility to control the precursor composition.

Moreover, it is also easier to understand dealloying behaviour with bi-elements/tri-elements precursors: phase diagrams are known and no interaction between elements except dealloying is expected. The addition of only one element Cr drastically changes the dealloying kinetics (cf. Chapter 6). Therefore it is difficult to predict the effect of the addition of many elements on dealloying kinetics and foam morphology.

8.1.2 Parting limit pressure

To dealloy the whole sample thickness, precursor composition should be above the parting limit otherwise the liquid does not percolate and is not able to travel from one side of the sample to the other. By controlling the precursor composition, it is easy to exceed the parting limit.

Recently, commercial alloys (TA6V, 316L, CCM) below the parting limit were dealloyed resulting in a formation of a porous layer. The porosity was present only at the surface as a partial dealloying [FUK 14, KAT 16, WEI 18] which can be however interesting for many applications.

Theoretical parting limit for FCC/BCC lattice as Fe/Ni based precursors is about 20/25 at.% Ni (cf. Chapter 1) which makes very difficult to find a suitable commercial precursor. One strategy to be above the parting limit was to add sacrificial element into commercial alloy, for instance adding 50 at% Mn into SUS316L alloyed, followed by vacuum dealloying [LI 17].

8.1.3 Industrial pressure

In order to apply liquid metal dealloying in an industrial context where low cost and easy to get precursors are necessary, a solution to replace pure metals home-made precursors should be found. The strategy involved here is the use of commercial alloy with amount of sacrificial element above parting limit as precursor. Therefore a steel with high amount of Ni or a Ni alloy with a high amount of Fe will be chosen.

8.1.4 Precursor's choice

In this chapter, *C* (considered as a polluting element) is disregarded for all SEM-EDX measurements. *Mn* and *Co* lines energies respectively (5.90 keV and 6.93 keV) being very close to respectively *Cr* (5.95 keV) and *Fe* (7.06 keV), they will not be quantified here [KAY]. Minor alloying elements < 0.5 at% as for example *Al*, *P* and *S* are not detected with the EDX analysis and will not be discussed here. From mixing enthalpy values (cf. Table 8.1 [TAK 05]), only *Ni* and *Cu* should be dealloyed.

Mixing enthalpy (kJ/mol)	Fe	Cr	Ni	Si	Ti	Cu	Mo	Mg
Fe		-1	-2	-35	-17	13	-2	18
Cr			-7	-37	-7	12	0	24
Ni				-40	-35	4	-7	-4
Si					-66	-19	-35	-26
Ti						-9	-4	16
Cu							19	-3
Mo								36

Table 8.1: Mixing enthalpy [TAK 05]. Negative values correspond to elements able to be mixed together. Only *Ni* and *Cu* should be dealloyed

For this study, 3 different precursors provided by Nilaco (Japan) have been selected:

1. **S310 stainless steel.** This Ni-rich steel is monophase FCC [NIL, NEZ 17, MIN 10]. The precursor composition is homogeneous on the sample and result is shown in Table 8.2. Theoretical and measured compositions are close, however the *Ni* amount is slightly below the expected value. Sacrificial element composition is ≈ 19 at% just below the theoretical parting limit [ART 09, MCC 16c], therefore a full sample dealloying looks difficult. Compared to the home-made precursor only one element (*Si*) is added.
2. **Incoloy 800 nickel superalloy.** It is difficult to find steel alloys with a high amount in sacrificial element therefore taking a nickel alloy can be a good option. Its composition is close to the home-made ($Fe_{80}Cr_{20}$) $_{70}Ni_{30}$ precursor: the differences are a different Fe/Cr ratio and the *Ti* and *Si* addition (cf. Table 8.2). The main difference with stainless steel S310 is the higher *Ni* amount. It has a monophase FCC crystal structure [MET]. The sacrificial element amount of ≈ 30 at% is above the theoretical parting limit [ART 09, MCC 16c]. Therefore a full sample dealloying is expected.
3. **Incoloy 825 nickel superalloy.** This precursor was selected because of its higher *Ni* and higher minor element concentration compared to Incoloy 800 (cf. Table 8.2) in order to obtain a higher porosity. The effect of impurities elements on the sample microstructure after dealloying will also be studied. This sample has the highest sacrificial element amount (≈ 44 at%). This composition is twice higher than the theoretical parting limit [ART 09, MCC 16c], therefore a full sample dealloying is expected.

Composition (%at)		Fe	Cr	Ni	Si	Ti	Cu	Mo
S310	Precursor theo	≈ 53	≈ 25	≈ 20	≈ 1.5	0	0	0
	Precursor EDX	≈ 53	≈ 26	≈ 18	≈ 2	0	0	0
	Porous theo	≈ 67	≈ 30	0	≈ 3	0	0	0
Incoloy 800	Precursor theo	> 40	≈ 21	≈ 32	< 0.1	≈ 0.4	0	0
	Precursor EDX	≈ 47	≈ 21	≈ 30	≈ 0.8	≈ 0.6	0	0
	Porous theo	≈ 67	≈ 30	0	≈ 0.9	≈ 0.1	0	0
Incoloy 825	Precursor theo	≈ 22	≈ 22	≈ 40	< 0.15	≈ 1	≈ 2	≈ 3
	Precursor EDX	≈ 26	≈ 25	≈ 42	≈ 0.6	≈ 0.8	≈ 2	≈ 3
	Porous theo	≈ 46	≈ 45	0	≈ 2	≈ 2	0	≈ 5

Table 8.2: Precursors theoretical composition (theo) [NIL] and experimental composition (EDX) and porous theoretical (theo) composition after dealloying etching.

All samples were dealloyed in a *Mg* bath then some samples were subsequently etched using aqueous 3 mol *HNO*₃ to remove the *Mg*-rich phase. Samples surface and cross-section were observed using SEM.

8.2 Case of S310 stainless steel

The 1 mm sheet was directly cut without further heat treatment into 30 x 20 mm rectangular samples. Samples was dealloyed for 1 h at 820 °C and for 10 min at 670, 720, 770 and 820 °C.

8.2.1 Dealloying result

The surface composition at the surface after dealloying and etching is presented in Table 8.2.1. As expected, *Ni* from surface is dealloyed and the composition measured by SEM-EDX is very closed to the one predicted in Table 8.2.

	Fe	Cr	Ni	Si	Mg
Porous EDX composition(%at)	69 ± 3	26 ± 5	≈ 0	5 ± 1	1.6 ± 0.8

Table 8.3: Surface composition after dealloying and etching from S310 precursor measured by SEM-EDX.

Fig. 8.1 presents a SEM micrograph of a cross-section after dealloying for 1 h at 820 °C. Red lines correspond to precursor grain boundaries. Dark grey corresponds to dealloyed region, light grey to precursor region and blue line to dealloying front reaction. Near dealloying interface, a channel structure can be observed. Many pores look spherical which is also observed on samples dealloyed from 70FeCr-Ni precursor (cf. Chapter 4). Inside the dealloyed region, some precursor inclusions with a higher *Cr* amount (36 at%) are remaining (highlighted by yellow circles in Fig. 8.1). *Cr* presents a higher melting temperature than *Fe* thus is more difficult to dealloy [MCC 18a, CHE 13a].

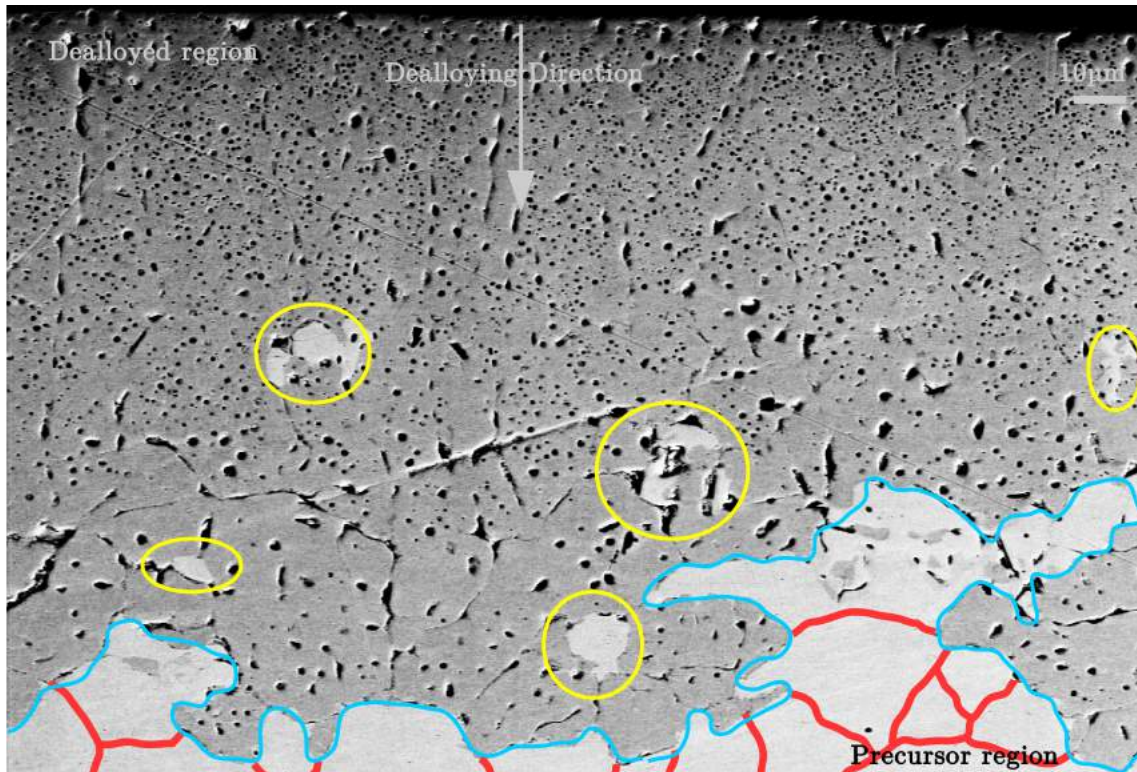


Figure 8.1: SEM micrograph of cross-section after dealloying S310 precursor during 1 h at 820 °C. Red lines correspond to precursor grain boundaries. Dark grey corresponds to dealloyed region, light grey to precursor region and blue line to the dealloying interface. The arrow corresponds to the dealloying direction.

8.2.2 Dealloying kinetics

Dealloying occurred only at the surface and the samples are not fully dealloyed which means that the amount of Ni here, was just below the theoretical parting limit, and was also below the experimental parting limit.

Fig. 8.2 shows cross-sections and surfaces after dealloying at 820 °C for 10 min and 1 h. Cross-sections present simultaneously a dealloyed part and precursor part. Both samples have the same thickness before and after dealloying. Even if dealloying time is different, dealloying depth presents only a small temporal evolution. This result is different from previous studies because this precursor contrary to other studies is below the parting limit. The dealloying depth stop to increase when the maximum depth controlled by the composition is reached [SAI 16, TSU 13, WAD 16b]. Surfaces show that ligaments grow with a longer dealloying time, therefore coarsening happened.

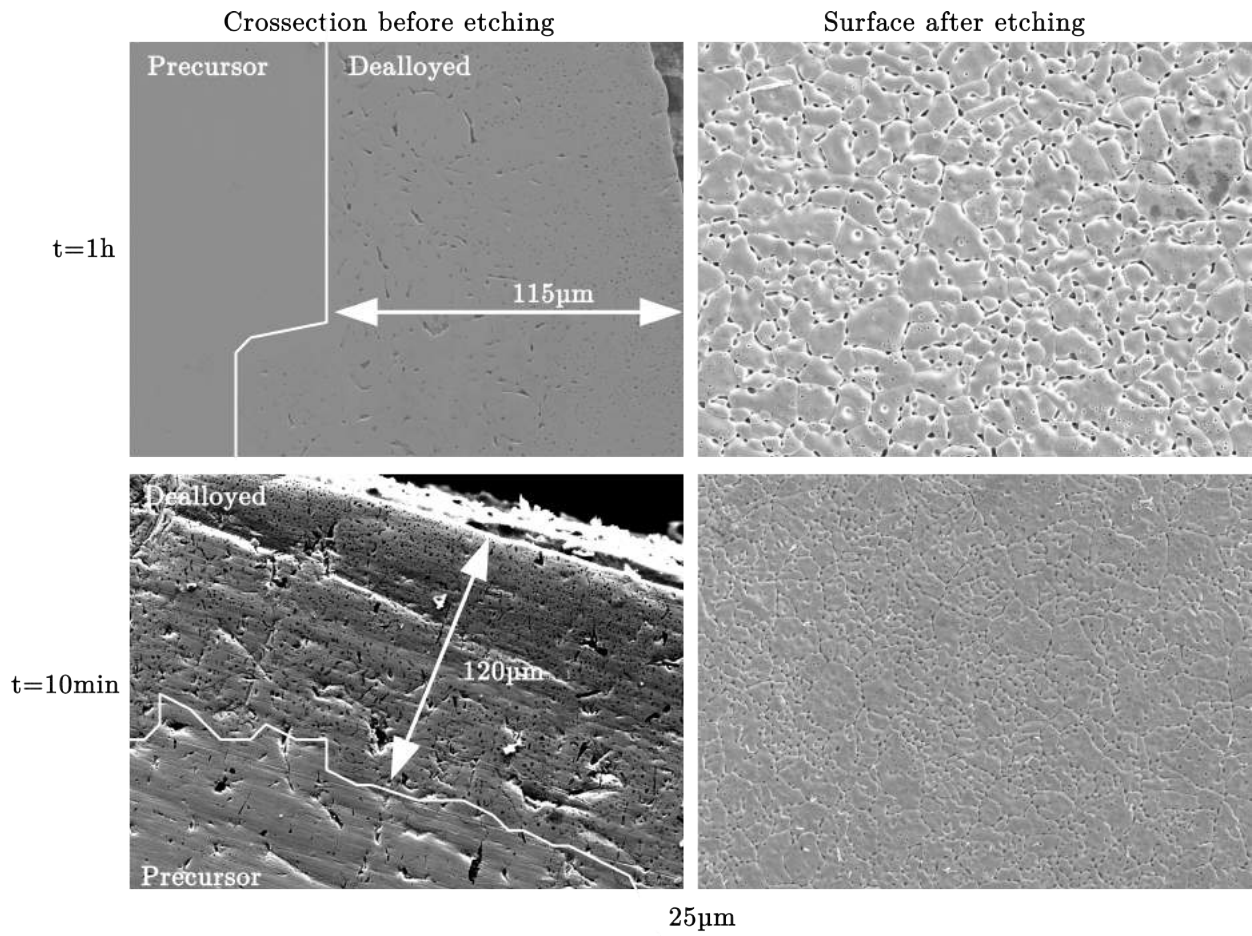


Figure 8.2: SEM micrograph of crossection after dealloying S310 precursor (left) and surface after etching (right) during 1 h (top) and 10 min (bottom) at 820 °C.

For different dealloying temperatures, dealloying depth is measured after 10 min and results are presented in Fig. 8.3. For comparison, data from a previous study [SAI 16] are also shown. At all temperature, the sample thickness was preserved during dealloying process. S310 dealloying depth presents almost no evolution with temperature. In 10 min the maximum dealloying depth was reached at all temperatures. When the precursor composition is above the parting limit (for example 50Fe-Ni) an evolution of dealloying depth with temperature is observed. To observe the evolution of dealloying thickness with S310, dealloying time should be shorter than 10 min.

Thinner samples (300 µm) were also dealloyed and results are similar to the one obtain for thicker samples (1 mm). To have a porous S310, sample thickness should be at 250 µm maximum.

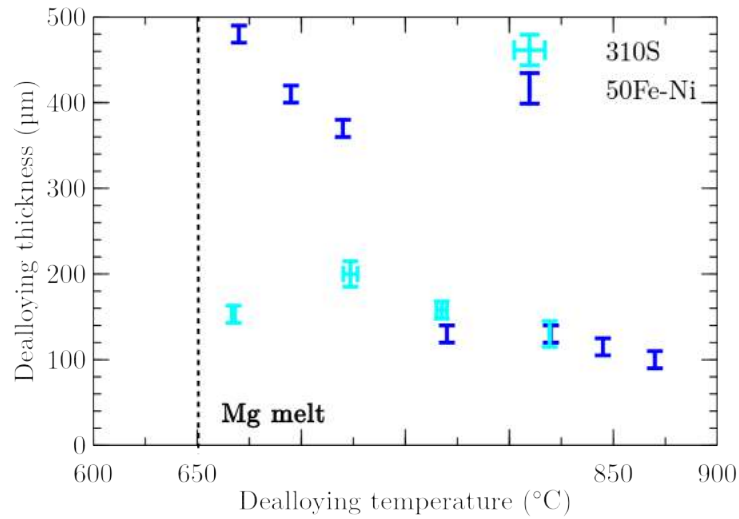


Figure 8.3: Evolution of dealloying thickness after 10min dealloying from S310 and 50Fe-Ni [SAI 16] precursors with dealloying temperature.

8.2.3 Coarsening behaviour

Fig. 8.4 presents SEM micrographs of surface after etching and after 10 min dealloying at different temperatures. While increasing temperature, ligaments become larger (from 1.5 to 6.5 µm).

The fabrication of a fully dealloyed sample from S310 stainless steel was impossible because of the low amount of *Ni*. However the maximum dealloying depth is reached in only 10 min and is not so sensitive to dealloying time and temperature what is suitable with an industrial process.

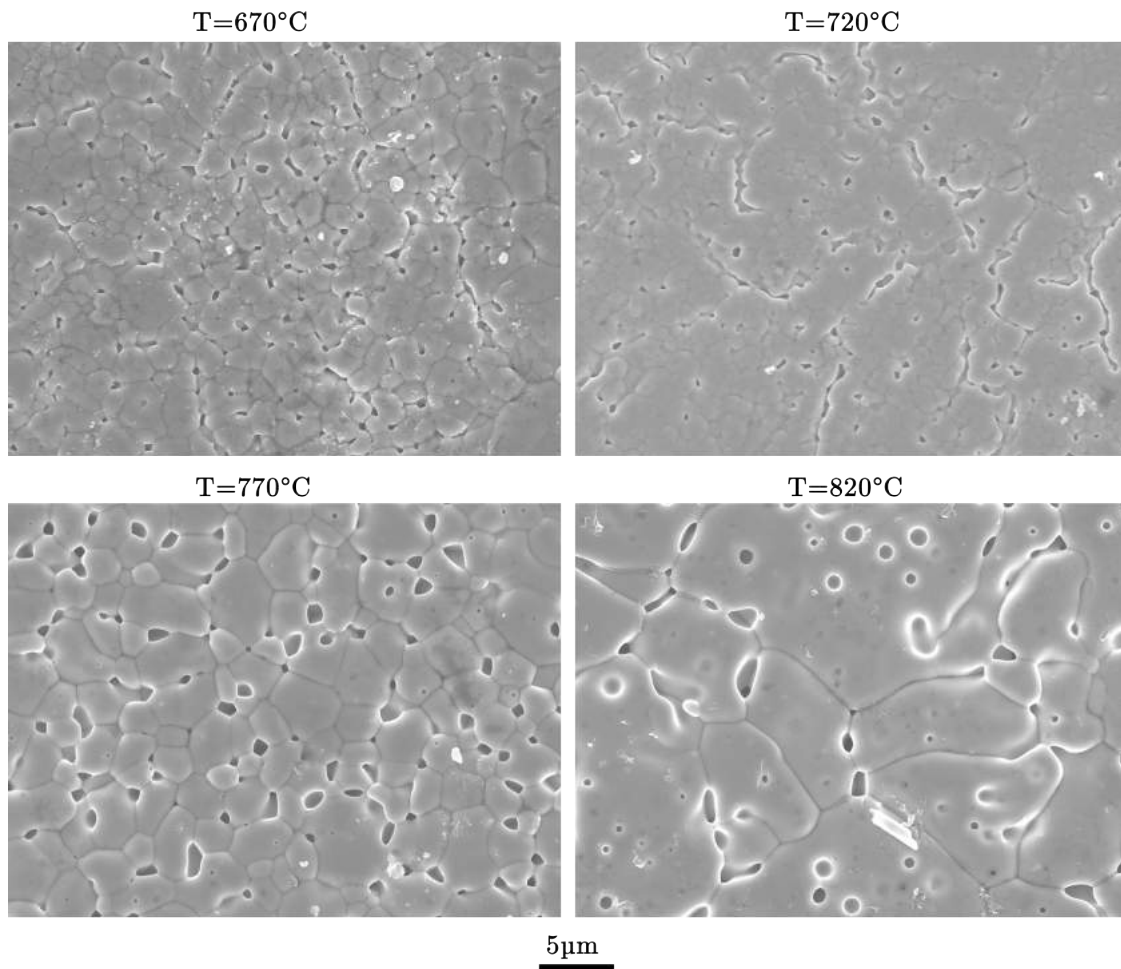


Figure 8.4: SEM micrograph of surface after etching, after 10 min dealloying S310 precursor at different temperatures.

8.3 Case of Incoloy 800 nickel superalloy

A 1.57 mm-thick Incoloy 800 sheet was not subjected to heat treatment, but cut into 29x22mm. Sample was dealloyed for 1 h at 820 °C.

	Fe	Cr	Ni	Ti	Si
Porous EDX composition (%at)	67.7	29.5	0	1	1.8

Table 8.4: Surface composition after dealloying from Incoloy 800 precursor and etching measured by SEM-EDX.

The surface composition after dealloying and etching is presented in Table 8.2.1. As expected, *Ni* from surface is dealloyed and the composition measured by EDX is very closed to the one predicted in Table 8.2.

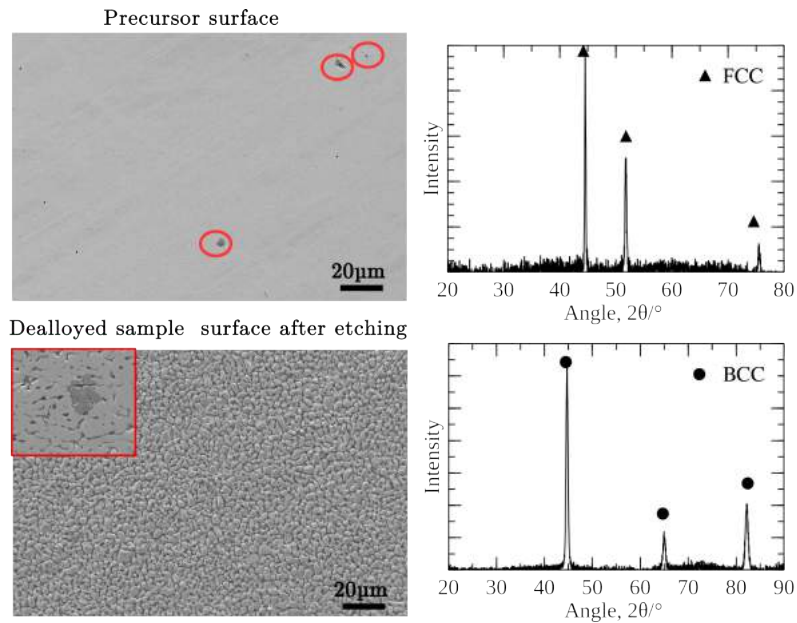


Figure 8.5: SEM micrograph and XRD pattern on Incoloy 800 precursor and porous sample. Red circles corresponds to Ti precipitated. The inset corresponds to SEM micrograph of Ti precipitate after dealloying.

Fig. 8.5 shows on the top a SEM micrograph of the precursor sample surface. The precursor sample presents an almost homogeneous contrast indicating an homogeneous composition on the surface. However some micro and nanoscale phases identified as TiN and TiC precipitates and highlighted with red circles are present. Those precipitates are also mentioned in the literature [DEH 09]. The XRD pattern for the precursor confirms that precursor is a single phase structure with FCC lattice.

Fig. 8.5 shows on the bottom a SEM micrograph of surface morphology of the precursor after dealloying and etching. Ligaments and pores can be observed. As inset, a SEM micrograph of sample cross-section after dealloying presents homogeneous microstructure but a darker phase can be observed. This darker phase is Ti-rich and may corresponds to precipitate observed on the precursor. Precipitates have also been dealloyed. This second phase does not seems to have impacted the dealloying process. On the bottom of Fig. 8.5 the XRD pattern of the porous sample is presented, confirming that porous sample is a single phase with an BCC lattice. Fig. 8.6 presents SEM micrograph of Incoloy 800 after dealloying. Sample thickness was preserved during the process. The sample was fully dealloyed.

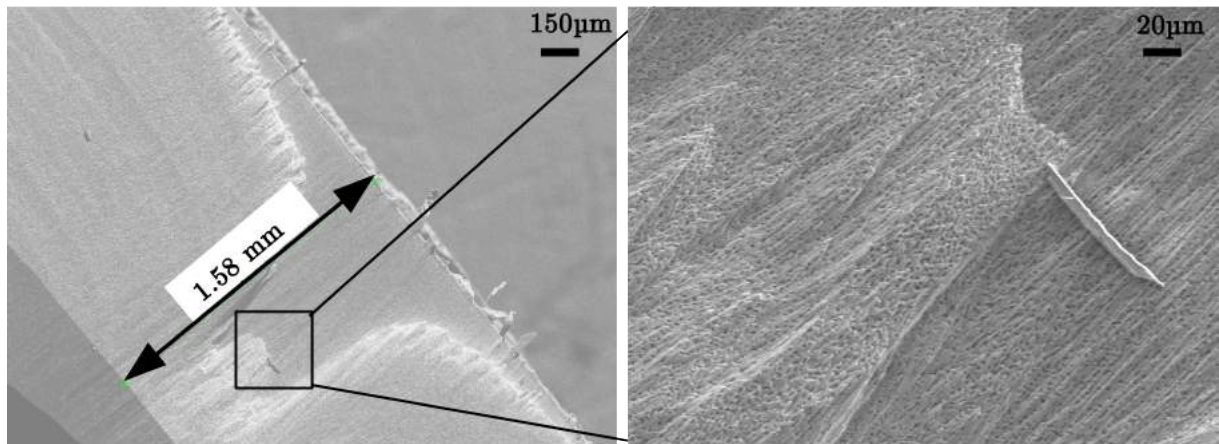


Figure 8.6: SEM micrograph of Incoloy 800 after dealloying. Sample thickness was preserved during the process and dealloying occurs on the whole thickness.

Average ligaments and pores size are estimated to be $2.5 \pm 1.0 \mu\text{m}$ and $1.3 \pm 0.5 \mu\text{m}$, respectively. The volume fraction of the pores is estimated to be $28 \pm 3\%$. This volume fraction is very similar to the one of the $(Fe_{80}Cr_{20})_{70}Ni_{30}$ precursor sample dealloyed with the same conditions because of the similarity of soluble element fractions. However, Incoloy 800 ligaments are slightly smaller ($2.5 \pm 1.0 \mu\text{m}$) compared to home-made precursor $5 \pm 2 \mu\text{m}$ (cf. Chapter 4). This difference might come from the effect of minor alloying elements. For an alloy with low Ni concentration, dissolution of Ni atoms at the dealloying front requires surface diffusion of the remaining *Fe*, *Cr*, and minor elements [WAD 13]. The presence of many minor elements in the Incoloy 800 seems to slow down the diffusion rate and therefore the dealloying rate. So the time given for ligament growth is lower than when using the home-made precursor with no minor element (pure *Fe* – *Cr* – *Ni* alloy). Such influence of minor-elements in dealloying rate is very comparable of the influence of these same elements on the critical cooling rate for martensite transformation, both phenomenons being diffusion driven processes.

The fabrication of a ferritic stainless steel sample from Incoloy 800 nickel superalloy was possible. The small *Si* and *Ti* addition makes ligaments smaller that is very useful to get a high specific surface.

8.4 Case of Incoloy 825 nickel superalloy

The initial precursor sheet of 1.57 mm thickness were cold-rolled until reaching the thickness of 1 mm. The cold rolled sheet were directly cut without further heat treatment into 30x20 mm² rectangular samples. 2 series of samples were dealloyed one for 3 min and the second for 1 h at 660, 710, 760, 820 880 °C. The 3 min serie corresponds to a partial dealloying.

8.4.1 Dealloying Results

8.4.1.1 Phase analysis

Fig. 8.7 presents the XRD pattern of Incoloy 825 before and after dealloying. As mentioned in literature, precursor presents FCC phase [KAN 17, THA 14]. However after dealloying with a temperature higher than 750 °C, dealloyed samples mostly include σ phase. σ phase is a hard but brittle tetragonal $FeCr$ lattice occurring for high Cr amount with high temperature as presented in Fig. 8.7(right). Formation temperature can be until 1000 °C and is stable until 425 °C, depending on minor alloying element. Cr , Mo and Si are well known as σ phase stabilizer [JAC 18, HSI 12, DUB 11], which explain the final microstructure.

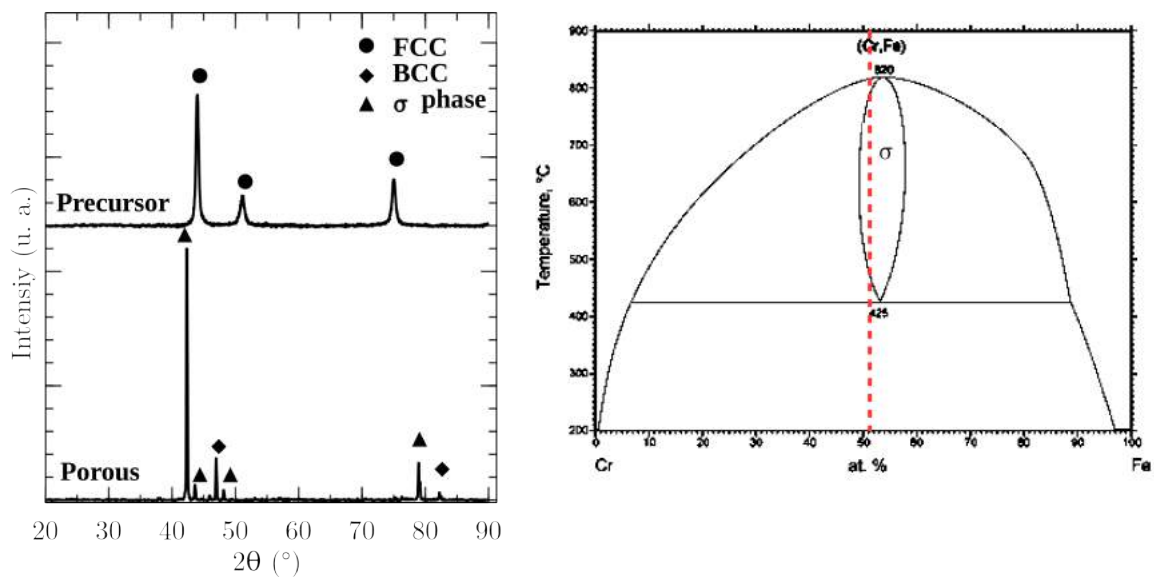


Figure 8.7: XRD pattern of Incoloy 825 before and after dealloying (left) Fe-Cr phase diagram [HAY 90]. The red line corresponds to Fe/Cr ratio after dealloying (right).

8.4.1.2 Dealloying at 660 and 710 °C

Fig. 8.8 presents at SEM micrograph of surface after etching and after 1 h dealloying at 660 and 710 °C. Typical structure of foam ligaments is not observed. The composition on

the surface presented in Table 8.5 for 660 °C is similar to precursor one. It means that dealloying has not occurred yet. At 710 °C *Ni* is partially removed from the surface.

Dealloying reaction hardly occurs for low temperature. This result was also notified for dealloying from *Nb-Ni* precursor in *Mg* melt [KIM 15].

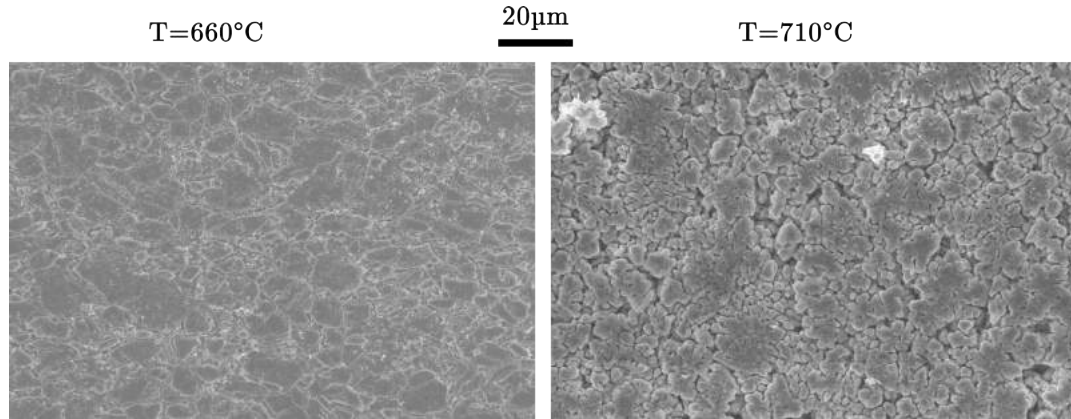


Figure 8.8: SEM micrograph of surface after etching after dealloying Incoloy 825 for 1 h at 660 and 710 °C.

	Fe	Cr	Ni	Cu	Mo	Ti	Si	Mg
EDX 660 (%at)	≈ 27	≈ 26	≈ 41	≈ 1	≈ 3	≈ 1	≈ 0.5	≈ 0.5
EDX 710 (%at)	≈ 35	≈ 34	≈ 21	≈ 1	≈ 3	≈ 0.5	≈ 0.5	≈ 5

Table 8.5: Real composition measured by SEM-EDX of etched surface sample after dealloying from Incoloy 825 precursor at 660 and 710 °C.

8.4.1.3 Dealloying at 760 °C

For $T=760\text{ °C}$, after 1 h dealloying, two types of regions could be distinguished: the main part with small ligaments ($0.11\pm 0.07\text{ }\mu\text{m}$) and some areas with larger ligaments ($0.7\pm 0.1\text{ }\mu\text{m}$). The regions with larger ligaments have a polygonal shape with a diameter about $15\text{ }\mu\text{m}$ as seen on the surface (cf. Fig. 8.9 highlighted by red circles). To explain the presence of areas with large ligaments a partial dealloying to observe precursor microstructure at high temperature was performed. Fig. 8.9 (top) presents the resulting microstructure. Some black inclusions of polygonal shape with a diameter of about $10\text{ }\mu\text{m}$ can be observed inside the matrix in this case. The presence of this polygonal shape inclusion is not noticed for higher dealloying temperature. The typical composition of these inclusions and the matrix is given in Table 8.6. Inclusions are Ti-rich. Ti-rich areas are also noticed in the ref. [KAN 17]. The composition of the regions with large ligaments and small ligaments are shown in Table 8.6. Large ligaments correspond to Ti-rich ligaments while small ligament corresponds to the expected composition after dealloying (cf. Table 8.2). From all these measurements, it can be concluded that Ti-rich inclusions induce regions with large ligaments.

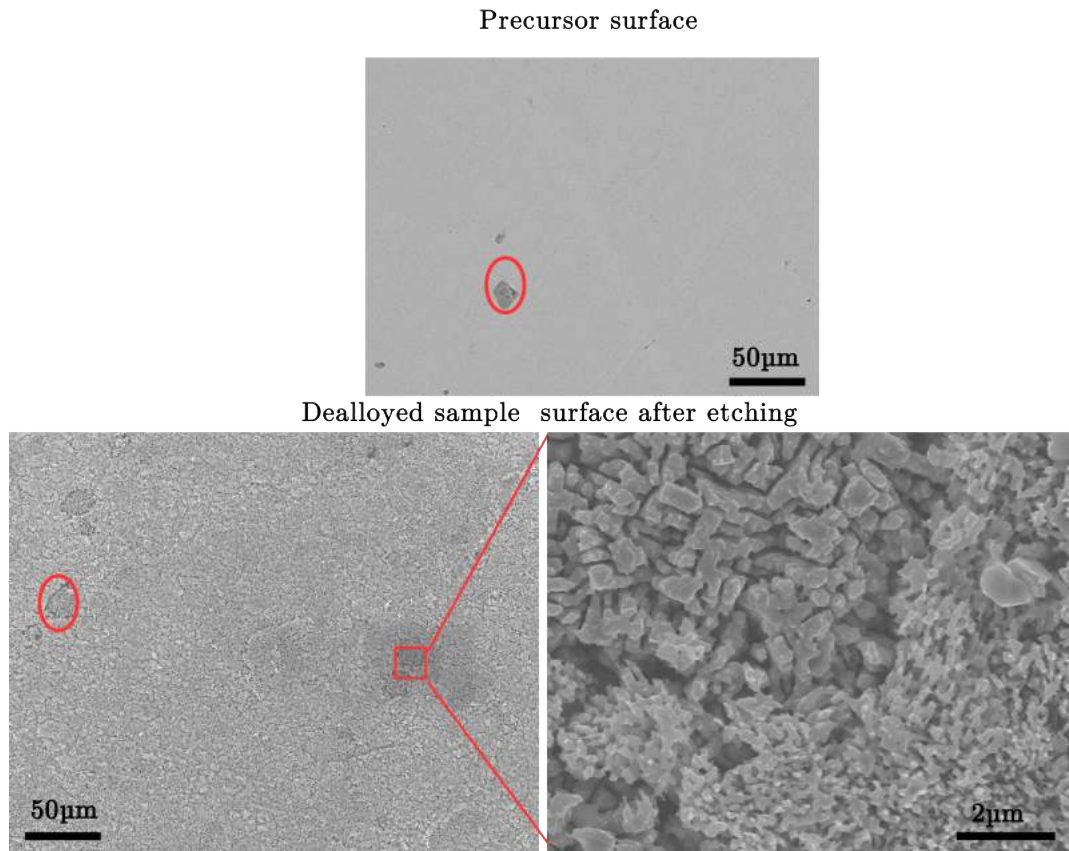


Figure 8.9: SEM micrograph of Incoloy 825 precursor sample after 5 h homogeneization at 760 °C and surface after etching after 1 h dealloying at 760 °C.

	Fe	Cr	Ni	Cu	Mo	Ti	Si	Mg
Precursor Matrix (%at)	≈ 28	≈ 29	≈ 39.4	≈ 2.7	≈ 2	≈ 1.7	≈ 1.2	≈ 0
Precursor Inclusion (%at)	≈ 14	≈ 14	≈ 18	≈ 0	≈ 1	≈ 0.2	≈ 53	≈ 0
Porous large ligaments (%at)	≈ 50	≈ 40	≈ 0.3	≈ 0	≈ 4	≈ 3	≈ 4.9	≈ 1
Porous small ligaments (%at)	≈ 14	≈ 12	≈ 0	≈ 0	≈ 1	≈ 0.2	≈ 70.3	≈ 1

Table 8.6: Composition of matrix and inclusion of Incoloy 825 precursor and areas with large and small ligaments of etched (porous) surface sample after dealloying at 760 °C measured by SEM-EDX.

8.4.1.4 Dealloying at 820 °C

The microstructure obtained after dealloying at 820 °C during 1 h is similar to the one usually obtained by liquid metal dealloying (cf. Chapter 4). The composition after dealloying is found in Table 8.7 and is very similar to the expected one (cf. Table 8.2).

Average ligaments size ($0.7 \pm 0.3 \mu\text{m}$) and pores size ($0.5 \pm 0.2 \mu\text{m}$) seem to be homogeneous but very small compared to samples obtained from homemade precursor (Chapter 4).

	Fe	Cr	Ni	Cu	Mo	Ti	Si	Mg
EDX 820 (%at)	≈ 52	≈ 40	≈ 0.3	≈ 0	≈ 4	≈ 1.7	≈ 0.8	≈ 0.1

Table 8.7: Real composition (EDX) measured by SEM-EDX of etched surface sample after dealloying Incoloy 825 precursor at 820 °C.

8.4.1.5 Dealloying at 880 °C

Fig. 8.10 presents SEM micrograph of sample cross-section after 3 min and 1 h dealloying at 880 °C, and surface after etching and 1 h dealloying. Surface after 1 h dealloying and etching presents a hierarchical structure. After 1 h dealloying, the sample cross-section shows a ≈ 30 μm layer with a fine dealloyed microstructure while the deeper microstructure obtained after 1 h dealloying corresponds to the coarsened microstructure of 3 min dealloying. The composition of the area near to the surface and deeper from the surface was analysed by SEM-EDX (cf. Table 8.8).

	Fe	Cr	Ni	Cu	Mo	Ti	Si	Mg
3 min surface (1) (%at)	≈ 39	≈ 31	≈ 4.7	≈ 0.3	≈ 3	≈ 0.8	≈ 1.5	≈ 20
3 min bulk (2) (%at)	≈ 40	≈ 34	≈ 9.4	≈ 0.2	≈ 3	≈ 1	≈ 1.4	≈ 11.6
1 h surface (3) (%at)	≈ 6	≈ 2	≈ 0.6	≈ 0.2	≈ 3	≈ 1.5	≈ 1.7	≈ 84.6
1 h bulk (4) (%at)	≈ 39	≈ 25	≈ 0.6	≈ 0.2	≈ 3	≈ 0.7	≈ 1.2	≈ 37

Table 8.8: Composition of cross-section near the surface (1, 3) and deeper (2, 4) after dealloying Incoloy 825 for 3 min and 1 h at 880 °C measured by SEM-EDX.

For 3 min dealloying, no remarkable evolution in the microstructure and the composition depending on the position is observed.

After 1 h, the composition of the area located deeper than 30 μm from the surface is the same as for the sample dealloyed for 3 min. However the ligaments near the surface present mostly *Mo*, *Si* and *Ti*. This layer could correspond to a second dealloying layer reaction: the first dealloying would lead to ligaments containing *Ti*, *Si*, *Mo*, *Fe* and *Cr* but if one waits longer at high temperature these ligaments could also start to be dealloyed from the surface (*Fe* and *Cr* would be removed from the initial ligaments), creating this hierarchical structure at the surface. This reaction could happen in this case because of the longer time and the higher temperature [KAT 16]. The average ligaments size is measured for 1 h dealloying, corresponding respectively to 1.8 ± 0.5 μm for deep ligaments and 0.47 ± 0.07 μm for surface ligaments.

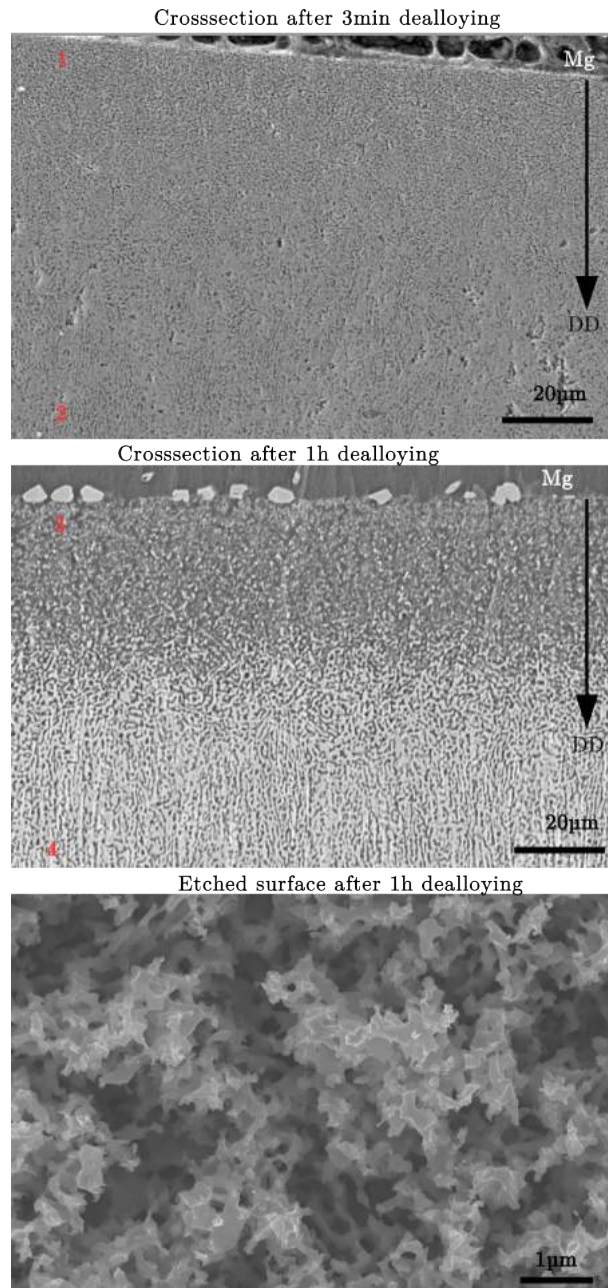


Figure 8.10: SEM micrograph of sample cross-section after 3 min and 1 h dealloying from Incoloy 825 precursor at 880 °C and surface after etching after 1 h dealloying. Figure corresponds to the SEM-EDX analysis position.

8.4.1.6 Foam morphology

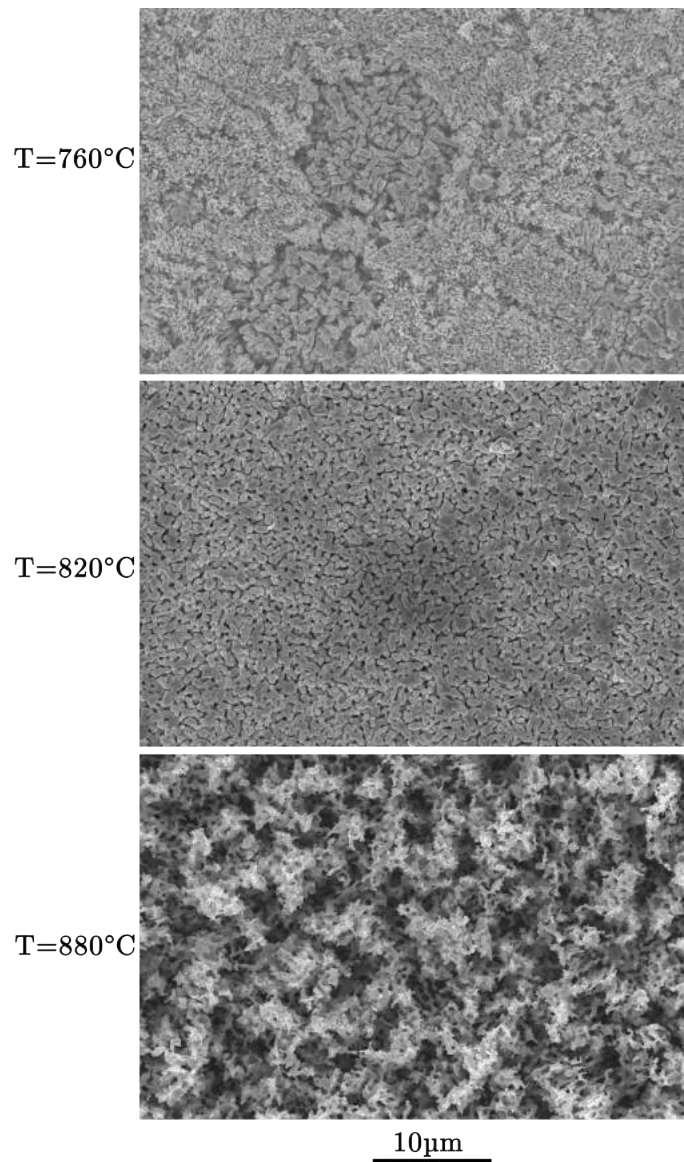


Figure 8.11: SEM micrograph of surface after etching after 1 h dealloying at 3 different temperatures from Incoloy 825 precursor. The microstructure depends on dealloying temperature. It was successively observed large ligaments inclusion into a small ligaments matrix, unimodal pores distribution and a hierarchical structure while increasing the temperature.

Fig. 8.11 presents the resulting microstructure after dealloying for 1 h at $T=760$, 820 and 880 °C. At 760 °C small ligaments (around 110 nm) matrix with inclusions of larger ligaments (about 700 nm) is observed. At 820 °C unimodal ligaments size (about 600 nm) is observed and at 880 °C bimodal ligaments distribution (about 1.8 µm and 500 nm) is observed. The fact that 3 different temperatures lead to 3 different microstructures

differs from previous observations (on more simple $FeCrNi$ or $TiCu$ precursors) where all temperatures led to a unimodal pore distribution [WAD 13, TSU 13].

After dealloying, Incoloy 825 resulting ligaments are very small compared to what could be expected from previous studies of $FeNi$ and $TiNi$ dealloying [WAD 13, TSU 13]. It was previously observed that ligaments should be $\approx 1 \mu m$ for porous Ti (dealloyed 200 s at $700^\circ C$) and $\approx 1.8 \mu m$ for porous Fe (dealloyed 1 h at $660^\circ C$) whereas $0.6 \mu m$ are measured in the present study in case of dealloying for 1 h at $820^\circ C$.

The ligaments size is generally expected to be inversely proportional to the melting point of targeted element [MCC 18a, CHE 13a]. This was verified by comparing ligaments size of pure Fe and pure Cr in [WAD 13]. Therefore, at the dealloying front, the surface diffusion of Mo (melting point about $2600^\circ C$) atoms is slower than Fe and Cr (melting point below $2000^\circ C$). Therefore, slower Mo atoms diffusion can delay the dealloying process. In addition, the kinetics of ligaments growth itself is considered to be a surface relaxation caused by surface-diffusing atoms. Therefore, Mo atoms on the ligament surface can act as “inhibitor” for the ligament growth as it was already observed with the Pt addition in $Au-Ag$ precursor [ERL 11, KOL 11, WIT 12, MCC 16a].

From the smallest ligaments size (around 110 nm mainly on the surface of sample dealloyed at $760^\circ C$) specific surface (S) can be calculated with the law formulated by Detsi et al. (cf. equation 5.2) as shown in Chapter 5 [DET 11]. Assuming that the value of the bulk density is equal to $7800 kg/m^3$ (density of steel) for this material, a specific surface about $4.10^3 m^2/kg$ is estimated, quite similar to what can be measured in nanoporous gold (S about $3.10^3 m^2/kg$ for 65 nm ligament thickness) [DET 11].

8.4.2 Dealloying kinetics

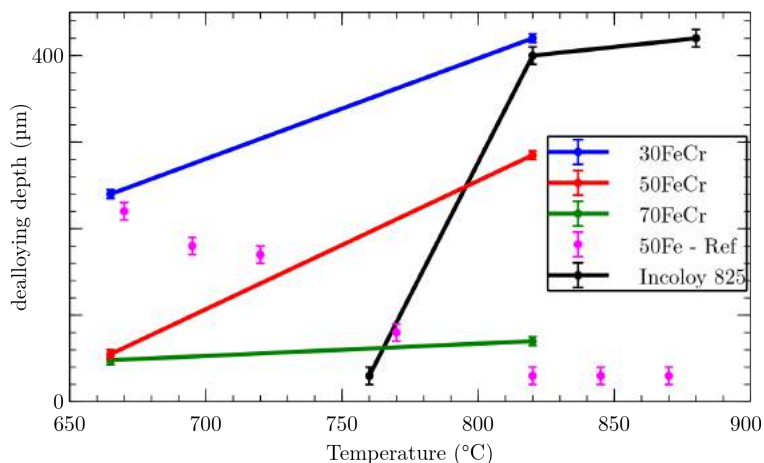


Figure 8.12: Evolution of dealloying depth with dealloying temperature from different homemade precursor and Incoloy 825 precursor.

Fig. 8.12 presents the evolution of dealloying depth with temperature. The data obtained with 50Fe-Ni precursor can be found in [SAI 16] and for 30FeCr, 50FeCr and 70FeCr in Chapter 6. Incoloy 825 (with Ni amount is between the one of 30FeCr-Ni

and 50FeCr-Ni). However dealloying kinetics behaviour differs from other compositions. Alloying elements play a key role for dealloying kinetics.

The fabrication of a porous FeCr sample from Incoloy 825 nickel superalloy was possible. The addition of minor elements has an influence on the foam morphology and dealloying/coarsening kinetics with the creation of complex microstructure depending on the local composition. The fabrication of a hierarchical structure in 1 step dealloying was also possible.

8.5 Conclusion

To create a porous stainless steel, a commercial S310 stainless steel was firstly studied. The amount of sacrificial element was below the parting limit which made full dealloying impossible for sample thicker than 250 μm . However the maximum dealloyed thickness is obtained is only 10 min and is not so sensitive to dealloying time and temperature which is convenient for industrial applications.

Then, to re-mediate to the parting limit, a commercial Incoloy 800 was selected. Fully porous ferritic stainless steel with micrometer scaled ligaments and pores was obtained.

To study the effect of minor alloying element, Incoloy 825 was selected as precursor. It was dealloyed at 3 different temperatures. Because this is a *Ni* alloy, the dealloying process was successful for the bulk sample. Ligaments coarsening is controlled by surface diffusion which can be controlled by dealloying temperature. Results show that a small amount of *Mo* or *Si* in the precursor is a solution to modify surface diffusion and slow down coarsening, which highly decreases ligaments size and drastically increases specific surface ($4.10^3 \text{ m}^2/\text{kg}$). At high temperature a second dealloying process happened at the surface, creating a layer of smaller ligaments size with different compositions.

Using a commercial precursor could be a solution for applying liquid metal dealloying in industry and those results show that the final composition after dealloying is predictable. Finally, it was demonstrated that dealloying commercial alloy opens many perspectives of new and possibly very complex and/or architected microstructures.

Conclusion and Perspectives

Conclusion

This study aims at fabricating and characterizing of FeCr composites made by liquid metal dealloying method from $FeCrNi$, based-alloy precursors.

Elaboration-microstructure relationship

From these precursors, metal/metal composites (dealloying), then porous metals (chemical etching) and finally metal/polymer composites (polymer infiltration) were fabricated. The key parameters of the processes to control microstructure and morphology were studied.

Precursor influence of ratio targeted elements/soluble elements, influence of minor alloying elements, microstructure...

- The possibility of full dealloying or only partial dealloying is driven by the composition of the precursor: full dealloying is possible only when Ni proportion is higher than the parting limit. Foam density and pore size are directly controlled by precursor composition: porosity is almost equal to Ni at% proportion.
- The possibility of creating a bicontinuous structure is driven also by the ratio targeted/soluble element. For the $(FeCr)_xNi_{1-x}$ a bicontinuous structure is present at least for $30 < x < 70$. In case of a bicontinuous structure, the tortuosity will be almost constant around 1 for both phase that should lead to good transport properties.
- The dealloyed grain formation mechanisms, based on diffusion, is dependant of the amount of $FeCr$: for low $FeCr$ amount, nucleation of new grains is the dominant behaviour (displacive transformation) while with high amount of $FeCr$ grain growth will be dominant (diffusive process). In the case of a displacive transformation, precursor grain size will influence the grain size and orientation after dealloying as it can be observed in austenite/ferrite phase transformation.

- The dealloying kinetics is influenced by the proportion of *Ni*: the higher the *Ni* amount, the faster the process. But minor alloying element can change the kinetics (activation energy, solubility, ... are changed), for example *Mo* seems to slow down the process.
- Precursors composition can also impact coarsening. Minor alloying element will change activation energy and diffusion kinetics, which can stabilize the morphology.
- Characteristic length distribution depends on the local composition which can create complex/architected microstructures.
- The addition of smaller *Cr* (20%) amount seems to have a limited impact on microstructure and foam morphology. However it passivates the ligaments surface during chemical etching.

Dealloying parameters (time and temperature of the liquid *Mg* metallic bath), control the kinetics of the dealloying process: the higher the temperature, the faster the process and the coarsening. This obvious result is in fact not so obvious: the dealloying kinetic of *FeNi* system behaves oppositely. For the *FeCrNi* system, and as function of the *Ni* concentration, dealloying and coarsening can be predicted.

As the foam morphology (mathematically speaking) is always the same, the relationship between ligament size and specific surface is independent of the foam density and ligaments size. Therefore the specific surface is directly dependant of the coarsening.

Effect of chemical etching and polymer infiltration steps The effect of the fabricating step after dealloying on the morphology was also studied. The etching is complete, the full second phase is dissolved. The foam morphology is almost not affected by chemical etching, *Cr* plays its role of passivation. However for samples with a low amount of targeted elements, some macroscopic peeling can be observed that make samples manipulation difficult and alter the integrity of macroscopic samples.

Polymer infiltration is the opposite of the etching step: all the porosities are fulfilled with polymer to produce a polymer/metal composite without any void or residual porosity. The different composition tested are fully polymerised.

Microstructure - Mechanical properties relationship

The mechanical properties of all composites were studied by nanoindentation and compression. The Young's modulus of foam samples of this study is only proportional to their density (ratio *FeCr*/air) and therefore independent on the ligament sizes. On the contrary hardness and more generally plastic properties are highly impacted by foam density, morphology and ligaments sizes.

The polymer's choice is important for the mechanical properties. In the worse case polymer filled just help to manipulate the samples (they are less brittle) ; in the best case mechanical properties are slightly improved. The choice of the polymer and the proportion polymer/metal determine the final properties.

The mechanical behaviour of low *FeCr* phase fraction is consistent with other dealloyed materials. The mechanical properties can be easily improved by optimizing density,

ligaments and grain size leading to new class of materials with low Young's modulus and high yield stress.

Elaboration studied by *in situ* experiments

The elaboration process was *in situ* studied by X-ray tomography and X-ray diffraction under synchrotron radiation. It was shown that the amount of *Mg* and precursor shape also impacts dealloying kinetics. XRD measurements show that at the early stage of coarsening, a strain relaxation probably due to the dissolution of remaining *Ni* in the solid phase after ligaments formation was observed. During cooling the interaction of ligaments and *Mg* phase is noticeable. This interaction will create residual strains due to differential thermal dilatation. Etching step shows a volumetric expansion of the foam due in part to strain relaxation created during the cooling step and mostly to the sample preparation for X-ray tomography. This relaxation is higher where the sample presents some defects (for example the shadow of precursor grain boundaries) therefore it is important to preserve sample from defects to avoid foam disruption.

Application of liquid metal dealloying in an industrial context

The application to the dealloying process in an industrial context requires to find low cost and easily obtainable precursors sample, therefore the use of commercial alloys as precursors was studied.

A commercial S310 stainless steel with an amount of soluble element near the parting limit was firstly studied. The low amount of *Ni* in this composition leads to partial dealloying only, *i.e.* a texturation and functionalization of the surface while keeping the full integrity of the macro-structure. The process is done with control of the ligaments size and dealloying depth: the maximum dealloying depth is reached in only 10 min and is not so sensitive to dealloying time and temperature (perfect for an industrial process).

Next, a commercial Incoloy 800 with high amounts of *Fe* and *Cr* and low minor alloying elements amounts was used to produce a fully porous ferritic stainless steel with micrometer scaled ligaments and pores after dealloying.

The studies on theoretical/perfect alloys gave the key parameters to control and predict the dealloying process. The application on complex commercial alloys have shown that despite the presence of many minor elements the thermodynamical approach is still valid, prediction of the final composition are consistent and key parameters are the same. The minor elements have shown to help to stabilize the systems and slow down the transformation, which makes the dealloying even easiest to control and leads to thinner microstructures (coarsening is much slower).

This proves the possibility of applying liquid metal dealloying in an industrial context.

In conclusion liquid metal dealloying and resulting composite materials are very promising materials for many applications like electrochemical and bio-compatible materials.

Perspectives

Elaboration-microstructure relationship

The influence of many parameters of the process on the microstructure was established, but the physical effects at the atomic level at the dealloying front are still not fully understood. Simulations help but *FeCrNi* system, which involves recrystallisation during the dealloying transformation, add a step of complexity. The diffusions and their influence on the transformation have to be studied deeper. The prediction of grains size and orientation has to be improved.

Microstructure - Properties relationship

There is a lot of perspectives about the mechanical properties : *in situ* experiment to follow with a large accuracy the sample strain and directly observe individual ligament behaviour. The effect of ligaments size should be further investigated and the effect of *Cr* addition should be checked. Solutions to control and improve the mechanical properties could be the target of future studies.

The magnetic and thermal properties or corrosion behaviour... were not involved in this study. However metallic foams show interesting thermal properties and steel shows interesting magnetic properties. Thus, new applications for these materials should be expected.

Elaboration studied by *in situ* experiments

Concerning the *in situ* observation of the process, some solutions to control the temperature and the *Mg* amount around the samples have to be found. One way could imply the use of *Mg* powder under inert gas atmosphere to mimic real dealloying conditions.

Application of liquid metal dealloying in an industrial context

The major perspective of this work is the application of dealloying in an industrial context. Using a commercial alloy as precursor was a first step and first results are very promising to create cheap and complex architectures. Other commercial alloys should be studied as precursor samples and the effect of dealloying parameters, precursor composition on final microstructure should be studied in a deeper way. To complete the industrialisation of the process a solution to replace *Mg* by more stable element at high temperature to perform experiment under air atmosphere should be considered.

References

- [ABE 17] ABEDI H., HANZAKI A. Z., LIU Z., XIN R., HAGHDADI N., HODGSON P.
Continuous dynamic recrystallization in low density steel. *Materials and Design*, vol. 114, 2017, p. 55-64.
- [ART 09] ARTYMOWICZ D. M., ERLEBACHER J., NEWMAN R. C.
Relationship between the parting limit for de-alloying and a particular geometric high-density site percolation threshold. *Philosophical Magazine*, vol. 89, n° 21, 2009, p. 1663-1693.
- [ASH 06] ASHBY M. F.
The properties of foams and lattices. *Philosophical Transactions of Royal Society. A*, vol. 364, 2006, p. 15-30.
- [BAD 17] BADWE N., CHEN X., SIERADZKI K.
Mechanical properties of nanoporous gold in tension. *Acta Materialia*, vol. 129, 2017, p. 251-258.
- [BAN 01] BANHART J.
Manufacture, characterisation and application of cellular metals and metal foams. *Progress in Materials Science*, vol. 46, n° 6, 2001, p. 559-632.
- [BAR 15] BARBIER D., GERMAIN L., HAZOTTE A., GOUNÉ M., CHBIHI A.
Microstructures resulting from the interaction between ferrite recrystallization and austenite formation in dual-phase steels. *Journal of Materials Science*, vol. 50, n° 1, 2015, p. 374-381.
- [BAR 16a] BARGMANN S., SOYARSLAN C., HUSSER E., KONCHAKOVA N.
Materials based design of structures: Computational modeling of the mechanical behavior of gold-polymer nanocomposites. *Mechanics of Materials*, vol. 94, 2016, p. 53-65.
- [BAR 16b] BARSUK D., ZADICK A., CHATENET M., GEORGARAKIS K., PANAGIOTOPOULOS N. T., CHAMPION Y., JORGE A. M.
Nanoporous silver for electrocatalysis application in alkaline fuel cells. *Materials and Design*, vol. 111, 2016, p. 528-536.
- [BAR 17] BARSUK D., JORGE A. M., LAURENT-BROCQ M., CHAMPION Y.
Structure and approach of the mechanical strength and deformation of nanoporous silver prepared by de-alloying. *JA SF2M*, , 2017.
- [BAU 10] BAUDIN T.
Analyse EBSD - principe et cartographies d'orientations. *Techniques de l'Ingénieur*, vol. M4138, 2010, p. 1-17.

- [BEA 72] BEAR J.
Dynamics of fluids in porous media. 1972.
- [BEE 01] BEELEY P.
Foundry technology. Butterworth-Heinemann, 2001.
- [BIE 05] BIENER J., HODGE A. M., HAMZA A. V., HSIUNG L. M., JR. J. H. S.
Nanoporous Au: A high yield strength material. *Journal of Applied Physics*, vol. 97, n° 2, 2005, Page 024301.
- [BIR 06] BIRD R. B., STEWART W. E., LIGHTFOOT E. N.
Transport phenomena, revised 2nd edition. Wiley, 2006.
- [BOK 05] BOKSTEIN B. S., MENDELEV M. I., SROLOVITZ D. J.
Thermodynamics and kinetics in materials science. Oxford University press, 2005.
- [BOR 01] BORNERT M., BRETHEAU T., GILORMINI P.
Homogénéisation en mécanique des matériaux, Tome 1 : Matériaux aléatoires élastiques et milieux périodiques. Hermes science, 2001.
- [BRI 14] BRIOT N. J., KENNERKNECHT T., EBERL C., BALK T. J.
Mechanical properties of bulk single crystalline nanoporous gold investigated by millimetre-scale tension and compression testing. *Philosophical Magazine*, vol. 94, n° 8, 2014, p. 847-866.
- [BRU 35] BRUGGEMAN D.
Berechnung verschiedener physikalischer Konstanten von heterogenen Substanzen. *Annals of Physics*, vol. 24, 1935, Page 636.
- [CAC 10] CACCIAMANI G., DINSDALE A., PALUMBO M., PASTUREL A.
The Fe-Ni system: Thermodynamic modelling assisted by atomistic calculations. *Intermetallics*, vol. 18(6), 2010, p. 1148-1162.
- [CHA 05] CHAMPION Y., FECHT H., Eds. *Nanoarchitected and nanostructured materials: Fabrication, control and properties*. Wiley VCH, 2005.
- [CHB 14] CHBIHI A., BARBIER D., GERMAIN L., HAZOTTE A., GOUNÉ M.
Interactions between ferrite recrystallization and austenite formation in high-strength steels. *Journal of Materials Science*, vol. 49, n° 10, 2014, p. 3608-3621.
- [CHE 93] CHEN S., SANZ F., OGLETREE D., HALLMARK V., DEVINE T., SALMERON M.
Selective dissolution of copper from Au-rich Cu-Au alloys: an electro chemical STM study. *Surface Science*, vol. 292, n° 3, 1993, p. 289-297.
- [CHE 08] CHEN P., TSAI Y., LAN C.
Phase field modeling of growth competition of silicon grains. *Acta Materialia*, vol. 56, n° 15, 2008, p. 4114-4122.
- [CHE 09] CHEN L., YU J., FUJITA T., CHEN M.
Nanoporous copper with tunable nanoporosity for SERS applications. *Advanced Functional Materials*, vol. 19, 2009, Page 1221-1226.
- [CHE 10] CHEN Y.-C. K., CHU Y. S., YI J., McNULTY I., SHEN Q., VOORHEES P. W., DUNAND D. C.
Morphological and topological analysis of coarsened nanoporous gold by X-ray nanotomography. *Applied Physics Letters*, vol. 96, n° 4, 2010, Page 043122.

- [CHE 12a] CHEN-WIEGART Y.-C. K., WANG S., CHU Y. S., LIU W., McNULTY I., VOORHEES P. W., DUNAND D. C.
Structural evolution of nanoporous gold during thermal coarsening. *Acta Materialia*, vol. 60, n° 12, 2012, p. 4972-4981.
- [CHE 12b] CHENG I. C., HODGE A. M.
Morphology, oxidation, and mechanical behavior of nanoporous Cu foams. *Advanced Engineering Materials*, vol. 14, n° 4, 2012, p. 219-226.
- [CHE 13a] CHEN Q., SIERADZKI K.
Spontaneous evolution of bicontinuous nanostructures in dealloyed Li-based systems. *Nature Materials*, vol. 12(12), 2013, p. 1102-1106.
- [CHE 13b] CHEN-WIEGART Y.-C. K., TAKESHI W., BUTAKOV N., XIAO X., DE CARLO F., KATO H., WANG J., DUNAND D. C., MAIRE E.
3D morphological evolution of porous titanium by X-ray micro- and nano-tomography. *Journal of Materials Research*, vol. 28, n° 17, 2013, Page 2444–2452.
- [CHE 13c] CHEN-WIEGART Y.-C. K., WANG S., LEE W.-K., McNULTY I., VOORHEES P. W., DUNAND D. C.
In situ imaging of dealloying during nanoporous gold formation by transmission X-ray microscopy. *Acta Materialia*, vol. 61, n° 4, 2013, p. 1118-1125.
- [CHE 13d] CHEN-WIEGART Y.-C. K., WANG S., McNULTY I., DUNAND D. C.
Effect of Ag–Au composition and acid concentration on dealloying front velocity and cracking during nanoporous gold formation. *Acta Materialia*, vol. 61, n° 15, 2013, p. 5561-5570.
- [CHE 13e] CHENG J., BORDES R., OLSSON E., HOLMBERG K.
One-pot synthesis of porous gold nanoparticles by preparation of Ag/Au nanoparticles followed by dealloying. *Colloids and Surfaces A: Physicochemical and Engineering Aspects*, vol. 436, 2013, p. 823-829.
- [CHE 16] CHEN F., CHEN X., ZOU L., YAO Y., LIN Y., SHEN Q., LAVERNIA E. J.
Fabrication and mechanical behavior of bulk nanoporous Cu via chemical de-alloying of CuAl alloys, Chemical de-alloying, Compressive strength. *Materials Science and Engineering A*, vol. 660, 2016, p. 152-159.
- [CHE 17] CHEN-WIEGART Y.-C. K., HARDER R., DUNAND D. C., McNULTY I.
Evolution of dealloying induced strain in nanoporous gold crystals. *Nanoscale*, vol. 9, 2017, p. 5686-5693.
- [DEH 09] DEHMOLAEI R., SHAMANIAN M., KERMANPUR A.
Microstructural changes and mechanical properties of Incoloy 800 after 15 years service. *Materials Characterization*, vol. 60, n° 3, 2009, p. 246-250.
- [DET 11] DETSI E., JONG E. D., ZINCHENKO A., VUKOVIĆ Z., VUKOVIĆ I., PUNZHIN S., LOOS K., TEN BRINKE G., RAEDT H. D., ONCK P., DE HOSSON J.
On the specific surface area of nanoporous materials. *Acta Materialia*, vol. 59, n° 20, 2011, p. 7488-7497.
- [DET 13] DETSI E., ONCK P., DE HOSSON J. T. M.
Metallic muscles at work: high rate actuation in nanoporous gold/polyaniline composites. *ACS Nano*, vol. 7(5), 2013, p. 4299-4306.

- [DON 93] DONA J. M., GONZALEZ-VELASCO J.
Mechanism of surface diffusion of gold adatoms in contact with an electrolytic solution. *The Journal of Physical Chemistry*, vol. 97, n° 18, 1993, p. 4714-4719.
- [DOR 72] DOROEOLSKII T., KARALNUK S., KOVAL A.
Solid solutions in the V-Ti, V-Fe, Fe-Cr and Fe-Ni systems. *Metallofizika*, vol. 41, 1972, p. 73-77.
- [DOU 09] DOU R., DERBY B.
A universal scaling law for the strength of metal micropillars and nanowires. *Scripta Materialia*, vol. 61, n° 5, 2009, p. 524-527.
- [DUB 99] DUBOIS S., MICHEL A., EYMERY J. P., DUVAIL J. L., PIRAUX L.
Fabrication and properties of arrays of superconducting nanowires. *Journal of Materials Research*, vol. 14, n° 3, 1999, p. 665-71.
- [DUB 11] DUBIEL S. M., CIESLAK J.
Sigma-phase in Fe-Cr and Fe-V alloy systems and its physical properties. *Critical Reviews in Solid State and Materials Sciences*, vol. 36, 2011, p. 191-208.
- [DUC 98] DUCHET J., LEGRAS R., DEMOUSTIER-CHAMPAGNE S.
Chemical synthesis of polypyrrole: structure-properties relationship. *Synthetic Metals*, vol. 98, n° 2, 1998, p. 113-122.
- [DUN 49] DUNN C., LIONETTI F.
The effect of orientation difference on grain boundary energies. *Journal of The Minerals, Metals and Materials Society*, vol. 1(2), 1949, p. 125-132.
- [DUŠ 77] DUŠEK K., BLEHA M., LUŇÁK S.
Curing of epoxide resins: Model reactions of curing with amines. *Journal of Polymer Science: Polymer Chemistry Edition*, vol. 15, n° 10, 1977, p. 2393-2400.
- [DUV 02] DUVAIL J., RÉTHO P., GARREAU S., LOUARN G., GODON C., DEMOUSTIER-CHAMPAGNE S.
Transport and vibrational properties of poly(3,4-ethylenedioxythiophene) nanofibers. *Synthetic Metals*, vol. 131, n° 1, 2002, p. 123-128.
- [DYS 70] DYSON D., HOLMES B.
Effect of alloying additions on the lattice parameter of austenite. *Journal of Iron Steel Institution*, vol. 208, 1970, p. 469-474.
- [ERL 01] ERLEBACHER J., AZIZ M., KARMA A., DIMITROV N., SIERADZKI K.
Evolution of nanoporosity in dealloying. *Nature*, vol. 410, 2001, p. 450-451.
- [ERL 03] ERLEBACHER J., SIERADZKI K.
Pattern formation during dealloying. *Scripta Materialia*, vol. 49, n° 10, 2003, p. 991-996.
- [ERL 04] ERLEBACHER J.
An atomistic description of dealloying. *Journal of Electrochemical Society*, vol. 151(10), 2004, p. C614-628.
- [ERL 09] ERLEBACHER J., SESHADRI R.
Hard materials with tunable porosity. *MRS Bulletin*, vol. 34, n° 8, 2009, Page 561-568.

- [ERL 11] ERLEBACHER J.
Mechanism of coarsening and bubble formation in high-genus nanoporous metals. *Physical Review Letters*, vol. 106, 2011, p. 225504-225507.
- [ERL 12] ERLEBACHER J., MCCUE I.
Geometric characterization of nanoporous metals. *Acta Materialia*, vol. 60, n° 17, 2012, p. 6164-6174.
- [ERN 17] ERNAULT E., RICHAUD E., FAYOLLE B.
Thermal-oxidation of epoxy/amine followed by glass transition temperature changes. *Polymer Degradation and Stability*, vol. 138, 2017, p. 82-90.
- [FAR 13] FARKAS D., CARO A., BRINGA E., CROWSON D.
Mechanical response of nanoporous gold. *Acta Materialia*, vol. 61, n° 9, 2013, p. 3249-3256.
- [FIC 55] FICK A.
Über diffusion. *Annalen der Physik und Chemie*, vol. 94, 1855, p. 59-86.
- [FIF 12] FIFE J. L., RAPPAZ M., PISTONE M., CELCER T., MIKULJAN G., STAMPANONI M.
Development of a laser-based heating system for in situ synchrotron-based X-ray tomographic microscopy. *Journal of Synchrotron Radiation*, vol. 19(3), 2012, p. 352-358.
- [FOR 79] FORTY A. J.
Corrosion micromorphology of noble metal alloys and depletion gilding. *Nature*, vol. 282, 1979, p. 597-598.
- [FUK 14] FUKUZUMI Y., WADA T., KATO H.
Surface improvement for biocompatibility of Ti-6Al-4V by dealloying in metallic melt, Chapter 8, p. 93-101. K. Sasaki, O. Suzuki and N. Takahashi, 2014.
- [GES 15] GESLIN P.-A., MCCUE I., GASKEY B., ERLEBACHER J., KARMA A.
Topology-generating interfacial pattern formation during liquid metal dealloying. *Nature communication*, vol. 8887(6), 2015, p. 1-8.
- [GIA 11] GIANOLA D. S., SEDLMAYR A., MÖNIG R., VOLKERT C. A., MAJOR R. C., CYRANKOWSKI E., ASIF S. A. S., WARREN O. L., KRAFT O.
In situ nanomechanical testing in focused ion beam and scanning electron microscopes. *Review of Scientific Instruments*, vol. 82, n° 6, 2011, Page 063901.
- [GIB 97] GIBSON L. J., ASHBY M. F.
Cellular solids: Structure and properties. Cambridge Solid State Science Series Cambridge University Press, 2 édition, 1997.
- [GOU 04] GOUSSERY V., BIENVENU Y., FOREST S., GOURGUES A.-F., COLIN C., BARTOUT J.-D.
Grain size effects on the mechanical behavior of open-cell nickel foams. *Advanced Engineering Materials*, vol. 6, n° 6, 2004, p. 432-439.
- [GRE 10] GRENET J., LEGENDRE B.
Analyse calorimétrique différentielle à balayage (DSC). *Techniques de l'Ingénieur*, vol. P1205, 2010, p. 1-32.

- [GRI 17] GRIFFITHS E., BARGMANN S., REDDY B.
Elastic behaviour at the nanoscale of innovative composites of nanoporous gold and polymer. *Extreme Mechanics Letters*, vol. 17, 2017, p. 16-23.
- [GUI 09] GUILLORY J. K.
Book review of CRC handbook of chemistry and physics. 90th Edition. *Journal of Medicinal Chemistry*, vol. 52, n° 17, 2009, p. 5560-5560.
- [GWA 16] GWAK E.-J., KIM J.-Y.
Weakened flexural strength of nanocrystalline nanoporous gold by grain refinement. *Nano Letters*, vol. 16, n° 4, 2016, p. 2497-2502.
- [HAK 07] HAKAMADA M., MABUCHI M.
Mechanical strength of nanoporous gold fabricated by dealloying. *Scripta Materialia*, vol. 56, n° 11, 2007, p. 1003-1006.
- [HAK 09a] HAKAMADA M., MABUCHI M.
Fabrication of nanoporous palladium by dealloying and its thermal coarsening. *Journal of Alloys and Compounds*, vol. 479, n° 1, 2009, p. 326-329.
- [HAK 09b] HAKAMADA M., MABUCHI M.
Preparation of nanoporous Ni and Ni-Cu by dealloying of rolled Ni-Mn and Ni-Cu-Mn alloys. *Journal of Alloys and Compounds*, vol. 485, n° 1, 2009, p. 583-587.
- [HAK 11] HAKAMADA M., TAKAHASHI M., YAMAMOTO T., MOTOMURA J., MABUCHI M.
Less noble nanoporous metals fabricated by dealloying. *Abstract Book of the seventh International Conference on Porous Metal and Metallic Foam*, , 2011, Page 169.
- [HAR 59] HARRISON J., WAGNER C.
The attack of solid alloys by liquid metals and salt melts. *Acta Metallurgica*, vol. 7, n° 11, 1959, p. 722-735.
- [HAS 63] HASHIN Z., SHTRIKMAN S.
A variational approach to the theory of the elastic behaviour of multiphase materials. *Journal of the Mechanics and Physics of Solids*, vol. 11, n° 2, 1963, p. 127-140.
- [HAY 90] HAYES F. H., HETHERINGTON M. G., LONGBOTTOM R. D.
Thermodynamics of stainless steels. *Materials Sciences and Technologies*, vol. 6, 1990, p. 263-272.
- [HEL 11] HELL J.-C., DEHMAS M., ALLAIN S., PRADO J. M., HAZOTTE A., CHATEAU J.-P.
Microstructure and Properties Relationships in Carbide-free Bainitic Steels. *ISIJ International*, vol. 51, n° 10, 2011, p. 1724-1732.
- [HER 50] HERRING C.
Effect of change of scale on sintering phenomena. *Journal of Applied Physics*, vol. 21, n° 4, 1950, p. 301-303.
- [HIL 96] HILDEBRAND T., RUESGSEGGER P.
A new method for the model-independent assessment of thickness in three-dimensional images. *Journal of Microscopy*, vol. 185, 1996, p. 67-75.

- [HOD 07] HODGE A., BIENER J., HAYES J., BYTHROW P., VOLKERT C., HAMZA A.
Scaling equation for yield strength of nanoporous open-cell foams. *Acta Materialia*, vol. 55, n° 4, 2007, p. 1343-1349.
- [HOD 09] HODGE A., DOUCETTE R., BIENER M., BIENER J., CERVANTES O., HAMZA A.
Ag effects on the elastic modulus values of nanoporous Au foams. *Journal of Materials Research*, vol. 24, n° 4, 2009, p. 1600-1606.
- [HOR 49] HORMAY A. L.
Getting better records of vegetation changes with line interception method. *Journal of Range Management*, vol. 2, 1949, p. 67-69.
- [HSI 12] HSIEH C.-C., WU W.
Overview of intermetallic Sigma (σ) phase precipitation in stainless steels. *Metallurgy*, vol. 732471, 2012, p. 1-16.
- [HU 16] HU K., ZIEHMER M., WANG K., LILLEODDEN E. T.
Nanoporous gold: 3D structural analyses of representative volumes and their implications on scaling relations of mechanical behaviour. *Philosophical Magazine*, vol. 96, n° 32-34, 2016, p. 3322-3335.
- [HUB 14] HUBER N., VISWANATH R., MAMEKA N., MARKMANN J., WEISSMÜLLER J.
Scaling laws of nanoporous metals under uniaxial compression. *Acta Materialia*, vol. 67, 2014, p. 252-265.
- [JAC 18] JACOB A., POVODEN-KARADENIZ E., KOZESCHNIK E.
Revised thermodynamic description of the Fe-Cr system based on an improved sublattice model of the σ phase. *Calphad*, vol. 60, 2018, p. 16-28.
- [JIN 09] JIN H.-J., KURMANAEVA L., SCHMAUCH J., ROSNER H., IVANISENKO Y., WEISSMULLER J.
Deforming nanoporous metal: Role of lattice coherency. *Acta Materialia*, vol. 57, n° 9, 2009, p. 2665-2672.
- [JIN 17] JIN Y., LI R., ZUO L., ZHANG T.
Correlation between dealloying conditions and coarsening behaviors of nanoporous silver produced by chemical dealloying of Ca-Ag metallic glass. *Journal of Alloys and Compounds*, vol. 695, 2017, p. 1600-1609.
- [KAN 17] KANGAZIAN J., SHAMANIAN M., ASHRAFI A.
Dissimilar welding between SAF 2507 stainless steel and Incoloy 825 Ni-based alloy: The role of microstructure on corrosion behavior of the weld metals. *Journal of Manufacturing Processes*, vol. 29, 2017, p. 376-388.
- [KAT 16] KATO H., WADA T., MARYAM S.
Dealloying toxic Ni from SUS316L surface, Chapter 3, p. 35-46. K. Sasaki, O. Suzuki and N. Takahashi, 2016.
- [KAY] KAYE, LABY N. P. L. Tables of physical and chemical constants, www.kayelaby.npl.co.uk.
- [KER 10] KERTIS F., SNYDER J., GOVADA L., KHURSHID S., CHAYEN N., ERLEBACHER J.

- Structure/processing relationships in the fabrication of nanoporous gold. *JOM*, vol. 62, n° 6, 2010, p. 50-56.
- [KIE 13a] KIEFFER J., KARKOULIS D.
PyFAI, a versatile library for azimuthal regrouping. *Journal of Physics: Conference Series*, vol. 425, 2013, p. 202012-202017.
- [KIE 13b] KIEFFER J., WRIGHT J.
PyFAI: A Python library for high performance azimuthal integration on GPU. *Powder Diffraction*, vol. 28(S2), 2013, p. S339-S350.
- [KIM 14] KIM J. W., WADA T., KIM S. G., KATO H.
Sub-micron porous niobium solid electrolytic capacitor prepared by dealloying in a metallic melt. *Materials Letters*, vol. 116, 2014, p. 223-226.
- [KIM 15] KIM J. W., TSUDA M., WADA T., YUBUTA K., KIM S. G., KATO H.
Optimizing niobium dealloying with metallic melt to fabricate porous structure for electrolytic capacitors. *Acta Materialia*, vol. 84, 2015, p. 497-505.
- [KIM 16] KIM J. W., WADA T., KIM S. G., KATO H.
Enlarging the surface area of an electrolytic capacitor of porous niobium by MgCe eutectic liquid dealloying. *Scripta Materialia*, vol. 122, 2016, p. 68-71.
- [KNO 12] KNORR D., YU J., RICHARDSON A., HINDENLANG M., MCANINCH I., SCALA J. L., LENHART J.
Glass transition dependence of ultrahigh strain rate response in amine cured epoxy resins. *Polymer*, vol. 53, n° 25, 2012, p. 5917-5923.
- [KOL 11] KOLLURI K., DEMKOWICZ M. J.
Coarsening by network restructuring in model nanoporous gold. *Acta Materialia*, vol. 59, n° 20, 2011, p. 7645-7653.
- [KON 15] KONG Q., LIAN L., LIU Y., ZHANG J., WANG L., FENG W.
Bulk hierarchical nanoporous palladium prepared by dealloying PdAl alloys and its electrochemical properties. *Microporous and Mesoporous Materials*, vol. 208, 2015, p. 152-159.
- [KRA 99] KRATZ M.
Fours à arc. *Techniques de l'Ingénieur*, vol. D5920., 1999, p. 1-22.
- [KRE 17] KREKELER T., STRASSER A. V., GRAF M., WANG K., HARTIG C., RITTER M., WEISSMULLER J.
Silver-rich clusters in nanoporous gold. *Materials Research Letters*, vol. 5, n° 5, 2017, p. 314-321.
- [KRI 03] KRISZT B., MARTIN U., MOSLER U., MAIRE E., DEGISCHER H. P., KOTTAR A.
Characterization of Cellular Metals, Chapter 4, p. 127-178. Wiley-Blackwell, 2003.
- [KUR 98] KURTZ W., FISHER K.
Fundamentals of solidification. Trans Tech Publications, Switzerland, 1998.
- [LAK 15] LAKSHMANAN C., VISWANATH R., POLAKI S., RAJARAMAN R., DASH S., TYAGI A.
Surface area of nanoporous gold: Effect on temperature. *Electrochimica Acta*, vol. 182, 2015, p. 565-572.

-
- [LAN 11] LANG X., HIRATA A., FUJITA T., CHEN M.
Nanoporous metal/oxide hybrid electrodes for electrochemical supercapacitors. *Nature Nanotechnology*, vol. 6, 2011, p. 232-236.
- [LAU] LAURENT-BROCQ M., BEJANIN E., CHAMPION Y.
Influence of roughness and tilt on nanoindentation measurements: A quantitative model. *Scanning*, vol. 37, n° 5, p. 350-360.
- [LEC 71] LECHTMAN H. N.
Ancient methods of gilding silver : examples from the old and the new worlds. *Science and Archeology*, , 1971, p. 2-30.
- [LEE 07] LEE D., WEI X., CHEN X., ZHAO M., JUN S., HONE J., HERBERT E. G., OLIVER W. C., KYSAR J. W.
Microfabrication and mechanical properties of nanoporous gold at the nanoscale. *Scripta Materialia*, vol. 56, n° 5, 2007, p. 437-440.
- [LEG 16] LEGLAND D., ARGANDA-CARRERAS I., ANDREY P.
MorphoLibJ: Integrated library and plugins for mathematical morphology with ImageJ. *Bioinformatics*, vol. 32, 2016, p. 3532-3534.
- [LEP 02] LE PLUART L.
Nanocomposites epoxyde/amine/montmorillonite : Rôle des interactions sur la formation, la morphologie aux différents niveaux d'échelle et les propriétés mécaniques des réseaux. Thèse de doctorat, INSA Lyon, 2002.
- [LI 16] LI R., LIU X., WANG H., ZHOU D., WU Y., LU Z.
Formation mechanism and characterization of nanoporous silver with tunable porosity and promising capacitive performance by chemical dealloying of glassy precursor. *Acta Materialia*, vol. 105, 2016, p. 367-377.
- [LI 17] LI J., LIU W., REN Y., SHEN M., YANG K.
Preparation of micro porous stainless steel by physical vacuum dealloying. *Acta Metallurgica Sinica*, vol. 53, n° 5, 2017, p. 524-530.
- [LIL 18] LILLEODDEN E. T., VOORHEES P. W.
On the topological, morphological, and microstructural characterization of nanoporous metals. *MRS Bulletin*, vol. 43, n° 1, 2018, p. 20-26.
- [LIU 06] LIU Y., SOMMER F., MITTEMEIJER E.
The austenite-ferrite transformation of ultralow-carbon Fe-C alloy; transition from diffusion to interface controlled growth. *Acta Materialia*, vol. 54, n° 12, 2006, p. 3383-3393.
- [LIU 08] LIU L., LEE W., HUANG Z., SCHOLZ R., GÖSELE U.
Fabrication and characterization of a flow-through nanoporous gold nanowire/AAO composite membrane. *Nanotechnology*, vol. 19, n° 33, 2008, Page 335604.
- [LIU 12] LIU W., ZHANG S., LI N., ZHENG J., AN S., XING Y.
A general dealloying strategy to nanoporous intermetallics, nanoporous metals with bimodal, and unimodal pore size distributions. *Corrosion Science*, vol. 58, 2012, p. 133-138.
- [LIU 16] LIU L.-Z., YE X.-L., JIN H.-J.
Interpreting anomalous low-strength and low-stiffness of nanoporous gold: Quantification of network connectivity. *Acta Materialia*, vol. 118, 2016, p. 77-87.

- [LON] LONGAIR M. Find connected regions, <https://www.longair.net/edinburgh/imagej/find-connected-regions/>.
- [LON 11] LONG Y.-Z., LI M.-M., GU C., WAN M., DUVAIL J.-L., LIU Z., FAN Z.
Recent advances in synthesis, physical properties and applications of conducting polymer nanotubes and nanofibers. *Progress in Polymer Science*, vol. 36, n° 10, 2011, p. 1415-1442.
- [LU 07] LU X., BALK T., SPOLENAK R., ARZT E.
Dealloying of Au-Ag thin films with a composition gradient: Influence on morphology of nanoporous Au. *Thin Solid Films*, vol. 515, n° 18, 2007, p. 7122-7126.
- [LU 18] LU Z., LI C., HAN J., ZHANG F., LIU P., WANG H., WANG Z., CHENG C., CHEN L., HIRATA A., FUJITA T., ERLEBACHER J., CHEN M.
Three-dimensional bicontinuous nanoporous materials by vapor phase dealloying. *Nature Communications*, vol. 9(276), 2018, p. 1-9.
- [LUO 13] LUO X., LI R., HUANG L., ZHANG T.
Nucleation and growth of nanoporous copper ligaments during electrochemical dealloying of Mg-based metallic glasses. *Corrosion Science*, vol. 67, 2013, p. 100-108.
- [MAC 07] MACIEJAK O., AUBERT P.
Mesure de dureté par nano-indentation. *Techniques de l'Ingénieur*, vol. NM7200, 2007, p. 1-15.
- [MAH 18] MAHR C., MÜLLER-CASPARY K., GRAF M., LACKMANN A., GRIEB T., SCHOWALTER M., KRAUSE F. F., MEHRTENS T., WITTSTOCK A., WEISSMÜLLER J., ROSENAUER A.
Measurement of local crystal lattice strain variations in dealloyed nanoporous gold. *Materials Research Letters*, vol. 6, n° 1, 2018, p. 84-92.
- [MAI 12] MAIRE E.
X-ray tomography applied to the characterization of highly porous materials. *Annual Review of Materials Research*, vol. 42, 2012, p. 163-178.
- [MAI 14] MAIRE E., WITHERS P. J.
Quantitative X-ray tomography. *International Materials Reviews*, vol. 59, n° 1, 2014, p. 1-43.
- [MAM 16] MAMEKA N., WANG K., MARKMANN J., LILLEODDEN E. T., WEISSMULLER J.
Nanoporous gold-testing macro-scale samples to probe small-scale mechanical behavior. *Materials Research Letters*, vol. 4, n° 1, 2016, p. 27-36.
- [MAN 16] MANGIPUDI K., RADISCH V., HOLZER L., VOLKERT C.
A FIB-nanotomography method for accurate 3D reconstruction of open nanoporous structures. *Ultramicroscopy*, vol. 163, 2016, p. 38-47.
- [MAN 17] MANGIPUDI K., EPLER E., VOLKERT C.
Morphological similarity and structure-dependent scaling laws of nanoporous gold from different synthesis methods. *Acta Materialia*, vol. 140, 2017, p. 337-343.
- [MAR 39] MARSH J.
Limits of new phase in the Fe-Cr-Ni system. *Metal Progress*, vol. 35, 1939, p. 269-272.

- [MAS 90] MASSALSKI T., OKAMOTO H., SUBRAMANIAN P., KACPRZAK L.
Mg-Ni phase diagram. *Binary Phase alloy diagrams*, vol. ASM international,(3) 2nd edition, 1990, Page 2530.
- [MCC 16a] McCUE I., BENN E., GASKEY B., ERLEBACHER J.
Dealloying and dealloyed materials. *Annual Review of Materials Research*, vol. 46, n° 1, 2016, p. 263-286.
- [MCC 16b] McCUE I., GASKEY B., CRAWFORD B., ERLEBACHER J.
Local heterogeneity in the mechanical properties of bicontinuous composites made by liquid metal dealloying. *Applied Physics Letters*, vol. 109, n° 23, 2016, Page 231901.
- [MCC 16c] McCUE I., GASKEY B., GESLIN P.-A., KARMA A., ERLEBACHER J.
Kinetics and morphological evolution of liquid metal dealloying. *Acta Materialia*, vol. 115, 2016, p. 10-23.
- [MCC 16d] McCUE I., RYAN S., HEMKER K., XU X., LI N., CHEN M., ERLEBACHER J.
Size effects in the mechanical properties of bulk bicontinuous Ta/Cu nanocomposites made by liquid metal dealloying. *Advanced Engineering Materials*, vol. 18, n° 1, 2016, p. 46-50.
- [MCC 18a] McCUE I., KARMA A., ERLEBACHER J.
Pattern formation during electrochemical and liquid metal dealloying. *MRS Bulletin*, vol. 43, n° 1, 2018, p. 27-34, Cambridge University Press.
- [MCC 18b] McCUE I., STUCKNER J., MURAYAMA M., DEMKOWICZ M. J.
Gaining new insights into nanoporous gold by mining and analysis of published images. *Scientific Report*, vol. 8, n° 6761, 2018, p. 1-11.
- [MEH 07] MEHRER H.
Diffusion in solids, fundamentals, methods, materials, diffusion-controlled processes. Springer, 2007.
- [MET] METAL S.Incoloy Alloy 800, <http://www.specialmetals.com/assets/smc/documents/alloys/incoloy/incoloy-alloy-800.pdf>.
- [MIC 03] MICHELSEN K., RAEDT H. D., HOSSON J. D.
Aspects of mathematical morphology. vol. 125 de *Advances in Imaging and Electron Physics*, p. 119 - 194 2003.
- [MIE 08a] MIETTINEN J.
Thermodynamic Description of Cu-Mg-Ni and Cu-Mg-Zn Systems. *Calphad*, vol. 32, 2008, p. 389-398.
- [MIE 08b] MIETTINEN J.
Thermodynamic description of CuNi and CuZn systems. *Calphad*, vol. 32, n° 2, 2008, p. 514-519.
- [MIK 07] MIKAMI K.-I., KAJIHARA M.
Growth rate of Nb₃Sn for reactive diffusion between Nb and Cu₉Sn_{0.3}Ti alloy. *Journal of Materials Science*, vol. 42, n° 19, 2007, p. 8178-8188.
- [MIN 94] MIN U.-S., LI J. C.
The microstructure and dealloying kinetics of a Cu-Mn alloy. *Journal of Materials Research*, vol. 9, n° 11, 1994, p. 2878-2883.

- [MIN 10] MINE Y., HORITA Z., MURAKAMI Y.
Effect of high-pressure torsion on hydrogen trapping in Fe–0.01mass% C and type 310S austenitic stainless steel. *Acta Materialia*, vol. 58, n° 2, 2010, p. 649-657.
- [MOH 17] MOHAMMADZADEH R., MOHAMMADZADEH M.
Correlation between stacking fault energy and lattice parameter in nanocrystalline FeNi austenitic stainless steels by atomistic simulation study. *International Journal of Modelling and Simulation*, vol. 37, n° 4, 2017, p. 227-233.
- [MOR 11] MORRISH R., DORAME K., MUSCAT A.
Formation of nanoporous Au by dealloying AuCu thin films in HNO₃. *Scripta Materialia*, vol. 64, n° 9, 2011, p. 856-859.
- [MUR 98] MURRY G.
Transformations dans les aciers. *Techniques de l'Ingénieur*, vol. base documentaire : TIB500DUO., n° ref. article : m1115, 1998.
- [NEZ 17] NEZAKAT M., AKHIANI H., SABET S. M., SZPUNAR J.
Electron backscatter and X-ray diffraction studies on the deformation and annealing textures of austenitic stainless steel 310S. *Materials Characterization*, vol. 123, 2017, p. 115-127.
- [NGU 16] NGUYEN T. K. L.
New generation of epoxy networks based on ionic liquids: From structuration to final properties. Thèse de doctorat, INSA Lyon, 2016.
- [NIC 16] NICHOLAS W., MATTHEW B., LIUYANG Z., XIANQIAO W.
Failure mechanisms and scaling laws of nanoporous aluminum: A computational study. *Advanced Engineering Materials*, vol. 18, 2016, p. 632-642.
- [NIL] NILACO Materials composition, <http://nilaco.jp/pdf/ALLOY.000121.pdf>.
- [NIM] NIMSDiffusion database (Kakusan), http://diffusion.nims.go.jp/index_en.html.
- [OHN 76] OHNO A.
The solidification of metals. Chijin Shokan, 1976.
- [OKU 17] OKULOV I. V., WEISSMULLER J., MARKMANN J.
Dealloying-based interpenetrating-phase nanocomposites matching the elastic behavior of human bone. *Scientific Reports*, vol. 7, n° 20, 2017, p. 77-87.
- [OKU 18a] OKULOV A., VOLEGOV A., WEISSMULLER J., MARKMANN J., OKULOV I.
Dealloying-based metal-polymer composites for biomedical applications. *Scripta Materialia*, vol. 146, 2018, p. 290-294.
- [OKU 18b] OKULOV I., OKULOV A., SOLDATOV I., LUTHRINGER B., WILLUMEIT-ROMER R., WADA T., KATO H., WEISSMULLER J., MARKMANN J.
Open porous dealloying-based biomaterials as a novel biomaterial platform. *Materials Science and Engineering: C*, vol. 88, 2018, p. 95-103.
- [OLI 92] OLIVER W., PHAR G.
An improved technique for determining hardness and elastic modulus using load and displacement sensing indentation experiments. *Journal of Materials Research*, vol. 7, 1992, p. 1564-1583.

- [OPP 91] OPPENHEIM I., TREVOR DENNIS J. AND CHIDSEY C. E. D., TREVOR P. L., SIERADZKI K.
In situ scanning tunneling microscopy of corrosion of silver-gold alloys. *Science*, vol. 254, n° 5032, 1991, p. 687-689.
- [PAG 02] PAGANIN D., MAYO S. C., GUREYEV T. E., MILLER P. R., WILKINS S. W.
Simultaneous phase and amplitude extraction from a single defocused image of a homogeneous object. *Journal of Microscopy*, vol. 206, 2002, p. 33-40.
- [PAR 83] PARNIERE P.
Métallographie par diffraction des rayons X, des électrons et des neutrons. *Techniques de l'Ingénieur*, vol. M100, 1983, p. 1-27.
- [PAR 06] PARIDA S., KRAMER D., VOLKERT C. A., RÖSNER H., ERLEBACHER J., WEISSMÜLLER J.
Volume change during the formation of nanoporous gold by dealloying. *Physic Review Letters*, vol. 97, 2006, Page 035504.
- [PAS 02] PASCAULT J. P., SAUTEREAU H., VERDU J., WILLIAMS R. J. J.
Thermosetting polymers. New York and Basel, Marcel Dekker, 2002.
- [PAS 10] PASCAULT J.-P., WILLIAMS R.
Epoxy polymers: New materials and innovations. 2010.
- [PET 09] PETEGEM S. V., BRANDSTETTER S., MAASS R., HODGE A. M., EL-DASHER B. S., BIENER J., SCHMITT B., BORCA C., VAN SWYGENHOVEN H.
On the microstructure of nanoporous gold: An X-ray diffraction study. *Nano Letters*, vol. 9, n° 3, 2009, p. 1158-1163.
- [PIA 13] PIA G., DELOGU F.
On the elastic deformation behavior of nanoporous metal foams. *Scripta Materialia*, vol. 69, n° 11, 2013, p. 781-784.
- [PIC 63] PICKERING H. W., SWANN P. R.
Electron metallography of chemical attack upon some alloys susceptible to stress corrosion cracking. *Corrosion*, vol. 19(11), 1963, p. 373-389.
- [PIC 67] PICKERING W., WAGNER C.
Electrolytic dissolution of binary alloys containing a noble Metal. *Journal of Electrochemical Society*, vol. 114(7), 1967, p. 698-706.
- [PIC 83] PICKERING H.
Characteristic features of alloy polarization curves. *Corrosion Science*, vol. 23, n° 10, 1983, p. 1107-1120.
- [POR 09] PORTER D. A., EASTERLING K. E., SHERIF M.
Phase transformations in metals and alloys. CRC press, 2009.
- [PUG 03] PUGH D. V., DURSUN A., CORCORAN S. G.
Formation of nanoporous platinum by selective dissolution of Cu from Cu_{0.75}Pt_{0.25}. *Journal of Materials Research*, vol. 18, n° 1, 2003, p. 216-221.
- [QIA 07] QIAN L. H., CHEN M. W.
Ultrafine nanoporous gold by low-temperature dealloying and kinetics of nanopore formation. *Applied Physics Letters*, vol. 91, n° 8, 2007, Page 083105.

- [QIN 16] QIN S., ZHANG H., LIU J., ZHENG W.
Electron backscattered diffraction analysis of the effect of deformation temperature on the microstructure evolution in a typical nickel-based superalloy during hot deformation. *Journal of Materials Research*, vol. 31, n° 9, 2016, p. 1348-1360.
- [QIU 14] QIU H.-J., ITO Y., CHEN M.
Hierarchical nanoporous nickel alloy as three-dimensional electrodes for high-efficiency energy storage. *Scripta Materialia*, vol. 89, 2014, p. 69-72.
- [RAJ 13] RAJPUT P., GUPTA A., DETLEFS B., KOLB D. M., POTDAR S., ZEGENHAGEN J.
Dealloying of CuAu studied by hard X-ray photoelectron spectroscopy. *Journal of Electron Spectroscopy and Related Phenomena*, vol. 190, 2013, p. 289-294.
- [REN 05] RENARD J., BLASSIAU S., BONNET B., CHEVALIER Y., COLIN C., DOMIZIO S. D., THIONNET A.
Elaboration, microstructure et comportement des matériaux composites à matrice polymère. Paris : Hermès Science publications, 2005.
- [REN 06] RENNER F. U., STIERLE A., DOSCH H., KOLB D. M., LEE T.-L., ZEGENHAGEN J.
Initial corrosion observed on the atomic scale. *Nature*, vol. 439(9), 2006, p. 701-710.
- [REN 08] RENNER F. U., STIERLE A., DOSCH H., KOLB D. M., LEE T. L., ZEGENHAGEN J.
In situ X-ray diffraction study of the initial dealloying and passivation of Cu₃Au(111) during anodic dissolution. *Physical Review B*, vol. 77, 2008, Page 235433.
- [REN 17] REN Y., LI J., YANG K.
Preliminary study on porous high-manganese 316L stainless steel through physical vacuum dealloying. *Acta Metallurgica Sinica (English Letters)*, vol. 30, n° 8, 2017, p. 731-734.
- [RIC 86] RICCARDI C. C., WILLIAMS R. J. J.
A kinetic scheme for an amine-epoxy reaction with simultaneous etherification. *Journal of Applied Polymer Science*, vol. 32, n° 2, 1986, p. 3445-3456.
- [ROL 04] ROLLETT A., HUMPHREYS F., GREGORY S., HATHERLY M.
Recrystallization and related annealing phenomena (second edition). Elsevier, Oxford, second edition édition, 2004.
- [ROU 07] ROUYA E., REED M., KELLY R., BART-SMITH H., BEGLEY M. R., ZANGARI G.
Synthesis of nanoporous gold structures via dealloying of electroplated Au-Ni alloy films. *ECS Trans*, vol. 6, 2007, p. 41-50.
- [RUS 13] RUSTE J.
Microscopie électronique à balayage - principe et équipement. *Techniques de l'Ingénieur*, vol. P825, 2013, p. 1-19.
- [SAI 94] SAITO T., TORIWAKI J.
New algorithms for euclidean distance transformation on an n-dimensional digitized picture with applications. *Pattern Recognition*, vol. 27, 1994, p. 1551-1565.

- [SAI 16] SAITO J.
Formation mechanism of porous Fe from Fe-Ni single crystal by dealloying in a Mg bath (in Japanese). Master's thesis, Tohoku University, 2016.
- [SAL 13] SALVO L., LOETENS P., MAIRE E., ZABLER S., BLANDIN J., BUFFIÈRE J., LUDWIG W., BOLLER E., BELLET D., JOSSEROND C.
X-ray micro-tomography an attractive characterisation technique in materials science. *Nuclear Instruments and Methods in Physics Research Section B: Beam Interactions with Materials and Atoms*, vol. 200, 2013, p. 273-286.
- [SBI 10] SBIAI A., MAAZOUZB A., FLEURY E., SAUTEREAU H., KADDAMI H.
Short date palm tree fibers/polyepoxy composites prepared using Rtm process: Effect of tempo mediated oxydation of the fibers. *BioResources*, vol. 5(2), 2010, p. 672-689.
- [SBI 11] SBIAI A.
Matériaux composites à matrice epoxyde chargée par des fibres de palmier dattier : Effet de l'oxydation au tempo sur les fibres. Thèse de doctorat, INSA Lyon, 2011.
- [SCA 12] SCAGLIONE F., RIZZI P., BATTEZZATI L.
De-alloying kinetics of an Au-based amorphous alloys. *Journal of Alloys and Compounds*, vol. 536, 2012, p. S60-S64.
- [SCH 12] SCHINDELIN J., ARGANDA-CARRERAS I., FRISE E., KAYNIG V., LONGAIR M., PIETZSCH T., PREIBISCH S., RUEDEN C., SAALFELD S., SCHMID B., TINEVEZ J., WHITE D., HARTENSTEIN V., ELICEIRI K., TOMANCAK P., CARDONA A.
Fiji: an open-source platform for biological-image analysis. *Nature Methods*, vol. 9(7), 2012, p. 676-682.
- [SEK 08] SEKER E., GASKINS J., BART-SMITH H., ZHU J., REED M., ZANGARI G., KELLY R., BEGLEY M.
The effects of annealing prior to dealloying on the mechanical properties of nanoporous gold microbeams. *Acta Materialia*, vol. 56, n° 3, 2008, p. 324-332.
- [SHI 15] SHI H., CHEN K., SHEN Z., WU J., DONG X., ZHANG L., SHAN A.
Twin boundary characters established during dynamic recrystallization in a nickel alloy. *Materials Characterization*, vol. 110, 2015, p. 52-59.
- [SNE 65] SNEDDON I.
The relation between load and penetration in the axisymmetric boussineq problem for a punch of arbitrary profile. *International Journal Engineering Science*, vol. 3, 1965, p. 47-57.
- [SNY 08] SNYDER J., LIVI K., ERLEBACHER J.
Dealloying silver/gold alloys in neutral silver nitrate solution: Porosity evolution, surface composition, and surface oxides. *Journal of Electrochemical Society*, vol. 155, 2008, p. C464-C473.
- [SNY 10] SNYDER J., FUJITA T., CHEN M., ERLEBACHER J.
Oxygen reduction in nanoporous metal-ionic liquid composite. *Nature Materials*, vol. 9, 2010, p. 904-907.
- [SRI 09] SRIVASTAVA R., MANI P., STRASSER P.
In situ voltammetric de-alloying of fuel cell catalyst electrode layer: A combined

- scanning electron microscope/electron probe micro-analysis study. *Journal of Power Sources*, vol. 190, n° 1, 2009, p. 40-47.
- [STE 16] STENNER C., SHAO L.-H., MAMEKA N., WEISSMÜLLER J.
Piezoelectric gold: Strong charge-load response in a metal-based hybrid nanomaterial. *Advances fonctionnal materials*, vol. 26(28), 2016, p. 5174-5181.
- [STO 08] STOCK S. R.
Recent advances in X-ray microtomography applied to materials. *International Materials Reviews*, vol. 53(3), 2008, p. 129-181.
- [SUN 08] SUN Y., BALK T. J.
A multi-step dealloying method to produce nanoporous gold with no volume change and minimal cracking. *Scripta Materialia*, vol. 58, n° 9, 2008, p. 727-730.
- [SUN 13] SUN X.-Y., XU G.-K., LI X., FENG X.-Q., GAO H.
Mechanical properties and scaling laws of nanoporous gold. *Journal of Applied Physics*, vol. 113, n° 2, 2013, Page 023505.
- [SUN 15] SUN S., CHEN X., BADWE N., SIERADZKI K.
Potential-dependent dynamic fracture of nanoporous gold. *Nature Materials*, vol. 14, 2015, p. 894-898.
- [SUN 16] SUN Y., REN Y., YANG K.
New preparation method of micron porous copper through physical vacuum dealloying of CuZn alloy. *Materials Letters*, vol. 165, 2016, p. 1-4.
- [TAK 05] TAKEUCHI A., INOUE A.
Classification of bulk metallic glasses by atomic size difference, heat of mixing and period of constituent elements and its application to characterization of the main alloying element. *Materials Transactions*, vol. 46, n° 12, 2005, p. 2817-2829.
- [TAP 10] TAPPAN B., STEINER S., LUTHER E.
Nanoporous metal foams. *Angewandte Chemie International Edition*, vol. 49, n° 27, 2010, p. 4544-4565.
- [THA 14] THAKUR A., MOHANTY A., GANGOPADHYAY S.
Comparative study of surface integrity aspects of Incoloy 825 during machining with uncoated and CVD multilayer coated inserts. *Applied Surface Science*, vol. 320, 2014, p. 829-837.
- [THI 13] THIERY C.
Tomographie à rayons X. *Techniques de l'Ingénieur*, vol. P950, 2013, p. 1-35.
- [THO 09] THORAT I. V., STEPHENSON D. E., ZACHARIAS N. A., ZAGHIB K., HARB J. N., WHEELER D. R.
Quantifying tortuosity in porous Li-ion battery materials. *Journal of Power Sources*, vol. 188, n° 2, 2009, p. 592-600.
- [TOU 75] TOULOUKIAN Y. S.
Thermal expansion: Metallic elements and alloys. New York: IFI Plenum, 1975.
- [TSU 13] TSUDA M., WADA T., KATO H.
Kinetics of formation and coarsening of nanoporous α -titanium dealloyed with Mg melt. *Journal of Applied Physics*, vol. 114, n° 11, 2013, Page 113503.

- [TSU 14] TSUDA M.
Formation mechanism of porous metals during liquid metal dealloying process (in Japanese). Thèse de doctorat, Tohoku University, 2014.
- [VOL 06] VOLKERT C. A., LILLEODDEN E. T.
Size effects in the deformation of sub-micron Au columns. *Philosophical Magazine*, vol. 86, n° 33-35, 2006, p. 5567-5579.
- [WAD 11a] WADA T., SETYAWAN A. D., YUBUTA K., KATO H.
Nano- to submicro-porous β -Ti alloy prepared from dealloying in a metallic melt. *Scripta Materialia*, vol. 65, n° 6, 2011, p. 532-535.
- [WAD 11b] WADA T., YUBUTA K., INOUE A., KATO H.
Dealloying by metallic melt. *Materials Letters*, vol. 65, n° 7, 2011, p. 1076-1078.
- [WAD 13] WADA T., KATO H.
Three-dimensional open-cell macroporous iron, chromium and ferritic stainless steel. *Scripta Materialia*, vol. 68, n° 9, 2013, p. 723-726.
- [WAD 14] WADA T., ICHITSUBO T., YUBUTA K., SEGAWA H., YOSHIDA H., KATO H.
Bulk-nanoporous-silicon negative electrode with extremely high cyclability for lithium-ion batteries prepared using a top-down process. *Nano Letters*, vol. 14, n° 8, 2014, p. 4505-4510.
- [WAD 16a] WADA T., YAMADA J., KATO H.
Preparation of three-dimensional nanoporous Si using dealloying by metallic melt and application as a lithium-ion rechargeable battery negative electrode. *Journal of Power Sources*, vol. 306, 2016, p. 8-16.
- [WAD 16b] WADA T., YUBUTA K., KATO H.
Evolution of a bicontinuous nanostructure via a solid-state interfacial dealloying reaction. *Scripta Materialia*, vol. 118, 2016, p. 33-36.
- [WAD 18] WADA T., GESLIN P.-A., KATO H.
Preparation of hierarchical porous metals by two-step liquid metal dealloying. *Scripta Materialia*, vol. 142, 2018, p. 101-105.
- [WAN 13] WANG K., WEISSMULLER J.
Composites of nanoporous gold and polymer. *Advanced Materials*, vol. 25, n° 9, 2013, p. 1280-1284.
- [WAN 14] WANG J., CHEN N., LIU P., WANG Z., LOUZGUINE-LUZGIN D., CHEN M., PEREPEZKO J.
The ultrastable kinetic behavior of an Au-based nanoglass. *Acta Materialia*, vol. 79, 2014, p. 30-36.
- [WAN 15a] WANG K., KOBLER A., KÜBEL C., JELITTO H., SCHNEIDER G., WEISSMULLER J.
Nanoporous-gold-based composites: toward tensile ductility. *NPG Asia Materials*, vol. 7(e187), 2015.
- [WAN 15b] WANG Y., ZHANG W., INOUE A.
Nanoporous Cu wide ribbons with good mechanical integrity. *Materials Science and Engineering B*, vol. 177, 2015, p. 532-535.

- [WAN 15c] WANG Z., LIU J., QIN C., LIU L., ZHAO W., INOUE A.
Fabrication and new electrochemical properties of nanoporous Cu by dealloying amorphous CuAl alloys. *Intermetallics*, vol. 56, 2015, p. 48-55.
- [WAN 15d] WANG Z., LIU J., QIN C., YU H., XIA X., WANG C., ZHANG Y., HU Q., ZHAO W.
Dealloying of Cu-based metallic glasses in acidic solutions: Products and energy storage applications nanomaterials. *Nanomaterials*, vol. 5, 2015, p. 697-720.
- [WAN 17] WANG K., HARTIG C., BLANKENBURG M., MÜLLER M., GÜNTHER R., WEISSMÜLLER J.
Local flow stresses in interpenetrating-phase composites based on nanoporous gold — In situ diffraction. *Scripta Materialia*, vol. 127, 2017, p. 151-155.
- [WEI 09] WEISSMULLER J., NEWMAN R. C., JIN H.-J., HODGE A. M., KYSAR J. W.
Nanoporous Metals by Alloy Corrosion: Formation and Mechanical Properties. *MRS Bulletin*, vol. 34, n° 8, 2009, p. 577-586.
- [WEI 18] WEI D., KOIZUMI Y., CHIBA A.
Porous surface structures in biomedical Co-Cr-Mo alloy prepared by local dealloying in a metallic melt. *Materials Letters*, vol. 219, 2018, p. 256-259.
- [WES 24] WESTBROOK J. H., CONRAD H.
The Science of hardness testing and its research applications. 1924.
- [WIL 18] WILMERS J., BARGMANN S.
Functionalisation of metal-polymer-nanocomposites: Chemoelectromechanical coupling and charge carrier transport. *Extreme Mechanics Letters*, vol. 21, 2018, p. 57-64.
- [WIR 14] WIRTH E., GUITTENY F., MATHONAT C.
Thermogravimétrie. *Techniques de l'Ingénieur*, vol. P1260, 2014, p. 1-29.
- [WIT 12] WITSTOCK A., BIENER J., ERLEBACHER J., BAUMER M., Eds. *Nanoporous gold: From an Ancient Technology to a High-Tech Material*. RSC Nanoscience and Nanotechnology The Royal Society of Chemistry, 2012.
- [XUE 14] XUE Y., MARKMANN J., DUAN H., WEISSMULLER J., HUBERT P.
Switchable imbibition in nanoporous gold. *Nature Communications*, vol. 5, 2014, p. 1-8.
- [YE 14] YE X.-L., LU N., LI X.-J., DU K., TAN J., JIN H.-J.
Primary and secondary dealloying of Au(Pt)-Ag: Structural and compositional evolutions, and volume shrinkage. *Journal of Electrochemical Society*, vol. 161(12), 2014, p. C517-526.
- [YE 16] YE X.-L., JIN H.-J.
Corrosion-induced strengthening: Development of high-strength nanoporous metals. *Advanced Engineering Materials*, vol. 182, n° 6, 2016, p. 1050-1058.
- [YU 16] YU S., YUBUTA K., WADA T., KATO H.
Three-dimensional bicontinuous porous graphite generated in low temperature metallic melt. *Carbon*, vol. 96, 2016, p. 403-410.
- [ZHA 10] ZHAO C., WANG X., QI Z., JI H., ZHANG Z.
On the electrochemical dealloying of Mg-Cu alloys in a NaCl aqueous solution. *Corrosion Science*, vol. 52, n° 12, 2010, p. 3962-3972.

-
- [ZHA 13] ZHANG X., LI Y., LIU Y., ZHANG H.
Fabrication of a bimodal micro/nanoporous metal by the Gasar and dealloying processes. *Materials Letters*, vol. 92, 2013, p. 448-451.
- [ZHA 15] ZHAO F., ZENG J., SANTOS G. M., SHIH W.-C.
In situ patterning of hierarchical nanoporous gold structures by in-plane dealloying. *Materials Science and Engineering: B*, vol. 194, 2015, p. 34-40.
- [ZHA 16] ZHAO Y., WANG X., HUANG J., CHEN X., CAO L., MU M.
Affection of Cu content on the phase evolution during the dealloying of Ag-Cu alloys using electrochemical noise with Hilbert spectra analysis. *Materials Letters*, vol. 183, 2016, p. 165-169.
- [ZHA 17] ZHAO C., WADA T., ANDRADE V. D., WILLIAMS G. J., GELB J., LI L., THIEME J., KATO H., CHEN KAREN Y., CHEN-WIEGART
Three-dimensional morphological and Chemical evolution of nanoporous stainless steel by liquid metal dealloying. *ACS Applied Materials Interfaces*, vol. 9(39), 2017, p. 34172-34184.
- [ZIE 16] ZIEHMER M., HU K., WANG K., LILLEODDEN E. T.
A principle curvatures analysis of the isothermal evolution of nanoporous gold: Quantifying the characteristic length-scales. *Acta Materialia*, vol. 120, 2016, p. 24-31.

